CYANIDE BRIDGED MOLECULAR MAGNETIC MATERIALS WITH ANISOTROPIC TRANSITION METAL IONS: INVESTIGATION OF BISTABLE MAGNETIC PHENOMENA

A Dissertation

by

CAROLINA AVENDAÑO

Submitted to the Office of Graduate Studies of
Texas A&M University
in partial fulfillment of the requirements for the degree of

DOCTOR OF PHILOSOPHY

May 2010

Major Subject: Chemistry

CYANIDE BRIDGED MOLECULAR MAGNETIC MATERIALS WITH ANISOTROPIC TRANSITION METAL IONS: INVESTIGATION OF BISTABLE MAGNETIC PHENOMENA.

A Dissertation

by

CAROLINA AVENDAÑO

Submitted to the Office of Graduate Studies of
Texas A&M University
in partial fulfillment of the requirements for the degree of

DOCTOR OF PHILOSOPHY

Approved by:

Chair of Committee,	Kim R. Dunbar
Committee Members,	Marcetta Y. Darensbourg
	Francois P. Gabbai
	Winfried Teizer
Head of Department,	David H. Russel

May 2010

Major Subject: Chemistry

ABSTRACT

Cyanide Bridged Molecular Magnetic Materials with Anisotropic Transition Metal Ions: Investigation of Bistable Magnetic Phenomena.

(May 2010)

Carolina Avendaño, B.S., Viterbo University

Chair of Advisory Committee: Dr. Kim R. Dunbar

The work presented herein focuses on the synthesis and characterization of new cyanide bridged molecular magnetic materials that form discrete molecules as well as three dimensional networks. This research is inspired by the recognition that the Prussian blue (PB) family exhibits a wide range of interesting magnetic properties such as photomagnetism, spin crossover, and high T_C magnets owing to the presence of the cyanide bridge that promotes magnetic communication between adjacent metal spins. An underexplored facet of this research is the systematic development of the topic with anisotropic metal ions research that was undertaken as part of this dissertation. The resulting discoveries are materials that exhibit a wide range of bistable magnetic properties, including photomagnetism, long range magnetic ordering, SMM, and exchange-biased SMM behavior.

New Prussian Blue analogs are presented in Chapter II of this thesis that are based on the nearly unexplored hexacyanoosmate(III) ion. A family of Co^{II} PB derivatives of Os^{III} were found to exhibit photomagnetic and charge transfer induced spin transition (CTIST) behavior and a study of alkali metal cation dependence revealed

marked differences in both the photomagnetic and CTIST properties, with the highest ordering temperature being observed for the K^+ analog which exhibits a T_C of 28.5 K.

The phenomenon of linkage isomerism reported for PB analogs and other molecular materials that incorporate the $[Cr(CN)_6]^{3-}$ ion wherein the CN ligand reverses its binding mode between the two metal centers was studied in detail as described in Chapter III. Small molecule models that incorporate $[Cr(CN)_6]^{3-}$ and Co^{II} ions were investigated by single crystal X-ray crystallography, magnetism, and solution IR studies and the data led to useful mechanistic information about the nature of the cyanide reversal process.

The use of the anisotropic hexacyanoosmate(III) anion to form a trinuclear species with Mn^{III} was undertaken in the study described in Chapter IV. The first SMM based on the hexacyanoosmate(III) ion was discovered and found to exhibit a very rare exchange biased SMM phenomena in one of its crystal forms. In Chapter V new building blocks with the pentadentate MPPA ligand are described which are ideally suited for the preparation of a range of model compounds of the dinuclear and trinuclear variety.

Para el amor de mi vida, Mateo

"It is human nature to stretch,
to go, to see, to understand.
Exploration is not a choice,
really; it's an imperative"

-Michel Collins,
Apollo 11Astronaut

ACKNOWLEDGEMENTS

At the beginning of this path it was very much emphasized that a Ph.D. degree was an individual effort and that only as your individual ideas developed would the final goal be achieved. Nevertheless, as time passed I realized that this goal required a network of individuals whose constant guidance and support would be essential and who would play a major role for my success as a Ph.D. candidate. Here are a few words of gratitude to all of those who made this dream a reality.

It is difficult to overstate my gratitude to my Ph.D. supervisor, Prof. Kim R. Dunbar. With her enthusiasm, her inspiration, and her great efforts to explain things clearly and simply, she helped to make chemistry fun for me. Throughout my thesis-writing period, she provided encouragement, sound advice, good teaching, and lots of good ideas. Her efforts as an advisor and as a role model have provided me the inspiration and the skills to face my future challenges. In addition, my success in graduate school would not be possible without the support, patience, and guidance of my committee members, Prof. Marcetta Y. Darensbourg, Prof. Francois P. Gabbai, and Prof. Winfried Teizer.

As I traveled the path of a graduate student I learned the importance and the need to share and collaborate with others in order to tackle our scientific inquiries. As a result, I must emphasize how significant the contributions of my collaborators were to the development of the projects presented in this dissertation. Thank you Dr. Corine Mathoniere, Dr. Wolfgang Wernsdorfer, Dr. Nattamai Bhuvanesh, and Dr. Andrey

Prosvirin for your commitment and enthusiasm to these projects and for giving me the opportunity to learn from you.

Neeedless to say, during your time as a graduate student, the lab and its members become your second home and family. My time in the Dunbar lab was filled with joyful and enjoyable moments due to the people who surrounded me. Thanks to all the Dunbar group members (Nazario Lopez, Kristen and Ed Funck, Ian Giles, Sarah Lane, Heather Southerland, Zhongyue Zhang, Codi Sanders, Darryl Stepien, Dr. Hanhua Zhao, Dr. Helen Chifotides, Dr. Akira Ota, and Dr. Xinyi Wang, Mayela Canales, and Charlene Campbell) for making my graduate experience a lifetime memory. I am especially grateful to Prof. Michael Shatruk for showing me the road to follow and his obvious love and passion for science which is contagious. To my closest friends and confidents Ferdi and Yagmur Karadas, Dafhne Aguirre, and Alfredo Angeles, words don't come close to express my gratitude for all the times, good and bad, that you were there for me. Thank you.

Once you accomplish your dreams, it is easy sometimes to forget those who steered you in that direction, and as result I would like to take a few words to thank those who inspired me. To the science faculty of Viterbo University, especially professors Michael Collins, Ron Amel, Vaughn Rodgers, Kyle Backstrand, and Glena Temple, thank you for believing in me and for giving me the tools and encouragement to follow this career path. I am especially grateful to my high school, Colegio Santa Francisca Romana, which gave me the wings to fly and taught me the value of perseverance, compassion, and the pursuit of knowledge. I am indebted to my undergraduate friends,

Claire and Brian Moore, and my high school friends and sisters at heart Natalia Fernandez, Carolina Avila, Paola Mejia, and Maria Isabel Venegas, for helping me get through the difficult times and for all the emotional support, camaraderie, entertainment, and caring they have provided throughout the years.

I wish to thank my family whose love and support has made me the person I am today. I wish to thank my entire extended family (grandparents, uncles, aunts, cousins and friends) for filling my life with happiness and for teaching me the value of unconditional love; my in-laws, Gary and Sharon Hilfiger, for treating me as their daughter and for giving me their love and guidance; my brother and sister-in-law, Raul David and Angela, for being my greatest supporters, my best friends, and the best roommates I will ever have; my little brother Dario for his kind heart and his loving words; and my parents, Raul Avendaño and Luz Marina Ovalle, who bore me, raised me, supported me, taught me, and loved me. To them I owe it all.

Lastly, and most importantly, I would like to express my most sincere gratitude to my husband, Matthew G. Hilfiger, who was the reason I started on this path and who has been my biggest fan and the foundation I stand on. Thank you Mateo for dreaming and believing we could make this happen.

TABLE OF CONTENTS

CHAPTER Page

CHAPTER Page

LIST OF FIGURES

Page

Page

Page

Page

Page

Page

LIST OF SCHEMES

LIST OF TABLES

Page

LIST OF COMPOUNDS

(1) $[PPN]_3[Os(CN)_6]$

(2) $Co_3[Os(CN)_6]_2 \cdot 21H_2O$

(3) $Li_{0.4}Co_4[Os(CN)_6]_{2.8} \cdot 18H_2O$

(4) $Na_{1.4}Co_4[Os(CN)_6]_{3.13} \cdot 24H_2O$

(5) $K_{1.8}Co_4[Os(CN)_6]_{3.26} \cdot 22H_2O$

(6) $Rb_{2.6}Co_4[Os(CN)_6]_{3.53} \cdot 22H_2O$

(7) $Cs_{3.8}Co_4[Os(CN)_6]_{3.93} \cdot 22H_2O$

(8) $[Co^{II}(dppe)_2(H_2O)][BF_4]_2$

(9) $\{[Co^{II}(dppe)_2]_2[Co^{III}(CN)_6]\}(BF_4)$

(10) $\{[Co^{II}(dppe)_2]_2[Fe^{III}(CN)_6]\}(BF_4)$

(11) $[Co^{II}(dppe)_2(CN)][BF_4]$

(12) $[Co^{III}(dppe)_2(CN)_2][BF_4]$

(13) $Co^{II}(triphos)(CN)_2$

(14) $\{[Co^{II}{}_3(dppe)_4(MeCN)][Cr^{III}(CN)_6]_2\}$

(15) $\{[Co^{II}(tmphen)_2]_3[Cr^{III}(CN)_6]_2\}$

(16) $[Mn(salphen)(H_2O)_2][BF_4]$

(17) $[PPN]_3[Fe(CN)_6]$

(18) $PPN\{[Mn(salphen)(MeOH)]_2[Fe(CN)_6]\}$

(19) $PPN\{[Mn(salphen)(MeOH)]_2[Os(CN)_6]\}$

(20) MPPA

(21) $[Mn(MPPA)(MeCN)_2][ClO_4]_2$

(22) $[Co(MPPA)][BF_4]_2$

(23) $[Ni(MPPA)(MeCN)][BF_4]_2$

(24) $Cr(MPPA)Cl_3$

(25) $[V(MPPA)Cl_2]Cl$

(26) $[Fe(MPPA)Cl_2]Cl$

(27) $Fe(MPPA)Cl_2$

(28) $\{[Fe(MPPA)]_2\text{-}\mu\text{-}O\}[BF_4]_4$

(29) Tl(TCNQ) Phase I

(30) Tl(TCNQ) Phase II

CHAPTER I

INTRODUCTION TO MOLECULAR MATERIALS:

A MAGNETISM PERSPECTIVE*

Research in molecule-based materials is an emerging area of chemistry that focuses on the preparation of materials using molecular building blocks. The aim is to design molecular architectures for new types of electronic and magnetic devices that are tailored to exhibit a specific physical property by a judicious choice of the molecular precursor(s).[1-4] These efforts have resulted in frameworks that offer numerous advantages over conventional solid state materials, *viz.*, lower density, higher solubility, lower temperature assembly, and mechanical flexibility.[5-7] These characteristics are complemented by the capacity to build materials in the nanoscale size regime thereby rendering molecular materials attractive for a variety of technological applications.[3, 8-10] One strategy that is being explored for the development of new device components is the pursuit of materials whose bistability is induced by a resistance change rather than current flow.[11] Such "non-volatile" memory devices are capable of operating at increased speeds with less energy expenditure. A second, complementary approach to advances in computing that is receiving attention is based on an entirely different

---

This dissertation follows the style and format of the *Journal of the American Chemical Society*.

paradigm, namely the manipulation of both spin and electronic degrees of freedom. This field, dubbed "spintronics",[12-15] encompasses a range of novel applications for magnetic materials (Figure 1.1).

Research in molecular magnetism has spawned a new collaborative spirit between the physical and chemical sciences, and has led to the development of countless new types of magnetic materials that exhibit unusual and unexpected behavior. These materials are promising for various present and future specialized applications of magnets that require monodisperse, small magnetic particles; additionally, the discovery of molecules that can function as nanoscale magnets has allowed for the study of the interface between classical and quantum mechanical behavior. Moreover, molecular magnets have also been important from a theoretical standpoint since they represent relatively simple models for understanding magnetic exchange interactions and the role of anisotropy in magnetic assemblies.

MOLECULAR MAGNETISM

The Basics [10, 16, 17]

The property of magnetism is primarily due to the motion of electrons. Atoms are composed of charged particles (protons and electrons) that are in constant motion. The processes that create magnetic fields in an atom are nuclear spin, electron spin, and electron orbital motion. In magnetic materials, the most important source of magnetization are the electrons' orbital angular motion around the nucleus, and the electrons' intrinsic magnetic moment or spin. When there are unpaired electrons in a

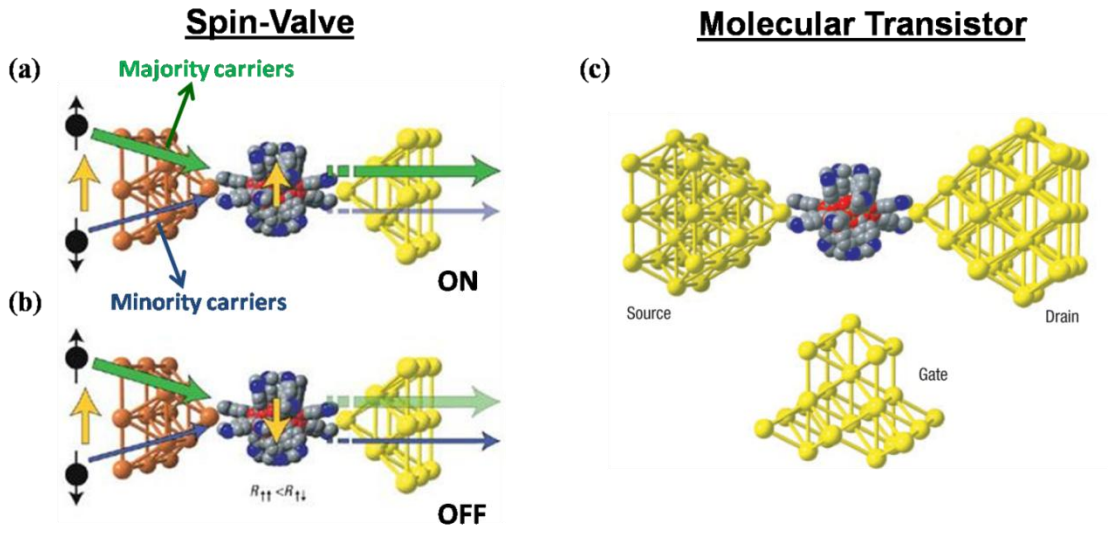

Figure 1.1. Schematic molecular spintronics based on single molecule magnets (SMM)**.** Yellow arrows represent the magnetization direction. Spin valves: (a) Parallel configuration of the magnetic source electrode (orange) and molecular magnetization, with diamagnetic drain electrode (yellow). Spin-up majority carriers (thick green arrow) are not affected by the molecular magnetization, whereas the spin-down minority carriers (thin blue arrow) are partially reflected back (magnetoresistance) (b) Antiparallel configuration: majority spin-up electrons are only partially transmitted by the differently polarized molecule, whereas the minority spin-down electrons pass unaffected. Assuming that the spin-up contribution to the current is larger in the magnetic contact, this configuration has higher resistance than that of the previous case. (c) Schematic of Single molecule magnet-based molecular transistors, in which a gate voltage can modulate transport. (Adapted from ref. 13)

solid magnetic behavior that is related to the number and orbital occupancies of the unpaired electrons is observed. In order to understand magnetic phenomena in solids it is necessary to know the following fundamental concepts: (1) a discrete magnetic moment can be associated with a particular ion or molecule in a solid and (2) these moments can interact with each other. From the point of view of the magnetic interactions, two cases can be distinguished. The first case is where the individual magnetic moments do not interact and behave without the influence of each others' existence and the second refers to the case were there are mutual interactions between individual magnetic moments which can lead to magnetic ordering.

Magnetic interactions in solids can be studied by the effect of an applied magnetic field on the magnetic moments of the ions or molecules in the material. In considering the first case in which the magnetic moments do not interact, two responses to the applied magnetic field can be observed. The first response refers to the scenario when all of the electrons in the ions or molecules of the material are paired. The field-induced electron circulations of the paired electrons generate a field opposed to the applied field resulting in *diamagnetism*. As such, a diamagnetic contribution can be calculated for any atom as well as groups of atoms. The diamagnetic susceptibility for a given electron is proportional to the square of its mean distance from the nucleus. Thus larger atoms are expected to have a larger diamagnetic interaction than smaller atoms. The contributions for common atoms are tabulated along with corrections for multiple bonds and are known as *Pascal's constants*.[18] Thus a diamagnetic susceptibility can be predicted merely by adding together the contributions from all of the atoms and bonds in

the molecule. Diamagnetic molar susceptibilities (χ_D) are negative and typically range from -1 to -100 $\times$ 10^{-6} emu/mol. They are also independent of field strength and temperature.

The second response to an external field refers to materials in which the constituent ions or molecules have unpaired electrons, i.e. atomic or molecular orbitals with one or more electrons in them, allowing the spin and orbital angular momenta of the unpaired electrons to interact with the field. In such a case the electrons align with the field and the material is said to be *paramagnetic*. Paramagnets do not retain any magnetization in the absence of an externally applied magnetic field because thermal motion causes the spins to become randomly oriented without it; thus the total magnetization becomes zero when the applied field is removed. Paramagnetic molar susceptibilities (χ_P) are positive and are typically temperature dependent. Temperature independent paramagnetism (TIP) can exist in systems wherein there is a permanent mixing of the wavefunctions of the ground (singlet) state and an excited state or states that are not thermally populated. Being on the order of 10^{-4} emu/mol, however, TIP is significantly smaller than temperature dependent paramagnetism at low temperatures. In both of the responses of a material to an external field presented so far the only scenario considered was the interaction of the spins with the applied field, and the interaction between the spins was purposely neglected.

Often, however, the individual magnetic moments or spins in a material interact in a cooperative fashion in such a manner that the direction of one spin influences the directions of its neighboring spins. These interactions are short-range and are only

important between nearest neighbors. In the bulk material, however, they can lead to long-range magnetic ordering which retains magnetization in the absence of an applied field below a certain critical temperature.

When the magnetic moments interact in such a way that all of them align in the same direction below a critical temperature (T_C) the material is a *ferromagnet*. In this type of material, the individual spins are *ferromagnetically coupled* to their neighboring spins meaning that the direction of one spin favors the parallel alignment of the neighboring spin(s). When the thermal fluctuations overcome the energy of the interactions between the spins, (known as the Curie temperature, T_C) the material will revert to a paramagnetic state.

The above described ferromagnetic case is the simplest case of a cooperative interaction between the individual magnetic moments (spins). Another relatively simple case results when the spins in a bulk sample interact in such a way that the spins align antiparallel to each other. This antiparallel alignment can result in two different magnetic behaviors depending on whether the magnitude of the spins is identical or not to each other. In the former case, the magnetic moments of the two spins compensate leading to a total cancellation of spin, and an *antiferromagnet* results, whereas in the latter situation the two moments do not compensate and a *ferrimagnet* is obtained. In antiferromagnets, the interaction between individual spins causes neighboring spin(s) to align in an antiparallel direction. This is referred to as *antiferromagnetic coupling*. Above the critical temperature (Néel Temperature, T_N) antiferromagnets typically behave as paramagnets, in the same manner as ferromagnetic materials. Ferrimagnets

typically behave like paramagnets above the T_N (T_C is not used to describe the critical temperature since the main interactions in ferrimagnetic materials are antiferromagnetic).

Graphic representations of the temperature dependence of the magnetic susceptibility (χ), are useful in identifying the magnetic character of a material. When measuring the magnetization (quantity of magnetic moment per unit volume; M) as a function of temperature in a constant applied field (H), it is possible to calculate the molar magnetic susceptibility ($M = \chi$ H). Plots of χT vs. T are the most informative for providing evidence of the magnetic character since each type of behavior has a characteristic curve as evidenced in Figure 1.2.

The nature of the interaction responsible for the coupling between the spins represented in Figure 1.2 can be classified into four categories based on the metallic/non-metallic properties of the material according to the literature: direct exchange, superexchange, indirect exchange and itinerant exchange. The latter two pertain to the coupling via the conduction electrons in magnetic metals. On the other hand, direct exchange and *superexchange* pertain to insulator cases where the magnetic moments are strongly localized on the magnetic centers and interact directly through space or through diamagnetic groups. Since the majority of the discussion in this dissertation pertains to the latter, the following brief explanation will be limited to the mechanism of the superexchange interactions.

The through-bond interaction, or superexchange, can be easily understood if one considers the case of two spin centers with completely quenched orbital contributions. In

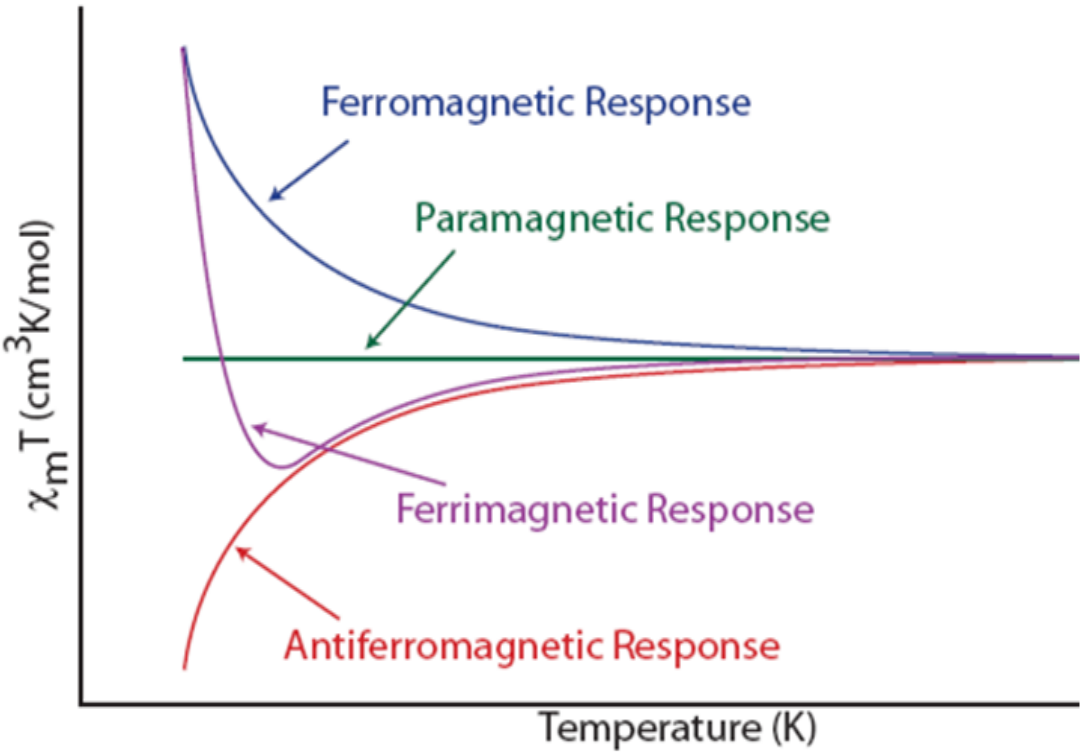

Figure 1.2. Representative plots of χT vs. T for the response to an external field for a paramagnetic (green), ferromagnetic (blue), antiferromagnetic (red), or ferromagnetic (purple) material.

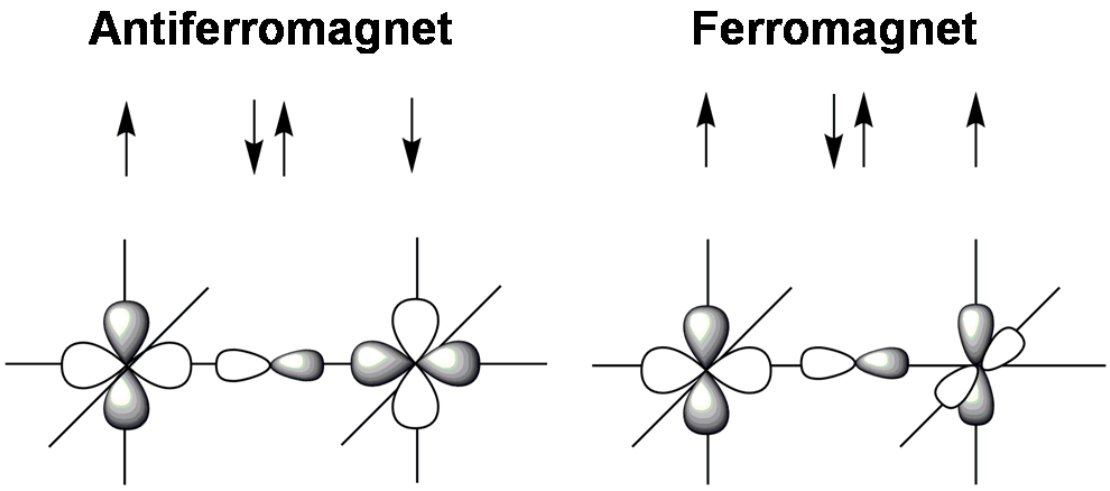

Scheme 1.1. Interactions of non-orthogonal orbitals through diamagnetic bridging ligands result in antiferromagnetic coupling ($J < 0$) while those of orthogonal orbitals result in ferromagnetic coupling ($J > 0$).

this case the superexchange pathway between the spins can be estimated by an assessment of the overlap of the orbitals containing the unpaired electrons, referred to as the magnetic orbitals. A large overlap between the magnetic orbitals tends to pair the spins, and the coupling is expected to be antiferromagnetic (Scheme 1.1). On the other hand, if the overlap is zero because the wavefunctions representing the magnetic orbitals have both large areas where they are both different from zero, but the overlaps are both positive and negative in such a way that the integral extended to the whole space is zero, then according to Hund's rule the spins will be parallel to each other, and a ferromagnetic coupling is established (Scheme 1.1). In both scenarios the magnetic exchange interaction between the spin centers can be described by using the well known Heisenberg, Dirac, Van Vleck Hamiltonian (HDVV), $H = -2JS_1S_2$, where the two spin centers are coupled by the exchange interaction parameter J. In this convention of the HDVV the magnetic exchange constant J is positive for ferromagnetic coupling and negative for antiferromagnetic coupling (Scheme 1.2). A more detailed explanation of the superexchange interaction will be presented when the role of cyanide as a bridging ligand is discussed (see pg. 29).

A Brief History

Molecular magnetism is a relatively recent scientific field which originated from the transformation of magnetochemistry into an interdisciplinary area when chemists and physicists began to collaborate very closely with the goal of designing, synthesizing, and characterising the magnetic properties of molecular based materials. The idea of using molecules, rather than the ionic and metallic lattices of typical solid state magnets, stems

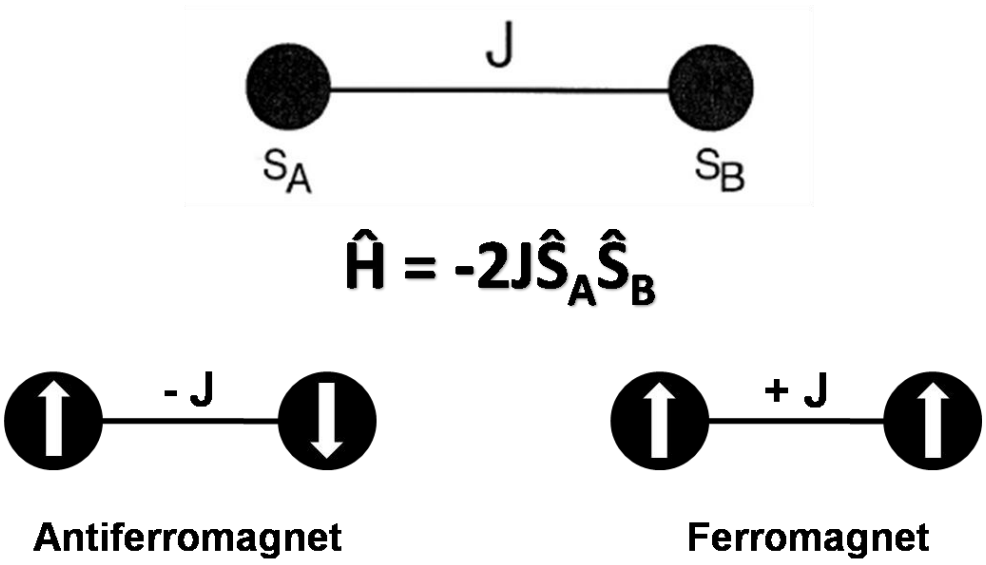

Scheme 1.2. The Heisenberg Hamiltonian: $\hat{H} = -2J\hat{S}_A\hat{S}_B$, where the two spins of the electron are effectively coupled by the exchange interaction parameter ***J***.

from the rapid development of functional molecular materials which commenced in the second half of the 20th century.

The transformation of the field of Magnetochemistry[17], i.e. the magnetic measurements of chemicals, into the field of Molecular Magnetism[16], i.e. the understanding of the design, preparation, and detailed spectroscopic and magnetic analyses of magnets based on paramagnetic molecules, would require time and effort from the chemists and the physicists in order to develop a deeper understanding of the magnetic phenomena. In the mid 20th century, while chemists were developing the initial topics of magnetism,[19] physicists were developing new methods for measuring magnetism (magnetometers, EPR) and phenomenological models to interpret them. The major contributions from the theoreticians at this stage were the Heisenberg, Dirac, Van Vleck[20] (HDVV) Hamiltonian describing spin interaction (H= -2J S_1S_2) and the Van Vleck equation, as well as the introduction by Néel[21] of a negative J value which together provided experimentalists with useful tools to compute the energy levels, the magnetic properties and to analyze magnetic data.

The transformation continued, and in the 1950's Bleaney and Bowers achieved what is considered the pioneering discovery in molecular magnetism. In 1952 both predicted the singlet-triplet gap in $Cu_2(O_2CCH_3)_4L_2$ (L = solvent) by fitting the temperature dependent magnetic behavior of the sample with the Van Vleck equation for two S=1/2 interacting spin centers[22, 23] (known today as the Bleaney-Bowers equation) (Figure 1.3). This prediction was quickly verified experimentally by subsequent

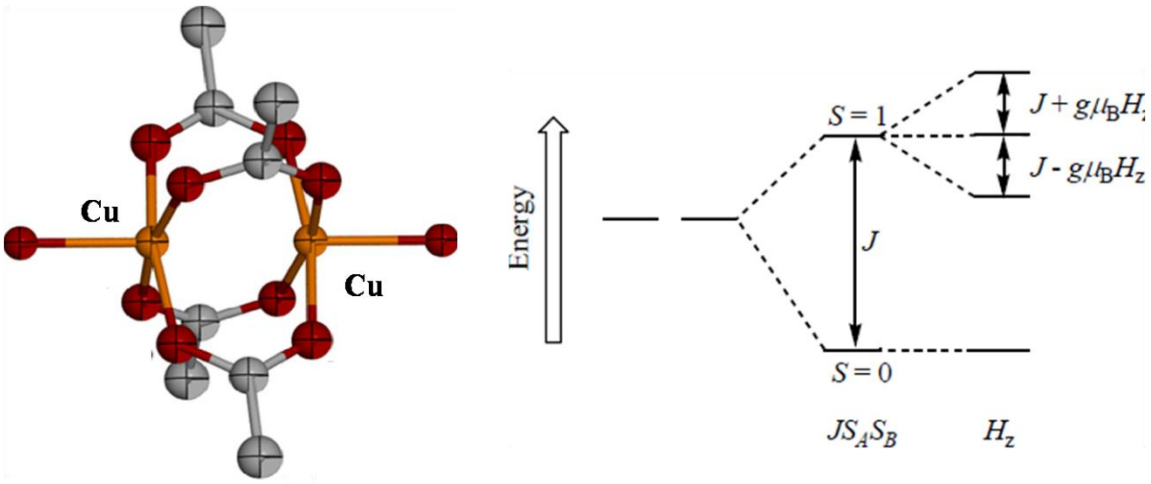

$$\chi = \frac{Ng_{av}^2\beta^2}{3kT}[1 + \frac{1}{3}(e^{-2J/kT})]^{-1}$$

Figure 1.3. The singlet-triplet gap in $Cu_2(O_2CCH_3)_4L_2$ (L = solvent) which was determined by fitting the temperature dependent magnetic behavior of the sample with the Van Vleck equation for two S=1/2 interacting spin centers, using what is known today as the Bleaney Bowers equation.

magnetic, crystallographic and spectroscopic studies.[24-31] This milestone in molecular magnetism led to a better understanding of the magnetic exchange interactions in molecular transition metal complexes. What followed was the collection of a plethora of data on molecular materials; while experimentalists focused on studying small dinuclear systems[32-38], theoreticians used already known 3D molecular systems[39-41] at that time, e.g., Prussian Blue, to develop theories that could explain the magnetic exchange interaction between spins through a molecular bridge, such as oxygen or cyanide.

The final steps to the full establishment of the field of molecular magnetism are many, but the major highlights can be summarized in the significant theoretical steps that were provided at the beginning of the 70's by the application of the models of chemical bonding and of exchange interactions to molecules as described by Anderson[42], Goodenough[43], and Kanamori[44] for three-dimensional solids, as well as a description of the interaction between unpaired electrons within a molecule in the modern language of molecular orbital theory. The description by Hoffman[45] of the exchange coupling for spin ½ dimers in which the antiferromagnetic contribution is expressed in terms of (ε_a-ε_b), where ε_a and ε_b are the energies of the bonding and antibonding combinations of the magnetic orbitals respectively was a language that chemist understood well, and was later exploited by Bencini[46] and Gatteschi[47] utilizing an angular overlap model (AOM)[48]. Similarly, Kahn used an approach based on a different quantum mechanical basis set to more clearly delineate the role of the overlap in determining the value of the exchange coupling [49] (Kahn Model). Kahn then continued to demonstrate these principles through the rational design of specific systems[50] exemplifying the success and promise of the

field of Molecular Magnetism in synthesizing magnets with tailored properties. This new insight into magnetic coupling provided the foundation for the study of structure-property relationships in magnetic materials.

The close interaction between physicists and chemist during the decades that followed allowed chemists to dare to tackle more complex materials, and convinced the physicists that it was indeed possible to observe new types of magnetic phenomena using molecular based materials. This multidisciplinary union allowed for the development of a common language and became the birth of the field known as *Molecular Magnetism.* [10, 16] The development of the field has been rapid and in the following sections several of the milestones of the field will be presented.

High T_C Magnets

In terms of obtaining useful compounds for the advancement of technology, the quest for molecular magnetic materials that order above room temperature was the initial goal of the field. While some pursued purely organic molecular materials, coordination chemists focused on materials that incorporated transition metals. The most exemplary results in the field incorporate paramagnetic transition metals, and, as a result, the vast majority of molecular magnets in the literature to date contain transition metal elements as the main constituent.

The first step towards room temperature ordered materials was achieved by Kahn's and Verdaguer's groups who reported the first example of a molecular ferrimagnet based on Cu^{II}-Mn^{II} derivatives.[51] The first major breakthrough in synthesizing high T_C magnets came in 1991 when Millers' group successfully

synthesized and characterized the first room temperature ferrimagnet, $V^{II}[TCNE]^{n-}{}_z[TCNE]^{2-}{}_{1-z/2}$ ($1< z < 2$; TCNE = tetracyanoethylene) (T_C = > 350K).[52] After this result, in 1993, Girolami's group reported a T_C of 230 K for the Prussian Blue analog (PB) $(TEA)_{0.5}Mn_{l.25}[V(CN)_5]\cdot 2H_2O$ (TEA = tetraethyl ammonium)[53], findings which were quickly followed by Verdaguer's group who reported the first room temperature cyanide based magnet, $V^{II}_{0.42}\, V^{III}_{0.58}[Cr^{III}(CN)_6]_{0.86}\cdot 2.8H_2O$ PB (T_C = 315 K).[54] This temperature was later (1999) surpassed by an analog of the same PB, $KV^{II}[Cr^{III}(CN)_6]\cdot 2H_2O$ which has a T_C = 376 K[55], the highest ordering temperature reported to date for a cyanide bridged molecular material (Figure 1.4).

Bistable Molecular Magnets

The primary goals of molecular magnetism have historically been directed towards increasing the T_C of magnetic materials for possible technological applications. In the past two decades, however, unexpected discoveries of exotic magnetic behavior in molecular materials have been noted. The underlying principle for the use of molecules or molecular assemblies in information processing or storage is *molecular bistability*. Molecular bistability may be defined as the ability for a molecular system to exhibit two stable states in a given range of external perturbation (*e.g.* temperature, light, pressure, field, etc.)[56, 57]. Usually, one of the states is the ground state and the other one is a metastable state. Some of the most studied bistable magnetic phenomena are *spin-crossover* (SCO), *photomagnetism*, and *single molecule magnetism* (SMM).[58, 59]

Thermally-induced SCO was observed for the first time more than half a century ago. It was only during the 1980's, however, that it was realized that spin-crossover

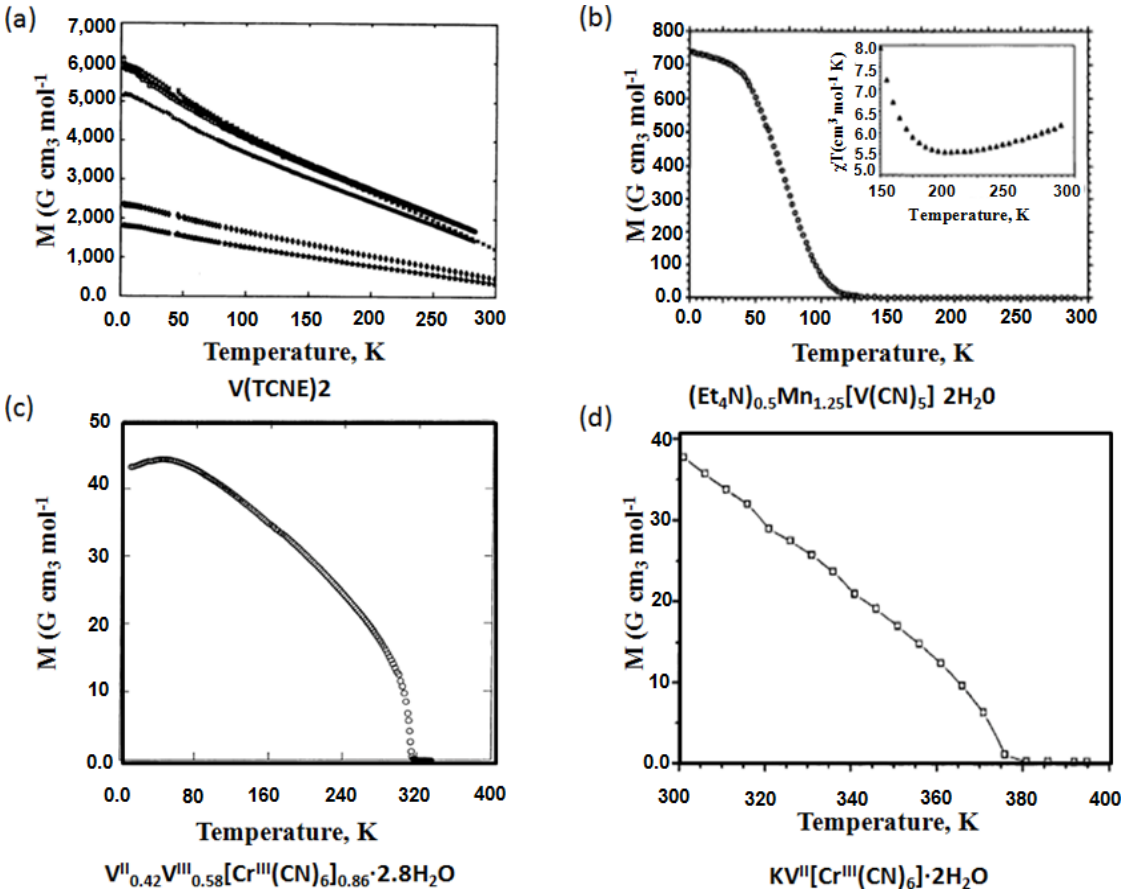

Figure 1.4. Plots of magnetization vs temperature of high Tc molecular magnets. (a)$V^{II}[TCNE]^{n-}{}_z[TCNE]^{2-}{}_{1-z/2}$ (1< z < 2) (T_C = > 350K), (b) $(TEA)_{0.5}Mn_{1.25}[V(CN)_5]\cdot 2H_2O$ (TEA = tetraethyl ammonium) (Tc = 230K), (c) $V^{II}{}_{0.42}\ V^{III}{}_{0.58}[Cr^{III}(CN)_6]_{0.86}\cdot 2.8H_2O$ PB (T_C = 315 K), and (d) $KV^{II}[Cr^{III}(CN)_6]\cdot 2H_2O$ which has a T_C = 376 K[55], the highest ordering temperature reported to date for a cyanide bridged molecular material.

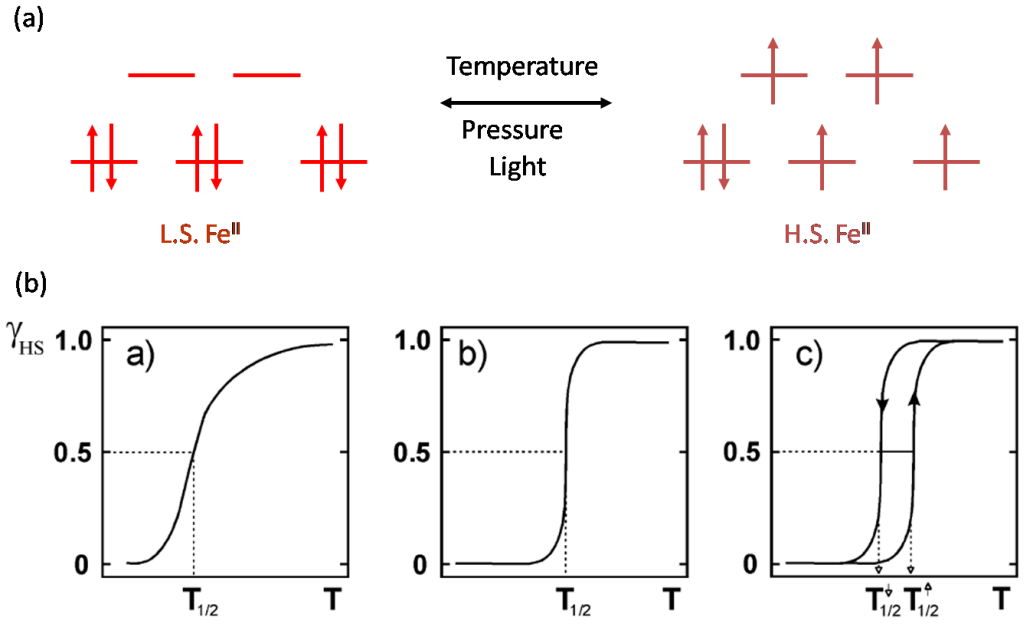

Figure 1.5. The spin crossover phenomenon. (a) Electron configurations of Fe^{II}, low spin to high spin. (b) Spin transition curves indicating increasing cooperativity (left to right).

compounds could be used as active elements of memory devices, and since then the topic has experienced a Renaissance.[60] The SCO phenomenon involves d^4, d^5, d^6, or d^7 first-row transition metal ions in octahedral surroundings that exhibit a crossover between a low-spin (LS) and a high-spin (HS) state (Figure 1.5a). This LS to HS crossover can be induced by a variation of an external stimuli, *e.g.* temperature, pressure, or light irradiation[61] (LIESST: Light Induced Exited Spin State Trapping[62] or LD-LISC: Ligand Driven Light-Induced Spin Changes[63]). When the process takes place in the solid state, it may be cooperative due to the inter- and intramolecular interactions resulting in a spin transition (Figure 1.5b). At low temperature, the thermodynamically stable state is the LS state, but above a certain temperature ($T_{1/2}$), the stable state is the HS state. This is due to the fact that the entropy associated with this HS state is much larger than the entropy associated with the LS state, and the entropy gain compensates the energy loss. The $T_{1/2}$ value is the temperature at which there is coexistence of 50% of molecules in the LS state and 50% of molecules in the HS state.[64] Another type of transition between spin states is the one driven by an intermolecular electron transfer. This phenomenon was discovered by Dei, Hendrickson and co-workers[65] in their studies of the electron transfer associated with the process: Co^{II}-semiquinonate^{-} → Co^{III}-catecholate^{2-} (Figure 1.6a). Similar behavior was later observed and extensively studied for the analogs of the PB family $A_xCo_y[Fe(CN)_6]_z \cdot nH_2O$ (A = alkali metal).[66-69] These studies by Hashimoto and Verdaguer's group revealed that the magnetic transition, known as a charge transfer induced spin transition (CTIST), is a result of an electron transfer between the Co and Fe

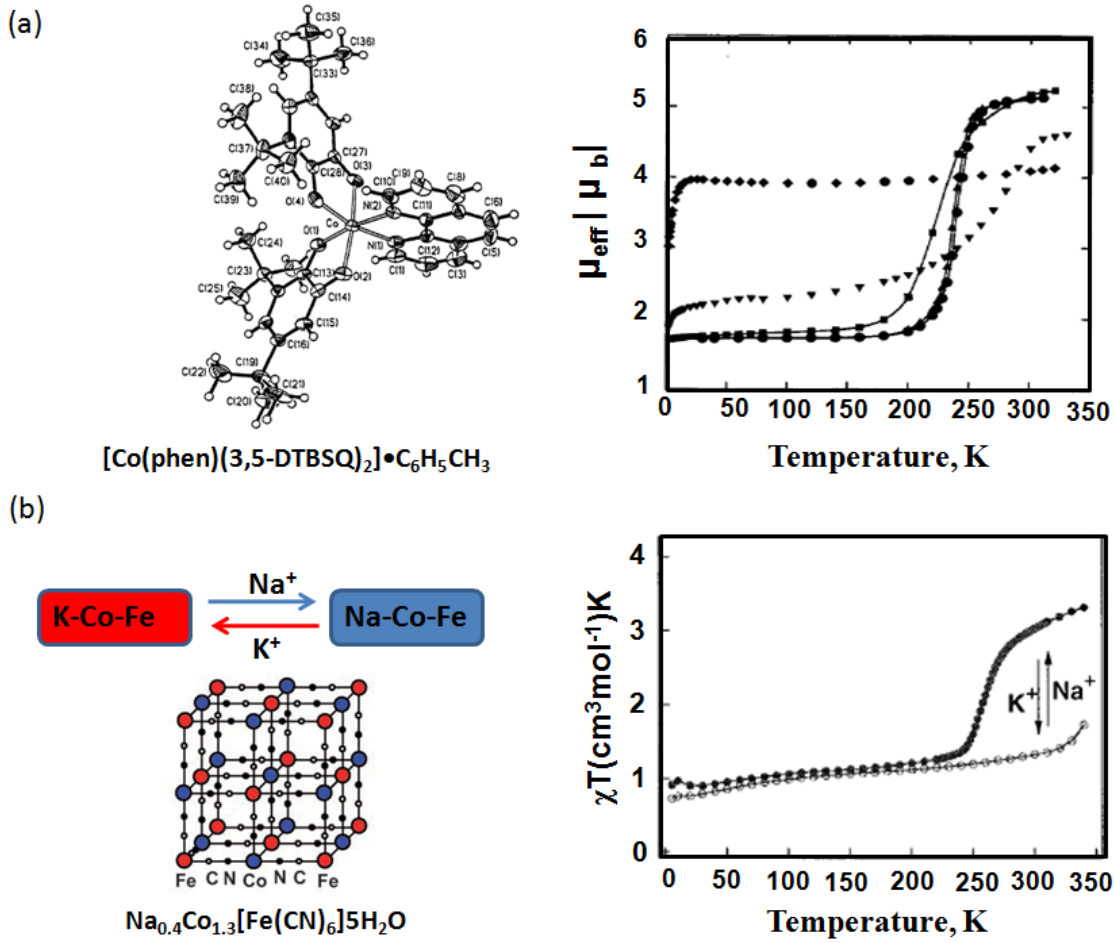

Figure 1.6. First examples of charge transfer induced spin transitions, (a) Co^{II}-semiquinonate^{-} → Co^{III}-catecholate^{2-} (b) $Na_{1.4}Co_{1.3}[Fe(CN)_6]_z \cdot 5H_2O$ Prussian Blue analog.

ions in the diamagnetic Co^{III}–Fe^{II} pair (LT phase) to form the paramagnetic Co^{II}–Fe^{III} pair (HT phase), which is accompanied by a related enhancement of the magnetization and the Curie temperature due to the increase in the number of magnetic pairs in the HT phase (Figure 1.6b).

Another type of bistable phenomenon results from the process that changes the magnetism of a system after absorption of a photon, referred to as *photomagnetism*.[70] The first observation of a photomagnetic process in molecular systems involving only transition metals was made by Gütlich, Decurtins and co-workers in 1984 and the phenomenon in these type of systems (SCO materials) became known as the LIESST effect (Figure 1.7a).[71, 72] These studies were followed by the discovery of Hashimoto and co-workers of the existence of a photomagnetic effect in the PB analog formulated as $K_{0.4}Co_{1.3}[Fe(CN)_6]_1 \cdot 5H_2O$ (or $K_{0.3}Co_1[Fe(CN)_6]_{0.77} \cdot 3.8H_2O$).[73] As previously discussed, some analogs in the CoFe PB family of compounds exhibit a metal-to-metal charge transfer (MM'CT) band ($Fe^{II} \rightarrow Co^{III}$) in the visible region, which gives rise to a CTIST and photomagnetism (Figure 1.7b). It is apparent that systems that can undergo these types of transitions can in principle be used for optical recording, data storage or display devices.[9, 60, 74, 75]

One of the most fascinating magnetic phenomenon that resulted from the field of molecular magnetism was the discovery that a high-spin molecule could retain its magnetization below a blocking temperature (T_B) and exhibit magnetic hysteresis of molecular origin; these molecules became known as *Single Molecule Magnets* (SMMs).[76, 77] This term is now used to describe any discrete molecular compound that

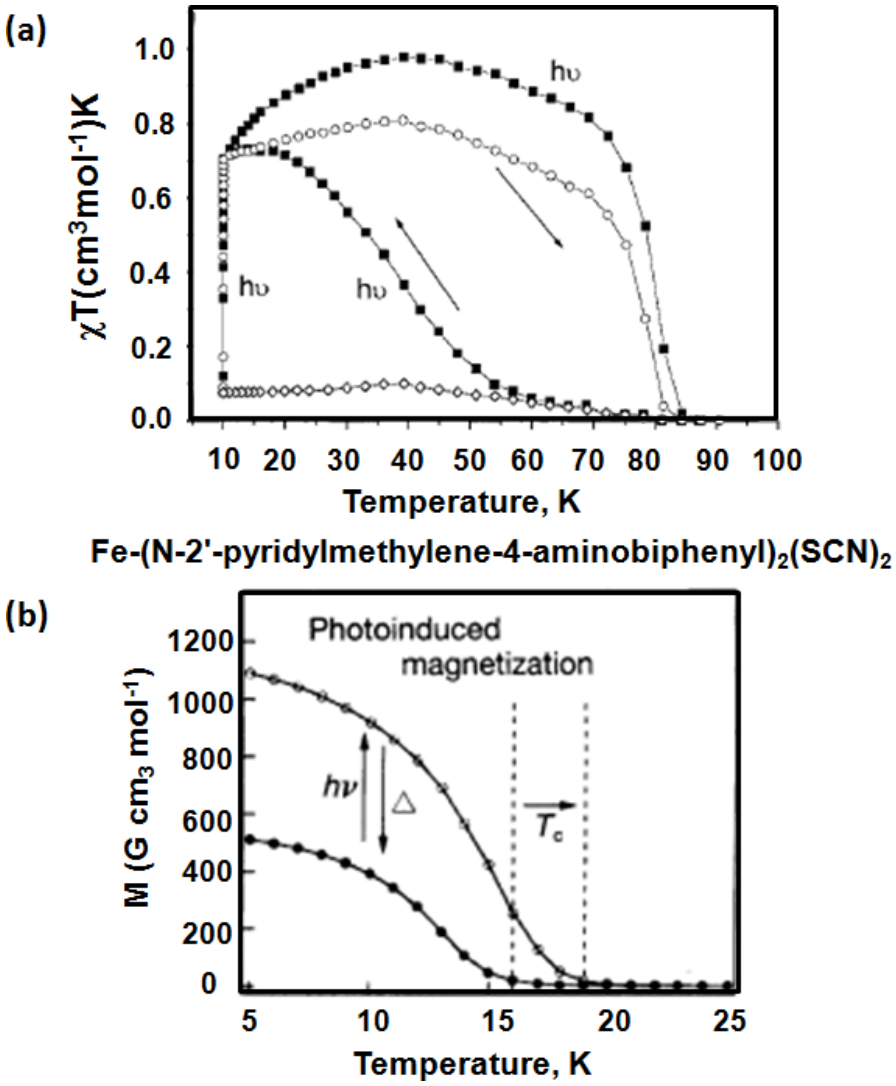

Figure 1.7. (a) Light induced excited spin state trapping in the SCO compound Fe(PM-BiA)$_2$(NCS)$_2$ (LIESST effect). (b) Photoinduced magnetic behavior of $K_{0.2}Co_{1.4}[Fe(CN)_6]\cdot 6.9H_2O$.

exhibits slow relaxation of the magnetization in the absence of an applied magnetic field.[78] Soon after, it was realized that these molecules were providing the long sought after magnetic "particles" that exhibit quantum effects[79] such as quantum tunneling[80], quantum size[81], quantum interference[82], etc.

The first and most widely studied SMMs are those of the mixed-valent $[Mn_{12}O_{12}(O_2\text{-}CR)_{16}(H_2O)_4]$ (Mn_{12}; R = various) family with an S = 10 ground state, which have been, until recently, the SMMs with the highest blocking temperatures (T_B = 3.5 K) and effective barrier values (U_{eff} - up to 74 K).[78, 83, 84] The first example of a Mn_{12} SMM was the R = Me derivative $[Mn_{12}O_{12}(O_2CMe)_{16}(H_2O)_4]\cdot 2MeCO_2H\cdot 4H_2O$ ($Mn_{12}OAc$) first synthesized by Lis[85] and later magnetically characterized by Gatteschi, Hendrickson, Christou and co-workers (Figure 1.8a).[76, 84, 86] In 2007, 15 years after the first discovery, Christou and co-workers showed that the deliberate structural distortion of the core of a hexametallic complex $[Mn^{III}_6O_2(sao)_6(O_2CPh)_2(EtOH)_4]$ ($saoH_2$ = salicylaldoxime or 2-hydroxybenzaldehyde oxime) switches the dominant magnetic exchange interactions among metal centers from antiferromagnetic to ferromagnetic resulting in a molecule with S = 12 and D = -0.43 cm^{-1} in the ground state resulting in a U_{eff} = 86.4 K and a $T_B \sim$ 4.5 K, finally breaking the long-standing record held by the Mn_{12} series (Figure 1.8b).[87]

The most important difference between bulk magnets and SMMs is the slow relaxation of magnetization observed for the latter. For example, Mn_{12} slowly relaxes to a non-magnetized state over a period of 2 months at 2 K.[79] In a bulk magnet,

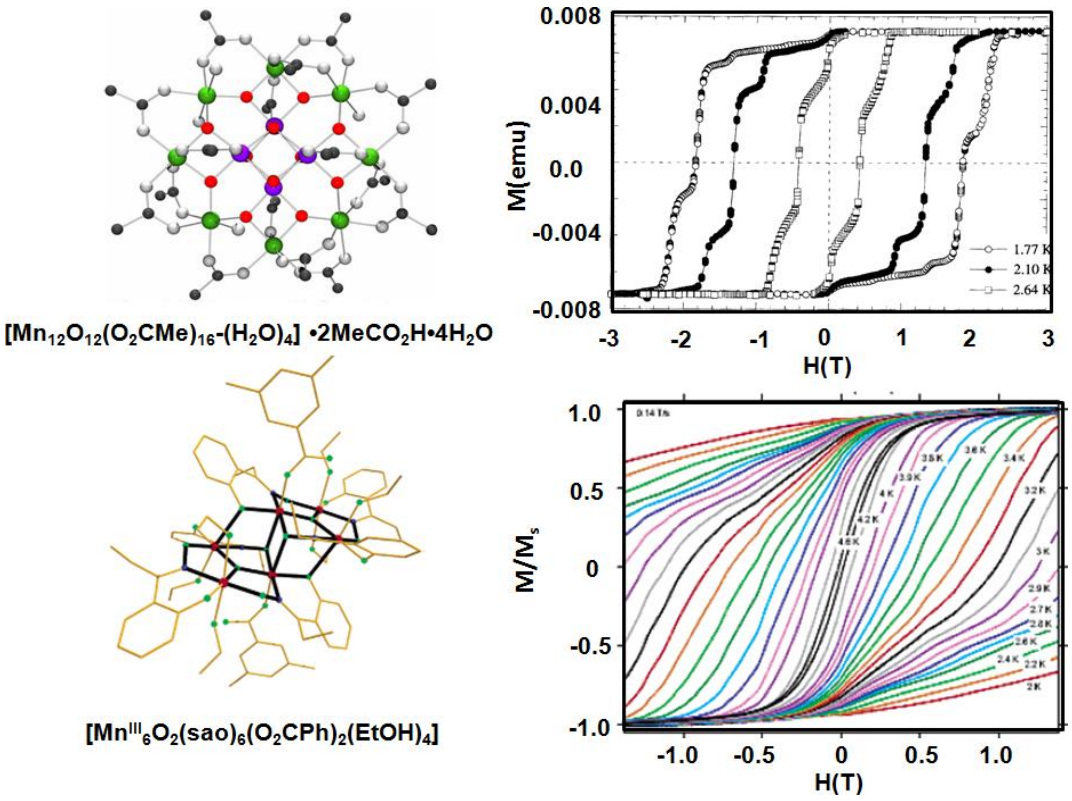

Figure 1.8. Single molecule magnets (a) $[Mn_{12}O_{12}(O_2CMe)_{16}(H_2O)_4]\cdot 2MeCO_2H\cdot 4H_2O$ ($Mn_{12}OAc$) and (b) $[Mn^{III}{}_6O_2(sao)_6(O_2CPh)_2(EtOH)_4]$ ($saoH_2$ = salicylaldoxime or 2-hydroxybenzaldehyde oxime).

magnetization hysteresis results from the magnetocrystalline anisotropy and the motion of domain walls and it can maintain its magnetization (remnant magnetization) upon removal of the field; an application of a magnetic field in the opposite direction (coercive field) is required to demagnetize the material. In contrast, a SMM magnetization hysteresis is due to the intrinsic magnetic properties of the individual molecules. In both cases field dependence of the magnetization leads to the well-known magnetic memory effect reflected by a hysteresis curve (Figure 1.8).

The SMM behavior results from a large value for the total spin ground state (S), which arises from magnetic superexchange, combined with a significant uniaxial anisotropy parameter (*D*) (axial zero-field splitting) leading to an energy barrier to the reversal of the magnetization. The parameter *D* must be negative in order for the ground state to have the maximum spin value. In the simplest model, the magnitude of the barrier for magnetization reversal is $U = S^2|D|$ for integer S and $U = (S^2–1/4)|D|$ for half-integer S (Scheme 1.3).

Apart from the oxo-bridged discrete clusters, another series of compounds that has significantly contributed to the developments of SMMs is cyanide-bridged discrete clusters.[88] The smallest cyanide clusters that are known to exhibit SMM behavior are the trinuclear complexes $\{[(pzTp)Fe^{III}(CN)_3]_2[Ni^{II}(bpy)_2]\}$[89] and $K\{[Mn^{III}(5\text{-}Brsalen)(H_2O)]_2[Fe^{III}(CN)_6]\}$[90] (Figure 1.9). Other examples of these systems will be discussed in Chapter IV. A number of cyanide-bridged SMMs have been reported to date; these molecules are listed in Table 1.1 in the order of increasing ground-state spin values. Interestingly, all cyanide SMMs reported thus far are characterized by the

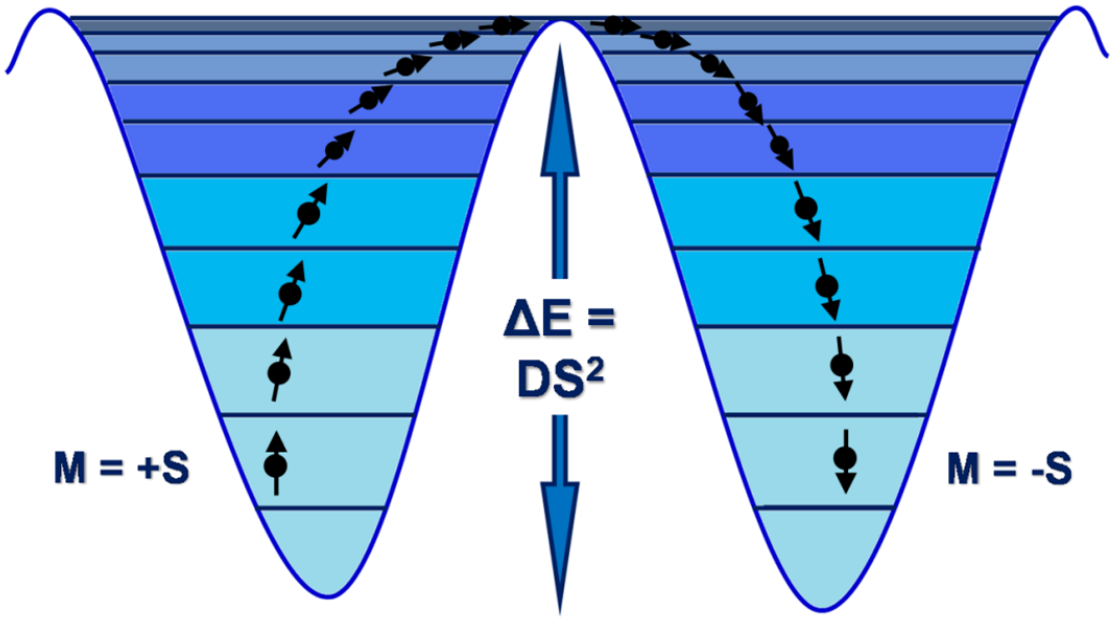

Scheme 1.3. The distribution of spin states for an SMM with $S = 10$ ground state in zero field reflecting the energy barrier ($\Delta E = U = S^2|D|$) to the reversal of magnetization.

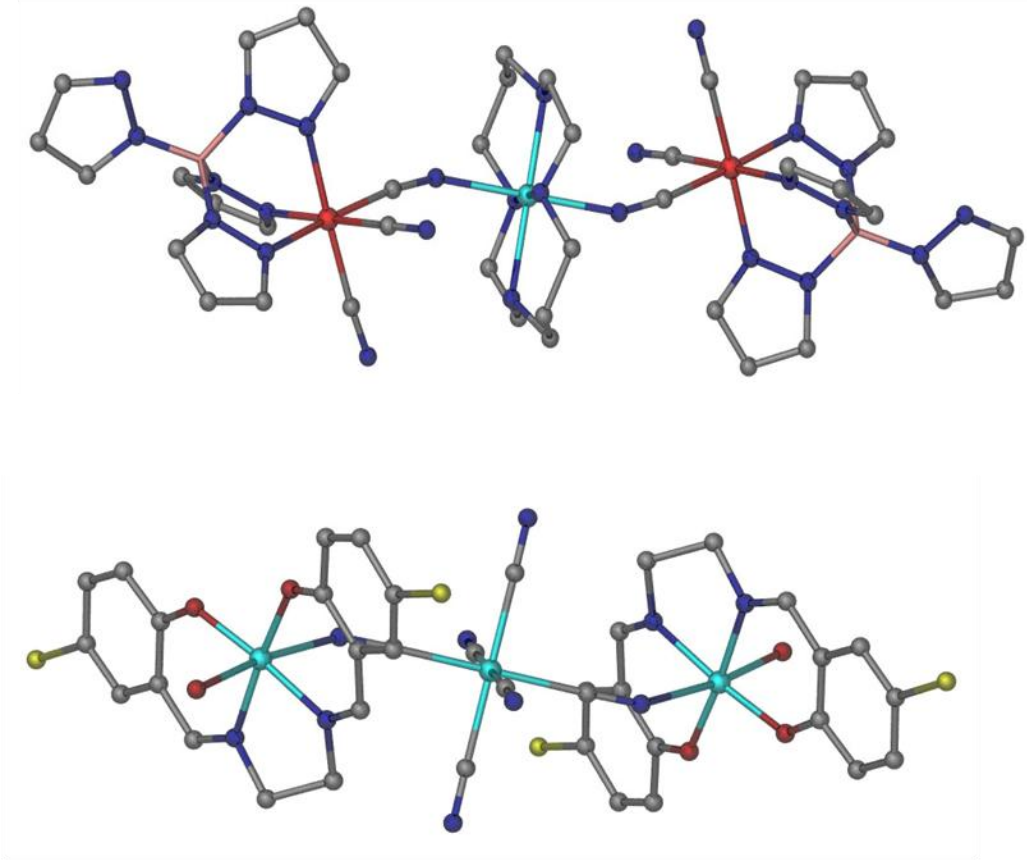

Figure 1.9. Crystal structures of two trinuclear SMMs: (a) [(5-Brsalen)$_2$(H_2O)$_2$$Mn_2$M($CN$)$_6$]·2$H_2O$, with M = Cr or Fe,[89] (b) {[(pzTp)Fe^{III}(CN)$_3$]$_2$[Ni^{II}(bipy)$_2$]}·2H_2O.[90]

Table 1.1. Cyanide-Based single molecule magnets.

Formula	Nuclearity	Ground State	U_{eff} (cm^{-1})	τ_0 (s)	Ref.
$\{[(pzTp)Fe^{III}(CN)_3]_2[Ni^{II}(bpy)_2]\}$	3	2	8.3	$4\cdot10^{-7}$	89
$\{[(Me_3tacn)Cu^{II}]_3[TpFe^{III}(CN)_3]_2\}(ClO_4)_4$	5	5/2	16	$4.8\cdot10^{-8}$	91
$\{[Tp^*Fe^{III}(CN)_3]_2[Ni^{II}(dmf)_4]_2\}(OTf)_2$	4	3			92
$\{[Tp^*Fe^{III}(CN)_3]_2[Ni^{II}(bpy)_2]_2\}(OTf)_2$	4	3	14	$5.4\cdot10^{-9}$	93
$\{[(cyclen)Ni^{II}]_3[TpFe^{III}(CN)_3]_2\}(BF_4)_4$	5	4	16	$4.8\cdot10^{-8}$	94
$K\{[Mn^{III}(5\text{-}Brsalen)(H_2O)]_2[Fe^{III}(CN)_6]\}$	3	9/2	25	$5.5\cdot10^{-10}$	90
$\{[(bpy)W^{V}(CN)_6]_2[Mn^{III}{}_2(Me_3salen)_2]\}$	4	5	22	$5.1\cdot10^{-12}$	95
$\{[TpFe^{III}(CN)_3]_4[Ni^{II}Tp]_4\}$	8	6			96
$K\{[(Me_3tacn)Mo^{III}(CN)_3]_6Mn^{II}\}(ClO_4)_3$	7	13/2	10	$7\cdot10^{-7}$	97
$\{[TpFe^{III}(CN)_3]_8[Cu^{II}(H_2O)]_6\}(ClO_4)_4$	14	7			98
$\{[Mn^{II}(tmphen)_2]_3[Mn^{III}(CN)_6]_2\}$	5	15/2	30[a]		99
$\{[Co^{II}[Co^{II}(MeOH)_3]_8[Mo^{V}(CN)_8]_6\}$	15	15/2	19	$7.4\cdot10^{-11}$	100
$\{[Co^{II}[Co^{II}(MeOH)_3]_8[W^{V}(CN)_8]_6\}$	15	15/2			100
$\{[Co^{II}[Co^{II}(MeOH)_3]_8[W^{V}(CN)_8]_5[Re^{V}(CN)_8]\}$	15	15/2			101
$\{[(triphos)Re^{II}(CN)_3]_4[Mn^{II}Cl]_4\}$	8	8	8.8	$3.3\cdot10^{-7}$	102
$\{[Mn^{II}(py5Me_2)]_4[Re^{IV}(CN)_7]\}(PF_6)_5$	5	21/2[b]	33	$2.4\cdot10^{-8}$	103
$\{[Ni^{II}[(bpy)Ni^{II}(H_2O)]_8[W^{V}(CN)_8]_6\}$	15	12	33	$1.5\cdot10^{-13}$	104
$\{[(L_4)Fe^{III}(CN)_2]_6[Mn^{III}(salen)]_6\}$[c]	12	15	5.2	$1.2\cdot10^{-7}$	105

[a] The value obtained by theoretical modeling of the magnetic behavior of the compound.
[b] The ground state is reported to occur from ferromagnetic coupling between Mn^{II} and Re^{IV} ions.
[c] A general formula for a series of complexes, in which L_4 = bpmb, bpClb, bpdmb, 5-Brsalpen, or 5-Clsalpen. The values of U_{eff} and τ_0 are provided only for one of the complexes.

presence of ions with appreciable spin–orbit coupling. In the prototypical Mn_{12} SMMs, the orbital angular momenta of Mn^{III} centers are quenched due to the tetragonal Jahn–Teller distortion. This is not the case for the compounds listed in Table 1.1. In the molecules based solely on 3*d* transition metals, important orbital contributions result from the presence of low-spin Fe^{III} centers. The only exception is the pentanuclear trigonal bipyramidal (TBP) cluster $\{[Mn^{II}(tmphen)_2]_3[Mn^{III}(CN)_6]_2\}$.[99] The ions of 4*d* and 5*d* transition elements are characterized by large spin–orbit coupling constants which contribute to the orbital angular momenta, leading to increase the magnetic anisotropy of the molecule. Illustrations of the successful implementation of this strategy are the pentanuclear $\{[Mn^{II}(py_5Me_2)]_4[Re^{IV}(CN)_7](PF_6)_5$,[103] heptanuclear $K\{[(Me_3tacn)Mo^{III}(CN)_3]_6Mn^{II}\}(ClO_4)_3$,[97] and octanuclear $\{[(triphos)Re^{II}(CN)_3]_4[Mn^{II}Cl]_4\}$[102, 106] clusters, all of which behave as SMMs (Figure 1.10).

WHY IS CYANIDE AN *IDEAL* LIGAND

The many advances that helped to establish the field, Molecular Magnetism still has much to offer and can be considered to be in its infancy.[107] The original goal to synthesize predesigned molecular magnets with specific tailored properties remains the focus of much of the ongoing research in molecular materials. In order to accomplish this goal it is necessary to have a deep understanding of the direct structure-property relations that are inherent to the material. As discussions in the previous sections point

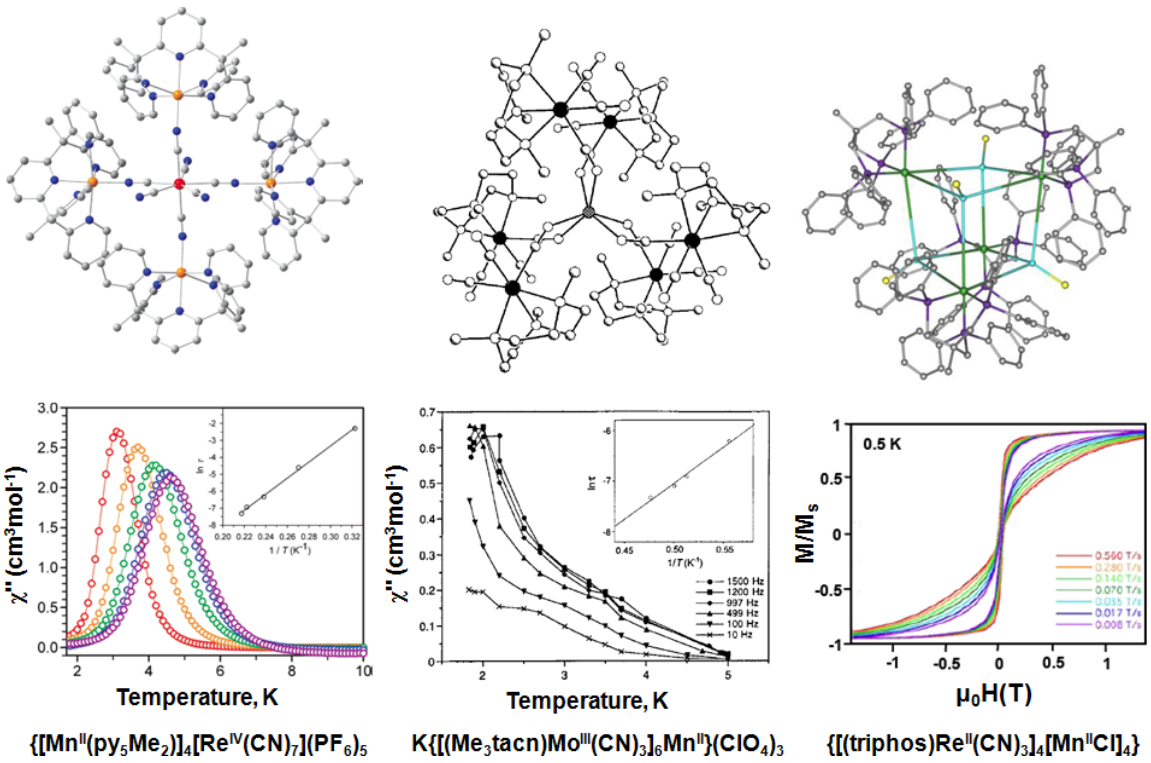

Figure 1.10. Cyanide based SMM's (a) $\{[Mn^{II}(py_5Me_2)]_4[Re^{IV}(CN)_7](PF_6)_5$, (b) $K\{[(Me_3tacn)Mo^{III}(CN)_3]_6Mn^{II}\}(ClO_4)_3$, and (c) $\{[(triphos)Re^{II}(CN)_3]_4[Mn^{II}Cl]_4\}$.

out, cyanometallate chemistry has played a major role in this endeavor and is especially attractive due to the fact that it uses cyanide as the diamagnetic linker.[88] The choice of cyanide as a bridging ligand is based on chemical and physical considerations. Chemically, (1) the cyanide ion is well known to bridge two transition metal atoms in a linear M-CN-M' fashion; (2) cyanide is a nonsymmetrical bridge, allowing it to bind selectively two different transition metals; and (3) the polycyanometallate precursors are typically stable in solution rendering them excellent building blocks for further chemistry.[6] In addition, as far as the magnetic properties are concerned, the cyanide, allows for predictable exchange coupling between the spin carriers as a result of the linear configuration of the M-CN-M' unit by considering the symmetry of the metal-based magnetic orbitals involved.[108] In cyanide complexes the observed magnetic coupling is governed by the possibility of mixing of the magnetic orbitals. If the magnetic orbitals are of the same symmetry and can overlap with the orbitals of the CN^- bridge, which mediates the exchange, then antiferromagnetic coupling is observed. Conversely, if the mixing is symmetry forbidden (*i.e.*, the magnetic orbitals are orthogonal), then the superexchange is ferromagnetic (Figure 1.11).

As the simplest example, let us first consider a dinuclear species composed of two octahedrally coordinated metal ions connected along the z axis through a CN ligand (Scheme 1.4). It is assumed that each metal ion is in an idealized local O_h geometry. The d_{xz} orbitals of both metal ions are allowed by symmetry to overlap with the *p* orbitals of the CN linker, (a), and therefore such coupling is antiferromagnetic. The same situation applies to the d_{yz}–d_{yz} orbital combination. Two d_z^2 orbitals overlap with the *s* orbital of

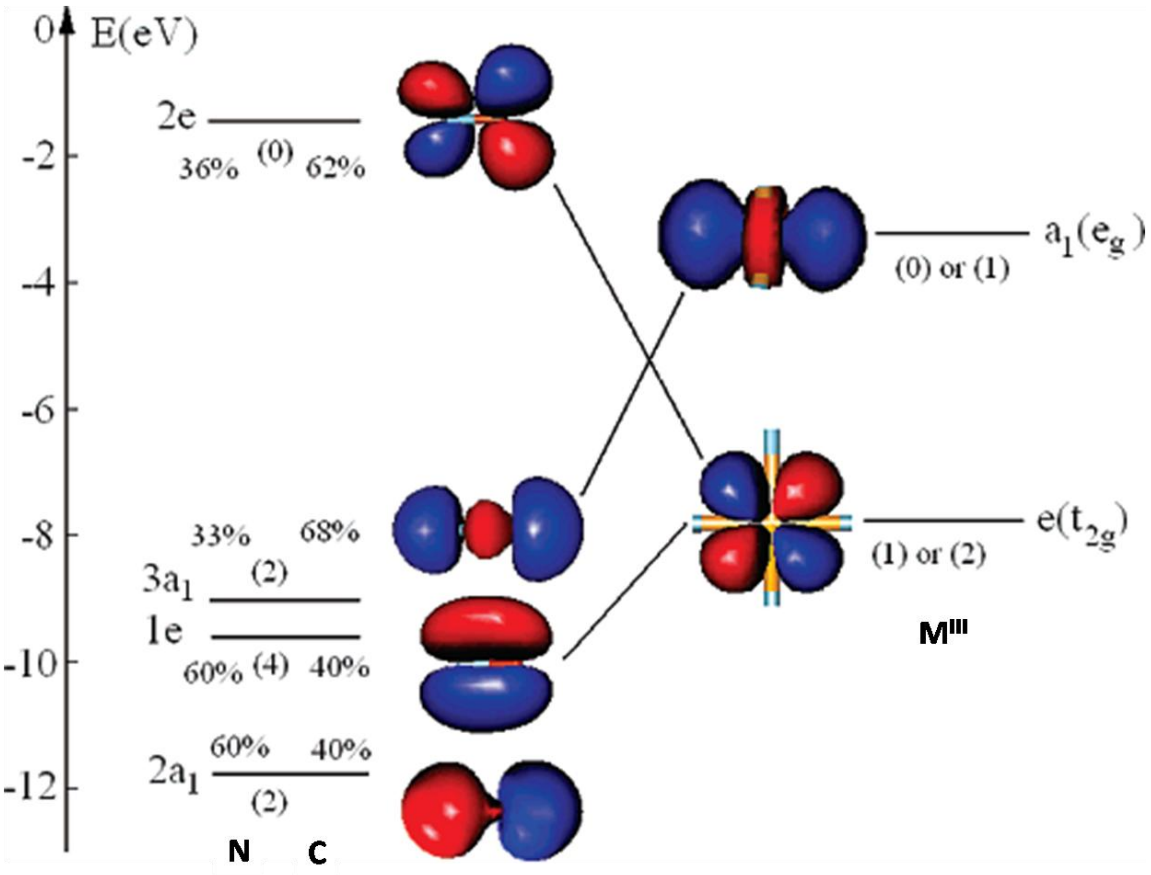

Figure 1.11. Orbitals on the CN^- bridges coupled with the e_g and t_{2g} orbitals of the transition-metal ions M^{III}.

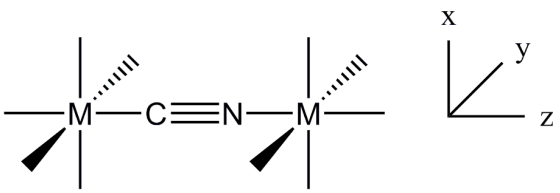

(a)

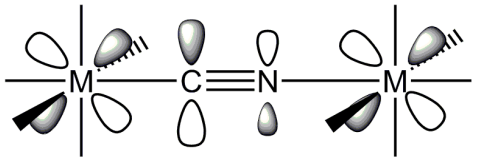

d_{xz} π^* d_{xz}

$d\pi - \pi^* - d\pi$

(b)

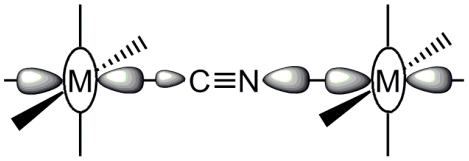

d_{z^2} σ d_{z^2}

$d\sigma - \sigma - d\sigma$

(c)

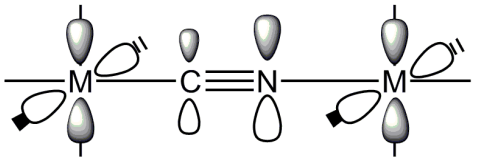

$d_{x^2-y^2}$ π $d_{x^2-y^2}$

$d\delta - \pi - d\delta$

Scheme 1.4. Interaction between the *d* orbitals of metal ions and σ and π orbitals of the cyanide bridge.

the CN- bridge, (b), also leading to antiferromagnetic coupling. Conversely, ferromagnetic coupling is predicted for the interaction between d_{xz} and d_z^2 orbitals, as they are of different symmetries and overlap with different types of cyanide orbitals. It should be pointed out that the $d_{x^2-y^2}$–$d_{x^2-y^2}$ or d_{xy}–d_{xy} combination, although involving orbitals of the same symmetry, is of the d–d type, (c), which leads to ferromagnetic coupling.

If both antiferromagnetic and ferromagnetic superexchange mechanisms operate simultaneously across the same CN- bridge, the overall magnetic coupling is determined by their relative contributions. In general, the strength of antiferromagnetic coupling propagated by the *d–p* and *d–s* overlaps is greater than the strength of ferromagnetic coupling arising from the localization of spins on non-mixing orbitals. This result is clearly demonstrated by a comparison of the ordering temperatures of the PB type magnets, $KV^{II}[Cr^{III}(CN)_6]$[55] and $CsNi^{II}[Cr^{III}(CN)_6]$,[109] materials that exhibit the most efficient combination of magnetic orbitals for antiferromagnetic ($t^2_{2g} - t^3_{2g}$) and ferromagnetic ($e^2_g - t^3_{2g}$) superexchange, respectively. The former compound is an antiferromagnet with T_N = 376 K, while the latter orders ferromagnetically at T_C = 90 K.

The precise coordination geometry of the metal ion can also affect the type and/or magnitude of magnetic coupling through the CN^- bridge. An excellent illustration of this point is found in the magnetic properties of three dinuclear complexes, $[Cu^{II}_2(bpy)_4(CN)](PF_6)_3$, $[Cu^{II}_2(phen)_4(CN)](PF_6)_3$, and $[Cu^{II}_2(tren)_2(CN)](PF_6)_3$.[28, 110] The magnetic exchange constants for the first two compounds were found to be ~9.4 and ~24 cm^{-1}, respectively, whereas, for the third complex, the value of *J* is substantially

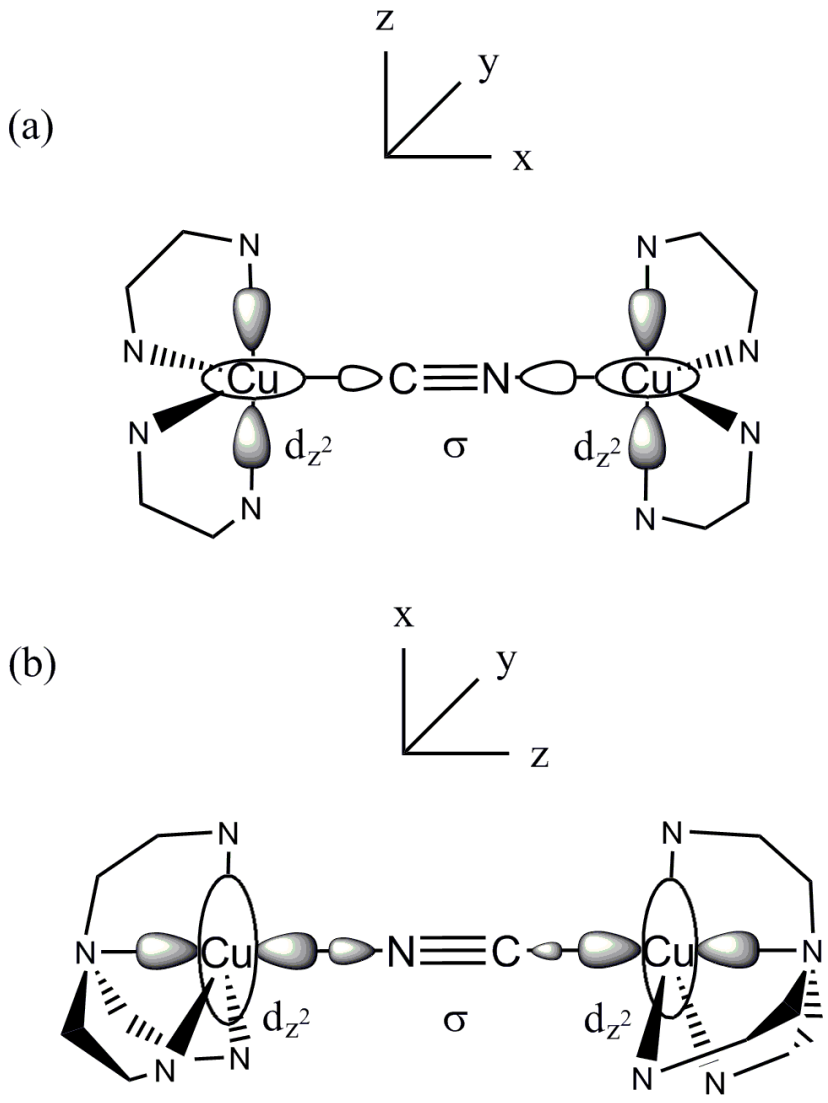

Scheme 1.5. The overlap of the magnetic d_{z2} orbitals of Cu^{II} ions with the σ orbital of the CN^- bridge in (a) $[Cu^{II}_2(bpy)_4(CN)](PF_6)_3$ and (b) $[Cu^{II}_2(tren)_2(CN)](PF_6)_3$.

larger at ~88 cm^{-1}. According to ligand field theory, the unpaired electron is localized in the predominantly d_z^2 orbital in the TBP coordinated Cu^{II} ion. When cyanide bridging occurs through the equatorial coordination sites of Cu^{II} ions (phen and bpy), this orbital is oriented perpendicular to the bridge (Scheme 1.5a) and only slightly overlaps with the *s* orbitals of the CN^- ligand by means of the low probability "doughnut"-shaped region of the d_z^2 orbital. Conversely, when the bridging cyanide occupies the axial positions (tren) of the TBP Cu^{II} ions (Scheme 1.5b), the d_z^2 orbitals are pointing directly toward the *s* orbitals of the bridge, which allows for the maximum overlap, hence the strongest antiferromagnetic coupling is observed.

Note that the aforementioned qualitative approach is an oversimplification of the factors (*e.g.* zero-field splitting, spin–orbit coupling, crystal-field splitting, and anisotropic exchange) that govern the type and the magnitude of the coupling, *J*. Other considerations notwithstanding, a simple orbital approach often provides a reasonable basis for tailoring and understanding the magnetic behavior in cyanide compounds.

Another consideration for the usefulness of cyanide as a bridging ligand, which is typically not emphasized as much in the field, but which is essential for the synthetic chemists involved in this area, is the ease of distinguishing between the M-C≡N-M' and the M-N≡C-M' bridging modes using IR spectroscopy. This is especially useful when the IR stretches of the final compound are compared to the IR stretches of its original building blocks. The factors that influence the shift of ν(C≡N) stretches of the cyanide-bridged complexes relative to those of the free CN^- ligand with ν(C≡N) = 2080 cm^{-1}, can be understood on the basis of the molecular orbital (MO) diagram of the CN^- anion

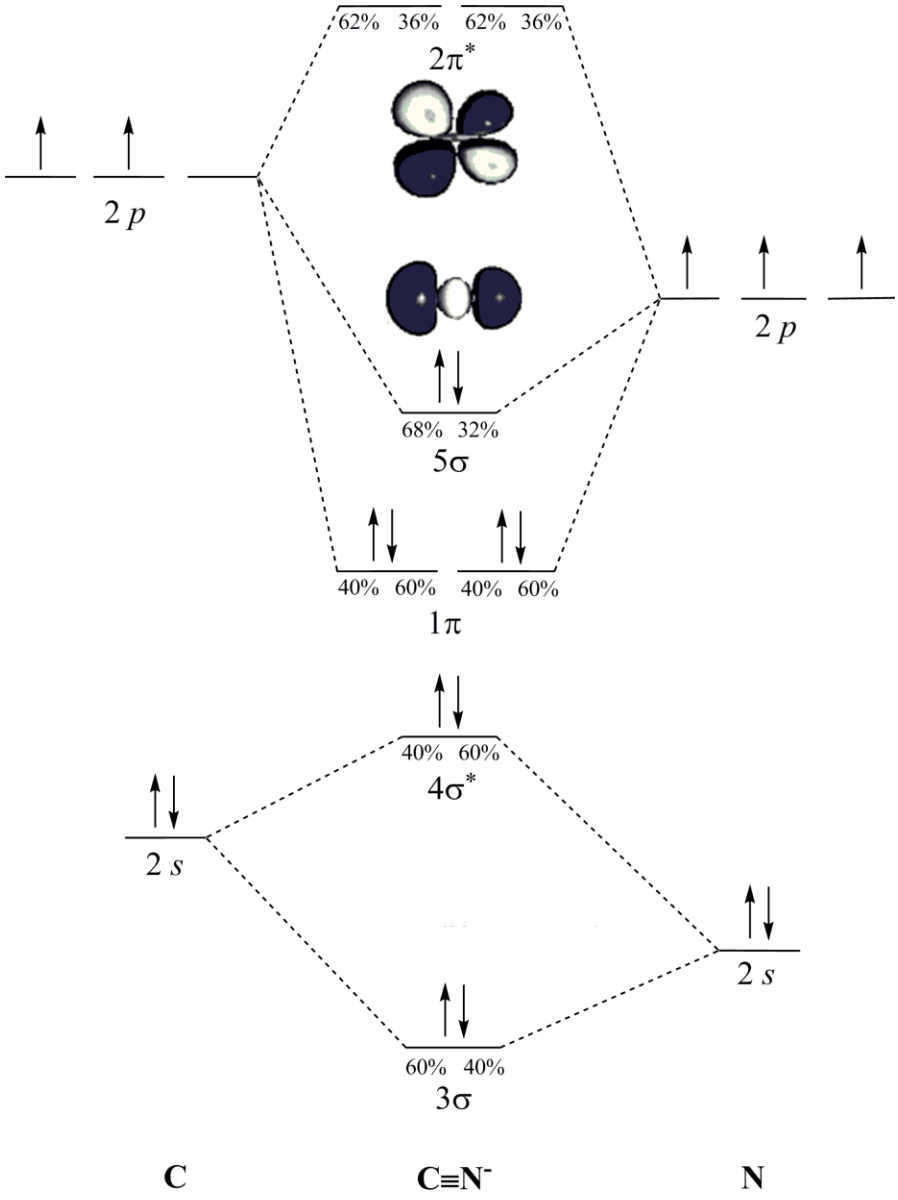

Scheme 1.6. Molecular orbital diagram of $C{\equiv}N^{-}$.

(Scheme 1.6). Upon coordination to a metal ion, the carbon end of the CN^- ligand acts as σ-donor by donating electron density from the highest occupied 5*s* MO, which is weakly antibonding. This interaction results in the increase in the ν(C≡N) mode that becomes more pronounced as the oxidation state of the metal increases. The opposite trend occurs with *d*–*p* back-bonding interaction involving electron donation from the *d* orbital of the metal ion to the vacant 2*p** MO of cyanide; this situation leads to an overall decrease in the C≡N bond strength, hence a shift of the stretching mode to lower frequencies. Since the 2*p** MO has a higher contribution from the carbon atom, the *d*–*p* back donation is more important at the C-bound metal ion (Scheme 1.6).[111]

Another general observation is that the formation of a cyanide bridge between two transition metal ions leads to an increase in the ν(C≡N) mode as compared to the starting material which contains terminal CN^- ligands, although exceptions to this rule are known.[112] This increase has typically been assigned to the mechanical constraint on the motion of the CN^-group generated by the presence of the second metal center (kinematic effect). There are, however, indications that electrostatic factors may actually be more important and that the increase in ν(C≡N) mainly stems from the depletion of electron density in the weakly antibonding 4*s* orbital because of σ-donating action of the nitrogen end of the bridging CN^- ligand.[113]

A curious phenomenon unique to the CN^- ligand is its ability, in some cases, to engage in *linkage isomerism*. A "flipping" of the CN^- group can lead to dramatic changes in the structure and properties of resulting compounds because the carbon end of the cyanide is a much stronger field ligand than the nitrogen end. This peculiar ability

of the cyanide ligand to flip was first noted in the PB family and was recently demonstrated by Coronado and coworkers to be a reversible process in $K_{0.4}Fe_4[Cr(CN)_6]_{2.8}\cdot 16H_2O$ PB analog.[114] The compound exhibits a pressure-induced linkage isomerization which results in pressure-induced magnetic bistability. Chapter III of this dissertation provides insight into the mechanism of the cyanide linkage isomerism phenomenon by presenting results from a systematic structural, spectroscopic and magnetic study using the Lewis acid, Co^{II}.[115] Other studies of cyanide linkage isomerism in discrete clusters have been reported, but so far none have been known to exhibit bistability as in the case of the $K_{0.4}Fe_4[Cr(CN)_6]_{2.8}\cdot 16H_2O$ PB analog.[88]

The recognition that high-spin clusters can exhibit magnetic bistability at the discrete molecular level has introduced a new era of transition metal-cyanide chemistry. Our research program has taken advantage of the fact that appropriate building blocks produce molecules with the desired structural and magnetic properties. The work described in this dissertation highlights our efforts in developing new building blocks, and gives insight into magnetic and physical phenomena observed in cyanide bridged molecular magnets. In Chapter II, a study on the use of the $[Os(CN)_6]^{3-}$, Co^{II}, and alkali metal building blocks for the synthesis of new PB analogs are presented; emphasis is made on the effect of the 5*d* ion and the type/quantity of alkali metal on the photomagnetic and CTIST observed compared to the analogous PB, $Co_3[Fe(CN)_6]_2$.

Prussian Blue's in general suffer of one significant drawback: the reaction of the building blocks usually leads to powders that display varying degrees of crystallinity, and structural-property correlations are hampered by the lack of exact structural

parameters. In order to obtain discrete polynuclear cyanide complexes we use an appropriate capping ligand to block coordination sites on the metal ion, the result of which is a mononuclear convergent precursor. This convergent precursor limits the growth of extended structures (PBs) and, when combined with divergent building blocks leads to molecular cyanide complexes that, in most cases, can be isolated as single crystals. This fact allows for more precise structure-property relationships, which is the main goal of our research program. The results presented in Chapters III – V demonstrate that the building block approach, with the use of capping ligands, is a viable synthetic route to various trinuclear discrete clusters. Chapters III and IV present the structural, spectroscopic and magnetic study of the trinuclear species obtained using the capping ligands 1,2-Bis(diphenylphosphino)ethane (dppe) and *N*,*N*'-bis(salicylidene)-1,2-diaminobenzene (salphenH_2) respectively. Chapter V describes the structural and magnetic properties of new building blocks based on the L_5 capping ligand, {[(6-(pivalamido)pyrid-2-yl]methyl}bis-(pyrid-2-ylmethyl)amine) (mppa). Overall, the work presented in this dissertation highlights the use of cyanide precursors for the synthesis of new magnetic molecular materials, and gives insight into bistable magnetic phemomena such as photomagnetism (Chapter II) and single molecule magnetism (Chapter III).

CHAPTER II

TEMPERATURE AND LIGHT INDUCED BISTABILITY IN $A_xCo_4[Os(CN)_6]_{(8+x)/3}\cdot nH_2O$ (A = Li, Na, K, Rb, Cs) PRUSSIAN BLUE ANALOGS

INTRODUCTION

In 1703, the German artist Diesbach accidentally discovered a new dark blue pigment.[116] Little could he have imagined that three hundred years later this compound, the mixed-valence iron cyanide material $Fe^{III}_4[Fe^{II}(CN)_6]_3 \bullet xH_2O$ dubbed Prussian blue (PB), would be at the core of one of the most developed and widely studied areas of coordination chemistry. In the year 2010, the breadth of research currently being conducted on the topic of cyanide complexes is nothing short of astonishing. PB itself has been extensively studied vis-à-vis it's structural, electronic, and magnetic properties.[41, 117-121] Moreover, various transition metal analogues of PB have been found to behave as high-temperature molecular magnets,[53-55] photo-switchable magnetic solids,[73, 122] antidotes for radioactive poisoning,[123] molecular sieves,[124] and hydrogen storage materials.[125, 126]

The research in the field of cyanide compounds has been the subject of several excellent reviews over the years. The comprehensive book published by Sharpe in 1976 is an essential reference to early research, including many preliminary findings, on cyanide coordination chemistry.[127] Ten years later, Babel published a review on extended cyanide-bridged complexes with one- and two-dimensional structures.[128] In 1997, our group reviewed the state-of-the-art of modern cyanide chemistry with a broad coverage of molecular as well as extended cyanide phases and various applications of

cyanide compounds.[112] Recently, due to the fast accumulating literature on cyanide molecular complexes, several reviews on discrete cyanide bridged clusters[88, 129-131] and cyanide bridged extended phases of the PB type have been published. [6, 132, 133] As evidenced in the literature, one of the main contributions of paramagnetic cyanide molecular materials has been the preparation of compounds that exhibit magnetic bistability. Of particular interest are those materials whose magnetic response change with external stimuli, such as temperature or irradiation. Light induced magnetic bistability is referred to as photomagnetism, and was first discovered in 1984 by Decurtins and coworkers in the SCO systems.[71]

Recently, an increasing number of photomagnetic molecular materials have been synthesized that exhibit remarkable magnetic properties governed by a variety of mechanisms. Among these compounds are the CoFe PB analogs. Hashimoto and co-workers discovered the photomagnetic properties of the material $K_{0.2}Co_{1.4}[Fe(CN)_6]_1 \bullet 6.9H_2O$ in 1996.[73] This was the first 3D compound for which a metal-to-metal photo-induced electron transfer ($[Co^{III}\text{-}Fe^{II}] \rightarrow [Co^{II}\text{-}Fe^{III}]^*$) at low temperatures was recognized as being a means to trigger changes in magnetic properties. The electronic structure of the states implied in the switching properties of the CoFe PB analogs is now well-known. The ground state is composed of diamagnetic $Fe^{II}_{L.S.}\text{-}Co^{III}_{L.S}$ pairs, which are transformed into $Fe^{III}_{L.S.}\text{-}Co^{II}_{H.S}$ ones upon irradiation. The photomagnetic effect is due to a photoinduced electron transfer accompanied by a spin-state change of the cobalt ion (Figure 2.1).

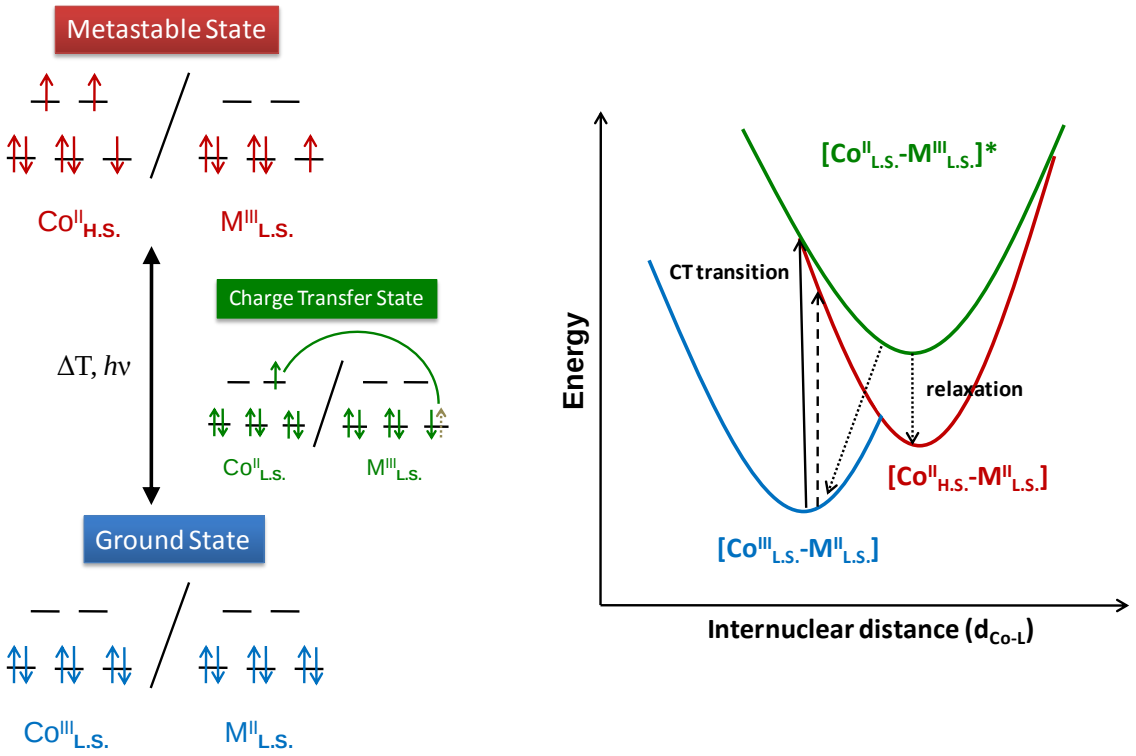

Figure 2.1. Photomagnetism in $Co_x[M(CN)_6]_y{\cdot}nH_2O$ PB (M = Fe, Os): (a) electron transfer coupled with spin state change in Co and (b) qualitative representation of the potential wells of the ground and metastable excited state of one Co-M photo-excitable pair.

Light is not the only way to trigger magnetic switching of the PB compounds: the magnetization can be changed by varying the temperature or pressure, or by replacing the alkali cation inserted in the 3D structure.[66-69, 134-148] The temperature induced bistability in this family of compounds is known as the charge transfer induced spin transition (CTIST) which corresponds to a change from the diamagnetic Co^{III}–Fe^{II} pair at low temperatures (LT phase) to the paramagnetic Co^{II}–Fe^{III} pair at room temperature (HT phase) accompanied by an enhancement of the magnetization and the Curie temperature due to the increase in the number of magnetic pairs in the HT phase.

Recently, our group has been focusing on the incorporation of 4*d* and 5*d* metal ions into magnetic materials, mostly inspired by the possibility of engendering anisotropy in the cyanide discrete clusters as a result of the increased spin orbit coupling of these ions.[102, 106, 149, 150] Consequently, we embarked on the design of new magnetic materials that incorporate the hexacyanoosmate(III) building block, $[Os(CN)_6]^{3-}$, efforts that led to new trigonal bipyramidal (TBP) clusters and extended networks.[151-153] To further expand the field of Os^{III} containing magnetic materials, we elected to study the incorporation of $[Os(CN)_6]^{3-}$ into Prussian Blue architectures in combination with the Co^{II} ion. The primary goal is to determine if this combination leads to the photomagnetic effect observed for the Co-Fe Prussian Blue family of materials.

In this present chapter a detailed synthetic and magnetic study of a CoOs Prussian Blue family will be presented. Specifically, the $(PPN)_3[Os(CN)_6]$ salt was reacted with Co^{II} ions which leads to the formation of a new PB analog, $Co_3[Os(CN)_6]_2 \cdot nH_2O$ (*idealized formula*). Magnetic measurements of this compound revealed that it

exhibits photomagnetic behavior as well as a CTIST. To further study this material, the effect of the Alkali metal cations (Li, Na, K, Rb, and Cs) on the magnetic properties of the CoOs PB analog was probed in depth. This new family of PB analogs constitutes the third PB series to exhibit photomagnetism and CTIST behavior. The results presented herein support the conclusion that this new CoOs PB family exhibits a variety of photomagnetism, thermal induced excited spin state trapping (TIESST), and CTIST behavior.

EXPERIMENTAL

Syntheses

Starting materials. The PPNCl (PPN = Bis(triphenylphosphine)iminium) starting material (Pfaltz and Bauer) was used as received and $K_4[Os(CN)_6]$ was prepared as previously reported.[153] Nitrate salts of Co^{II}, Li, Na, K, Rb, and Cs were purchased from Aldrich and used as received. Reagent grade methanol (MeOH) was purchased from Aldrich and used as received. The reactions were performed with the help of Darryl Stepien as part of an undergraduate research program. Elemental analyses were performed by Chemisar in Guelph, Ontario. According to thermal gravimetric analysis the products consistently contain between 18-22 molecules of water per formula unit.

$[PPN]_3[Os(CN)_6]$ (1). A sample of $K_4Os(CN)_6$ (1 g, 2 mmol) was dissolved in 50 mL of H_2O and stirred for 20 min. to give a clear, colorless solution and treated with $Ce^{IV}(SO_4)_2$ (0.662 g, 2 mmol) which led to an instantaneous change to yellow followed by dark green and finally back to bright yellow. The yellow solution was quickly filtered

and then slowly added to a hot solution of PPNCl (3.4 g, 6 mmol) which led to the formation of a yellow solid which was filtered, washed with 3 x 100 mL of hot water to dissolve impurities, and finally washed with 100 mL of diethyl ether and vacuum dried. Yield = 2.4 g, 62%. Elemental analysis calcd. for $C_{114}H_{90}N_9OsP_6$: N, 6.42; C, 69.7; H, 4.62. Found: N, 6.44; C, 68.98; H, 4.62%. IR(Nujol): ν(C≡N) 2085, 2092 cm^{-1}.

$Co_3[Os(CN)_6]_2 \cdot 21H_2O$ (2). A sample of $Co(NO_3)_2 \cdot 6H_2O$ (0.046 g, 0.21 mmol) was dissolved in 20 mL of water for ~10 min until all the solids had dissolved and a clear magenta solution was obtained. The resulting solution was quickly combined with a 20 mL solution (50:50 mixture of MeOH/H_2O) of $(PPN)_3[Os(CN)_6]$ (0.275 g, 0.14 mmol) in a 50 mL erlenmeyer flask. The mixture was stirred for 5 minutes during which time a purple solid was observed to precipitate. The flask was placed in refrigerator at 10° C overnight and then filtered to collect the product which was washed with methanol (3 x 30 mL) and diethyl ether (15 mL). Yield = 46 mg, 77%. TGA data indicate that there are between 20-21 H_2O molecules in the sample. Elemental analysis calcd. for $Co_3Os_2C_{12}N_{12} \cdot 6H_2O$: N, 17.13; C, 14.68; H, 1.23; Co, 18.02. Found: N, 16.91; C, 14.46; H, 0.93; Co, 18.58%. IR(Nujol): ν(C≡N) 2085, 2134 cm^{-1}.

$A_xCo_4[Os(CN)_6]_{(8+x)/3} \cdot nH_2O$. Co-Os PB analogs with different types of alkali metals (A = Li **(3)**, Na **(4)**, K **(5)**, Rb **(6)**, Cs **(7)**) were prepared by a similar route. For simplicity each compound will be refer to by its alkali metal, *e.g.* Li analog, throughout the text. In a sample reaction, a mixed aqueous solution (25 mL) of $Co(NO_3)_2 \cdot 6H_2O$ (0.09 g, 0.31 mmol) and $A(NO_3)$ (0.02 mmol) was slowly added to a mixed MeOH/H_2O (50:50, 50

Table 2.1. Elemental analysis results and proposed formulas for compounds **2-7**.

Compound	Alkali Metal	Co	Os	C	N	H	O
2							
% exp.		18.58	40.82	14.46	16.91	0.93	7.65
(calc.)		(18.02)	(39.14)	(14.68)	(17.13)	(1.23)	(7.78)
Proposed formula: $Co_3[Os(CN)_6]_2 \cdot 6H_2O$							
3	Li						
% exp.		14.46		13.56	15.75	2.52	
(calc.)	(0.18)	(15.33)	(34.97)	(13.11)	(15.30)	(2.36)	(18.73)
Proposed formula: $Li_{0.4}Co_4[Os(CN)_6]_{2.80} \cdot 18H_2O$							
4	Na						
% exp.		13.02		12.03	13.98	2.62	
(calc.)	(1.80)	(13.17)	(33.58)	(12.59)	(14.69)	(2.70)	(21.45)
Proposed formula: $Na_{1.4}Co_4[Os(CN)_6]_{3.13} \cdot 24H_2O$							
5	K						
% exp.		12.42		13.52	14.69	2.83	
(calc.)	(3.72)	(12.83)	(34.07)	(12.78)	(14.91)	(2.41)	(19.16)
Proposed formula: $K_{1.8}Co_4[Os(CN)_6]_{3.26} \cdot 22H_2O$							
6	Rb						
% exp.		10.89		11.95	13.75	1.85	
(calc.)	(10.61)	(11.32)	(32.56)	(12.21)	(14.25)	(2.13)	(16.98)
Proposed formula: $Rb_{2.6}Co_4[Os(CN)_6]_{3.53} \cdot 22H_2O$							
7	Cs						
% exp.		9.13		11.59	12.42	1.59	
(calc.)	(20.16)	(9.41)	(30.12)	(11.29)	(13.18)	(1.77)	(14.04)
Proposed formula: $Cs_{3.8}Co_4[Os(CN)_6]_{3.93} \cdot 22H_2O$							

resulted in the precipitation of a dark purple solid. The mixture was placed in a 10° C refrigerator overnight. After this period of time, the sample was washed with methanol (3 x 30 mL) and diethyl ether (15 mL) and allowed to air dry. The samples were then analyzed and their molecular formulas determined by elemental analysis and TGA. Table 2.1 summarizes the results from these analyses.

RESULTS AND DISCUSSION

Syntheses

Prussian Blue analogs are typically synthesized by reacting an aqueous solution of a hydrated transition metal cation with an aqueous solution of a hexacyanometallate. In our synthetic strategy, however, we require the presence of an organic solvent in order to dissolve the PPN salt of $[Os(CN)_6]^{3-}$. The starting materials are reacted in a 2:3 ratio of $PPN_3[Os^{III}(CN)_6]$:Co^{II} in a mixture of H_2O and methanol. In all cases the reactions led to the formation of the Prussian Blue analog as an insoluble purple microcrystalline powder.

It is well known in the chemistry of PB analogs that when a divalent cation, e.g. Co^{II}, is mixed with a hexacyanometallate bearing three negative charges, e.g. $[Os(CN)_6]^{3-}$, two extreme stoichiometries can be obtained according to the electroneutrality of the compound. Considering the present reactants, a lacunary structure, $Co^{II}_3[Os^{III}(CN)_6]_2 \cdot 21H_2O$ is obtained for compound **2**, where the $[Os(CN)_6]^{3-}$ vacancies are filled with H_2O molecules coordinated to the Co^{II} cation. The presence of

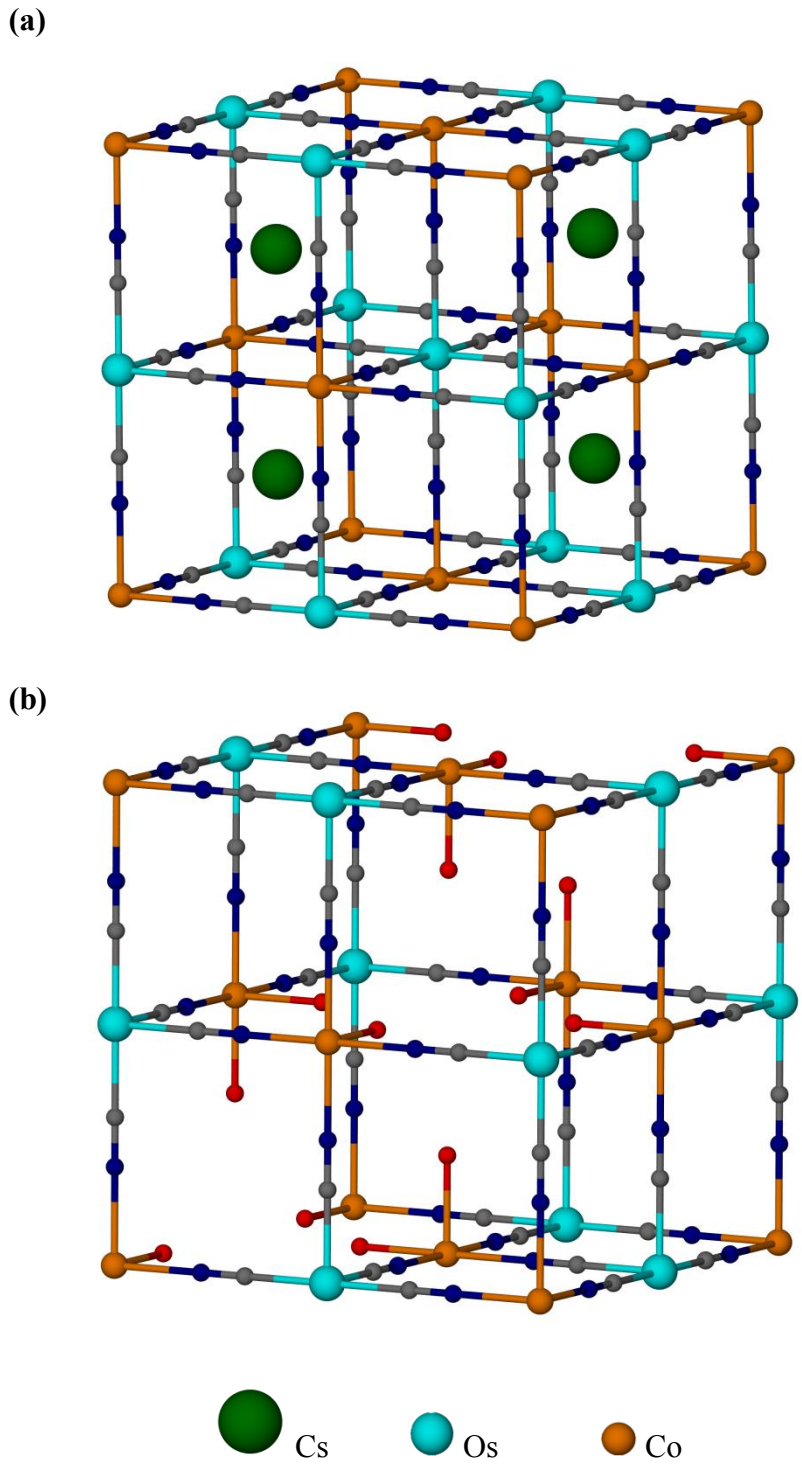

Scheme 2.1. Schematic cell representation of compound (a) **7** (Cs analog) and (b) **2** (CoOs PB).

excess alkali metal cations during the synthesis leads to a perfect face cubic centered (fcc) structure $A^{I}Co^{II}[Os^{III}(CN)_6]$ in which the alkali cations occupy half of the interstitial tetrahedral sites which is the case observed for the Cs analog (**7**) (Scheme 2.1). In intermediate cases, *e.g.* compounds **3-6**, the divalent cation (Co^{II}) occupies all the fcc sites whereas the occupation of the octahedral sites by the hexacyanometallate ($[Os^{III}(CN)_6]^{3-}$) varies as a function of the amount of alkali metal cation inserted in the structure. Considering the eletroneutrality of the compounds, in one unit cell the number of transition metal cations is always four and the number of hexacyanometallate units and alkali metal ions are equal to (8+x)/3 and x respectively. The formulae of compounds **3-7,** given for one unit cell, are $A^{I}_{x}Co^{II}_{4}[Os(CN)_6]_{(8+x)/3}$ and are reported in Table 2.1. The Co^{II}-Os^{III} pairs or Co^{III}-Os^{II} pairs generated by the internal redox reaction, cannot be differentiated by considering only charge distribution therefore the oxidation states of the metal cations are not assigned. As evidenced by elemental analysis, the percentage of the alkali metal cation in the compound increases with the size of the cation.

Powder Diffraction Studies

Single crystals of Prussian Blue analogs are challenging to obtain, and it is an endeavor that is an ongoing effort in this project. Nevertheless, the necessity of obtaining single crystal data can be mitigated by the fact that powder X-ray diffraction is quite useful for such high symmetry materials and, indeed, it is the standard method for confirming the existence of an extended Prussian Blue structure. All samples were collected on a holder

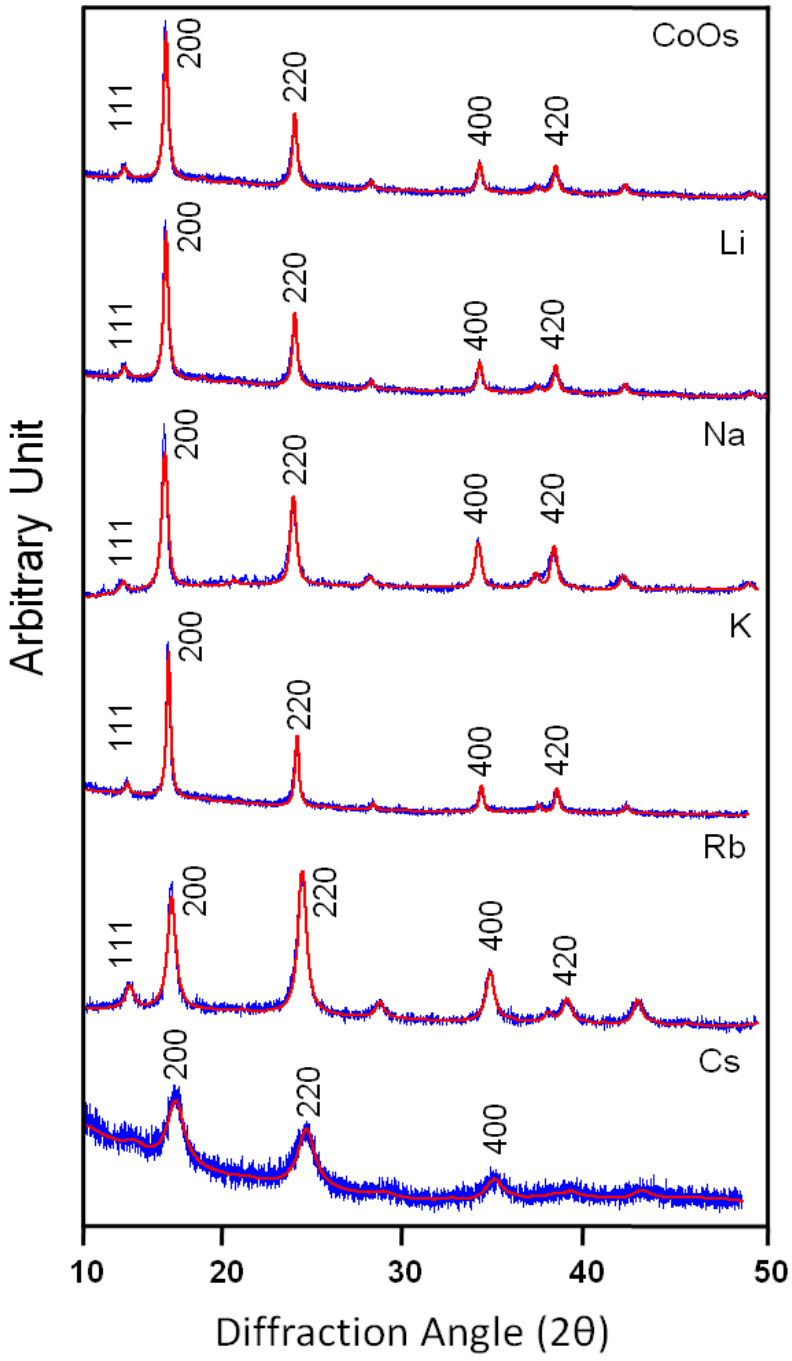

Figure 2.2. Powder X-ray diffraction patterns collected from 5-55° in 2θ in blue and their calculated fittings (red line).

Table 2.2. Structural parameters determined from the fittings of the diffraction patterns of compounds **2-7**.

Compound	Alkali Metal	Space Group	Lattice Parameter
2		P23	10.45 Å
3	Li	P23	10.48 Å
4	Na	P23	10.51 Å
5	K	P23	10.48 Å
6	Rb	P23	10.35 Å
7	Cs	P23	10.29 Å

composed of a single silicon crystal to minimize background interference. Samples were ground and gently pressed onto the surface and the data were collected from 5 – 55° in 2θ at room temperature (Appendix A). The experimental powder diffraction patterns of compounds **2-7** are shown in Figure 2.2. The fittings of the patterns provided by Dr. Nattamai Bhuvanesh indicate that the compounds exhibit the characteristic fcc structure (Table 2.2).

The diffraction patterns of compounds **2-5** exhibit intense peaks. The first feature observed in these patterns is the reflection 111 which is not totally suppressed. This is expected for a fcc lattice with Co^{II} atoms located on the corners and at the center of the faces of the cube and a partial occupation of the octahedral sites by the Os^{III} atoms. For the Rb analog (**6**) the Os/Co ratio is higher than in compounds **2-5** as evidenced by a decrease in the intensity of the 111 reflection. Moreover, the powder pattern for compound **6** shows an increase in the 220 and 400 reflections, while the 200 and 420 reflections are less intense. This is consistent with the metal atoms and the alkali metal cations scattering "in-phase" for the 220 and 400 reflections and "out-of-phase" for the 200 and 420 reflections which corresponds to a quarter occupation of the tetrahedral sites with rubidium atoms. These observations are consistent with the data previously reported for the CoFe PB family.[67] The powder pattern for the Cs analog (**7**) exhibits very weak reflections, which is due, in part, to X-ray radiation absorption by the cesium ion. As noted previously for the Cs analog of the Co-Fe PB compound,[67] the most intense reflections for **7** are 220 and 400, whereas the 200 and 420 reflections are nearly absent. This change in the intensity of the reflections is a result of the destructive

scattering of the metal atoms and the cesium atoms which occupy half of the tetrahedral sites, and the nearly total occupation of the octahedral sites by the osmium atoms. The structural results obtained for the new family of CoOs PB analogs resemble the data obtained for the CoFe PB series which indicates that the replacement of the Fe^{III} ion by the Os^{III} ion does not result in a significant change in the structure of the resulting 3D phases.

Infrared Spectroscopy

Analyses of the ν(C≡N) stretches for the new materials were performed by FTIR spectroscopy (Appendix A) for all of the materials at room temperature. The IR spectrum of the CoOs PB (**2**) exhibits two bands. The sharp band observed at 2134 cm^{-1} is attributed to the CN stretching mode for the Os^{III}-CN-Co^{II} pair. The weak band at 2085 cm^{-1} is attributed to either a terminal cyanide stretching mode or the cyanide stretching vibration mode in a Os^{II}-CN-Co^{III} environment. The Li, Na, and K analogs (**3-5**) exhibit IR stretching features similar to those of compound **2**. On the other hand, the Rb and Cs analogs (**6-7**) exhibit only one broad absorption band at 2115 and 2119 cm^{-1} respectively. This feature can be attributed to the overlap of the two main contributions: namely the stretching modes of cyanide in the Os^{II}-CN-Co^{III} and Os^{III}-CN-Co^{II} environments. The presence of various oxidation states of the metal ions would explain the breadth of the signal. It is important to point out that the ambiguity of the assignments of the IR stretching modes is a result of the inadequacy of this technique to precisely determine the oxidation states of the metal ions. In order to properly assign the IR bands observed for these compounds, further analysis of the oxidation states of the

Table 2.3. IR $\upsilon_{C\equiv N}$ stretches for CoOs Prussian Blue materials.

Compound	Alkali Metal	ν(C≡N) stretches (cm^{-1})
$(PPN)_4[Os(CN)_6]$	-	2044 (s)
$(PPN)_3[Os(CN)_6]$	-	2076 (s), 2085 (s)
2	-	2085 (w), 2134 (s)
3	Li	2088 (m), 2138 (m)
4	Na	2081 (w), 2138(w)
5	K	2096 (w), 2138 (w)
6	Rb	2118 (b)
7	Cs	2119 (b)

b = broad, s = sharp, m = medium intensity, w = weak intensity

metal ions via XANES (X-ray Absorption Near Edge Structure) is required. In addition, comparison of these results to data recorded in the literature is hampered by the lack of examples of extended materials or discrete clusters based on the Os-CN-Co unit. A summary of the IR data for each new PB is provided in Table 2.3.

Gas Absorption Properties

A widely studied area of PB chemistry is the potential of these 3D materials to store hydrogen. Significant work in this area has been reported by Long and co-workers, who have been able to achieve up to a 1.8% uptake of H_2 in the $Cu_3[Co(CN)_6]_2$ PB analog.[126] Studies have demonstrated that the gas absorption ability of PB analogs results from the statistically distributed vacancies in their structures and that there is a positive correlation between the number of vacancies present and the gas uptake ability of the solid.[126, 154-162] As a result, only the $Co_3[Os(CN)_6]_2$ PB analog (**2**) was used for this study. The alkali metal analogs were not investigated due to the fact that the alkali metal ions serve to fill the vacancies whichwould result in a decrease of the gas uptake. In contrast, the $Co_3[Os(CN)_6]_2$ PB analog (**2**) is missing approximately 1/3 of the $[Os(CN)_6]^{3-}$ sites in the structure.

The gas uptake study of compound **2** was performed with the help of Dan Zhao in the in the group of Dr. Hong-Cai Zhou. After degassing the sample at 50 °C for 10 h under dynamic vacuum, the N_2 adsorption data at 77 K for **2** revealed a type I isotherm (Figure 2.3) consistent with a microporous adsorbent, with a BET surface area of 149 m^2/g. As a result of the low surface area observed for compound **2** in comparison to the BET surface area reported for the $Cu_3[Co(CN)_6]_2$ PB (730 m^2/g), compound **2** displays

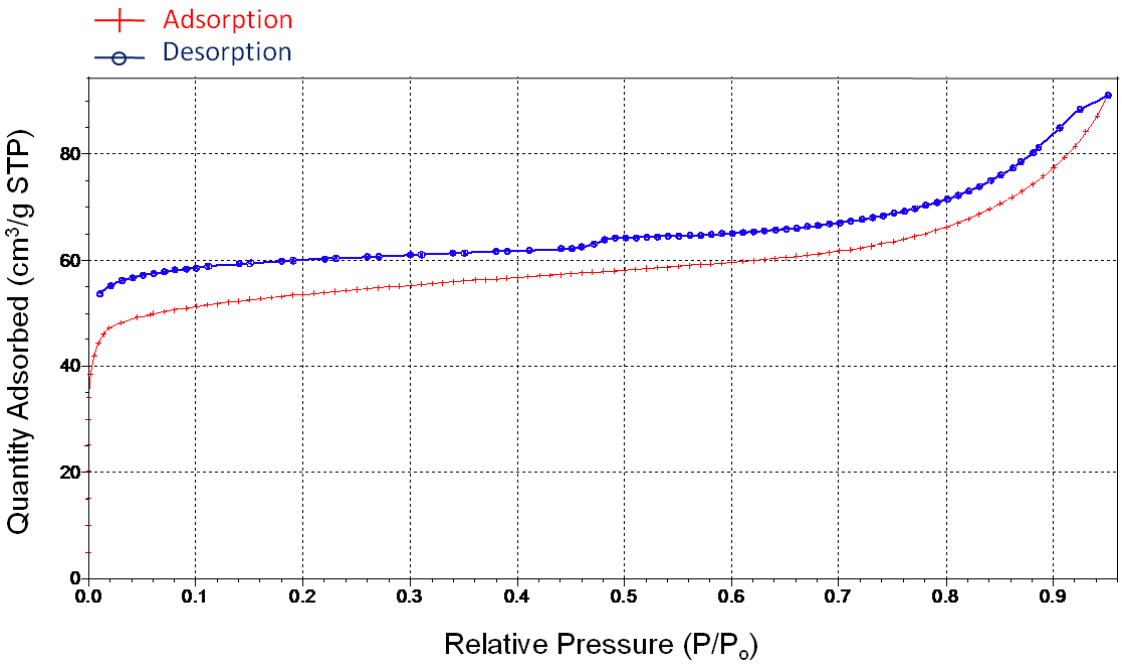

Figure 2.3. Nitrogen sorption isotherms for the CoOs PB (**2**): adsorption (red) and desorption (blue) curves.

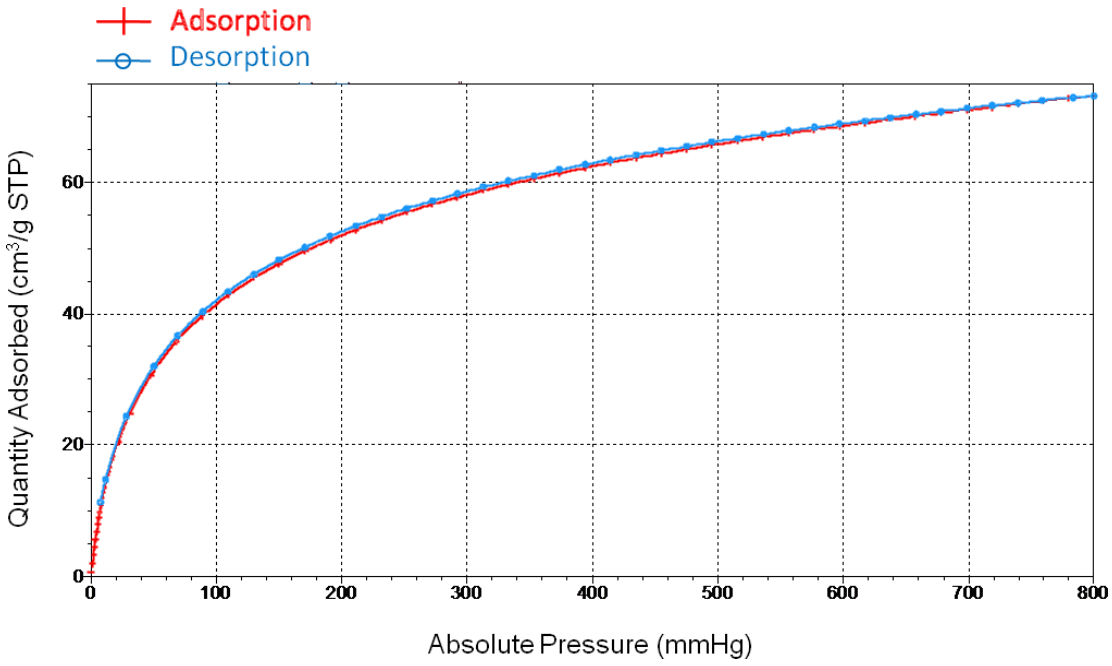

Figure 2.4. Hydrogen sorption isotherms for the CoOs PB (**2**): adsorption (red) and desorption (maroon) curves.

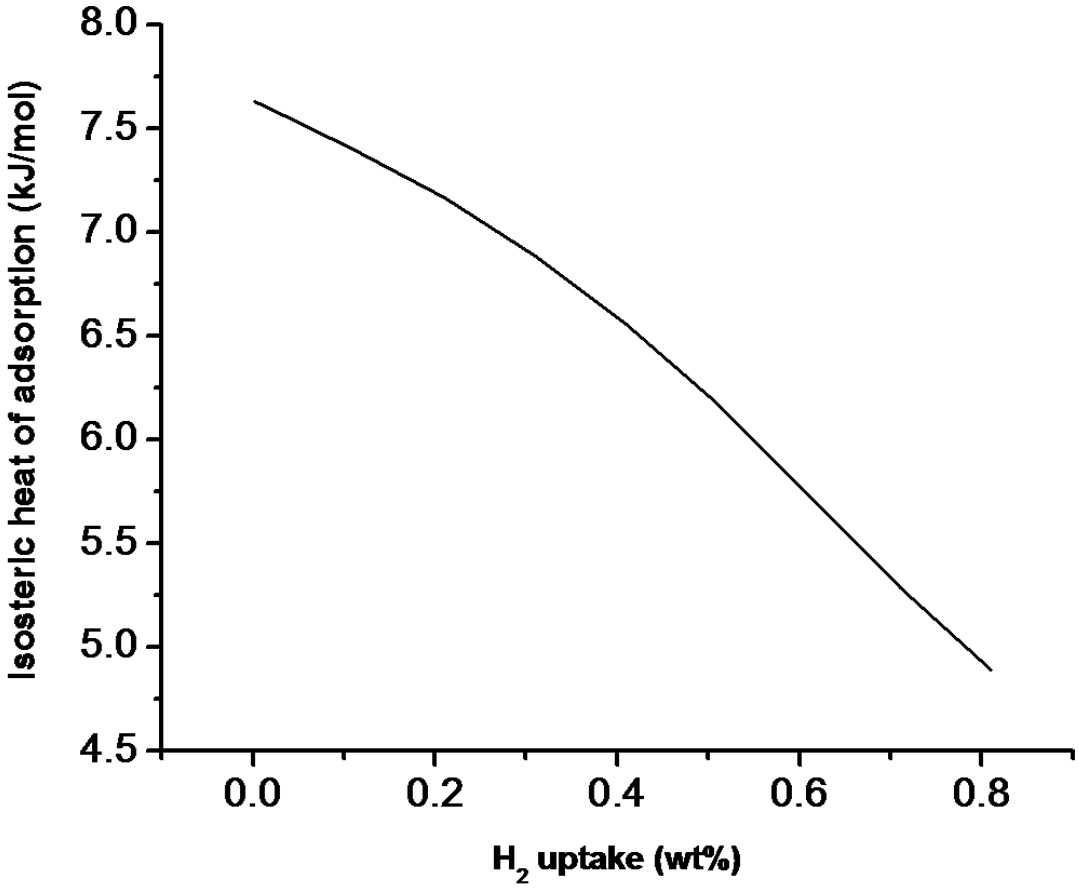

Figure 2.5. Enthalpy of H_2 adsorption for $Co_3[Os(CN)_6]_2$ PB (**2**).

an H_2 uptake of only 0.66 wt % at 77 K and 760 Torr (Figure 2.4). The degree of gas uptake observed for the $Co_3[Os(CN)_6]_2$ PB analog (**2**) is comparable to the uptake observed in other PB frameworks[126], particularly those containing $[Ru(CN)_6]^{n-}$ units.[163] The strength of the interaction of H_2 with the framework was probed by measuring a second hydrogen sorption isotherm for compound **2** at 87 K. Taking both the 77 and 87 K data, the enthalpy of adsorption as a function of the quantity of hydrogen adsorbed was calculated using a variant of the Clausius-Clayperon equation (Figure 2.5).[164]

Although the value of H_2 gravimetric uptake of PB frameworks, such as compound **2**, is relatively lower than some reported porous MOFs with higher gravimetric H_2 storage at 77 K and 760 torr (e.g. MOF-177: 1.25 wt%,[165] MOF-505: 2.47 wt%,[166] NOT-112: 2.3 wt%[167]), the PB materials are still a potential viable hydrogen storage media for future mobile applications. In contrast to other cubic frameworks reported by Yaghi and coworkers consisting of tetrahedral $[Zn_4O]^{6+}$ units linked via linear aryldicarboxylates which were shown to adsorb significant quantities of hydrogen reversibly ($Zn_4O(BDC)_3$: 1.3 wt % H_2 at 77 K and 760 torr; BDC = 1,4-benzenedicarboxylate)[168, 169], the Prussian blue analogues reported by Long[126] as well as compound **2** show enthalpies of adsorption higher (**2:** 7.6 kJ/mol) than the 4.7-5.2 kJ/mol observed for $Zn_4O(BDC)_3$. Thus, the Prussian Blue frameworks can be expected to store hydrogen at higher temperatures and lower pressures.

Magnetic Properties

Magnetic measurements were carried out on powder samples of the materials from the same batches used for powder X-ray diffraction studies (Figure 2.2). The magnetic

susceptibility was measured in an applied field of 1Tesla on a SQUID magnetometer (Appendix A). Measurements of variable oscillating AC frequencies in combination with field-cooled/zero-field-cooled (FC/ZFC) measurements were performed in order to determine the ordering temperatures, T_C, of the solids. The TIESST (Temperature Induced Excited Spin State Trapping) experiment was carried out by cooling the SQUID apparatus down to 2K while keeping the sample above the level of the dewar (Appendix A). The sample was then quickly dropped into the 2K sample chamber, essentially trapping the material in its room temperature magnetic state, allowing for susceptibility, AC, and ZFC/FC measurements to be performed. Photomagnetic measurements were performed in the SQUID using a fiber optic sample rod attachment, with white light as the irradiation source.

$Co_3[Os(CN)_6]_2 \cdot 6H_2O$ (2). The room temperature χT value is 4.12 emu·K/mol consistent with one high spin (H.S.) Co^{II} and one low spin (L.S.) Os^{III} ion (Figure 2.6a). As the temperature slowly decreases, the compound undergoes a reversible CTIST centered at 240 K. The CTIST is a result of a change in the electronic state of the PB solid from $[Co^{II}_{H.S.}\text{-}Os^{III}_{L.S.}]$ to $[Co^{III}_{L.S.}\text{-}Os^{II}_{L.S.}]$. After the transition, the χT value decreases slowly until reaching a value of 1.7 emu·K/mol, indicating that the spin transition to the diamagnetic state $[Co^{III}_{L.S.}\text{-}Os^{II}_{L.S.}]$ is not entirely complete. At 37 K, an increase in the susceptibility occurs which is an indication of magnetic ordering at low temperatures. Magnetization measurements can typically give insight into the type of coupling present in the solid, but, in this case the magnetization plot does not saturate. It is therefore not possible to determine the ground state and hence the coupling. Nevertheless, the slow

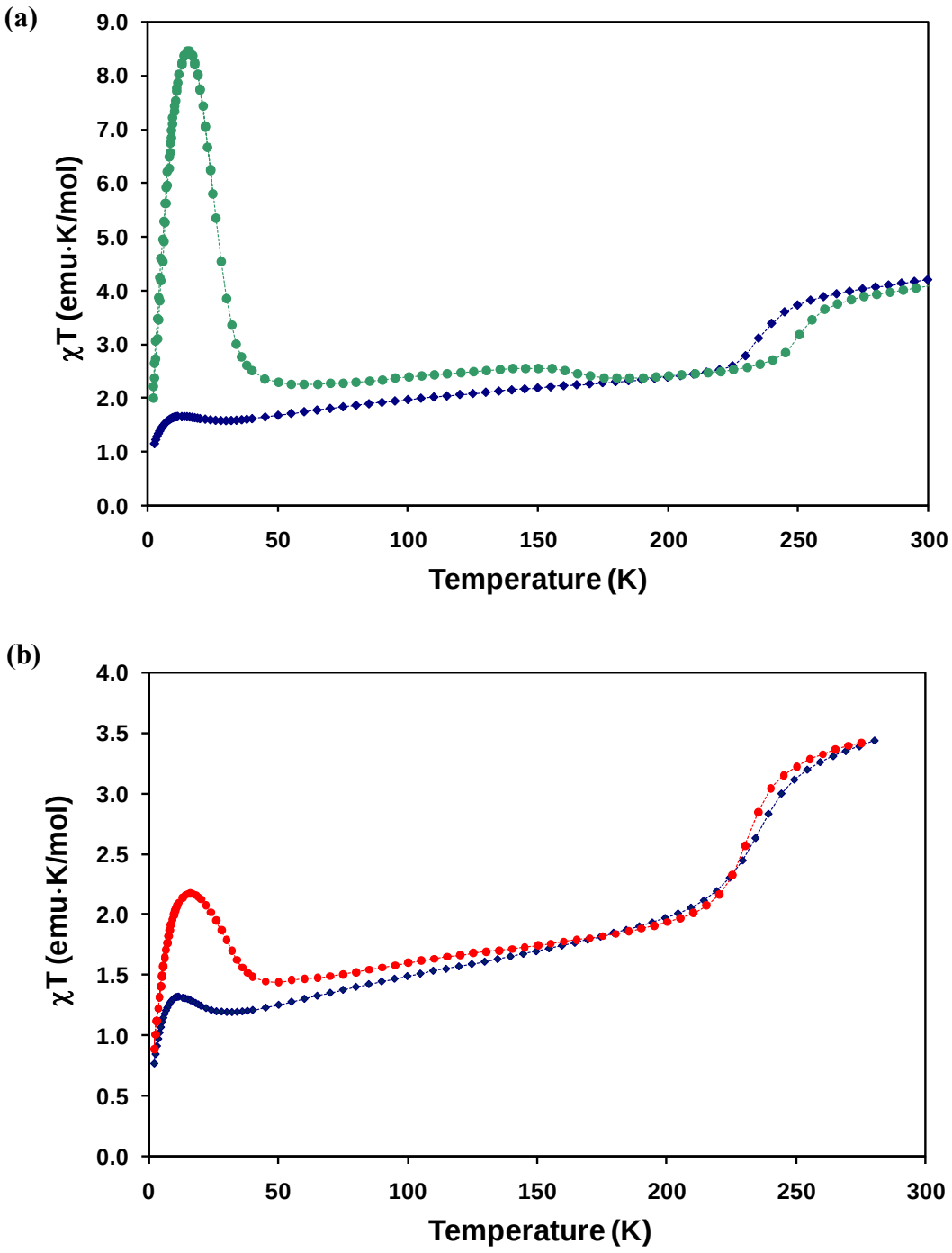

Figure 2.6. Temperature dependence of χT from 300 K to 2 K for (a) CoOs PB (blue) and the room temperature trapped state (TIESST: green), and (b) the non-irradiated (blue) and irradiated (red) sample of Co_3Os_2 PB.

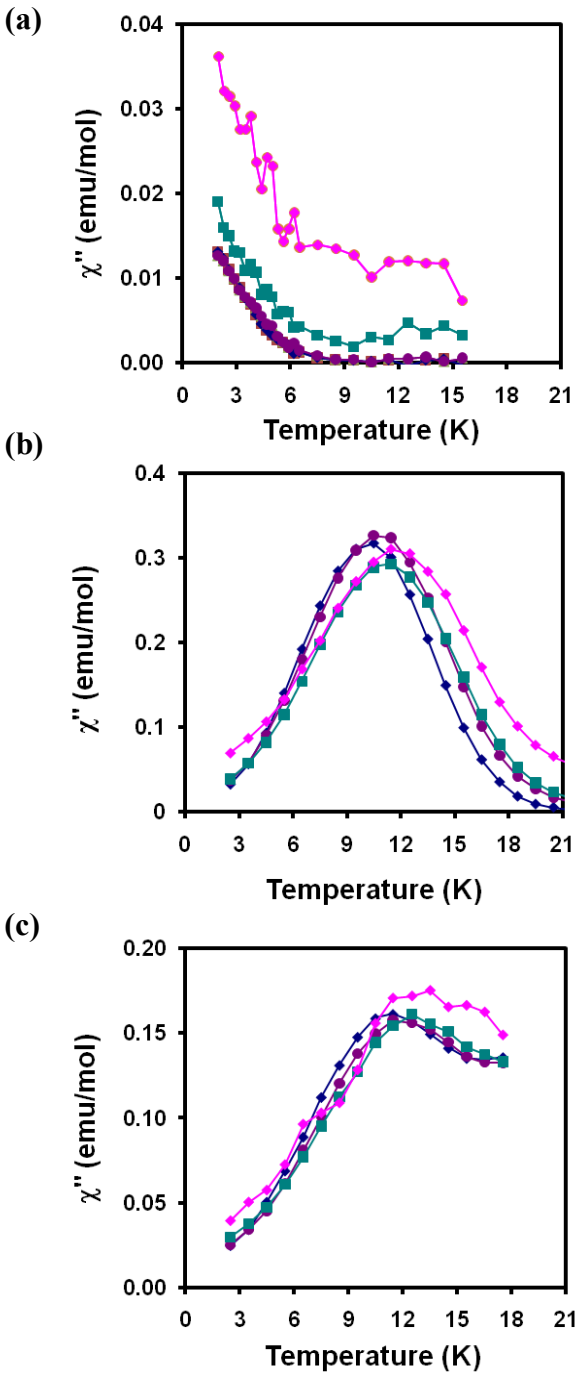

Figure 2.7. The imaginary part (χ'') of AC magnetic susceptibility at different frequencies from 1Hz to 1kHz (H_{AC} = 3 Oe and H_{DC} = 0 Oe) exhibiting the ferrimagnetic ordering for the (a) CoOs PB, the (b) CoOs PB TIESST state, and the (c) photomagnetic state, with ordering temperatures of <1.8K, 12.4, and 11.5 K respectively.

decrease of χT as the temperature decreases suggest that the Co^{II} and Os^{III} ions are antiferromagnetically coupled similar to what was observed by Sato and Verdaguer in their studies of the CoFe BP analogs. The incomplete cancellation of spins from the antiferromagnetic coupling of the Co^{II} and Os^{III} ions results in ferrimagnetic ordering. AC susceptibility measurements revealed that the compound has an ordering temperature ~2 K. (Figure 2.7a).

TIESST measurements are often useful as a quick indicator of photomagnetic behavior. When the sample is quickly cooled there is no thermal relaxation from the high temperature (HT) phase to the low temperature (LT) phase, which leaves the majority of the sample "trapped" in the $[Co^{II}_{H.S.}\text{-}Os^{III}_{L.S.}]$ state. As the temperature is increased from 2 K to 300 K (Figure 2.6a) there is a rapid increase in χT and a maximum is observed at 18 K. At higher temperatures there is a rapid decrease and the appearance of a plateau at 50 K. The sample reverts to the LS state at 170 K. As the sample is heated further a CTIST is observed at 250 K. The difference in the CTIST temperature between the DC and the TIESST measurements results in the onset of a hysteresis centered at 245 K. AC susceptibility measurements performed on the TIESST state showed an increase in the ordering temperature to ~11.5 K (Figure 2.7b). In the TIESST experiment, as explained previously, the majority of the sample is "trapped" in the $[Co^{II}_{H.S.}\text{-}Os^{III}_{L.S.}]$ state resulting in an enhancement of the Curie temperature (T_C) due to an increase in the number of paramagnetic pairs present in the trapped state.

The observation of TIESST for compound **2** indicated that the solid has potential for exhibiting photomagnetic properties. As a result, photomagnetic measurements

(Appendix A) on the CoOs PB were performed using white light as the irradiation source. The measurement involved a slow cooling of the sample and irradiation at low temperatures until the χT value reaches saturation. At this stage the light is turned off and the temperature is slowly increased. The photo-excited state exhibits the same magnetic behavior as the TIESST state including the CTIST hysteresis (Figure 2.6b). AC measurements revealed an ordering temperature of ~12.5 K for the photomagnetic state (Figure 2.7c).

$A_xCo_4[Os(CN)_6]_{(8+x)/3}\cdot nH_2O$ (A = Li **(3)**, Na **(4)**, K **(5)**, Rb **(6)**, Cs **(7)).** Many studies have been reported in the literature on the topic of CoFe PB analogs, particularly in the effect of incorporating various alkali metal ions on the magnetic properties such as the CTIST and the Curie temperatures. The independent work performed by Verdaguer and Sato demonstrated that the presence of alkali metal in the framework dramatically changes the CTIST and ordering temperature.[66-69, 134-148] Based on these highly interesting changes observed, a similar study was performed on the new CoOs PB material. The alkali metal ions were included during the reaction process to ensure inclusion of these cations into the structure. DC and AC measurements, as well as the TIESST experiment were performed on compounds **3-7**.

Measurements of the magnetic susceptibility of the alkali metal doped CoOs PB's indicate that the magnetic properties vary based on the type of alkali metal used in the preparation of the solid (Figures 2.8-2.10). For example, the Li and Na analogs show similar behavior with a room temperature χT value of 3.6 and 3.9 emu·K/mol respectively (Figure 2.8). As the temperature decreases, both compounds show a sharp

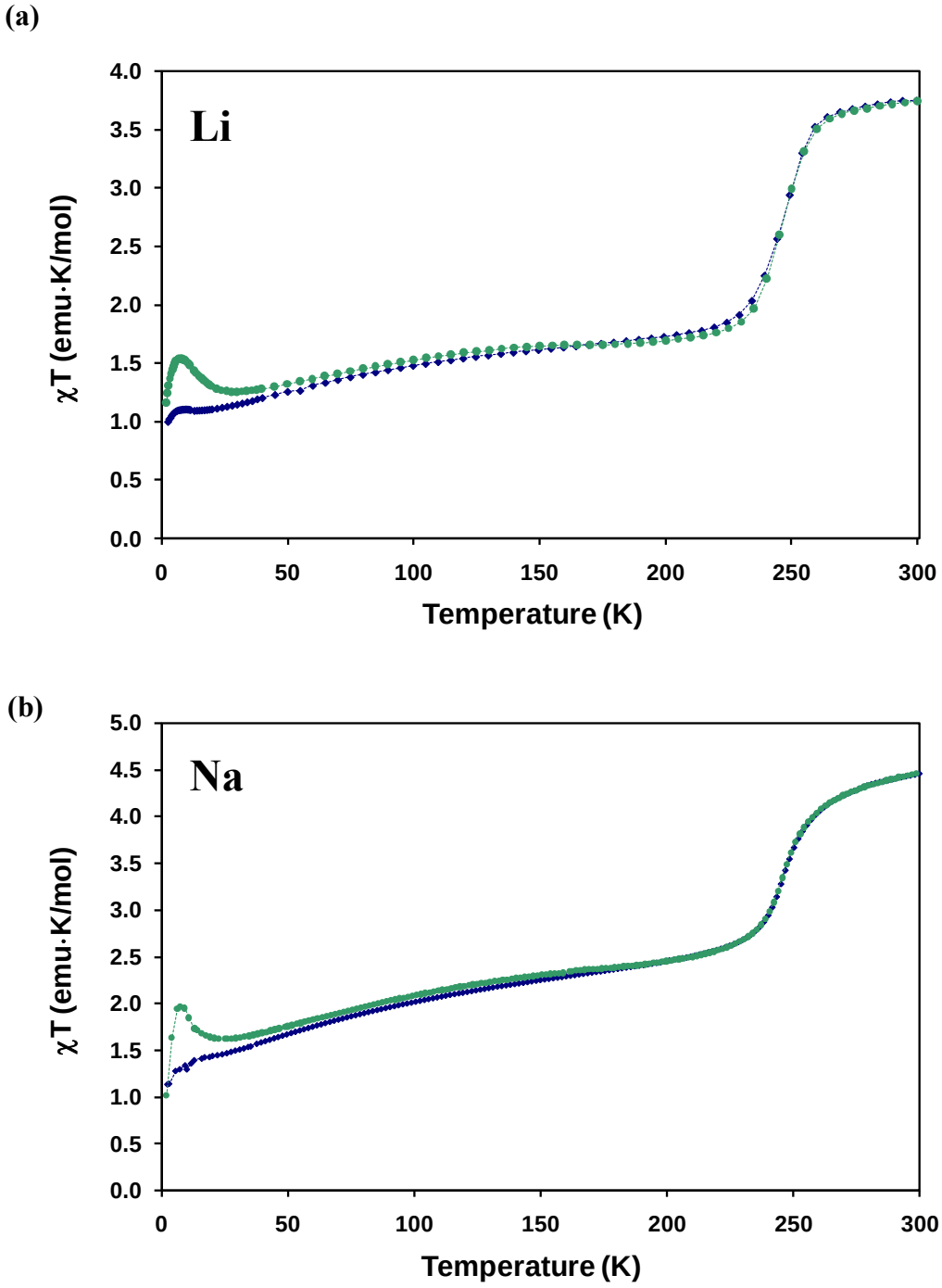

Figure 2.8. Temperature dependence of the χT from 300 K to 2 K (blue) and from 2 K to 300 K for the TIESST experiment (green) for the CoOs PB analogs of (a) Li (**3**) and (b) Na (**4**).

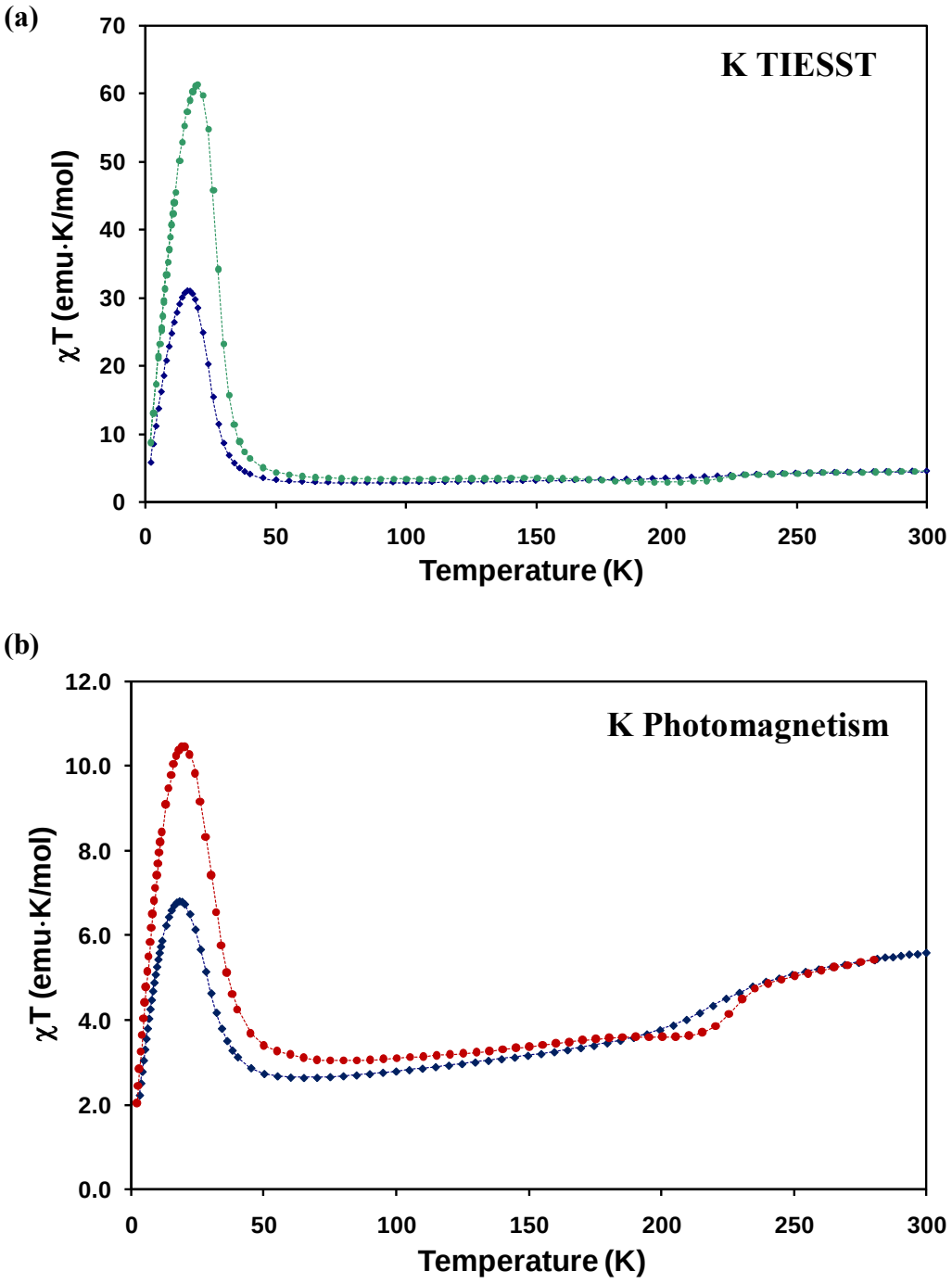

Figure 2.9. Temperature dependence of χT from 300 K to 2 K for (a) K-CoOs PB analog (**5**: blue) and the room temperature trapped state (TIESST: green), and (b) the non-irradiated (blue) and irradited (red) sample of K-CoOs PB analog.

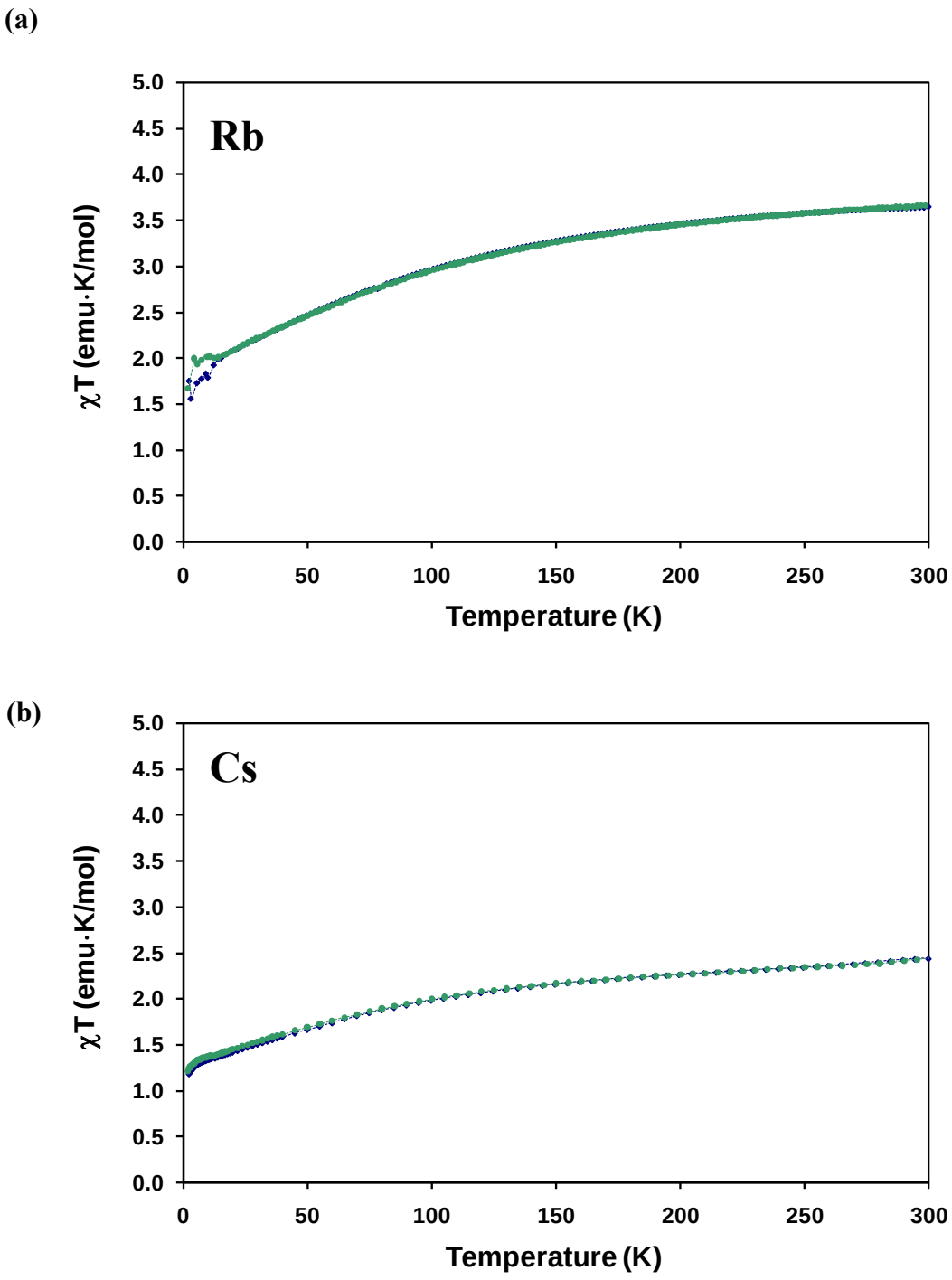

Figure 2.10. Temperature dependence of the χT from 300 K to 2 K (blue) and from 2 K to 300 K for the TIESST experiment (green) for the CoOs PB analogs of (a) Rb (**6**) and (b) Cs (**7**).

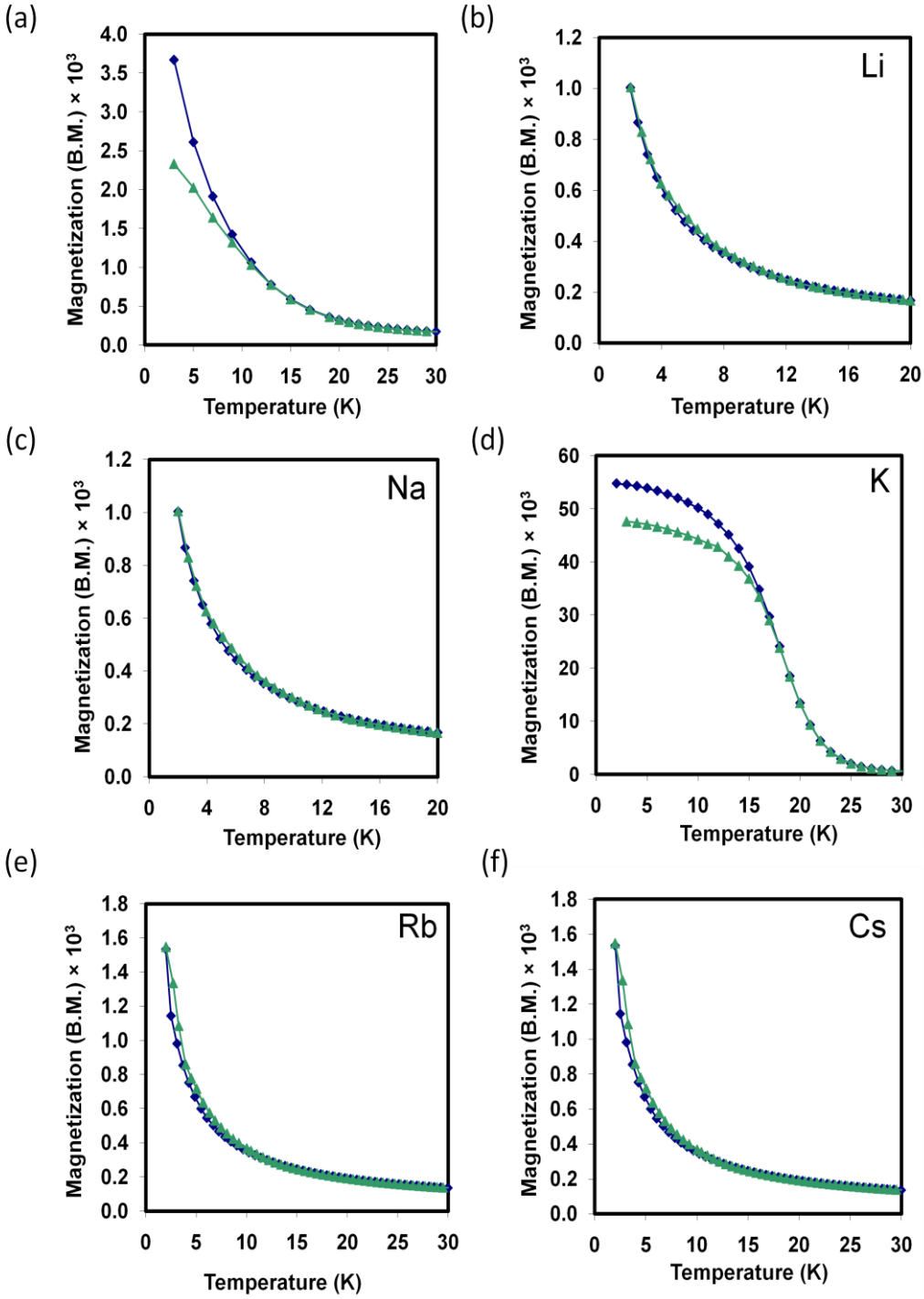

Figure 2.11. Zero Field Cooled/Field Cooled plots for (a) the CoOs PB (**2**) and its alkali metal analogs: (b) Li (**3**), (c) Na (**4**), (d) K (**5**), (e) Rb (**6**), and (f) Cs (**7**).

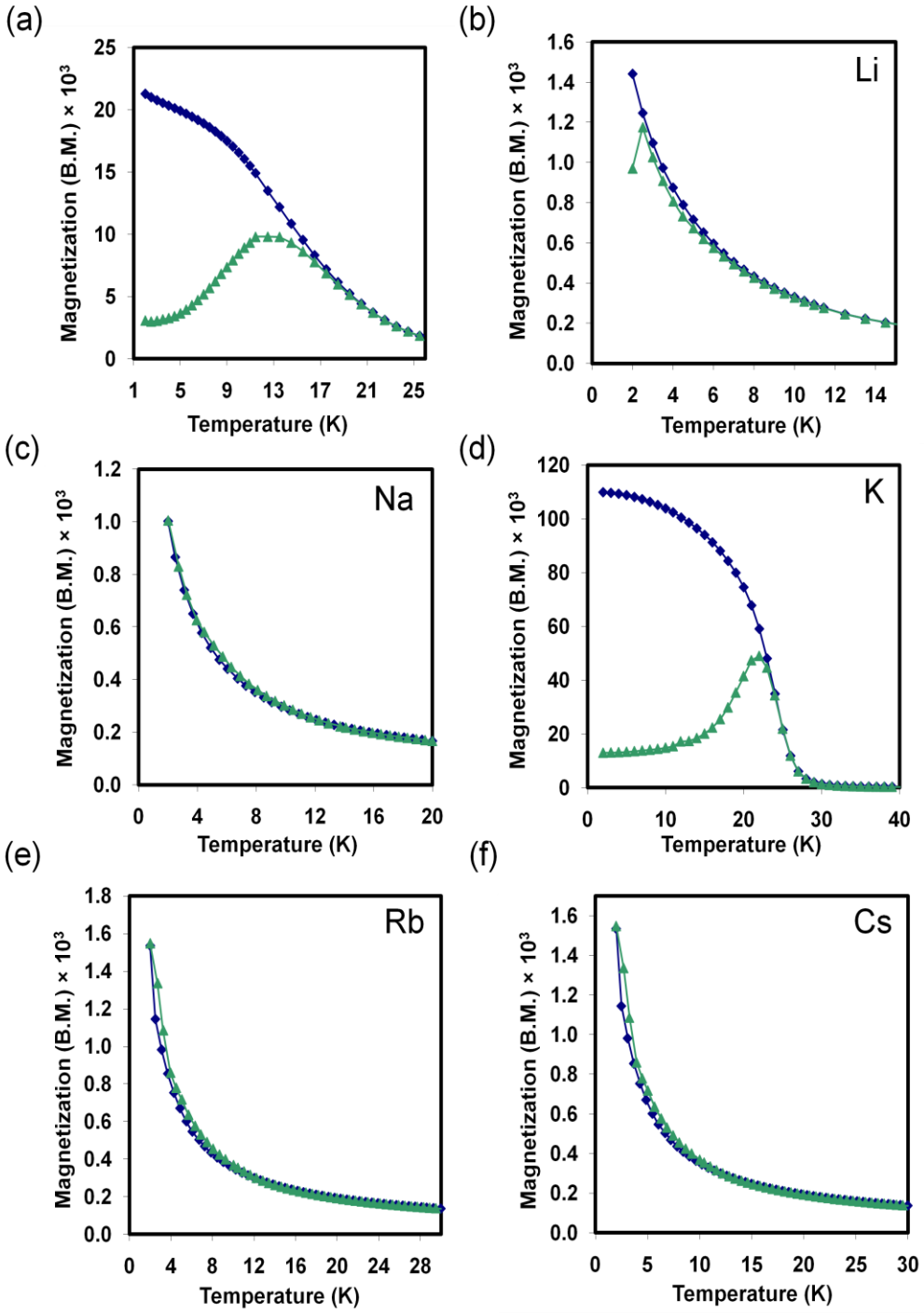

Figure 2.12. Zero Field Cooled/Field Cooled plots for the TIESST state of (a) the CoOs PB (**2**) and its alkali metal analogs: (b) Li (**3**), (c) Na (**4**), (d) K (**5**), (e) Rb (**6**), and (f) Cs (**7**).

CTIST centered at 250 K. Both, the Li and Na analogs exhibit a slow decrease of the χT vs. T plot until it reaches a value of 1.6 and 1.1 emu·K/mol at 1.8 K respectively. A very weak maximum at ~ 10 K is indicative of antiferromagnetic coupling that leads to weak ferrimagnetic ordering. The ZFC/FC measurements suggest that the Li and Na analogs order below 1.8 K (Figure 2.11). In contrast, the K analog shows a room temperature χT value of 4.1 emu·K/mol and exhibits a gradual CTIST centered at 235 K (the χT curve plateaus at ~3.8 emu·K/mol: Figure 2.9). A rapid increase is observed at 45 K which is indicative of ferrimagnetic ordering. The remnant magnetization for the ordered state is much greater than the values observed for the Li or Na analogs. This is consistent with an increase in the number of magnetic pairs present at low temperatures in the K analog. ZFC/FC measurements revealed that compound **5** displays a T_C = 16.9 K (Figure 2.11). The Rb analog exhibits a room temperature χT value of 3.7 emu·K/mol and exhibits no CTIST behavior. The χT value decreases to a low temperature value of 1.1 emuK/mol, with a slight increase at 12 K indicative of very weak ferrimagnetic ordering (Figure 2.10). ZFC/FC measurements indicate that the T_C is below 1.8 K (Figure 2.11). The Cs analog, however, exhibits different behavior from all the other analogs. The room temperature value is 2.4 emu·K/mol (Figure 2.10), which is much lower than the data for the other analogs, indicating that even at room temperature a majority of the sample is already partially converted to the diamagnetic [$Co^{III}_{L.S.}$-$Os^{II}_{L.S.}$] state. The χT curve gradually decreases down to 1.3 emu·K/mol which indicates antiferromagnetic coupling. No ordering was observed for the Cs material (Figure 2.11).

Table 2.4. Summary of magnetic data for compounds **2-7**.

Comp.	Alkali Metal	T_C	T_C TIESST/Photo	T_{TIESST}	$T_{1/2}$ CTIST
2	-	8.9	16.5/21.5	170	240, 250(TIESST)
3	Li	<1.8	<1.8	140	250
4	Na	<1.8	<1.8	170	247
5	K	15.9	20.9/28.5	180	235
6	Rb	-	-	-	-
7	Cs	-	-	-	-

Three of these five analogs, namely the Li, Na, and K compounds exhibit TIESST behavior, with a significant increase in the magnetic ordering temperature being observed for the K analog as compared its non-excited state. In each of these analogs, the TIESST magnetic susceptibility behavior follows the same trends as the corresponding non-excited state, with the exception that at low temperatures there is an increase in the ferrimagnetic ordering temperature. The most significant increase occurred for the K analog. In comparison to the CoOs Prussian blue material, no hysteresis behavior was observed. The ordering temperature for the K analog increased by ~5 K and the TIESST temperatures for the series of analogs ranged from 150-180 K as shown in Figures 2.12-2.13 and summarized in Table 2.4. The Li, Na, Rb and Cs analogs showed no increase in their magnetic moment at low temperatures (Figure 2.12).

Photomagnetic measurements were performed on the K analog since this compound showed the greatest response in the TIESST experiment. The photo-excited state showed the same magnetic susceptibility behavior as in the TIESST experiment including the observed CTIST (Figure 2.9b). ZFC/FC measurements indicate that the ordering temperature of the photomagnetic state is 28.5 K which is a dramatic change in the ordering temperature when compared to the non-excited state (15.9 K).

General Discussion of Magnetic Properties

The CoOs PB analogs exhibit similar magnetic behavior to the one observed in the CoFe PB analogs, which have been extensively studied for the past 16 years. The CoOs material synthesized from the PPN salt yielded a PB analog devoid of alkali metal contribution where the only two metals present are the Co and Os ions, in which 1/3 of

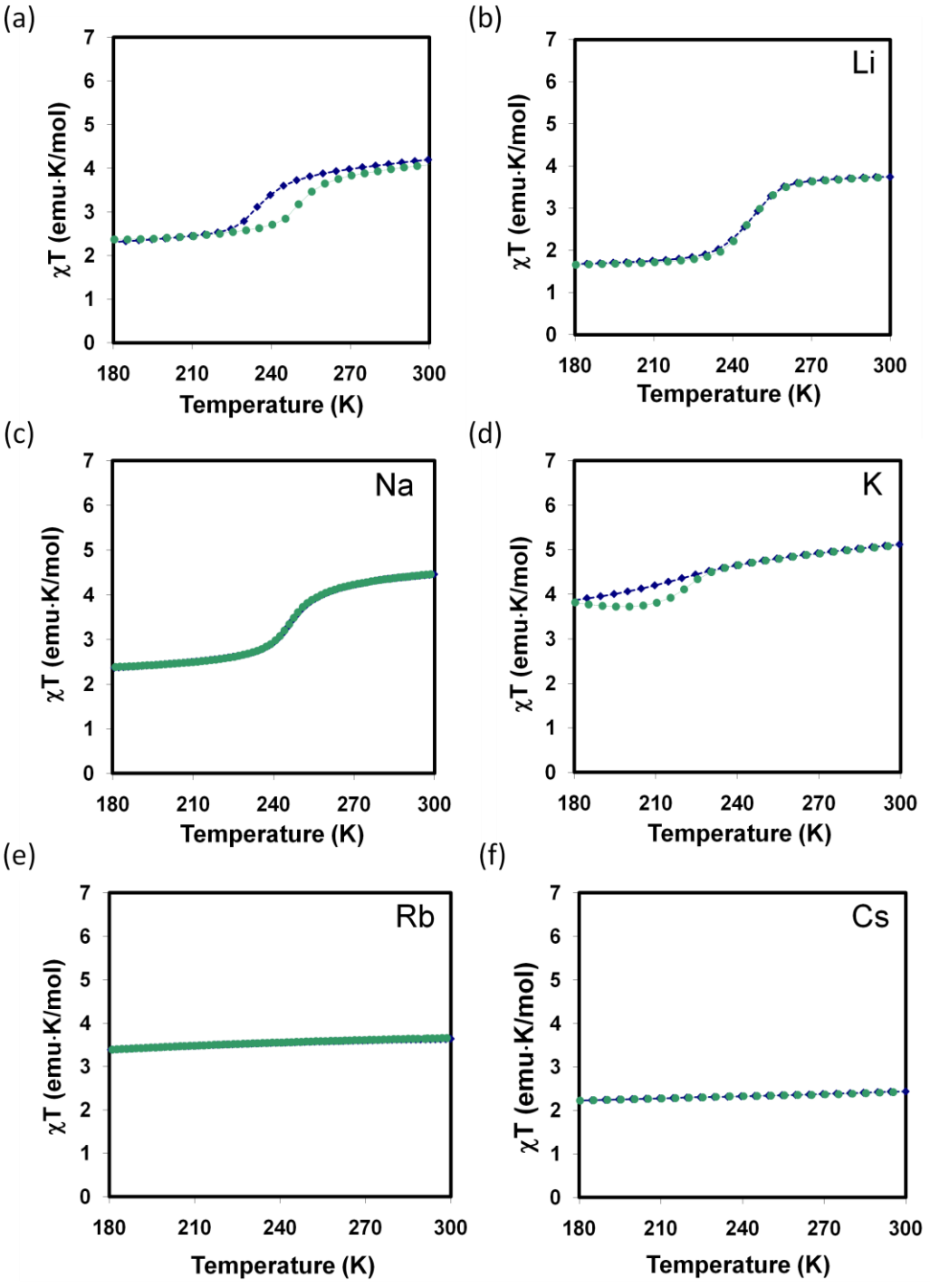

Figure 2.13. Temperature dependence of the χT from 300 K to 180 K (blue) and for the TIESST experiment (green) for (a) the CoOs PB (**2**) and its alkali metal analogs: (b) Li (**3**), (c) Na (**4**), (d) K (**5**), (e) Rb (**6**), and (f) Cs (**7**).

the $[Os(CN)_6]^{3-}$ vacancies are not filled. This material exhibits a CTIST at 230 K and a T_C of less than 1.8 K. This material undergoes a dramatic transition when the excited state is trapped by quickly cooling the solid or when the solid is photo-excited resulting in an increase of the T_C and CTIST temperatures to 12.3 K and 250 K respectively. Alkali metal ion inclusion has traditionally been used to dramatically alter the magnetic properties of the CoFe PB family. In the present study, an excess amount of alkali metal ion was included in the reaction of the CoOs PB to ascertain the effect of the alkali metal on the magnetic properties of the heavier Os^{III} congeners. Our results show that there is a substantial effect on the magnetic properties, both in the CTIST (Figure 2.13) and TIESST behavior. The Li and Na analogs exhibit the sharpest CTIST of the alkali metal ions, but do not show any evidence of ordering down to 1.8 K. No photomagnetism was observed, however the Li and Na analog show a small response in the TIESST experiment. In comparison, the magnetic moment of the K analog remains higher even at low temperatures, an indication of more $[Co^{II}_{H.S.}\text{-}Os^{III}_{L.S.}]$ pairs and hence a higher Curie temperature. The TIESST experiment indicates an increase in the ordering temperature (Table 2.4), but only by about 6 K, while the photoexcited state results in an increase of 12.6 K. While the Li, Na, and K ions lead to the observation of a CTIST, these results are in contrast to what is observed for the Rb and Cs analogs for which no CTIST was observed. For the Cs material, no ordering or CTIST is observed under any circumstances. The inclusion of Cs ions into the PB frameworks has been well studied, and it has been shown that this ion often facilitates an internal redox process between the metal ions during the synthesis, resulting in PB analogs with more of the diamagnetic

pairs being present at room temperature. The Cs analog of the CoOs PB shows a magnetic moment of 2.4-1.3 emu·K/mol from 2-300 K indicative of a large amount of the diamagnetic [$Co^{III}_{L.S.}$-$Os^{II}_{L.S.}$] pairs across the temperature range, which is consistent with the lack of magnetic ordering.

Optical Reflectivity Studies

Variable temperature UV-visible spectroscopy is a useful technique to support the observation of temperature and photon induced intramolecular electron transfer. In the photomagnetic CoFe PB analogs there is a shift in the solid state UV-vis spectra from red to blue, which correspond to the energies that switch the photomagnetic behavior on and off at low temperatures.

Preliminary optical reflectivity data (Appendix A) were collected on samples of the Na analog (**4**) and the K analog (**5**) in the laboratories of Prof. Corine Mathoniere at ICMCB in France, a leading expert in this area. The reflectivity spectra of compounds **4** and **5** were collected between 280 K to 10 K (cooling mode) and from 10 K to 280 K (heating mode) under white-light irradiation of ~100 mW/cm^2 at a sweeping temperature rate of 4 K/min. An alternative way to visualize the change of the spectra as function of temperature under light irradiation is presented in the form of the thermal dependence of the reflectivity at selected wavelenghts. The Na analog (**4**) shows significant optical changes. In particular the absolute reflectivity at 900 nm (Figure 2.14) shows temperature dependence between 200 and 280 K and between 170 K and 50 K. In accord with the magnetic data, the dependence between 200 and 280 K is due to the themal-induced electron transfer and the dependence between 170 and 50 K is due to the

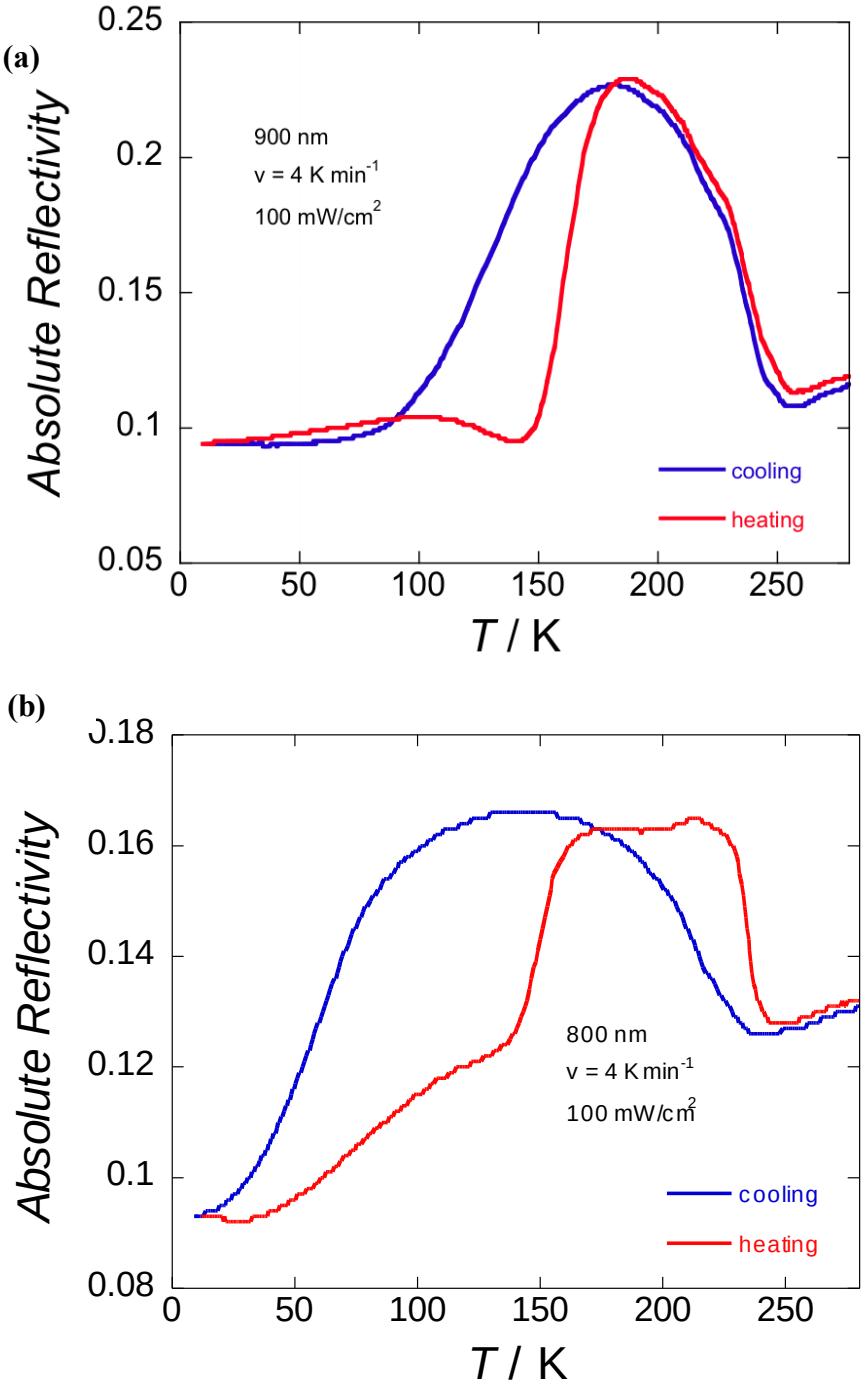

Figure 2.14. Optical reflectivity data plots for the CoOs PB analogs of (a) Na at 900 nm and (b) K at 800 nm in the cooling (blue) and heating (red) modes. Both compounds exhibit a thermal hysteresis event between 100-150 K.

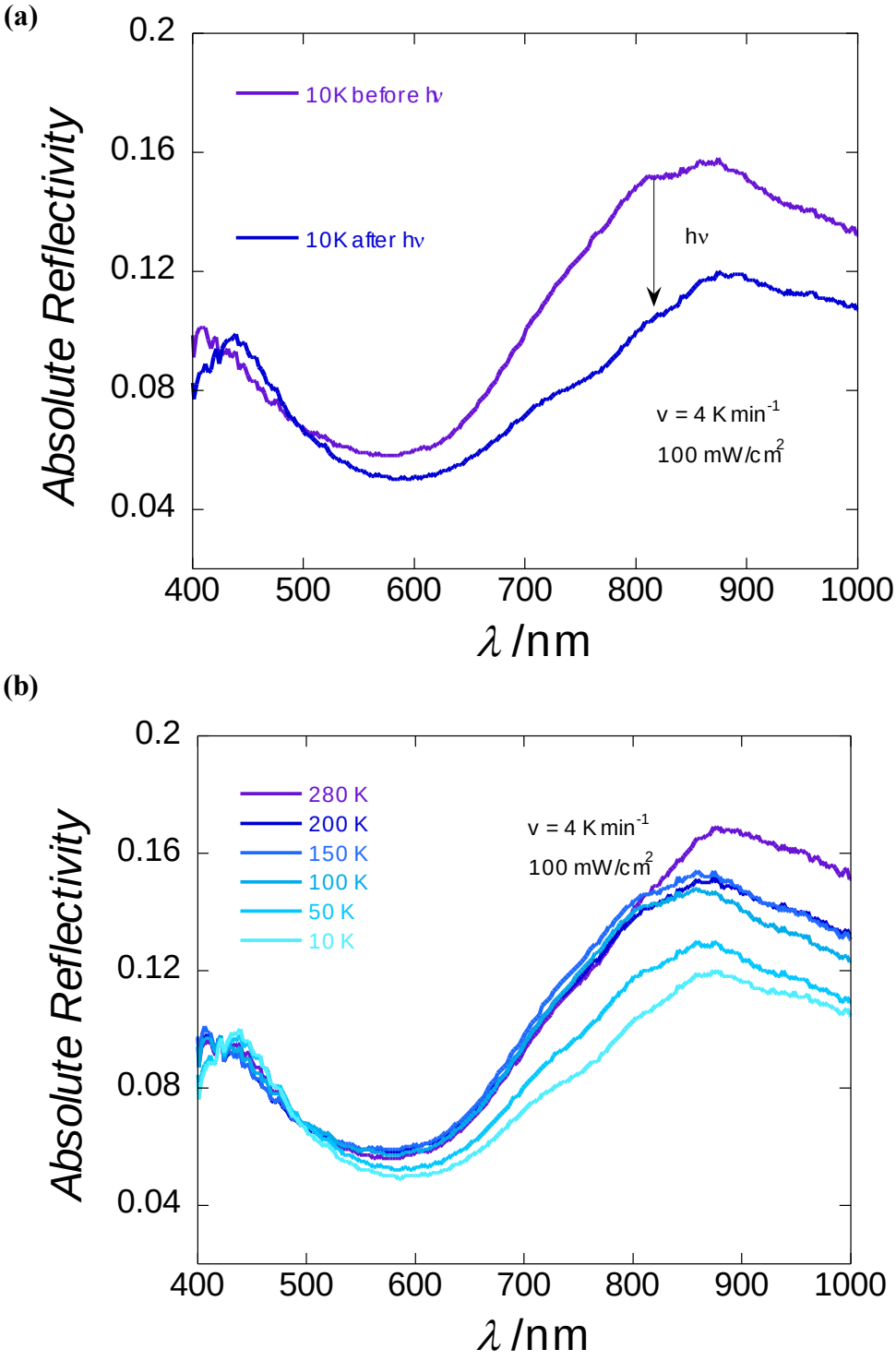

Figure 2.15. Optical reflectivity plots for the KCoOs PB analog collected at (a) 10K before (purple) and after (blue) irradiation and (b) between 10 to 280 K at a sweeping temperature rate of 4 K/min.

light-induced electron transfer. The thermal hysteresis between 100-150 K is a result of the slow saturation of the photoexcited state during the cooling process. The K analog (**5**) shows similar behavior to the one observed for the Na analog (Figure 2.14). In this case, however, additional measurements were performed by recording spectra before and after irradiation at 10 K. The spectrum recorded after irradiation is close to the spectrum at 280 K, suggesting that the same state as the HT state is formed at low temperatures (10 K) under light excitation (Figure 2.15).

CONCLUSIONS

The results in this chapter have led to the syntheses and characterization of new members of the Prussian blue family and the first with Os^{III} ions that exhibits photomagnetism. In a similar vein as the CoFe PB analogs, this family of compounds exhibits a wide variety of properties such as CTIST, TIESST, magnetic ordering, and photomagnetic behavior. The CoOs analog has been thoroughly characterized by IR, magnetism, and gas uptake, leading to the discovery of the newest photomagnetic Prussian blue which can exhibit a bistability of the CTIST at temperatures near to room temperature, as well as photomagnetic and temperature trapping bistability at very low temperatures in most cases.

The new findings lend insight into the nature of 5*d* transition metal analogs for which the 3*d* congener has been thoroughly studied. As the structural parameters are essentially the same, differences in magnetic phenomena can be directly linked to the

nature of the interactions between the 5*d* hexacyanoosmate(III) unit and the 3*d* cobalt(II) ion.

The data obtained thus far have revealed exciting behavior and they provide a bench mark for a more indepth investigation similar to those carried out in the literature for the CoFe PB analogs. These studies will include alkali metal dilution studies, complex spectroscopic measurements, such as EXAFS and XANES, which can give insight into the electronic states and bond distances, and MXCD (magnetic x-ray circular dichroism) measurements which can help to determine the coupling between the metal ions present. The CoOs PB materials represent a valuable addition to the Prussian blue literature, and will provide a great deal of interest to both chemists and physicists alike as they strive to understand the parameters that influence the properties of such an important class of magnetic materials.

CHAPTER III

CYANIDE LABILITY AND LINKAGE ISOMERISM OF HEXACYANOCHROMATE(III) INDUCED BY THE Co^{II} ION*

INTRODUCTION

Transition metal cyanide chemistry is in a renaissance period that began over a decade ago and is now one of the central themes of molecular magnetism research. The increased activity is due, in large measure, to the discovery that certain analogues of the Prussian blue (PB) family exhibit spontaneous magnetization at temperatures as high as 376 K.[55, 170, 171] These findings helped to fuel interest in the topic of paramagnetic cyanide complexes, particularly mixed metal/transition metal clusters.[129, 130, 172] The preparation of finite complexes rather than face-centered cubic PB phases relies on the use of capping ligands, typically multidentate organic molecules that block a number of coordination sites on metal ions and prevent the growth of extended structures. Many multinuclear cyanide-bridged complexes with novel magnetic properties have been prepared by such an approach.[88]

In our quest for unusual cyanide compounds with various coligands we turned to the tripodal phosphine ligand 1,1,1-tris(diphenylphosphinomethyl)ethane (triphos) for the preparation of molecular cubes $\{[MCl]_4[Re(triphos)(CN)_3]_4\}$[102, 106, 149] and squares

---

* Reprinted with permission from Avendano, C.; Karadas, F.; Hilfiger, M.; Shatruk, M.; Dunbar, K. R. **2010**, *Inorg. Chem.,* 49, 583-594, Copyright [2008] by American Chemical Society.

$\{[M^{II}Cl_2]_2[Co^{II}(triphos)(CN)_2]_2\}$[173, 174] (M = Mn, Fe, Co, Ni, Zn; Scheme 3.1). The formation of these species is dictated by the geometry of mononuclear building blocks, $[Re(triphos)(CN)_3]$[175] and $[Co(triphos)(CN)_2]$,[176] with three and two orthogonal CN^- ligands respectively that serve as bridges in the resulting multinuclear complexes.

Of relevance to this chapter, the tendency of the Co^{II} ion to form pentacoordinate complexes with phosphine ligands is well-known.[177, 178] Our successful use of $[Co(triphos)(CN)_2]$ for the preparation of molecular squares prompted us to synthesize other cyanide-bridged complexes with phosphine groups. Trinuclear species are the simplest model systems for the study of magnetic properties as a function of the nature of metal ions and their coordination geometries; hence, we sought to identify starting materials that would lead to products with three metal ions. The bidentate ligand 1,2-bis(diphenylphosphino)ethane (dppe) affords the pentacoordinate building block $[Co(dppe)_2(H_2O)]^{2+}$ which, when combined with a hexacyanometallate anion in a 2:1 ratio, leads to the desired trinuclear complex (Scheme 3.1b). This approach, while convenient for Co^{II}, does not translate well to other first row transition metals, as they are not prone to forming pentacoordinate precursors with dppe or other phosphine ligands.[179]

In this chapter we highlight the success of the outlined synthetic strategy to prepare cyanide-bridged molecular trimers with $[Fe^{III}(CN)_6]^{3-}$ and $[Co^{III}(CN)_6]^{3-}$ anions; however, an unexpected result occurred with $[Cr^{III}(CN)_6]^{3-}$, namely, the formation of a trigonal-bipyramidal (TBP) cyanide-bridged cluster. In this molecule, three equatorial positions are occupied by Co^{II} ions and the two axial positions are filled by $[Cr^{III}(CN)_6]^{3-}$

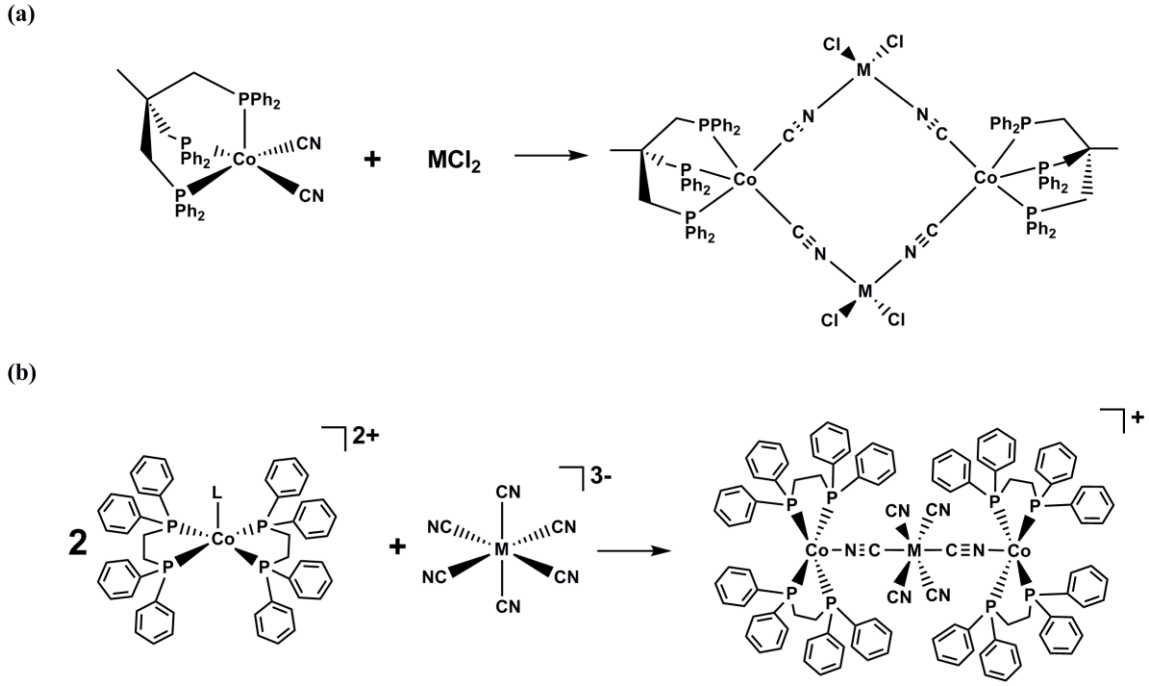

Scheme 3.1. Scheme depicting the formation of (a) molecular squares $\{[M^{II}Cl_2]_2[Co^{II}(triphos)(CN)_2]_2\}$ (M^{II} = Mn, Fe, Co, Ni, and Zn) and (b) trimers $\{[Co^{II}(dppe)_2]_2[M^{III}(CN)_6\}^+$ (M^{III} = Fe, Co).

ions. A study of the formation and structure of this complex revealed that the Co^{II} ions are bound to the C atoms of the bridging CN^- ligands as a consequence of cyanide linkage isomerism. Reversal of the orientation of the cyanide ligand has been observed for several other cyanide-bridged compounds containing Cr^{III}.[180, 181] For example, many years ago, Brown and Shriver observed that a $Co^{II}_3[Cr^{III}(CN)_6]_2$ Prussian blue analogue undergoes a cyanide flip process when heated in an inert atmosphere to 100 °C [182] and recently, Coronado and *et al*. discovered that the cyanide linkage isomerism of the Prussian blue analog $K_{0.4}Fe_4[Cr(CN)_6]_{2.8}•16H_2O$ can be reversed with the application of pressure.[181] Our group reported facile, albeit partial isomerization of the CN moiety for the $\{[Co^{II}(tmphen)_2][Cr^{III}(CN)_6]_2\}$ cluster with a TBP core.[183] A complete reversal of cyanide bridges was established for the related complex $\{[Fe^{II}(tmphen)_2][Cr^{III}(CN)_6]_2\}$,[184] as well as for the adduct of $[Cr^{III}(CN)_6]^{3-}$ with triphenylboron, $[Cr^{III}(NCBPh_3)_6]^{3-}$.[185]

Herein, we report a detailed investigation of cyanide linkage isomerism in the aforementioned Co^{II}-Cr^{III} complexes with the aim of demonstrating the generality of this phenomenon for $[Cr^{III}(CN)_6]^{3-}$in the presence of Lewis acids such as Fe^{II} and Co^{II} ions and BPh_3.

EXPERIMENTAL

Syntheses

Starting materials. $K_3[Cr(CN)_6]$ (Aldrich), $K_3[Co(CN)_6]$ (Pfaltz and Bauer), $(TBA)_3[Fe(CN)_6]$ (Fluka; TBA = tetrabutylammonium), 18-crown-6 (Aldrich), 1,1,1-

tris(diphenylphosphinomethyl)ethane (triphos; Aldrich), and $Co(BF_4)_2 \cdot 6H_2O$ (Aldrich) were used as received. The ligand 1,2-bis(diphenylphosphino)ethane (dppe; Aldrich) was recrystallized from ethanol before use. $[Co(triphos)(CH_3CN)_2](BF_4)_2$ was prepared as previously reported.[176] Acetonitrile and methanol were dried over 3 Å molecular sieves and distilled prior to use. Unless stated otherwise, all compounds were prepared under anaerobic conditions.

$[Co^{II}(dppe)_2(H_2O)][BF_4]_2$ (8). A quantity of dppe (2.34 g, 5.6 mmol) was added to a solution of $Co(BF_4)_2 \cdot 6H_2O$ (1.0 g, 2.8 mmol) in 70 mL of acetonitrile. The peach-colored mixture was stirred for 12 h, during which time a bright yellow precipitate was observed to form. The solid was collected by filtration in air, washed with dichloromethane (3 × 10 mL) and diethyl ether (3 × 5 mL), and air-dried. Yield = 2.58 g (88%). Elemental analysis: Calcd. for $CoP_4F_8OC_{52}B_2H_{50}$ values: C, 59.63; H, 4.81; F, 14.51; Found: C, 60.89; H, 4.71; F, 14.27%.

$\{[Co^{II}(dppe)_2]_2[Co^{III}(CN)_6]\}(BF_4)$ (9). A solution of $[(18\text{-crown-6})K]_3[Co(CN)_6]$ was prepared by stirring 56.5 mg (0.170 mmol) of $K_3[Co(CN)_6]$ and 113 mg (0.430 mmol) of 18-crown-6 in 13 mL of methanol for 6 h. The resulting solution was filtered to remove excess $K_3[Co(CN)_6]$. A second solution was prepared by stirring 300 mg (0.28 mmol) of **8** in 7 mL of acetonitrile to give a dark orange solution. The $[(18\text{-crown-6})K]_3[Co(CN)_6]$ solution was slowly added to the dark orange solution, and the mixture was left to stand undisturbed for 3 days. The crop of orange-red crystals that formed was filtered in air and washed with copious amounts of methanol. Yield = 225 mg (78%). Elemental analysis indicated the presence of interstitial water and methanol molecules:

Calcd. for $Co_3P_8F_4O_5N_6C_{111}BH_{108}$ (**9**·CH_3OH·$4H_2O$): C, 62.93; H, 5.14; N, 3.97; F, 3.58; Found: C, 63.69; H, 5.10; N, 4.29; F, 3.03%. IR(Nujol): ν(C≡N) 2126, 2148 cm^{-1}. ESI^+-MS (CH_3CN): m/z 1926 ($[M]^+$), 964 ($[M-H]^{2+}$). UV-vis(CH_3CN): λ_{max}, nm (ε, $M^{-1}cm^{-1}$) = 255 ($5.8\cdot10^4$), 315 ($2.1\cdot10^4$), 383 (5951).

{[Co^{II}(dppe)$_2$]$_2$[Fe^{III}(CN)$_6$]}(BF$_4$) (10). Compound **10** was prepared in a fashion analogous to that described above for compound **9**. The acetonitrile soluble salt $(TBA)_3[Fe(CN)_6]$ (62 mg per 10 mL of solvent) was used as the source of $[Fe(CN)_6]^{3-}$ anions. Yield = 205 mg (71%). Elemental analysis: Calcd. for $Co_2FeP_8F_4N_6C_{110}BH_{96}$: C, 65.28; H, 4.94; N, 4.11; F, 3.72; Found: C, 65.37; H, 4.80; N, 4.23; F, 3.52%. IR(Nujol): ν(C≡N) 2108, 2129 cm^{-1}. ESI^+-MS (CH_3CN): m/z 1923 ($[M]^+$), 962 ($[M-H]^{2+}$). UV-Vis(CH_3CN), λ_{max}, nm (ε, $M^{-1}cm^{-1}$): 253 (5.4×10^4), 320 (2.7×10^4), 394 (6857).

[Co^{II}(dppe)$_2$(CN)][BF$_4$] (11). This compound was synthesized using a different route than the previously reported procedure.[186] A solution of $[(18\text{-crown-}6)K]_3[Cr(CN)_6]$ was prepared by stirring 81.3 mg (0.250 mmol) of $K_3[Cr(CN)_6]$ and 159 mg (0.6 mmol) of 18-crown-6 in 10 mL of methanol for 6 h. The resulting solution was filtered to remove excess $K_3[Cr(CN)_6]$. A second solution was prepared by stirring 321 mg (0.3 mmol) of **8** in 10 mL of acetonitrile to give a dark orange solution. The $[(18\text{-crown-}6)K]_3[Cr(CN)_6]$ solution was slowly added to the dark orange solution, and the mixture was left to stand undisturbed. After 3 days, dark red-brown block crystals were present. The crystals were collected in air and washed with acetonitrile/diethyl ether. Yield = 193 mg (42%). Elemental analysis: Calcd. for $CoP_4F_4NC_{53}BH_{48}$: C, 65.72; H, 4.99; F, 7.85;

N, 1.45; Found: C, 65.20; H, 4.95; F, 7.78; N, 1.65%. IR(Nujol): ν(C≡N) 2096 cm^{-1}. ESI$^+$-MS (CH_3CN): m/z 882 ($[M]^+$). UV-vis (CH_3CN): λ_{max}, nm (ε, $M^{-1}cm^{-1}$) 502 (327).

$[Co^{III}(dppe)_2(CN)_2][BF_4]$ (12). A solution of $[(18\text{-crown-6})K]_3[Cr(CN)_6]$ was prepared by stirring 81.3 mg (0.250 mmol) of $K_3[Cr(CN)_6]$ and 159 mg (0.6 mmol) of 18-crown-6 in 10 mL of methanol for 6 h. The resulting solution was filtered to remove excess $K_3[Cr(CN)_6]$. A second solution was prepared by stirring 321 mg (0.3 mmol) of **8** in 10 mL of acetonitrile to give a dark orange solution and the $[(18\text{-crown-6})K]_3[Cr(CN)_6]$ solution was slowly added to it. The resulting mixture was left to stand undisturbed for 3 days, after which time the solution was filtered in air. After one week, the filtrate had produced yellow block-shaped crystals which were collected by filtration and washed with copious amounts of methanol followed by 5 mL of diethyl ether. Yield = 98 mg (33%). Elemental analysis: Calcd. for $CoP_4F_4N_2C_{55}BH_{52}O$: C, 64.31; H, 5.10; F, 7.40; N, 2.72; Found: C, 64.64 ; H, 4.94 ; F, 7.38 ; N, 2.72 %. IR(Nujol): ν(C≡N) 2114 cm^{-1}. ESI$^+$-MS (CH_3CN): m/z 908 ($[M]^+$). UV-vis(CH_3CN): λ_{max}, nm (ε, $M^{-1}cm^{-1}$) 299 (3.3×10^4), 353 (3.5×10^4).

$Co^{II}(triphos)(CN)_2$ (13). This compound was synthesized using a different route than the previously reported procedure.[177] A solution of $[(18\text{-crown-6})K]_3[Cr(CN)_6]$ was prepared by stirring 81.3 mg (0.250 mmol) of $K_3[Cr(CN)_6]$ and 159 mg (0.6 mmol) of 18-crown-6 in 10 mL of methanol for 6 h. The resulting solution was filtered to remove excess $K_3[Cr(CN)_6]$. A second solution was prepared by stirring 290 mg (0.3 mmol) of $[Co(triphos)(CH_3CN)_2](ClO_4)_2$ in 10 mL of acetonitrile to give a dark green solution. The $[(18\text{-crown-6})K]_3[Cr(CN)_6]$ solution was slowly added to the dark green solution to

yield a dark orange solution. The mixture was left to stand undisturbed for 3 days, during which time dark-red block-shaped crystals formed. The crystals were collected in air and washed with diethyl ether. Yield = 59 mg (27%). Elemental analysis: Calcd. for $CoP_3N_2C_{43}H_{39}$: C, 70.21; H, 5.34; N, 3.81; Found: C, 69.95; H, 5.55; N, 3.77%. IR(Nujol): ν(C≡N) 2096(s), 2101(w) cm^{-1}.

{[Co^{II}_3(dppe)$_4$(MeCN)][Cr^{III}(CN)$_6$]$_2$} (14). A solution of [(18-crown-6)K]$_3$[Cr(CN)$_6$] was prepared by stirring 55.2 mg (0.170 mmol) of K_3[Cr(CN)$_6$] and 113 mg (0.430 mmol) of 18-crown-6 in 7 mL of acetonitrile for 6 h and was filtered to remove excess K_3[Cr(CN)$_6$]. This solution was slowly added to a dark orange solution of 300 mg (0.28 mmol) of **8** in 3 mL of acetonitrile. Crystals were observed after 30 min. Surprisingly, the few orange crystals obtained were of sufficient quality for single-crystal X-ray analysis.

{[Co^{II}(tmphen)$_2$]$_3$[Cr^{III}(CN)$_6$]$_2$} (15). Five different samples of this complex were prepared by Dr. Mikail Shatruk according to the general method reported earlier[183] by varying the solvent, temperature, and reaction time (Table 3.1). In all reactions, a 4 mM solution of Co^{II} salt was treated with 2 equiv of tmphen, and the solution was stirred for ~30 min, after which time a 4 mM solution of [K(18-crown-6)]$_3$[Cr(CN)$_6$] was added. The product that formed was recovered by filtration, washed with the same solvent as used for the reaction, and dried *in vacuo*. No structural characterization of these samples was undertaken, but, as established in our previous reports,[183] they contain varying amounts of interstitial solvent, which exchanges for water with exposure of solid samples to humid laboratory air.

Table 3.1. Reaction conditions used along with colors and IR data for different batches of $\{[Co(tmphen)_2]_3[Cr(CN)_6]_2\}$.

Sample	Solvent	Co(II) source	Time	Temp.	Color	$\nu(C\equiv N)$,[a] cm^{-1}
15a[b]	MeCN	$CoCl_2$	24 h	25°C	brown	2157(b), 2133(t), 2105(i)
15b	MeCN	$Co(BF_4)_2 \cdot 6H_2O$	24 h	25°C	yellow/brown	2155, 2147(b), 2135, 2126 (t), 2103(i)
15c[c]	MeCN	$Co(BF_4)_2 \cdot 6H_2O$	5 min	25°C	yellow	2155, 2147(b), 2123(t), 2103(i)
15d[c]	MeCN	$Co(BF_4)_2 \cdot 6H_2O$	1 min	0°C	peach-yellow	2155, 2147(b), 2123(t)
15e	MeOH	$CoCl_2 \cdot 6H_2O$	24 h	25°C	peach	2157(b), 2125(t)

[a] t = terminal, b = bridging normal, i = bridging isomerized

[b] The sample was prepared under anaerobic conditions.

[c] Reactions were performed with stirring.

Single Crystal X-ray Diffraction

In a typical experiment, a crystal selected for study was suspended in polybutene oil (Aldrich) and mounted on a cryoloop which was placed in a N_2 cold stream. Single-crystal X-ray data were collected on a Bruker APEX or Bruker SMART 1000 diffractometer equipped with a CCD detector at 110 K. The data sets were recorded as three ω scans of 606 frames each, at a 0.3° step width, and integrated with the Bruker SAINT[187] software package. The absorption correction (SADABS[188]) was based on fitting a function to the empirical transmission surface as sampled by multiple equivalent measurements. Solution and refinement of the crystal structures was carried out using the SHELX[189] suite of programs and the graphical interface X-SEED.[190] Structure solution by direct methods resolved positions of all metal and P atoms as well as most of the C and N atoms. The remaining non-hydrogen atoms were located by alternating cycles of least-squares refinements and difference Fourier maps. Hydrogen atoms were placed at calculated positions. In the case of compounds with $[BF_4]^-$ counterions, these were disordered and were restrained to meaningful geometries. The final refinement was performed with anisotropic thermal parameters for all non-hydrogen atoms. A summary of pertinent information relating to unit cell parameters, data collection, and refinements is provided in Table 3.2. Selected metal–ligand bond distances are provided in Table 3.3 for compounds **9-12** and in Table 3.4 for compound **14**.

Table 3.2. Crystal structural data and refinement parameters for compounds **9–14**.

Compound	**(9)**	**(10)**	**(11)**	**(12)**	**(14)**
Space group	$P2_1/n$	$P2_1/n$	$P2_1/c$	P-1	*Aba*2
Unit cell	a = 12.653(1)Å b = 21.718(2)Å c =19.395(1) Å β = 92.207(1)°	a = 12.718(4)Å b = 21.726(7)Å c = 19.360(6)Å β =91.837(5) °	a = 12.572(2)Å b = 25.590(3)Å c = 14.669(2)Å β = 106.029(2))°	a = 10.498(1) Å b =13.092(2)Å c =19.029(2)Å α=97.372(2)° β =92.307(2)°, γ=111.080(1)°	a = 51.547(10)Å b = 26.188(5)Å c =19.705(4)Å
Unit cell volume, V	5325.7(6)Å^3	5347(3) Å^3	4536.0(10)Å^3	2409.9(5)Å^3	26600(9)Å^3
Z	2	2	1	2	8
Density, ρ_{calc}	1.335 g/cm^3	1.353 g/cm^3	1.418 g/cm^3	1.416 g/cm^3	1.236 g/cm^3
Abs. coeff., μ	0.644 mm^{-1}	0.627 mm^{-1}	0.575mm^{-1}	0.547mm^{-1}	0.676 mm^{-1}
Crystal color and habit	orange-red needle	dark-green needle	red-brown block	yellow block	orange plate
Crystal size	0.18 x 0.10 x 0.08 mm	0.16 x 0.11 x 0.07 mm	0.11x0.10x0.09 mm	0.20 x 0.20 x 0.10 mm	0.15 x 0.11 x 0.07 mm
Temperature	110 K	110 K	110 K	110 K	110 K
Radiation, λ	Mo-Kα, 0.71073 Å	Mo-Kα, 0.71073 Å	Mo-Kα, 0.71073 Å	Mo-Kα, 0.71073 Å	Mo-Kα, 0.71073 Å
Min. and max. θ	1.86 to 25.00º	1.41 to 28.43º	1.59 to 28.30º	1.69 to 28.44º	1.35 to 26.37º
Reflections collected	44963 [R_{int} =0.0320]	32303 [R_{int} =0.2242]	25866 [R_{int} = 0.0342]	25826[R_{int} =0.0297]	101233 [R_{int} =0.1948]
Independent reflections	9010	9158	10270	10940	23377
Data/parameters/ restraints	9010/724/237	9158/641 /746	10270/577/1	10940/626 /0	23377 /1397/4
R [$F_o > 4\sigma(F_o)$]	R_1 = 0.086 wR_2 = 0.203	R_1 = 0.092 wR_2 = 0.194	R_1 = 0.060 wR_2 = 0.146	R_1 = 0.042 wR_2 = 0.1116	R_1 = 0.126 wR_2 =0.283
G.o.f. on F^2	1.280	1.084	1.087	1.034	1.027
Max./min. residual densities, e·Å^{-3}	1.63, -0.78	1.23, -0.92	1.96, –0.51	1.14, -0.68	1.91, -0.76

Table 3.3. Metal-ligand bond distances (Å) and bond angles (°) in the crystal structures of compounds **9-12**.[a]

$\{[Co(dppe)_2]_2[Co(CN)_6]\}(BF_4)$ **(9)**			
Co(1)-N≡C	1.983(5)	Co(1)-N≡C	178.5(5)
Co(2)-C≡N_{br}	1.925(7)	Co(2)-C≡N_{br}	176.4(6)
Co(2)-C≡N_{ter}	2.08(1)	Co(2)-C≡N_{ter}	176.1(9)
$(C≡N)_{br}$	1.099(9)	P(1)-Co-P(2)	81.83(6)
$(C≡N)_{ter}$	1.08(1)	P(2)-Co-P(3)	97.72(6)
Co(1)-P_{avg}	2.27(1)	P(3)-Co-P(4)	81.16(6)
		P(4)-Co-P(1)	99.03(6)
$\{[Co(dppe)_2]_2[Fe(CN)_6]\}(BF_4)$ **(10)**			
Co(1)-N≡C	1.982(4)	Co(1)-N≡C	176.9(5)
Fe-C≡N_{br}	1.997(5)	Fe-C≡N_{br}	175.9(5)
Fe-C≡N_{ter}	2.102(7)	Fe-C≡N_{ter}	175.4(6)
$(C≡N)_{br}$	1.069(7)	P(1)-Co-P(2)	81.00(6)
$(C≡N)_{ter}$	1.031(8)	P(2)-Co-P(3)	99.21(6)
Co(1)-P_{avg}	2.279(1)	P(3)-Co-P(4)	81.62(7)
		P(4)-Co-P(1)	97.95(6)
$[Co(dppe)_2(CN)][BF_4]$ **(11)**			
Co-C≡N_{ter}	1.986(3)	Co-C≡N_{ter}	178.3(3)
Co(1)-P_{avg}	2.278(1)	P(1)-Co-P(2)	86.00(3)
		P(2)-Co-P(3)	106.35(3)
		P(3)-Co-P(4)	89.12(3)
		P(4)-Co-P(1)	167.95(3)
$[Co(dppe)_2(CN)_2][BF_4]$ **(12)**			
Co-C≡N_{ter}	1.889(2)	Co-C≡N_{ter}	175.2(2)
Co(1)-P_{avg}	2.317(1)	P(1)-Co-P(2)	82.99(2)
		P(2)-Co-P(3)	97.01(2)
		P(3)-Co-P(4)	82.99(2)
		P(4)-Co-P(1)	97.01(2)

[a] ter = terminal, br = bridging

Table 3.4. Metal to ligand bond distances (Å) and bond angles (°) in the crystal structures of compound **14**.

$\{[Co_3(dppe)_4(MeCN)][Cr(CN)_6]_2\}$ **(14)**			
	Bond Distance (Å)		Angle (°)
Cr(1)-(C ≡N)$_{terminal}$	2.047(17)	Cr(1)-N(1)≡C(1)-Co(1)	174.8(12)
Cr(1)-N(1)≡C(1)-Co(1)	2.042(15)	Cr(1)-N(3)≡C(3)-Co(2)	171.1(10)
Cr(1)- N(3)≡C(3)-Co(2)	2.023(12)	Cr(1)-N(2)≡C(2)-Co(3)	175.3(10)
Cr(1)- N(2)≡C(2)-Co(3)	2.021(16)		
Cr(2)- (C ≡N)$_{terminal}$	2.032(16)	Cr(2)-N(4)≡C(4)-Co(1)	169.4(10)
Cr(2)- N(4)≡C(4)-Co(1)	2.005(12)	Cr(2)-N(6)≡C(6)-Co(2)	175.0(10)
Cr(2)- N(6)≡C(6)-Co(2)	2.036(13)	Cr(2)-N(5)≡C(5)-Co(3)	174.1(11)
Cr(2)- N(5)≡C(5)-Co(3)	2.034(15)		
Co(1)-P(1)	2.242(4)	C(4)-Co(1)-C(1)	90.2(5)
Co(1)-P(2)	2.230(4)	C(4)-Co(1)-P(2)	173.6(4)
Co(1)-P(3)	2.269(4)	C(1)-Co(1)-P(2)	93.1(4)
Co(1)-C(1)≡N(1)-Cr(1)	1.910(12)	C(4)-Co(1)-P(1)	88.7(4)
Co(1)-C(4)≡N(4)-Cr(2)	1.865(16)	C(1)-Co(1)-P(1)	103.9(3)
		P(2)-Co(1)-P(1)	85.21(15)
		C(4)-Co(1)-P(3)	84.4(4)
		C(1)-Co(1)-P(3)	97.0(3)
		P(2)-Co(1)-P(3)	100.60(16)
		P(1)-Co(1)-P(3)	158.01(16)
Co(2)-P(4)	2.310(5)	C(3)-Co(2)-C(6)	87.4(5)
Co(2)-P(6)	2.230(4)	C(3)-Co(2)-P(5)	90.4(4)
Co(2)-P(5)	2.228(4)	C(6)-Co(2)-P(5)	155.9(4)
Co(2)-C(3)≡N-Cr(1)	1.830(14)	C(3)-Co(2)-P(6)	162.4(5)
Co(2)-C(6)≡N-Cr(2)	1.867(14)	C(6)-Co(2)-P(6)	92.3(4)
		P(5)-Co(2)-P(6)	82.79(15)
		C(3)-Co(2)-P(4)	95.8(4)
		C(6)-Co(2)-P(4)	98.2(4)
		P(5)-Co(2)-P(4)	105.85(17)
		P(6)-Co(2)-P(4)	101.61(16)
Co(3)-P(8)	2.225(4)	C(5)-Co(3)-C(2)	88.7(6)
Co(3)-P(7)	2.242(4)	C(5)-Co(3)-N(13)	96.4(5)
Co(3)-N(13)-CMe	2.035(11)	C(2)-Co(3)-N(13)	98.1(5)
Co(3)-C(2)≡N-Cr(1)	1.916(15)	C(5)-Co(3)-P(8)	89.6(4)
Co(3)-C(5)≡N-Cr(2)	1.868(14)	C(2)-Co(3)-P(8)	170.5(4)
		N1(3)-Co(3)-P(8)	91.4(3)
		C(5)-Co(3)-P(7)	171.0(4)
		C(2)-Co(3)-P(7)	93.3(4)
		N(13)-Co(3)-P(7)	92.1(4)
		P(8)-Co(3)-P(7)	87.08(16)

RESULTS AND DISCUSSION

Syntheses and Single Crystal X-ray Structures

The Co^{II} center in $[Co^{II}(dppe)_2(X)]^{2+}$, where X = MeCN or H_2O, is in a square-pyramidal geometry, which is typical for most phosphine complexes of Co^{II}, including those with chelating and monodentate phosphine ligands.[176, 191-193] The presence of two dppe capping ligands and a single open site available for further chemistry renders this compound a convenient precursor for the assembly of linear trinuclear molecules.

An orange solution of $[Co^{II}(dppe)_2(H_2O)][BF_4]_2$ (**8**) in acetonitrile was reacted with solutions of $[M^{III}(CN)_6]^{3-}$ (M = Co and Fe) in methanol to form the isostructural linear cyanide-bridged trimers **9** and **10** (Figure 3.1). The compounds are stable in solution and in the solid state and are soluble in MeCN, CH_2Cl_2, and DMF. In both **9** and **10**, the ligand environment and geometries of each metal ion are the same as in the starting material, with the P atoms of dppe occupying the equatorial plane and the N-bound bridging cyanide from the hexacyanometallate fragment coordinating to the apical position of the square pyramid.

Surprisingly, the reaction of an acetonitrile solution of **8** and a methanol solution of $[Cr^{III}(CN)_6]^{3-}$ led to the formation of red crystals of the mononuclear complex $[Co^{II}(dppe)_2(CN)][BF_4]$ (**11**). After removal of the crystals and exposure of the mother liquor to air for a week, yellow crystals of $[Co^{III}(dppe)_2(CN)_2][BF_4]$ (**12**) were obtained.

In the structure of **11**, the geometry around the Co^{II} ion is substantially altered, as the dppe ligands have rearranged around the cobalt ion and the CN^- ligand is positioned in the equatorial plane of the square pyramid (Figure 3.2a). The source of this cyanide is

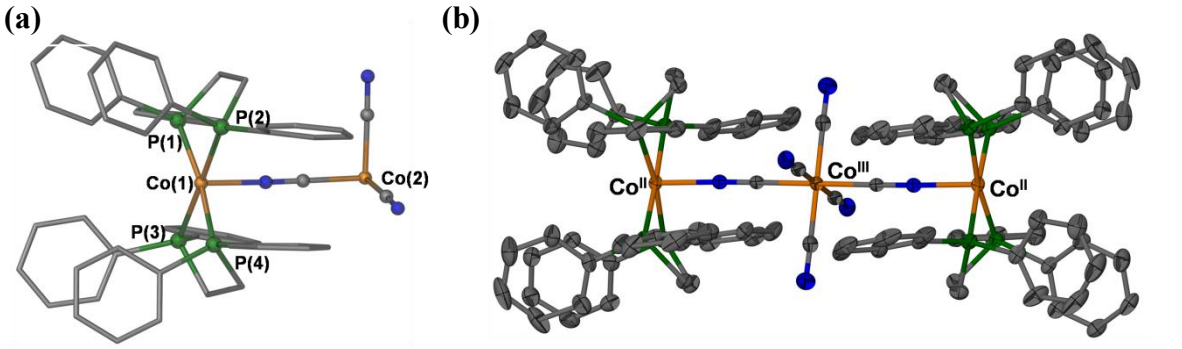

Figure 3.1. (a) Molecular structure of the asymmetric unit of $\{[Co^{II}(dppe)_2]_2[Co^{III}(CN)_6]\}^+$ and (b) the thermal ellipsoid plot of the trinuclear cation $\{[Co^{II}(dppe)_2]_2[Co^{III}(CN)_6]\}^+$ in **9**. Ellipsoids projected at the 50% probability level.

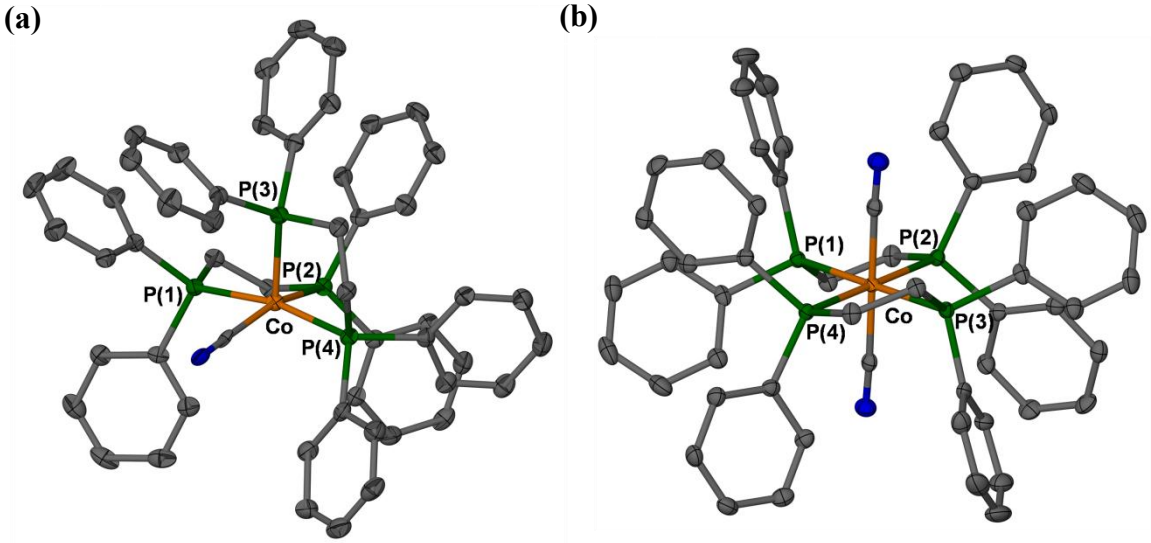

Figure 3.2. Thermal ellipsoid plots of the cation (a) $[Co(dppe)(CN)]^+$ in **11** and (b) $[Co(dppe)(CN)_2]^+$ in **12**. Ellipsoids projected at the 50%probability level.

obviously the $[Cr^{III}(CN)_6]^{3-}$ ion as it is the only cyanide-containing starting material used in the reaction. Moreover, $[Cr^{III}(CN)_6]^{3-}$ has been shown to undergo cyanide linkage isomerism, leading to new cyano complexes that contain an N-bound Cr^{III} ion.[181, 184, 185] The observed products invoke two possible mechanisms, one in which a cyanide ligand of $[Cr^{III}(CN)_6]^{3-}$ is labilized, which frees it up to coordinate to the $[Co(dppe)_2(solv)]^{2+}$ complex, and another in which an intermediate bridging state is formed which assists in the cyanide flip and eventual formation of **11**. The latter mechanism is strongly supported by the present experimental evidence, as we were able to isolate an intermediate compound for the cyanide-bridged complex. The reaction of $[Co^{II}(dppe)_2(H_2O)]^{2+}$ and $[Cr^{III}(CN)_6]^{3-}$ in acetonitrile led to the isolation of crystals of the kinetic product $\{[Co^{II}_3(dppe)_4(MeCN)][Cr^{III}(CN)_6]_2\}$ (**14**). Compound **14** exhibits a TBP structure in which the $[Cr^{III}(CN)_6]^{3-}$ ions reside in the apical sites of the bipyramid and the equatorial sites are occupied by the Co^{II} ions (Figure 3.3a). Each Co center is coordinated to one chelating dppe ligand and two bridging cyanides from the apical hexacyanochromate fragments. The fifth site on the Co(1) and Co(2) ions is occupied by a P atom of a shared bridging dppe ligand, while the fifth site on Co(3) is occupied by an acetonitrile molecule (Figure 3.3b).

As the reaction progresses, it leads to the decomposition of the TBP cluster and subsequent formation of the final product **11**, with the result that all of the dppe ligands assume a typical chelating mode to a single Co^{II} ion (Scheme 3.2). It is proposed that compound **14** is an unstable intermediate that crystallizes during the course of the

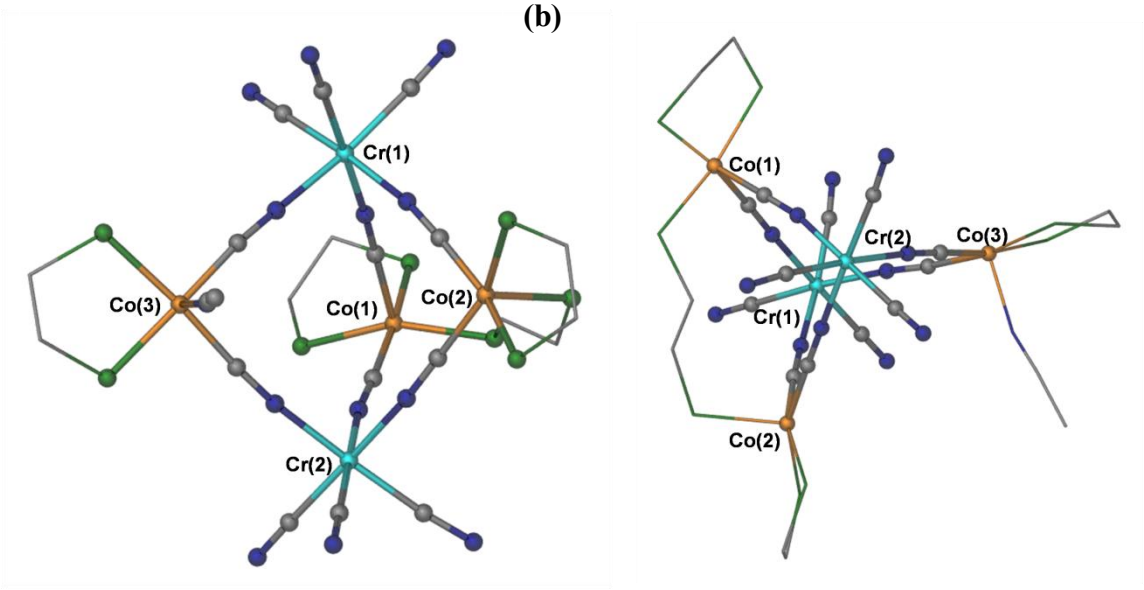

Figure 3.3. (a) Side view and (b) top view of the structure of $\{[Co^{II}_3(dppe)_4(MeCN)][Cr^{III}(CN)_6]_2\}$. (Phenyl rings omitted for the sake of clarity.)

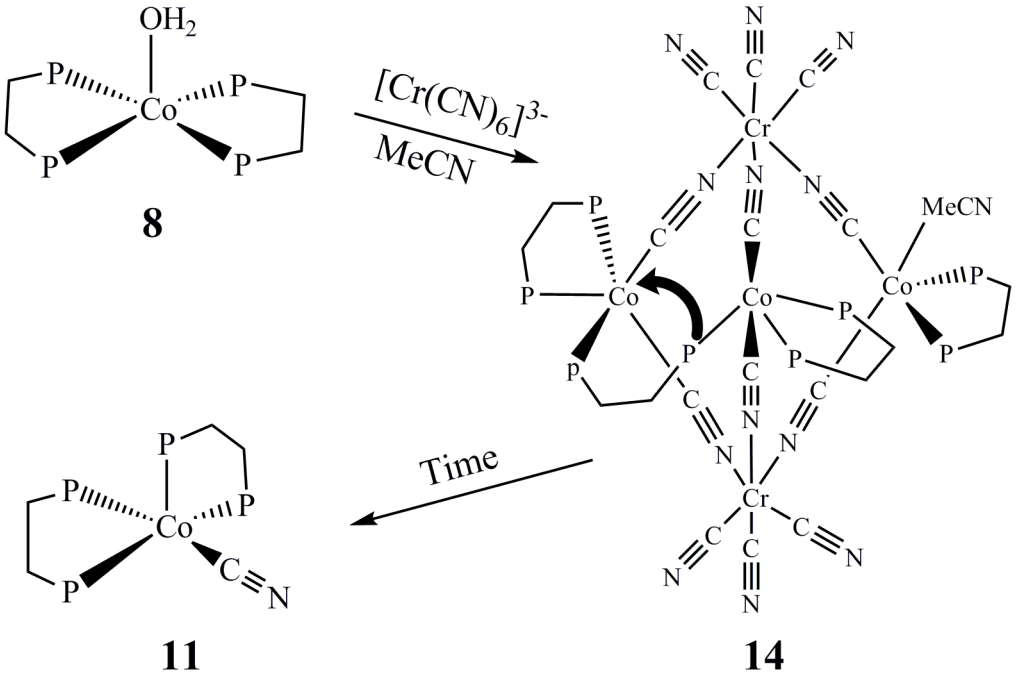

Scheme 3.2. Conversion of the mononuclear complex **8** to the mononuclear complex **11** via the formation of the pentanuclear TBP intermediate **14.**

reaction. The isolation of this molecule provides crucial insight into the mechanism of linkage isomerism.

Further characterization of the $\{[Co^{II}_3(dppe)_4(MeCN)][Cr^{III}(CN)_6]_2\}$ species was hampered by an insufficient amount of material due to its facile conversion to compound **11**. Attempts to isolate pure samples of **14** by using other solvents were unsuccessful. In a similar manner, we found that, when an acetonitrile solution of $[Co(triphos)(CH_3CN)_2]^{2+}$ is treated with a methanol solution of $[Cr(CN)_6]^{3-}$ in a 2:1 ratio, the result is not the expected cyanide-bridged species but rather the previously reported mononuclear precursor $Co(triphos)(CN)_2$.[176] Unfortunately, we were not able to isolate any intermediates in this reaction.

The isomerization and loss of cyanide ligands from $[Cr^{III}(CN)_6]^{3-}$ is not particularly surprising, as we had previously noted the cyanide flip issue in the reactions used to prepare the trigonal-bipyramidal complexes $\{[M(tmphen)_2]_3[Cr(CN)_6]_2\}$ (M = Fe, Co). Whereas the Fe-containing complex exhibited fast and essentially complete reversal of the bridging CN^- ligands,[184] the Co-containing TBP showed varying degrees of linkage isomerism depending on the experimental conditions.[183] To carry out a more detailed analysis of the isomerization process and to probe its ramifications on the properties of $\{[Co(tmphen)_2]_3[Cr(CN)_6]_2\}$ (**15**), we prepared several samples of the material by varying the solvent, time, and temperature of the reaction (Table 3.1).

The first suspicion of cyanide linkage isomerism during the preparation of **15** came from our observation of the mixed colors of the product which first crystallized as a yellow solid but, after some time, reverted to an admixture of a yellow and brown

(sample **15b** in Table 3.1). When the reaction was carried out with stirring for a short time (5 min) and immediately filtered, the product was recovered as a yellow solid (**15c**). Lowering the reaction temperature to 0 °C and shortening the reaction time to 1 min led to the isolation of a peach-yellow product (**15d**). In order to slow down the reaction and favor the formation of the brown product observed in **15b**, we used anhydrous $CoCl_2$ as a starting material because the chloride ligands tend to be less labile than water. Indeed, this reaction (**15a**) resulted in the crystallization of a brown product. When the same reaction is performed in the more polar solvent methanol (**15e**), which enhances dissociation of the $CoCl_2$ starting material, rapid precipitation of a peach solid ensues. The color of the product did not change even after storage in the mother liquor for 24 h. These collective observations suggest the occurrence of cyanide linkage isomerism that can be controlled by reaction conditions. This hypothesis has been confirmed by a combination of IR spectroscopic and magnetic measurements (see below).

Infrared Spectroscopy

Compounds **9** and **10** exhibit characteristic bands in the ν(C≡N) stretching region. A comparison of the observed IR data to the ν(C≡N) stretches reported for extended Prussian blue phases and the free hexacyanometallate anions aids in the assignment of the bands in the new compounds to bridging or terminal CN^- ligands. As the data in Table 3.5 indicate, the IR spectra of **9** and **10** exhibit lower-frequency stretches that are only slightly shifted as compared to the corresponding modes of the $[M^{III}(CN)_6]^{3-}$ ions (M = Co, Fe) and, therefore, are reasonably assigned to the terminal cyanides. Upon formation of the M^{III}-CN-Co^{II} bridge, the CN stretching frequency increases.[88]

Table 3.5. ν(C≡N) stretching frequencies in the complexes $\{[Co^{II}(dppe)_2]_2[M'^{III}(CN)_6]\}$ (M′ = Co, Fe), corresponding PB analogues, and free hexacyanometallate anions.

Complex	ν(C≡N), cm^{-1}		
	bridging	**terminal**	$[M'(CN)_6]^{3-}$ **anion**[a]
(**9**) Co^{II}–Fe^{III}–Co^{II}	2129	2108	2101
(**10**) Co^{II}–Co^{III}–Co^{II}	2148	2126	2126

[a] As measured for $(TMA)_3[Fe(CN)_6]$ and $[(18\text{-crown-6})K]_3[Co(CN)_6]$ (TMA = tetramethylammonium).

Consequently, the IR stretches of complexes **9** and **10** that appear at ~20 cm^{-1} higher than the ν(C≡N) of the free $[M^{III}(CN)_6]^{3-}$ ions are assigned to the bridging CN^- ligands.

For compounds **11** and **12**, the expected characteristic IR bands were observed (Table 3.6).[176, 186, 194] It should be noted at this point that the stretch for complex **11** located at 2096 cm^{-1} is significantly lower than the ν(C≡N) mode for the free $[Cr^{III}(CN)_6]^{3-}$ ion (2116 cm^{-1}) or of any possible cyanide-bridged species that could result from the reaction of $[Co^{II}(dppe)_2(H_2O)]^{2+}$ and $[Cr^{III}(CN)_6]^{3-}$; as such, its appearance can be easily monitored by solution IR spectroscopy. The slow formation of **11** from the reaction of $[Co^{II}(dppe)_2(H_2O)]^{2+}$ and $[Cr^{III}(CN)_6]^{3-}$ in acetonitrile prompted us to perform a detailed solution IR study of this reaction in order to obtain insight into the mechanism of the dissociation of $[Cr^{III}(CN)_6]^{3-}$.

The solution IR study was carried out by taking a ~1 mL aliquot from the reaction mixture at various intervals (Table 3.6 and Figure 3.4). The first aliquot was collected immediately after mixing the solutions of $[Cr^{III}(CN)_6]^{3-}$ and $[Co^{II}(dppe)_2(H_2O)]^{2+}$. The IR spectrum of this first aliquot contains two ν(CN) stretches at 2140 and 2113 cm^{-1}. The latter feature corresponds to the ν(C≡N) stretch observed for $[Cr^{III}(CN)_6]^{3-}$ in acetonitrile (2115 cm^{-1}) and the former, which is ~30 cm^{-1} higher in energy, is attributed to a CN-bridged species. A second aliquot, collected after 30 min from the beginning of the reaction, shows the same two ν(C≡N) stretches as the first (initial) aliquot, but with two shoulders at ~2130 and 2090 cm^{-1}. A third aliquot collected after 1 h shows an IR stretch at 2130 cm^{-1} which can be attributed to a CN-

Table 3.6. ν(C≡N) stretching frequencies for complexes **11** and **12** and a summary of the solution IR study of the reaction of $[Co^{II}(dppe)_2(H_2O)]^{2+}$ with $[Cr^{III}(CN)_6]^{3-}$ in acetonitrile.

Complex	ν(C≡N), cm^{-1}	
	bridging	**terminal**
(**11**) $[Co^{II}(dppe)_2(CN)][BF_4]$	—	2096
(**12**) $[Co^{III}(dppe)_2(CN)_2][BF_4]$	—	2114
Solution IR data		
$[Cr^{III}(CN)_6]^{3-}$	—	2115[a]
initial	2140	2113
30 minutes	2140, 2130	2113, 2090
1 hour	2130	2098
3 days	—	2113, 2098

[a] As measured for $[(18\text{-crown-6})K]_3[Cr(CN)_6]$.

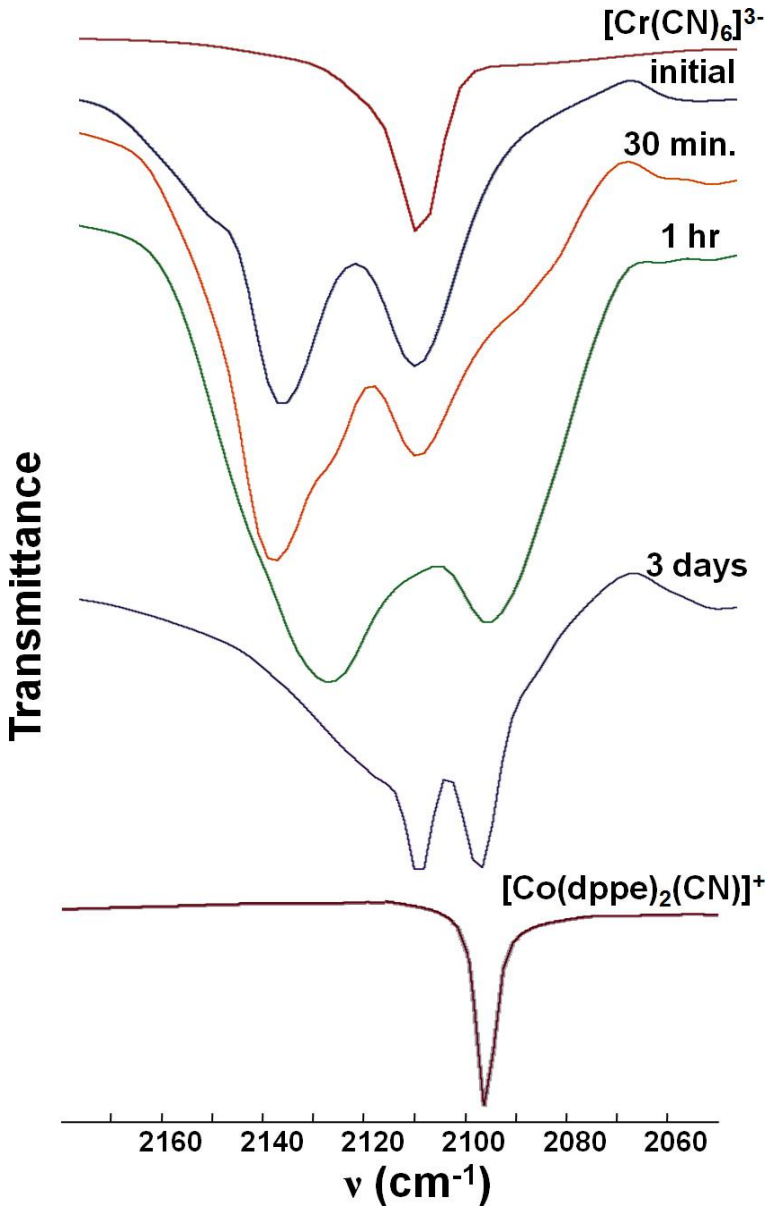

Figure 3.4. Solution IR spectra from samples taken from the reaction of $[Co^{II}(dppe)_2(H_2O)]^{2+}$ and $[Cr^{III}(CN)_6]^{3-}$ in acetonitrile.

bridged species and, more importantly, a ν(C≡N) stretch at 2098 cm^{-1} which corresponds to the ν(C≡N) stretch of a *bona fide* sample of $[Co^{II}(dppe)_2(CN)]^+$. After the reaction had proceeded for 3 days, crystals of $[Co^{II}(dppe)_2(CN)][BF_4]$ (**11**) were obtained, and a fourth aliquot was sampled from the mother liquor. An IR spectrum of this aliquot exhibits two ν(C≡N) stretches at 2112 and 2098 cm^{-1} with no discernible features at higher frequencies. The feature at 2112 cm^{-1} corresponds to the ν(C≡N) stretch of $[Cr^{III}(CN)_6]^{3-}$ in acetonitrile , and the ν(C≡N) stretch at 2098 cm^{-1} is assigned to $[Co^{II}(dppe)_2(CN)]^+$. The presence of a bridging species in solution cannot be completely ruled out due to the breadth of the signals; nevertheless, we can conclude that the dominant species in solution after 3 days are $[Cr^{III}(CN)_6]^{3-}$ and $[Co^{II}(dppe)_2(CN)]^+$.

The solution IR data clearly indicate the formation of an initial bridging complex followed by the formation of **11**. The structure of the bridging pentanuclear intermediate **14** that we accidentally isolated suggests that some CN^- ligands of $[Cr^{III}(CN)_6]^{3-}$ are labilized and bind through the carbon ends to the Co^{II} centers. This is a reasonable explanation for the displacement of the chelating dppe ligands observed in the structure of **14**. As monitored by solution IR spectroscopy, the reaction progresses to the stage where there are two dominant ν(C≡N) stretches which correspond to free $[Cr^{III}(CN)_6]^{3-}$ and $[Co^{II}(dppe)_2(CN)]^+$, the latter of which crystallizes from solution as a $[BF_4]^-$ salt. Both solution and solid-state IR data confirm the assignment of the ν(C≡N) stretch to this material.

In addition, solution IR studies of the reaction of $[Co(triphos)(CH_3CN)_2]^{2+}$ and $[M^{III}(CN)_6]^{3-}$ (M = Cr, Fe, and Co) in MeCN were also performed. The IR spectrum of

Table 3.7. Summary of the ν(C≡N) stretches for reaction solutions of $[Co^{II}(triphos)(CN)_2]^{2+}$ with $[M^{III}(CN)_6]^{3-}$ (M = Cr, Fe, Co) in acetonitrile.[a]

$[Co(triphos)(CH_3CN)_2]^{2+}$ + $[M^{III}(CN)_6]^{3-}$	**ν(C≡N), cm^{-1}**	
	bridging	**terminal**
$[Co(triphos)(CH_3CN)_2]^{2+}$		2300, 2317
$[Cr^{III}(CN)_6]^{3-}$	—	2115[b]
initial	**2146, 2164, 2170**	2300, 2317, 2115
1 hour	**2146, 2164, 2170**	2300, 2317, 2115
2 days	—	2115, **2101, 2097**
$[Co(triphos)(CN)_2]$		2101, 2096
$[Fe^{III}(CN)_6]^{3-}$	—	2116[b]
initial	**2141**	2116
1 hour	**2141, 2152**(sh)[c]	2116
2 days	**2141, 2152**(sh)[c]	2116
$[Co^{III}(CN)_6]^{3-}$	—	2127[b]
initial	**2145, 2165, 2174**(sh)	2127
1 hour	**2145, 2165, 2174**(sh)	2127
2 days	**2145, 2165, 2174**	2127

[a] IR stretches in bold correspond to new species formed in solution.
[b] As measured for acetonitrile solutions of $[(18\text{-crown-6})K]_3[Cr(CN)_6]$, $[TMA]_3[Fe(CN)_6]$ and $[(18\text{-crown-6})K]_3[Co(CN)_6]$.
[c] sh = shoulder

$[Co(triphos)(CH_3CN)_2]^{2+}$ in acetonitrile exhibits two ν(C≡N) stretches at 2317 and 2300 cm^{-1} (Table 3.7), values that are in reasonable accord with those reported for $[Co^{II}(CH_3CN)_6][BF_4]_2$ [195] (2292 and 2316 cm^{-1}). The first aliquot of the $[Co(triphos)(CH_3CN)_2]^{2+}/[Cr^{III}(CN)_6]^{3-}$ (2:1) reaction mixture collected after 5 min contains peaks at 2115, 2300, and 2317 cm^{-1} associated with the reactants, along with three new ν(C≡N) stretches at 2146, 2164, and 2170 cm^{-1} that are in the region of cyanide-bridged species. Aliquots collected after 1 and 3 h exhibit the same features, the only significant difference being a decrease in the intensity of the ν(C≡N) stretches of the reactants as compared to those of the product cyanide-bridged species. The last aliquot (collected after two days) exhibits stretches corresponding to the starting materials as well as two new stretches at 2097 and 2101 cm^{-1} and no evidence for the previously observed ν(C≡N) stretches assigned to the CN-bridged species. The new stretches at 2097 and 2101 cm^{-1} are due to the presence of $Co(triphos)(CN)_2$ (**13**).

The solution IR study revealed that the reaction between $[Co(triphos)(CH_3CN)_2]^{2+}$ and $[Cr^{III}(CN)_6]^{3-}$ results in the formation of intermediate cyanide-bridged species. The latter react further to form **13** via labilization of cyanide ligands from $[Cr(CN)_6]^{3-}$ which are sequestered by the low-spin Co^{II} complex. Lability of the cyanide ligand is observed only in the case of $[Cr(CN)_6]^{3-}$. Reactions of $[Co(triphos)(CH_3CN)_2]^{2+}$ with $[Fe(CN)_6]^{3-}$ and $[Co(CN)_6]^{3-}$ result in cyanide-bridged species whose ν(C≡N) stretches are persistent in the IR spectra of the aliquots collected after two days (2141, 2152 cm^{-1} and 2146, 2164, and 2173 cm^{-1}, respectively). Attempts to crystallize these cyanide-bridged species were unsuccessful.

We also performed an IR study of different forms of the TBP complex **15** obtained under different reaction conditions (Table 3.1). In a previous study, we investigated a whole family of such complexes formed with different transition metals, and the majority of them exhibit two ν(C≡N) stretches, one that is very close in energy to the free hexacyanometallate anion and the other one which is higher in energy by ~20-30 cm^{-1}. These bands are assigned to terminal and bridging CN^- ligands, respectively. All samples of **15** reveal the presence of these two bands (Figure 3.5).

Note that three of the five samples exhibit a third band at ~2103 cm^{-1}. The latter feature is assigned to the Co–CN–Cr configuration of the CN^- bridge. Indeed, this band is the most intense in sample **15a** which, according to the preparation conditions, should exhibit the highest degree of cyanide linkage isomerism. Moreover, the absorption at 2057 cm^{-1}, assigned to the normal Co–NC–Cr bridging mode, exhibits very low intensity in this sample. In sample **15b**, the intensity of the higher-frequency band increases at the expense of the lower-frequency band at 2103 cm^{-1}, in accord with the faster crystallization of this sample as compared to **15a** and a lower degree of cyanide reversal. This trend continues for sample **15c**, the rapid precipitation of which was enhanced by stirring the mixture. For samples **15d** and **15e**, the band at 2103 cm^{-1} is absent, a confirmation that a lower reaction temperature or the use of methanol as solvent results in a slower rate of CN^- bridge reversal. The magnetic data, however, reveal that appreciable cyanide linkage isomerism has taken place even in these two samples. It must be pointed out that sample **15e** precipitated instantaneously upon mixing methanolic solutions of the reactants and was kept under the mother liquor for

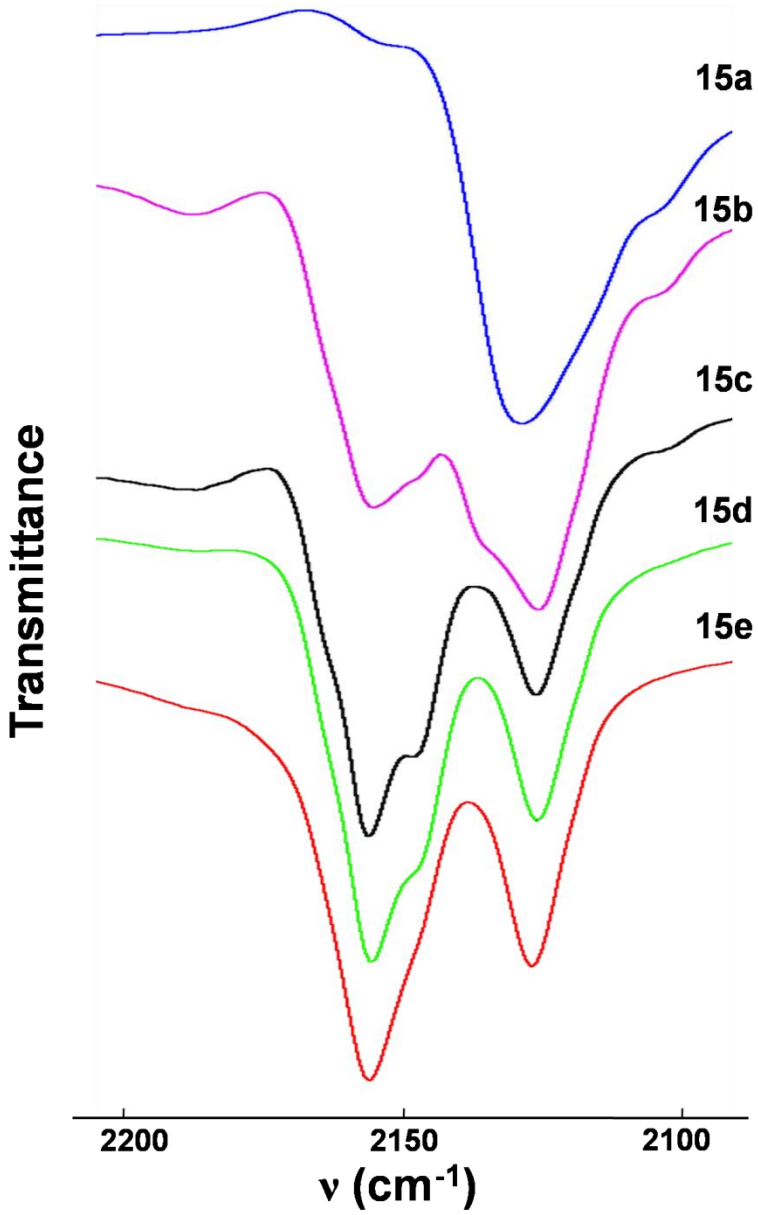

Figure 3.5. Cyanide stretching bands in the IR spectra of complex **15** prepared by varying the Co(II) starting material, solvent, time and temperature of the reaction (**15a**: $CoCl_2$ in MeCN, 24 h, 25°C; **15b**: $Co(BF_4)_2{\cdot}6H_2O$ in MeCN, 24 h, 25°C; **15c**: $Co(BF_4)_2{\cdot}6H_2O$ in MeCN, 5 min, 25°C; **15d**: $Co(BF_4)_2{\cdot}6H_2O$ in MeCN, 1 min, 0°C; **15e**: $CoCl_2{\cdot}6H_2O$ in MeOH, 24 h, 25°C).

24h before being recovered by filtration. Nevertheless, the IR spectrum of this sample is essentially the same as that of sample **15d,** which was isolated from the reaction mixture after stirring for only 1 min at 0 °C. Obviously, the cyanide "flip" occurs rapidly in solution upon formation of the complex. After precipitation of the material, the cyanide bridges remain intact and do not reverse in the solid state.

Magnetic Properties

DC magnetic measurements were performed on freshly prepared crushed polycrystalline samples in the temperature range of 2–300 K in an applied magnetic field of 1000 Oe. Compound **8** exhibits a χT value of 0.68 emu·mol^{-1}·K at 300 K, which is substantially higher than expected for a single S = 1/2 center (0.375 emu·mol^{-1}·K). Upon lowering temperature, the susceptibility decreases linearly to 0.53 emu·mol^{-1}·K at 2 K (Figure 3.6a), indicating significant temperature-independent paramagnetism (TIP) of the Van Vleck type, which is due to low-lying excited states. Both the temperature dependence of χT and the field-dependent magnetization data were satisfactorily fitted to an S = 1/2 system with g = 2.41 and TIP = 4.8·10^{-4} emu·mol^{-1} (Figure 3.6a). In order to account for the slight decrease of χT at low temperatures, a molecular field correction (zJ = –0.10 cm^{-1}) was added to include intermolecular interactions.[17] The 300-K χT value of **11** is slightly lower, namely 0.47 emu·mol^{-1}·K, and decreases linearly to reach 0.43 emu·mol^{-1}·K at 2 K (Figure 3.6b). Thus, the TIP contribution is lower (1.5·10^{-4} emu·mol^{-1}) compared to that of complex **8**. Such behavior is in agreement with a greater separation between the ground and excited states for **11**, as expected for the stronger ligand field created by the presence of the carbon-bound cyanide in this complex. The temperature

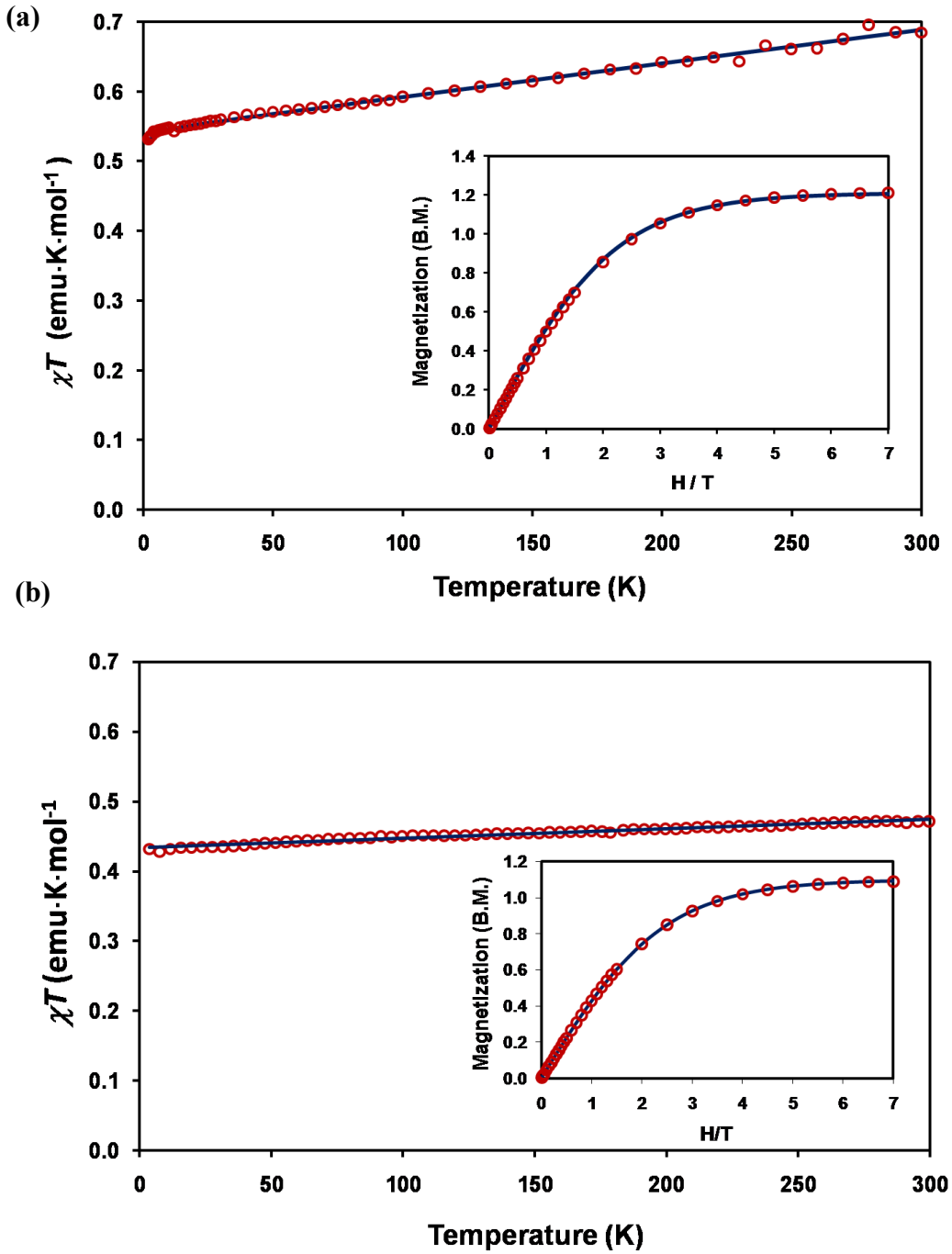

Figure 3.6. Temperature dependence of χT for **(a)** compound **8** (S = 1/2, g = 2.41, TIP = $4.8 \cdot 10^{-4}$ emu mol^{-1}, zJ = -0.1 cm^{-1}) and **(b)** compound **11** (S = 1/2, g = 2.20, TIP = $1.5 \cdot 10^{-4}$ emu mol^{-1}). Inset: Field-dependent magnetization curve at 1.8 K. Experimental points are depicted with open circles and solid lines correspond to the best-fit curves.

dependence of χT and field-dependent magnetization data fit the behavior of an $S = 1/2$ system with $g = 2.20$ (Figure 3.6b, inset).

Compound **9** exhibits a value of $\chi T = 0.95$ emu·mol^{-1}·K at 300 K, higher than the spin-only value expected for two noninteracting low-spin $S = 1/2$ Co^{II} ions (0.75 emu·mol^{-1}·K). The susceptibility value decreases linearly as the temperature is lowered (Figure 3.7), once again due to the TIP contribution of Co^{II} ions ($2.1 \cdot 10^{-4}$ emu·mol^{-1} per ion). The sharp decrease in the susceptibility at very low temperatures is due to intramolecular antiferromagnetic exchange between $S = 1/2$ Co^{II} centers through the diamagnetic Co^{III} ion ($J = -0.4$ cm^{-1}). The same model satisfactorily describes the field-dependent magnetization data (Figure 3.7, inset).

For compound **10**, the χT value at 300 K is 1.72 emu·mol^{-1}·K which is higher than the spin-only value of 1.13 emu·mol^{-1}·K expected for noninteracting two low-spin $S = 1/2$ Co^{II} ions and one low-spin $S = 1/2$ Fe^{III} ion. Such a deviation is mainly due to the significant orbital contribution characteristic of the orbitally degenerate $^2T_2$ ground state of the low-spin Fe^{III} ion and the TIP contribution of Co^{II} ions, as observed in the isostructural complex **9**. The value of χT decreases upon cooling until $T \sim 60$ K, and then the value abruptly increases to a maximum of 1.87 emu·mol^{-1}·K at ~ 6 K (Figure 3.8) which is indicative of the stabilization of an $S = 3/2$ ground state, suggesting a ferromagnetic superexchange between the Co^{II} and Fe^{III} centers rather than antiferromagnetic coupling, which would result in an $S = 1/2$ ground state. It must be noted that the gradual decrease of χT from room temperature cannot be taken as an

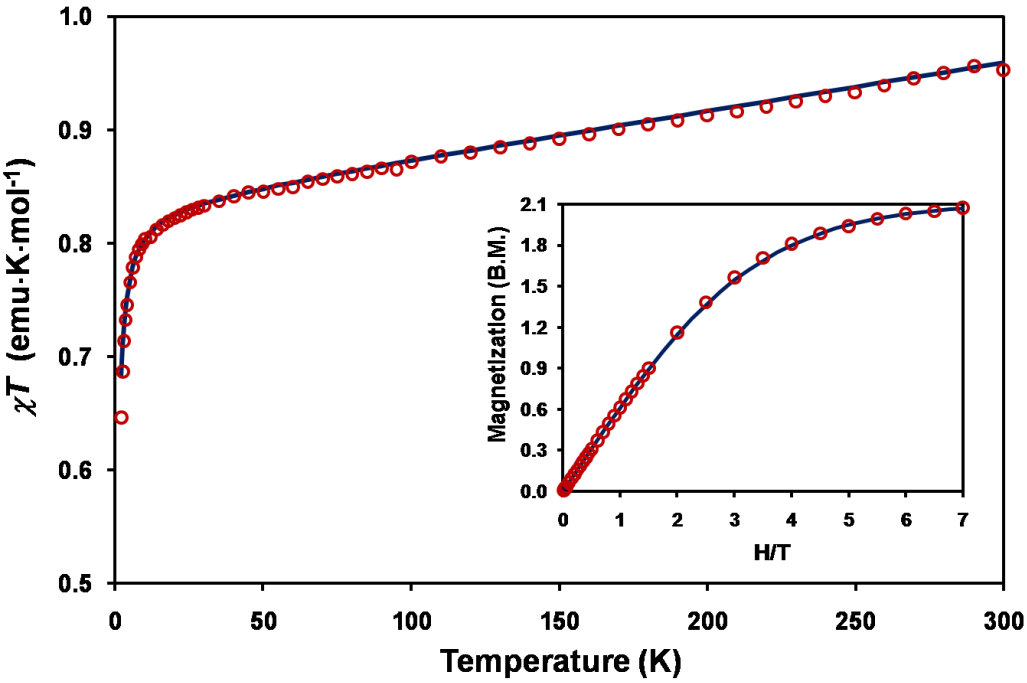

Figure 3.7. Temperature dependence of χT for **9** (two S = 1/2 centers, g = 2.11, TIP = $2.1 \cdot 10^{-4}$ emu·mol^{-1}, J = –0.4 cm^{-1}). Inset: Field-dependent magnetization curve at 1.8 K. Experimental points are shown with open circles. Solid lines correspond to the best-fit curves obtained by MAGPACK[196].

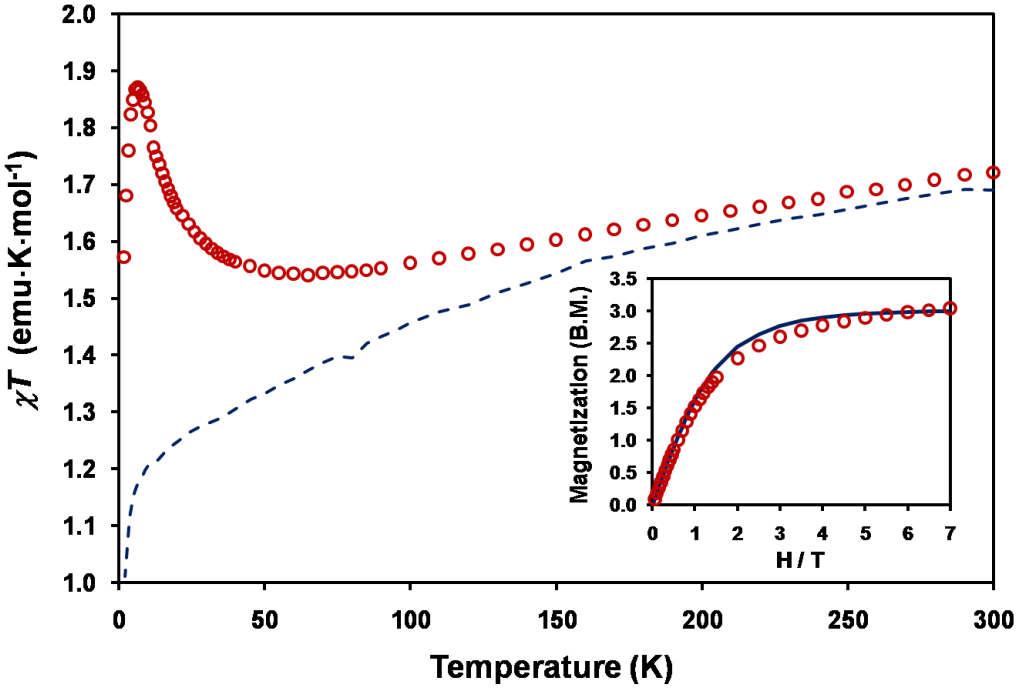

Figure 3.8. Temperature dependence of χT for **10**. For comparison, the dashed line shows a combined contribution from isostructural complex **9** and $TBA_3[Fe(CN)_6]$ (see the text). Inset: Field dependent magnetization at 1.8 K, with the solid line depicting the Brillouin function for $S = 3/2$, $g = 2$.

indication of antiferromagnetic coupling because spin-orbit coupling of the low-spin Fe^{III} ion and the TIP of the Co^{II} centers are important contributors. For comparison, Figure 3.8 depicts the sum of χT plots for compound **9** and $(TBA)_3[Fe(CN)_6]$. The χT vs. T dependence for **10** shows an obvious deviation to higher values as compared to the combined curve. This deviation increases with decreasing temperature, thus confirming that remote ferromagnetic coupling is occurring between the Co^{II} and Fe^{III} centers in **10**. Stabilization of the high-spin ground state was further corroborated by field-dependent magnetization data (Figure 3.8, inset), which saturate at a value of 3.05 μ_B as expected for a ferromagnetic $S = 3/2$ ground state. The observed decrease in χT below 6 K and the slight deviation of the magnetization data from the Brillouin function calculated for $S = 3/2$ are attributed to the weak intermolecular antiferromagnetic interactions and zero-field splitting effects.

Due to the varying degrees of cyanide linkage isomerism observed in samples of compound **15** (Table 3.1), an accurate treatment of its magnetic behavior is not possible. Nevertheless, the magnetic properties of the samples follow the qualitative trend expected for the mixture of isomerized and nonisomerized TBP clusters. First of all, we note that, in the nonisomerized form, each Co^{II} ion is equipped with two tmphen ligands and two N-bound cyanides. As demonstrated previously by our study of the model compound $\{[Co^{II}(tmphen)_2]_3[Co^{III}(CN)_6]_2\}$, such a coordination results in a high-spin $S = 3/2$ state for the Co^{II} centers.[183] After the cyanide flipping event, however, the equatorial Co^{II} ions are coordinated to the strong-field C-bound end of the CN^- ligands

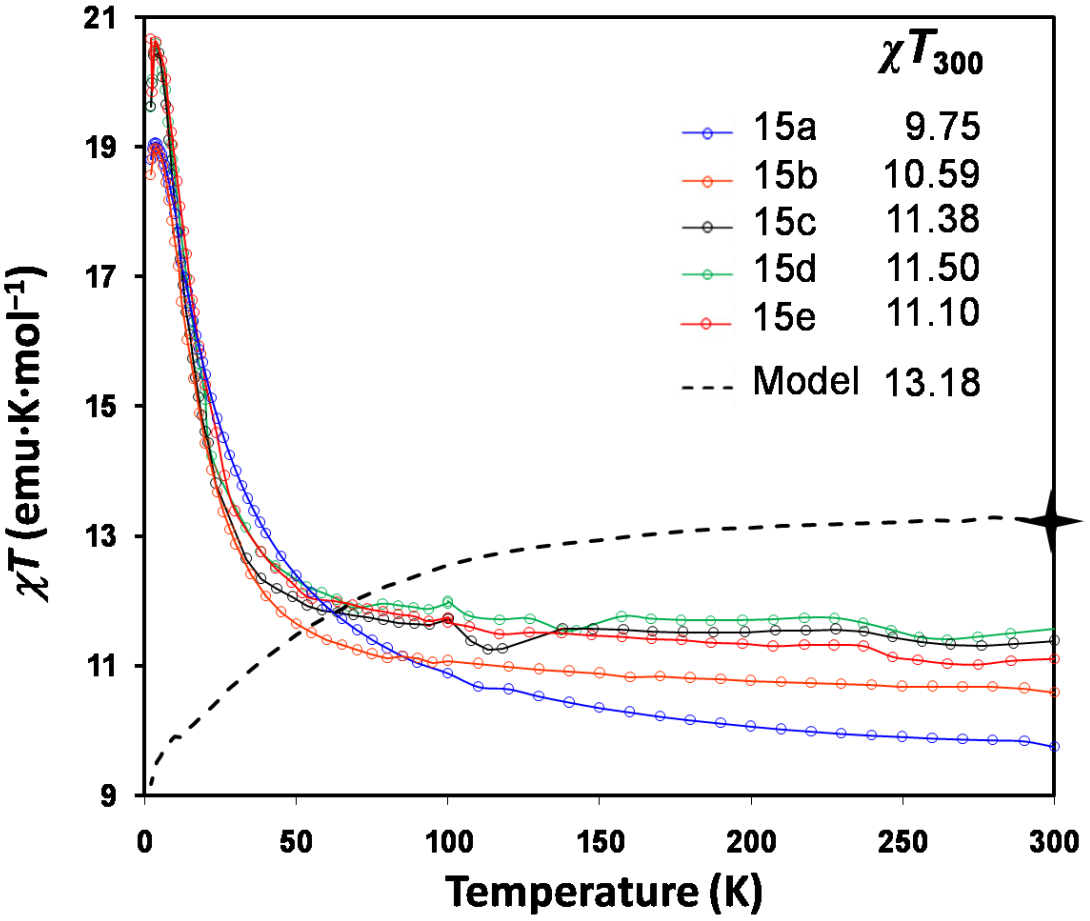

Figure 3.9. Temperature dependence of χT for different samples of **15**. The solid lines are guides for the eye. The dashed line represents a combined contribution from two model isostructural complexes, namely $\{[M(tmphen)_2]_3[M'(CN)_6]_2\}$ (M/M′ = Co/Co and Zn/Cr; see the text).

and are in the low-spin $S = 1/2$ state.[197] (Of course, intermediate forms of the cluster can exist, in which cyanide bridges are only partially reversed, but the overall trend for the Co^{II} centers to assume the low-spin electronic configuration upon increasing extent of cyanide linkage isomerism is evident.)

The conversion of the equatorial Co^{II} ions from the high-spin $S = 3/2$ to the low-spin $S = 1/2$ state results in a spin-pairing of electrons in the t_{2g} orbitals and has two major ramifications on the magnetic behavior of **15**: (1) The room-temperature value of χT decreases as the degree of cyanide flip increases. As a means of comparison, the dashed line in Figure 3.9 shows a combined contribution from three equatorial high-spin $S = 3/2$ Co^{II} and two axial $S = 3/2$ Cr^{III} ions in the absence of magnetic coupling. This was calculated by adding the χT versus T dependences of the model compounds $\{[Co^{II}(tmphen)_2]_3[Co^{III}(CN)_6]_2\}$ and $\{[Zn^{II}(tmphen)_2]_3[Cr^{III}(CN)_6]_2\}$,[183] which contain diamagnetic metal ions in the axial and equatorial positions, respectively. (2) The ferromagnetic coupling between the Co^{II} and Cr^{III} centers becomes stronger as the cyanide linkage isomerism occurs. This fact has been explained by the removal of the antiferromagnetic contribution to the Co^{II}–Cr^{III} magnetic superexchange upon going from the high-spin $t_{2g}^5e_g^2$ to the low-spin $t_{2g}^6e_g^1$ Co^{II} ion.[183] Indeed, the high-temperature part of the χT versus T curve is much steeper for sample **15a** (Figure 3.9), for which the extent of cyanide flip is the greatest; this observation is in accord with stronger ferromagnetic exchange.

CONCLUSIONS

Contrary to the commonly held notion that Cr^{III} is a rather inert ion due to the half-filling of its t_{2g} orbitals, we found that the presence of certain Lewis acids (e.g., Co^{II} and Fe^{II} ions, BPh_3), leads to facile labilization of cyanide ligands from the $[Cr(CN)_6]^{3-}$ anion. Results of the detailed study presented herein obtained by a combination of X-ray crystallography, infrared spectroscopy, and magnetic measurements provide unequivocal evidence for this phenomenon during reactions of various Co^{II} complexes with the hexacyanochromate(III) anion. The final products of such reactions are mono- or polynuclear complexes in which the CN^- ligand is carbon-bound to the Co^{II} ion rather than to the Cr^{III} center. Reactions of $[Co(dppe)_2(H_2O)](BF_4)_2$ and $[Co(triphos)(CH_3CN)_2](BF_4)_2$ with $[Cr(CN)_6]^{3-}$ yield the mononuclear complexes $[Co(dppe)_2(CN)](BF_4)$ and $[Co(triphos)(CN)_2]$, respectively. In the former case, we were able to isolate the pentanuclear intermediate $\{[Co^{II}_3(dppe)_4(MeCN)][Cr^{III}(CN)_6]_2\}$. A study of this reaction by solution IR spectroscopy reveals a gradual conversion of the ν(C≡N) stretches of the starting materials to those of the CN-bridged intermediate and finally to the single ν(C≡N) stretch of the mononuclear product. The loss of carbon-bound CN^- ligands from $[Cr(CN)_6]^{3-}$ is on a sufficiently slow time-scale for observation of varying degrees of cyanide linkage isomerism in the trigonal-bipyramidal complex $\{[Co(tmphen)_2]_3[Cr(CN)_6]_2\}$, aided by the use of different Co^{II} starting materials. The varying extent of the cyanide flip in this complex leads to a variable ratio of the N-coordinated high-spin $S = 3/2$ form to the C-coordinated low-spin $S = 1/2$ Co^{II} form, a fact that is reflected in the magnetic behavior of the mixtures. These results are in

contrast to the fast and complete reversal of cyanide bridges that we observed in the chemistry leading to $\{[Fe(tmphen)_2]_3[Cr(CN)_6]_2\}$ and $(Et_4N)_3[Cr(NCBPh_3)]$.

CHAPTER IV

SINGLE MOLECULE MAGNETS BASED ON HEXACYANOOSMATE(III) AND HEXACYANOFERRATE(III)

INTRODUCTION

The current explosion of activity in the chemistry of multinuclear cyanide complexes is being fueled, in part, by the interest in discrete molecules that exhibit magnetic bistability, commonly referred to as Single-Molecule Magnets (SMM's). The term "single molecule magnet" was coined in the mid-1990s to describe molecular compounds that exhibit slow relaxation of their magnetization in the absence of an applied magnetic field.[76, 77]

The phenomenon of single molecule magnetism was first noted for the family of mixed-valence Mn^{III}/Mn^{IV} carboxylates, generally referred to as "Mn_{12}" complexes. [76, 84, 86] The occurrence of hysteresis and remnant magnetization in these materials is due to the intrinsic magnetic properties of the individual molecules. A large value for the total spin ground state *S*, which arises from magnetic superexchange, combined with a significant uniaxial anisotropy parameter *D* (axial zero field splitting) results in magnetic bistability (Scheme 1.3). The parameter *D* must be negative in order for the ground state to have the maximum spin value. In the simplest model, the magnitude of the barrier for magnetization reversal is $U = S^2|D|$ for integer *S* and $U = (S^2–1/4)|D|$ for half-integer *S*.

The phenomenon of slow paramagnetic relaxation of the magnetization of a system is reflected in the temperature dependence of the imaginary part (χ'') of AC

magnetic susceptibility. For a typical paramagnet, cycling the magnetic field between two opposite polarities has no discernible effect. When such measurements are performed on an SMM, however, an out-of-phase signal appears below a certain temperature called a blocking temperature. When the rate at which the magnetic moment of a molecule reverses sign is close to the oscillating frequency, a χ'' signal is observed. Such an out-of-phase signal is also observed in the case of bulk magnetic ordering, but the principal feature that distinguishes SMM behavior is the dependence of the maximum of the χ'' signal on the frequency, ν, of the applied AC magnetic field. If a SMM is cooled below the blocking temperature, and the frequency of the AC field is varied, a maximum in χ'' is observed when the frequency of the applied AC magnetic field equals the rate at which a molecule can interconvert between the two magnetic states of +S and -S. The frequency dependence is a signature of the thermally activated relaxation process, and the blocking temperature T, at which the maximum of the $\chi''(T)$ curve is observed, is related to the relaxation time $\tau = 1/2\pi\nu$ by the Arrhenius law. Therefore, an examination of this dependence permits the calculation of the activation barrier U_{eff}.

Since the discovery of the original SMM, the Mn_{12} complex, much work has focused on increasing the intrinsic barrier height to the reversal of magnetization. While most of the research in this area has focused on increasing the barrier by increasing the ground state spin value, this has not led to an appreciable increase in the barrier height. Recent theoretical work has suggested a focus on the inherent anisotropy of the clusters as a method for increasing the blocking temperature, T_B, of SMM materials.

Cyanide complexes are attractive candidates for the development of SMMs. The synthetic approaches to the preparation of such compounds generally can be controlled, thereby allowing for the deliberate introduction of specific metal ions into the cyanide-bridged core. A number of cyanide-bridged SMMs have been reported to date; these molecules are listed in Table 1.1 in the order of increasing ground state spin values. Interestingly, all cyanide SMMs reported thus far are characterized by the presence of ions with appreciable spin-orbit coupling. In the molecules based solely on 3*d* transition metals, orbital contributions result from the presence of low spin Fe^{III} and/or Mn^{III} centers. The importance of the single ion anisotropy of these ions in engendering SMM behavior in discrete clusters is supported by the observation of slow relaxation of the magnetization in the trinuclear complexes $\{[(pzTp)Fe^{III}(CN)_3]_2[Ni^{II}(bpy)_2]\}$[89] and $K\{[Mn^{III}(5\text{-Brsalen})(H_2O)]_2[Fe^{III}(CN)_6]\}$[90] (Figure 1.9) which have small spin ground state values.

Another strategy that is being used to increase the anisotropy value of a cluster is incorporation of 4*d* and 5*d* transition metal ions into the clusters. These ions are characterized by large spin-orbit coupling constants which contribute to the orbital angular momenta, leading to an increase in the magnetic anisotropy of the molecule. In order to exploit this property several groups have endeavored to increase magnetic anisotropy in cyanide-bridged complexes by using heavier transition metal congeners of the 3*d* elements. Illustrations of the successful implementation of this strategy are the pentanuclear $\{[Mn^{II}(py_5Me_2)]_4[Re^{IV}(CN)_7](PF_6)_5$,[103] heptanuclear $K\{[(Me_3tacn)Mo^{III}(CN)_3]_6Mn^{II}\}(ClO_4)_3$,[97] and octanuclear

{[(triphos)$Re^{II}(CN)_3]_4[Mn^{II}Cl]_4$}[102, 106] clusters, all of which behave as SMMs (Figure 1.10).

In order to better understand the complex nature of these ions, simple model compounds need to be synthesized which reduce the number of metal ions and as a result simplify the theoretical models necessary to understand fully the magnetic properties of the compounds. As presented earlier, the simplest magnetic models are linear trinuclear molecules. Given the success of the Mn^{III} Schiff base building blocks for the isolation of linear cyanide-bridged clusters[198], we chose to use the $\{Mn^{III}(salphen)(solv)_2\}^+$ for the synthesis of new clusters (salphen = *N*,*N*'-bis(salicylidene)-1,2-diaminobenzene; Scheme 4.1) and set out to probe the effect of also incorporating the 5*d* metal ion Os^{III} on the properties of the resulting paramagnets. Herein we report the synthesis, structure and magnetic properties of the new trinuclear cluster, PPN$\{[Mn^{III}(salphen)]_2[Os^{III}(CN)_6]\}$, which is the first reported SMM with an Os^{III} ion. Also presented is the synthesis, structure and magnetic properties of the Fe^{III} analog which was prepared as a reference compound for assessing the effect of the 5*d* metal ion on the magnetic properties of the related compounds.

EXPERIMENTAL

Syntheses

Starting materials. All chemicals and solvents were of reagent grade quality. $K_3[Fe(CN)_6]$ (Aldrich) and PPNCl (Aldrich; PPN = bis(triphenylphosphine)nitrogen) were used as received. The tetradentate Schiff base ligand H_2-salphen was prepared by

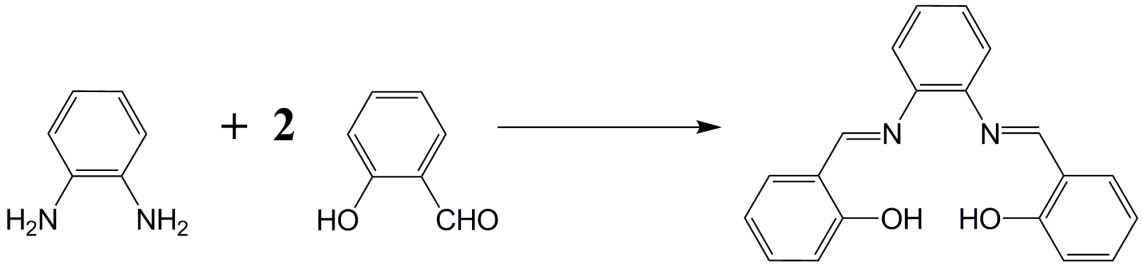

SalphenH$_2$

Scheme 4.1. Synthesis of the tetracoordinate ligand salphenH$_2$.

mixing the 2-salicylaldehyde and *o*-phenylenediamine in a 2:1 mol ratio in ethanol, according to the literature (Scheme 4.1).[199] The $[Mn^{II}(H_2O)_4][BF_4]_2$ salt was prepared as previously reported.[200] The $PPN_3[Os^{III}(CN)_6]$ precursor was synthesized as described in the experimental section of chapter II. All reactions were performed in air unless stated otherwise.

$[Mn(salphen)(H_2O)_2][BF_4]_2$ (16). This compound was synthesized using a different route than the previously reported procedure.[199] A quantity of salphen (1.0 g, 3.16 mmol) was added to a solution of $Mn(BF_4)_2{\cdot}4H_2O$ (0.782 g, 3.16 mmol) in 100 mL of ethanol. The dark red-brown mixture was stirred for 10 minutes. An equimolar amount of sodium hydroxide was then added, the resulting mixture was stirred for 2 h and filtered. The filtrate evaporated slowly at room temperature. The dark red-brown needles that formed after several days were filtered in air, washed with hexanes and diethyl ether, and air-dried. Yield = 1.08 g (70%). Elemental analysis: Calcd. for $MnC_{20}N_2O_2H_{14}BF_4$: C, 48.77; H, 3.69; N, 5.69; F, 15.44; Found: C, 49.38; H, 3.82; N, 5.60; F, 15.49 %.

$PPN_3[Fe(CN)_6]$ (17). This compound was synthesized by a previously reported procedure.[201] A warm (~45 °C) aqueous solution of $K_3[Fe(CN)_6]$ (0.3 g in 20 ml of water) was added dropwise to a warm stirred solution of (PPN)Cl (1 g in 60 ml of water). After mixing, instantaneous formation of a microcrystalline yellow precipitate was observed. After stirring the mixture for 10 minute the solid was filtered, washed with warm water and then dried at 80 °C under vacuum. Yield = (90%). IR(Nujol): $\nu(C{\equiv}N)$ 2104 cm^{-1}.

PPN{[Mn(salphen)(MeOH)]$_2$[Fe(CN)$_6$]} (18). A solution of **17** (0.250 g, 0.15 mmol) in methanol (30 mL) was added to three separate 20 mL vials in 10 mL aliquots. In a separate flask a solution of **16** (0.067 g, 0.15 mmol) in methanol (30 mL) was prepared. A quantity of the methanol solution of **16** (10 mL) was then layered over each of the 10 mL aliquots of the methanol solution of **17**. The layered solutions were left to stand undisturbed and after a few days red-orange block crystals had formed which were collected by suction filtration, washed with a minimum volume of methanol and diethyl ether and air dried. The crystals were found to be suitable for single crystal X-ray crystallography. Yield = 0.069 g (59%). Elemental analysis: Calcd. for $Mn_2FeC_{84}N_{11}O_6H_{66}P_2$: C, 61.83; H, 4.08; N, 9.45; O, 8.44; Found: C, 62.20; H, 4.15; N, 9.72; O, 8.45 %. IR(Nujol): ν(C=N) 1601 cm^{-1} (imine); ν(C≡N) 2105, 2114 cm^{-1} (cyanide).

PPN{[Mn(salphen)(MeOH)]$_2$[Os(CN)$_6$]} (19). Compound **19** was prepared in a fashion analogous to that described above for compound **18**. The methanol soluble salt $(PPN)_3[Os(CN)_6]$ was used as the source of $[Os(CN)_6]^{3-}$ anions. Yield = 0.075 g (61%). Elemental analysis: Calcd. for $Mn_2OsC_{84}N_{11}O_6H_{66}P_2$: C, 56.68; H, 3.74; N, 8.66; O, 8.10; Found: C, 56.47; H, 3.76; N, 8.92; O, 8.62%. IR(Nujol): ν(C=N) 1601 cm^{-1} (imine); ν(C≡N) 2086, 2092 cm^{-1} (cyanide).

Single Crystal X-ray Diffraction

In a typical experiment, a crystal selected for study was mounted on a cryoloop which was placed in a N_2 cold stream. Single-crystal X-ray data were collected on a Bruker APEX diffractometer equipped with a CCD detector at 110 K. The data sets were

recorded as four ω scans of 606 frames each, at a 0.3° step width, and integrated with the Bruker SAINT[187] software package. The absorption correction (SADABS[188]) was based on fitting a function to the empirical transmission surface as sampled by multiple equivalent measurements. Solution and refinement of the crystal structures was carried out using the SHELX[189] suite of programs and the graphical interface X-SEED.[190] Structure solution by direct methods resolved positions of all metal atoms as well as most of the P, C and N atoms. The remaining non-hydrogen atoms were located by alternating cycles of least-squares refinements and difference Fourier maps. Hydrogen atoms were placed at calculated positions. The final refinement was performed with anisotropic thermal parameters for all non-hydrogen atoms. A summary of pertinent information relating to unit cell parameters, data collection, and refinements is provided in Table 4.1. Selected metal–ligand bond distances and angles are provided in Table 4.2.

RESULTS AND DISCUSSION

Syntheses and Infrared Spectroscopy

Compounds **18** and **19** were synthesized by the assembly reaction of $[Mn^{III}(salphen)(H_2O)_2][BF_4]$ with $PPN_3[Fe^{III}(CN)_6]$ and $PPN_3[Os^{III}(CN)_6]$ respectively in a molar ratio of 1:1 in methanol. The reactions were also attempted in other organic solvents such as acetonitrile and a mixture of methanol/H_2O, but in both cases immediate precipitation of a brown powder occurred and was determined to be different from the desired compounds by magnetic measurements. Both compounds are air stable but loss of interstitial solvent occurs as soon as the crystals are removed from their

Table 4.1. Crystal structural data and refinement parameters for compounds **18** and **19.**

Formula	$Mn_2FeC_{84}N_{11}O_6H_{66}P_2 \cdot 4CH_3OH$ (**18**·$4CH_3OH$)	$Mn_2OsC_{84}N_{11}O_6H_{66}P_2 \cdot 4CH_3OH$ (**19**·$4CH_3OH$)
Space group	*C2/c*	*C2/c*
Unit cell	a = 17.042(6) Å	a= *17.170(2)*Å
	b = 13.827(5)Å	b = 13.8418(18)Å
	c = 37.258(13)Å	c =37.158(5)Å
	β = 103.222(1)°	β = 102.787(2)
Unit cell volume, V	8547(5)Å^3	8611.9(19)Å^3
Z	4	4
Density, ρ_{calc}	1.389 g/cm^3	1.482 g/cm^3
Abs. coeff., μ	0.556 mm^{-1}	1.868 mm^{-1}
Crystal color and habit	Red orange block	Red orange block
Crystal size, mm^3	0.60x0.35x0.33	.44x.34x.30
Temperature	110 K	110 K
Radiation, λ	Mo-Kα, 0.71073 Å	Mo-Kα, 0.71073 Å
Min. and max. θ	1.92 to 28.77 º	1.44 to 26.18 º
Reflections collected	23856 [R_{int} =0.0593]	10586 [R_{int} =.0374]
Independent reflections	6445	10586
Data/parameters/restraints	6445 /262 /0	10586 /277 /0
R [$F_o > 4\sigma(F_o)$]	R_1 = 0.0706	R_1 = 0.0396
	wR_2 = 0.207	wR_2 = 0.0986
G.o.f. on F^2	1.105	1.092
Max./min. residual densities, e·Å^{-3}	1.06, -0.64	1.42, -1.00

Table 4.2. Selected average metal-to-ligand bond distances (Å) and bond angles (°) for compounds **18** and **19.**

Compound **18**	Distance (Å)		Angle (°)
$Os(1)–N_{(N\equiv C)}$	2.038(2)	Mn(1)-O(3)-C(24)	125.53(2)
$Mn(2)–N_{(N\equiv C)}$	2.228(1)	O(1)-Mn(1)-O(2)	91.50(1)
$Mn(3)–O_{MeOH}$	2.315(2)	N(4)-Mn(1)-N(5)	82.59(2)
$Mn(1)–O_{salphen}$	1.868(1)	Mn(1)-N(1)-C(1)	136.40(2)
$Mn(2)–N_{salphen}$	1.987(1)	Os(1)-C(1)-N1)	177.03(2)
$C\equiv N_{bridging}$	1.149(1)		
$C\equiv N_{terminal}$	1.153(1)		
Compound **19**	Distance (Å)		Angle (°)
$Fe(1)–N_{(N\equiv C)}$	1.921(2)	Mn(1)-O(3)-C(24)	125.79(1)
$Mn(2)–N_{(N\equiv C)}$	2.248(1)	O(1)-Mn(1)-O(2)	91.86(2)
$Mn(3)–O_{MeOH}$	2.345(1)	N(4)-Mn(1)-N(5)	82.61(1)
$Mn(1)–O_{salphen}$	1.866(2)	Mn(1)-N(1)-C(1)	138.05(2)
$Mn(2)–N_{salphen}$	1.982(5)	Fe(1)-C(1)-N1)	177.49(2)
$C\equiv N_{bridging}$	1.148(1)		
$C\equiv N_{terminal}$	1.159(2)		

mother liquor. In addition, if the crystals of compound **18** or **19** are placed back in methanol or if they are left for too long (~ 1 month) in their mother liquors they slowly decompose resulting in the formation of a grey powder whose composition has not been determined.

Compounds **18** and **19** exhibit characteristic bands in the ν(C≡N) stretching region. A comparison of the observed IR data to the ν(C≡N) stretches determined for free hexacyanometallate anions aids in the assignment of the bands in the new compounds to bridging or terminal CN^- ligands. The IR spectrum of **18** exhibits two low-frequency stretches at 2105 and 2114 cm^{-1} that are only slightly shifted as compared to the corresponding mode of the $[Fe^{III}(CN)_6]^{3-}$ ion (2112 cm^{-1}) and, therefore, these modes are reasonably assigned to the terminal cyanides. Similarly, the ν(C≡N) stretches observed for compound **19** at 2086 and 2092 cm^{-1} can be assigned to the terminal cyanides of the coordinated $[Os(CN)_6]^{3-}$ building block.

Single Crystal X-ray Diffraction Study

Single crystal X-ray diffraction studies revealed that compounds **18** and **19** are isostructural and crystallize in the monoclinic space group *C*2/c (Table 4.1). It should be noted that the overall structural features of **18** and **19** are similar to those of the A{[Mn(salen-type ligand)(solv)]$_2$[M(CN)$_6$]} family.[198] The molecular structures consist of a trinuclear core composed of a central hexacyanometallate anion bound to two $\{Mn(salphen)(MeOH)\}^+$ units resulting in a linear cluster with an overall negative charge. As illustrated for **19** in Figure 4.1, the Mn^{III} centers are bound through the nitrogen ends of *trans* cyanide groups, with a long Mn-N(1) separation of 2.228(3) Å

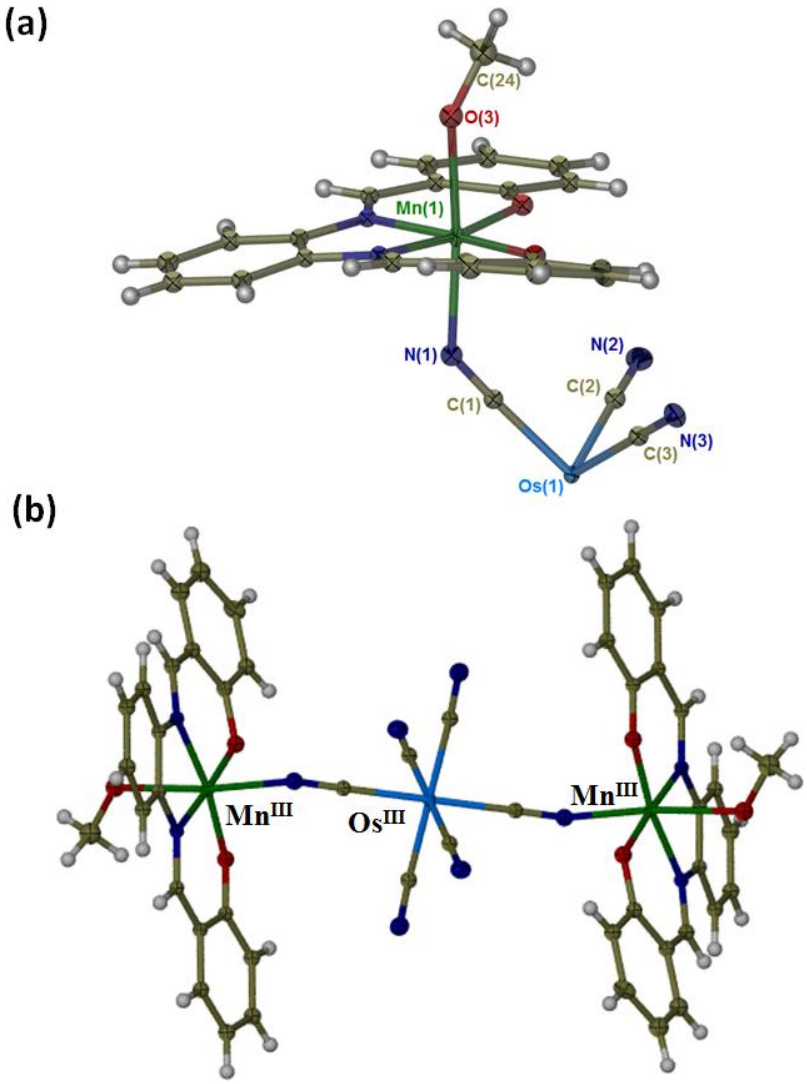

Figure 4.1. Thermal ellipsoid plots of (a) the asymmetric unit of $\{[Mn(salphen)(MeOH)]_2[Os(CN)_6]\}^-$ and (b) the trinuclear anion $\{[Mn(salphen)(MeOH)]_2[Os(CN)_6]\}^-$ in **19**. Ellipsoids are projected at the 50% probability level.

and a significantly bent Mn–N(1)–C(1) angle of 136.4(1)°. While such a low angle is atypical for most cyanide bridged complexes it is actually very similar to previously reported trimers in the A{[Mn(salen-type ligand)(solv)]$_2$[M(CN)$_6$]} family.[90, 198, 202] The coordination around the Mn^{III} ion is an elongated square bipyramid in which the equatorial sites are occupied by the N_2O_2 donor atoms of the salphen ligand with one of the two apical sites occupied by a cyanide group of $[M(CN)_6]^{3-}$ (M^{III} = Fe, Os) and the other site occupied by a methanol molecule with a Mn-O(3) distance of 2.315(2) Å. As expected for Mn^{III} ions, a Jahn-Teller distortion is observed which induces a strongly distorted square bipyramidal geometry around the Mn^{III} site with an elongated axis along the N(1)-Mn(1)-O(1) direction (N(1) – Mn(1) = 2.228(2) Å and Mn(1) – O(1) = 2.315 Å). It is worth noting that the Jahn-Teller axis is parallel to the chain direction.

A packing diagram projected on the *ab*-plane is provided in Figure 4.2, which shows the arrangement of the trimers in the layer. The closest contact between the pseudo chains of trimers is 3.895(1) Å between the phenyl rings of the salphen ligands from neighboring clusters (Figure 4.2). A projection of the structure along the *c*-axis is given in Figure 4.3 which illustrates the stacking of the trimer layers and shows the PPN^+ cations positioned between the layers. After further examination of the packing of the trimers in the *ab*-plane, it was possible to discern two important intermolecular interactions that result in the 1D arrangement of the trimers highlighted in Figure 4.2. These two intermolecular interactions correspond to a π-π interaction between the phenyl rings of the nearest neighbor {Mn(salphen)(MeOH)} moieties where the closest contact

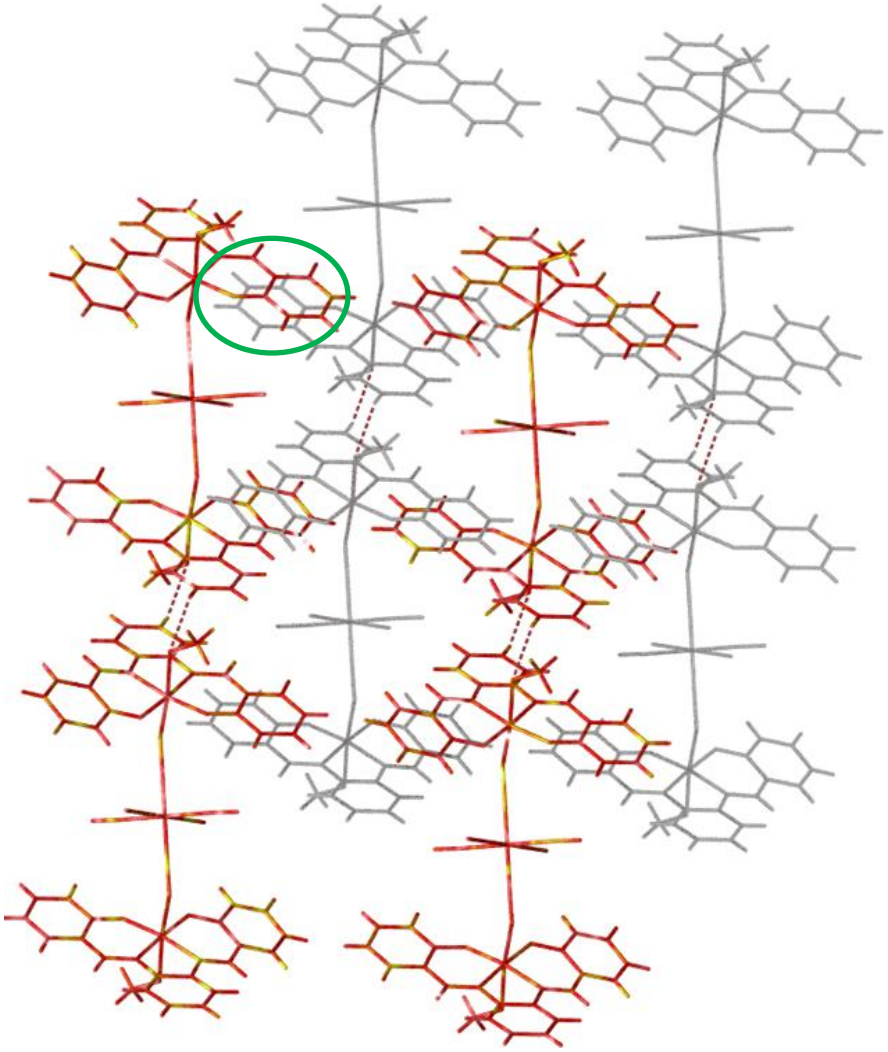

Figure 4.2. Molecular representation of the crystal packing of **19** in the *ab*-plane. The green circle highlights the closest contact between the chains.

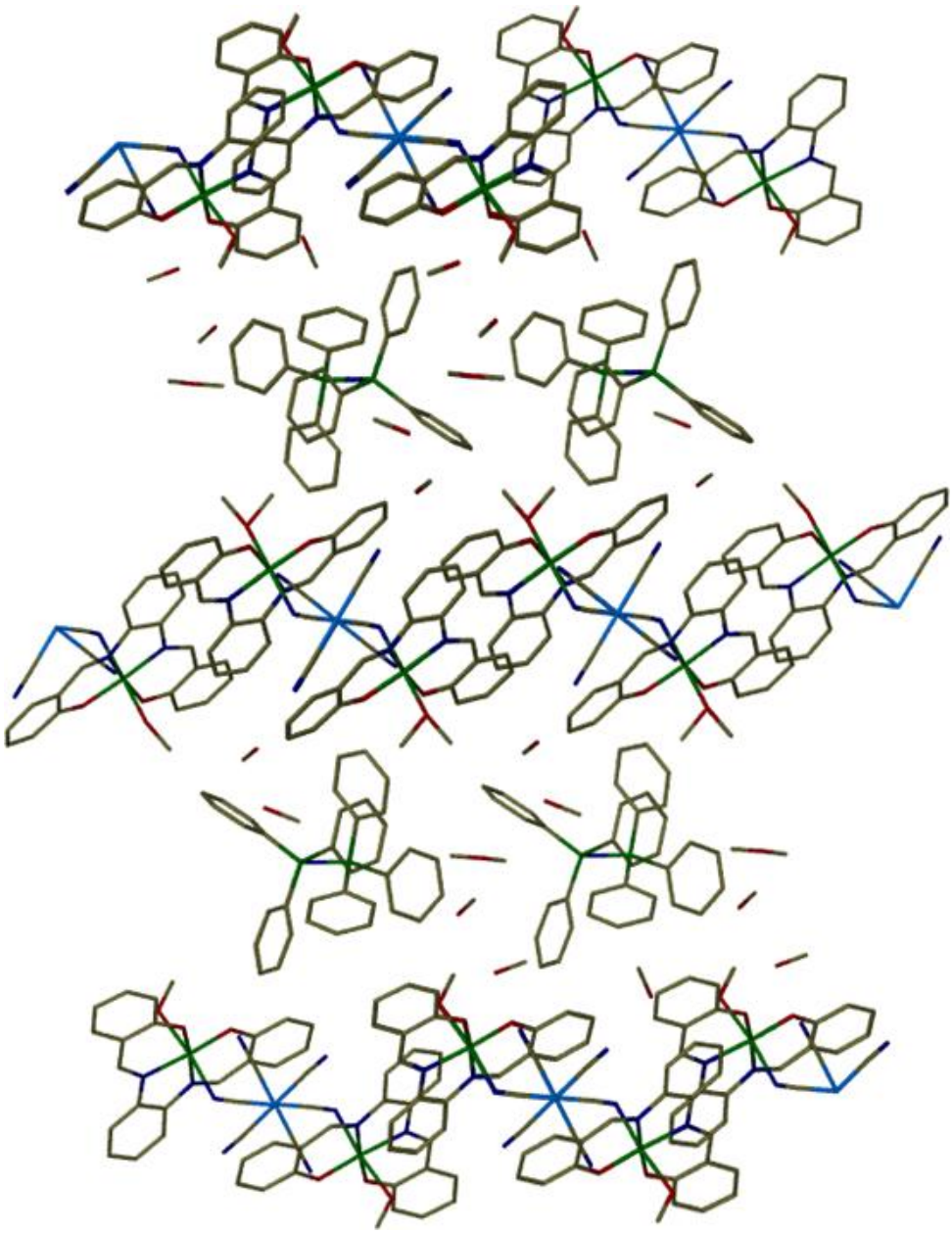

Figure 4.3. Molecular representation of the crystal packing of **19** along the *c*-axis showing the alternating layers of trimers and PPN cations.

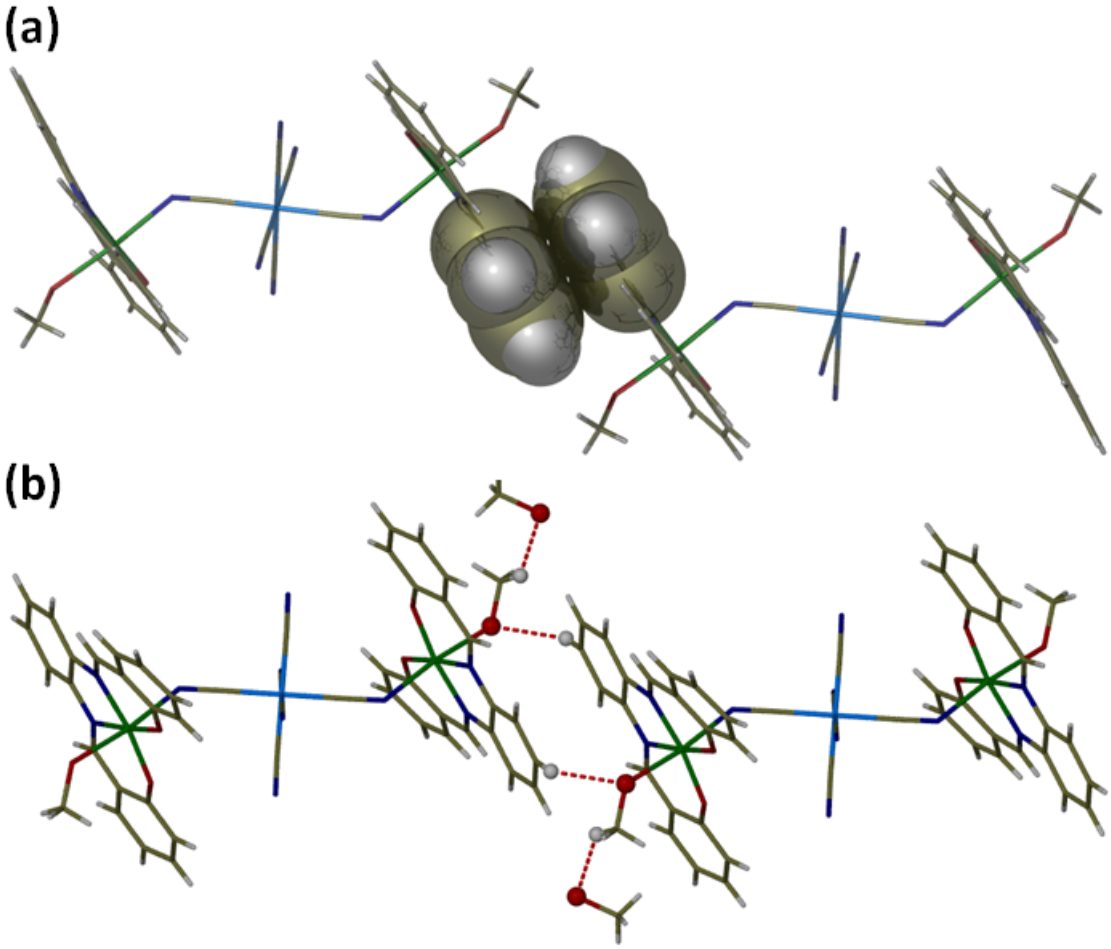

Figure 4.4. Molecular representation of (a) the π-π stacking and (b) H-bonding molecular interactions between trimers that are responsible for the 1D arrangement of the clusters along the *b*-axis.

is 3.487(1) Å, which is typical of aromatic-aromatic edge-to-edge π-π stackings,[203] and a H-bonding interaction between the coordinated MeOH and the phenyl hydrogen of the nearest neighbor trimer as shown in Figure 4.4. The distance between the $O_{MeOH}\cdots H_{salphen}$ is 2.755 Å, which is at the limit of conventional hydrogen bonding.[203] In addition to the intercluster interactions, the coordinated MeOH molecule also participates in a much stronger hydrogen bonding interaction (2.678 Å) with an interstitial methanol molecule.

Given these observations it is possible to suggest that if the stronger hydrogen bonding interactions between the trinuclear cluster and the interstitial solvent were removed by dessolvation of the material, the hydrogen bonding interaction between the trinuclear clusters would likely increase in strength potentially leading to a magnetic phenomenon recently coined as "exchanged biased SMMs".

Magnetic Properties

The analysis of the magnetic data was performed with the help of Dr. Andrey Prosvirin and the measurements at mK temperatures were performed in collaboration with Dr. Wolfgang Wernsdorfer using microSQUID techniques available in Grenoble. The DC susceptibility data for compounds **18** and **19** were measured from 2-300 K in an applied magnetic field of 1000 G (Appendix A). Both compounds showed an increase in χT as the temperature is lowered, an indication of ferromagnetic exchange interactions between the Fe^{III}, Os^{III} and the Mn^{III} centers mediated through the cyanide bridge. To model the magnetic behavior the spin-orbital contribution of the metal ions is neglected

and the isotropic Heisenberg-Dirac-Van Vleck Hamiltonian was used assuming an external field (H) along the z axis ($H = H_z$):

$$H = -2J_{Mn-Fe}(S_{Mn1}S_M + S_{Mn2}S_M) + \mu_B H_Z(2g_{Mn}S_{Mn} + g_M S_M) + D[S_T - (1/3)S_{Mn}(S_{Mn} + 1)] \quad (Eq. 4.1)$$

were $J_{Mn\text{-}Fe}$ is the isotropic exchange constant, M corresponds to the central Fe^{III} or Os^{III} atoms, and S_T is the total spin operator of the trimer with $S_T = S_{Mn1} + S_{Fe} + S_{Mn2}$. The simulation of the magnetic susceptibility curves were carried out using MAGPACK in addition to incorporating intertrimer interactions, J', in the frame of the mean-field approximation:

$$\chi = \frac{\chi_{trimer}}{1 - \frac{2zJ'}{Ng^2\mu_B^2}\chi_{trimer}} \quad (Eq. 4.2)$$

PPN{[Mn(salphen)(MeOH)]$_2$[Fe(CN)$_6$]} (18). Temperature-dependent magnetic susceptibility data for **18** are dominated by the signature of ferromagnetic coupling between the high spin S = 2 Mn^{III} and S = 1/2 Fe^{III} ions (Figure 4.5a). The room-temperature χT vs T value of 6.51 emu·K·mol^{-1} is consistent with two isolated Mn^{III} ions and one isolated Fe^{III} ion (6.35 emu·K·mol^{-1}). The value of the χT product increases with temperature reaching a maximum at 8 K, indicating ferromagnetic coupling between the Mn^{III} and Fe^{III} ions, resulting in an S = 9/2 ground state. The drop in χT at very low temperatures is attributable to zero field splitting and/or intermolecular interactions. The field dependence of the magnetization data at temperatures between 2 and 20 K show a nonsuperposition of the isofield lines indicating the presence of significant zero field

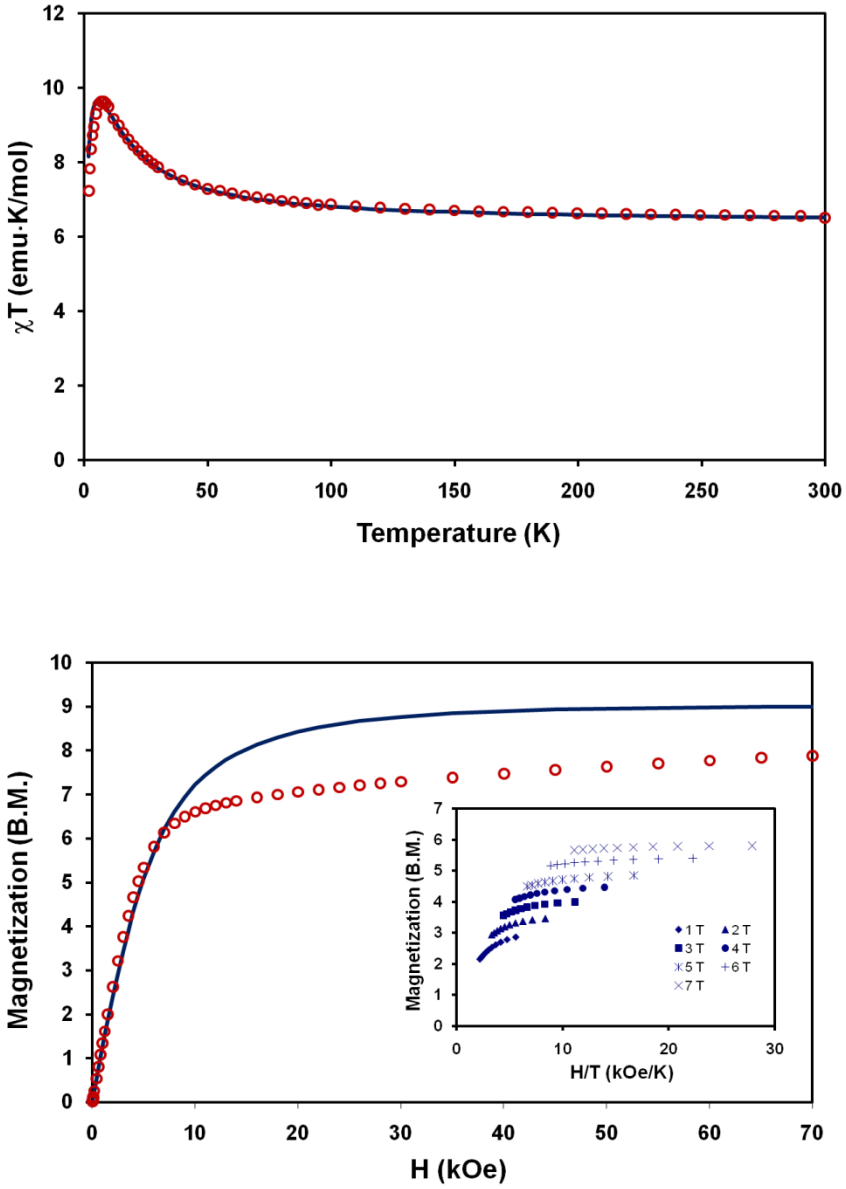

Figure 4.5. (a) Temperature dependence of χT product for **18** (**O**). The solid line corresponds to the MAGPACK[196] simulation (g_{Fe} = 2.0, g_{Mn} = 2.0 , J = 4.7 cm^{-1}, D = -0.3 cm^{-1}, zJ' = -0.05 cm^{-1}). (b) Field dependent magnetization for **18**. The solid line corresponds to the Brillouin function (S = 9/2, g_{avg} = 2.0). Inset: Reduced magnetization data at different external fields.

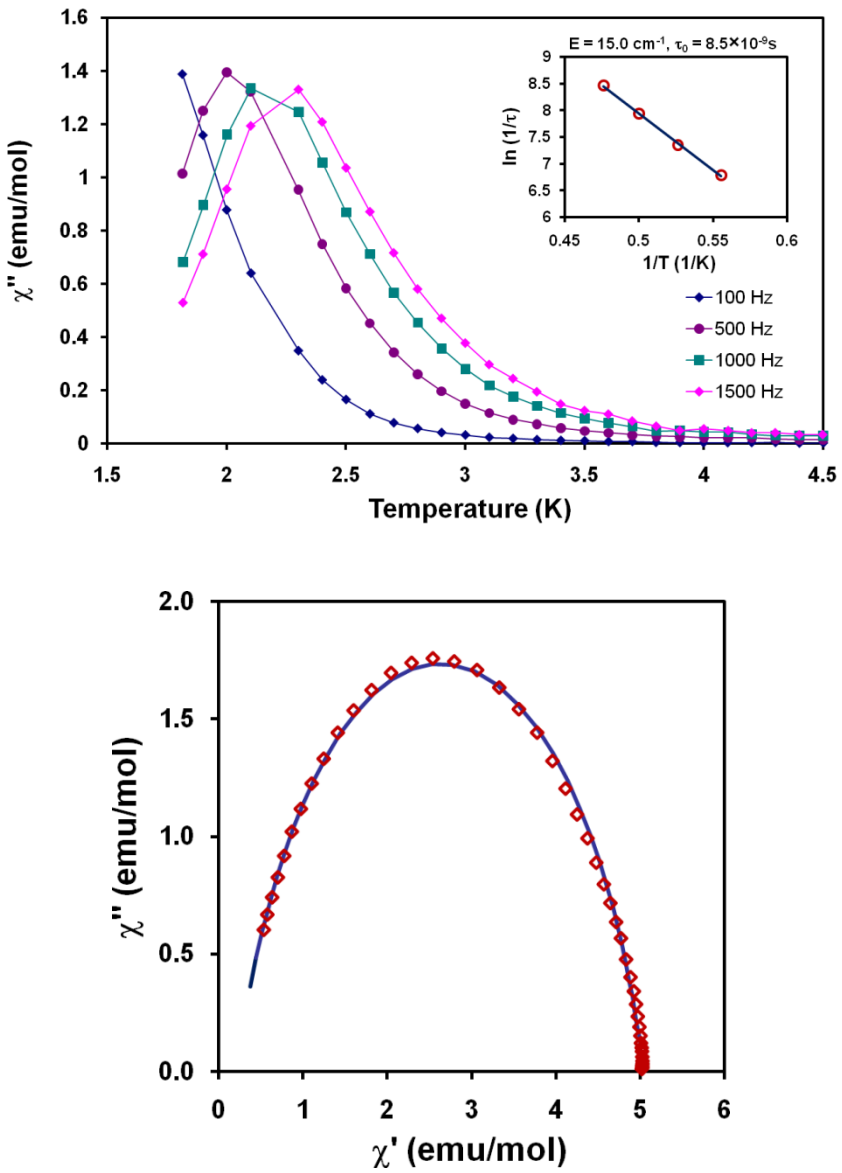

Figure 4.6. (a) Temperature dependence of the imaginary (χ″) part of the ac susceptibility for **18** measured under various oscillating frequencies (1-1500 Hz). The solid lines are a guide for the eyes. Inset: dependence of the logarithm of the relaxation rate ($1/\tau$) on the inverse temperature ($1/T$). The solid line represents the best linear fit to the Arrhenius law (U_{eff} = 15 cm^{-1} and τ_0 = 8.5 x 10^{-9} s). (b) Cole-Cole plot for **18** at 1.8 K. The solid line represents the least squares fit by a generalized Debey model.

splitting (Figure 4.5b, inset). Additionally, even at 7 T and 2 K, the magnetization is well below the saturation value of 9.0 μ_B expected for an $S = 9/2$ ground state with a $g = 2.0$ in the absence of zero field splitting (Figure 4.5b), indicating the presence of accessible low-lying excited states. The simulation of the magnetic susceptibility using Eq. 4.1 and the program MAGPACK resulted in best fit parameters of $J = 4.7$ cm^{-1}, $zJ' = -0.05$ cm^{-1}, $g_{Mn} = 2.0$, $g_{Fe} = 2.0$, and $D = -0.3$ cm^{-1} (Figure 4.5a).

Given that the family of compounds of general type A{[Mn(salen-type ligand)(solv)]$_2$[M(CN)$_6$]} has been shown to exhibit SMM behavior[90, 204, 205], the magnetization reversal dynamics of compound **18** were probed with the use of AC susceptometry. The AC magnetic susceptibility data in zero applied DC field manifest slow relaxation of the magnetization (Figure 4.6a). The corresponding rise in the out-of-phase susceptibility, χ_M'', is shown in Figure 4.7 for frequencies of 100, 500, 1000, and 1500 Hz. In each case, χ_M'' achieves a maximum at a temperature at which the switching of the magnetic field matches the relaxation rate, $1/\tau$, for the magnetization of the cluster. The χ_M'' data indicates a blocking temperature, T_B, of 2.3 K at 1.5 kHz. In addition, the shape of the Cole-Cole plot is nearly symmetrical (Figure 4.6b) indicating that a single relaxation time, τ, can be considered. As for typical SMMs, the relaxation times follow an Arrhenius relationship: $\tau = \tau_o \exp(U_{eff}/k_BT)$. Accordingly, a plot of $\ln(1/\tau)$ vs $1/T$ is linear (Figure 4.6a, inset) with a least-square fit yielding $\tau_o = 8.5 \times 10^{-9}$ s and $U_{eff} = 15$ cm^{-1}. The value for U_{eff} is similar to the value reported by Miyasaka *et. al.* for the SMM (NEt$_4$){[Mn(salmen)(MeOH)]$_2$[Fe(CN)$_6$]} ($U_{eff} = 10$ cm^{-1}; salmen = N,N′-(1-methylethylene)bis-(salicylideneiminate))[205] and in very good agreement with the

value calculated from INS experiments for the trinuclear cluster K{[Mn(5-Brsalen)(H_2O)]$_2$[Fe($CN)_6$]} (U_{eff} = 11.5 cm^{-1}; salmen = N,N′-(ethylene)bis-(5-bromosalicylideneiminate)).[204]

In conclusion, the combined AC and DC measurements gathered at low temperatures on **18** indicate unambiguously that it exhibits SMM behavior induced by a high-spin ground state, S_T = 9/2, and uniaxial anisotropy where D = -0.3 cm^{-1}.

PPN{[Mn(salphen)(MeOH)]$_2$[Os($CN)_6$]} (19). The magnetic properties of a polycrystalline sample of **19** behave very similarly to compound **18**. The room-temperature χT vs T value of 6.47 emu·K·mol^{-1} is consistent with two isolated Mn^{III} ions and one isolated Os^{III} ion (6.35 emu·K·mol^{-1}; Figure 4.7). The value of χT increases with decreasing temperature reaching a maximum at 8 K consistent with ferromagnetic coupling between the Mn^{III} and Os^{III} ions and an S = 9/2 ground state. The drop in χT at very low temperatures is attributable to zero field splitting and/or intermolecular interactions. As in the case of compound **18**, the nonsuperposition of the isofield lines of the field dependence of the magnetization data at temperatures between 2 and 20 K (Figure 4.7, inset) and the lack of saturation of the magnetization curve for compound **19** indicate the presence of significant zero-field splitting and the existence of accessible low-lying excited states. The simulation of the magnetic susceptibility data using Eq. 4.1 and the simulation program MAGPACK resulted in the best fit parameters of J = 5.1 cm^{-1}, zJ' = -0.05 cm^{-1}, g_{Mn} = 2.0, g_{Fe} = 2.0, and D = -0.3 cm^{-1} (Figure 4.7).

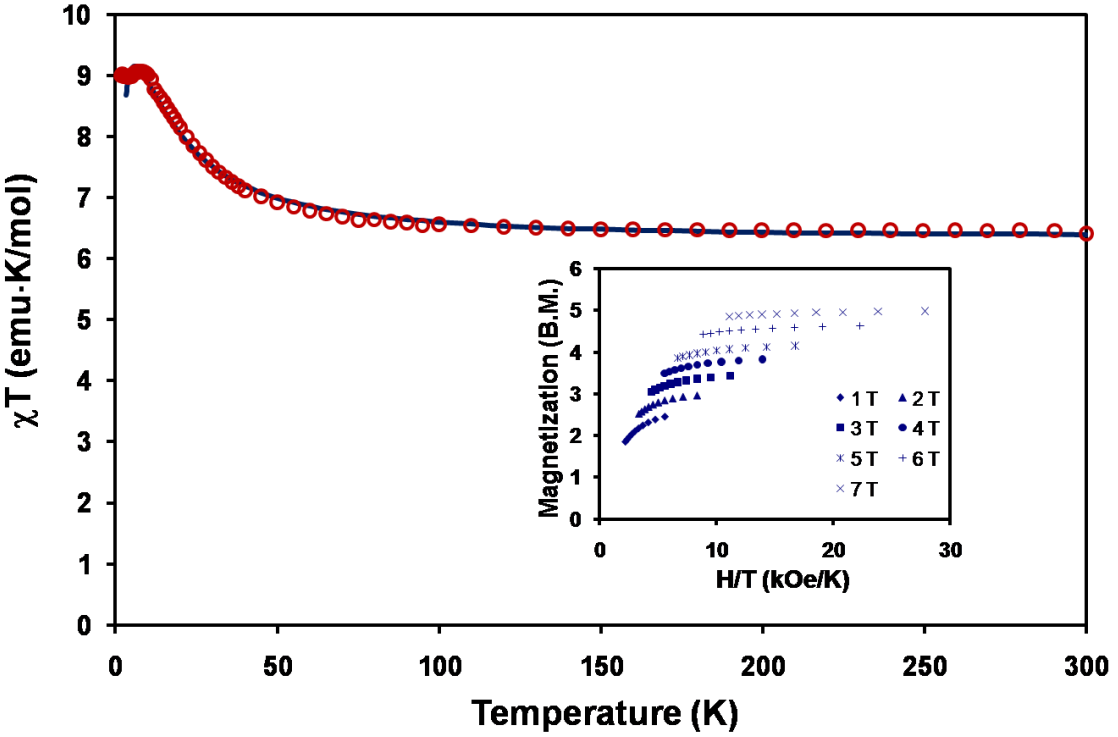

Figure 4.7. Temperature dependence of χT for **19** (**O**). The solid line corresponds to the MAGPACK[196] simulation (g_{Fe} = 2.0, g_{Mn} = 2.0 , J = 5.1 cm^{-1}, D = -0.3 cm^{-1}, zJ' = -0.05 cm^{-1}). Inset: Reduced magnetization data at different external fields.

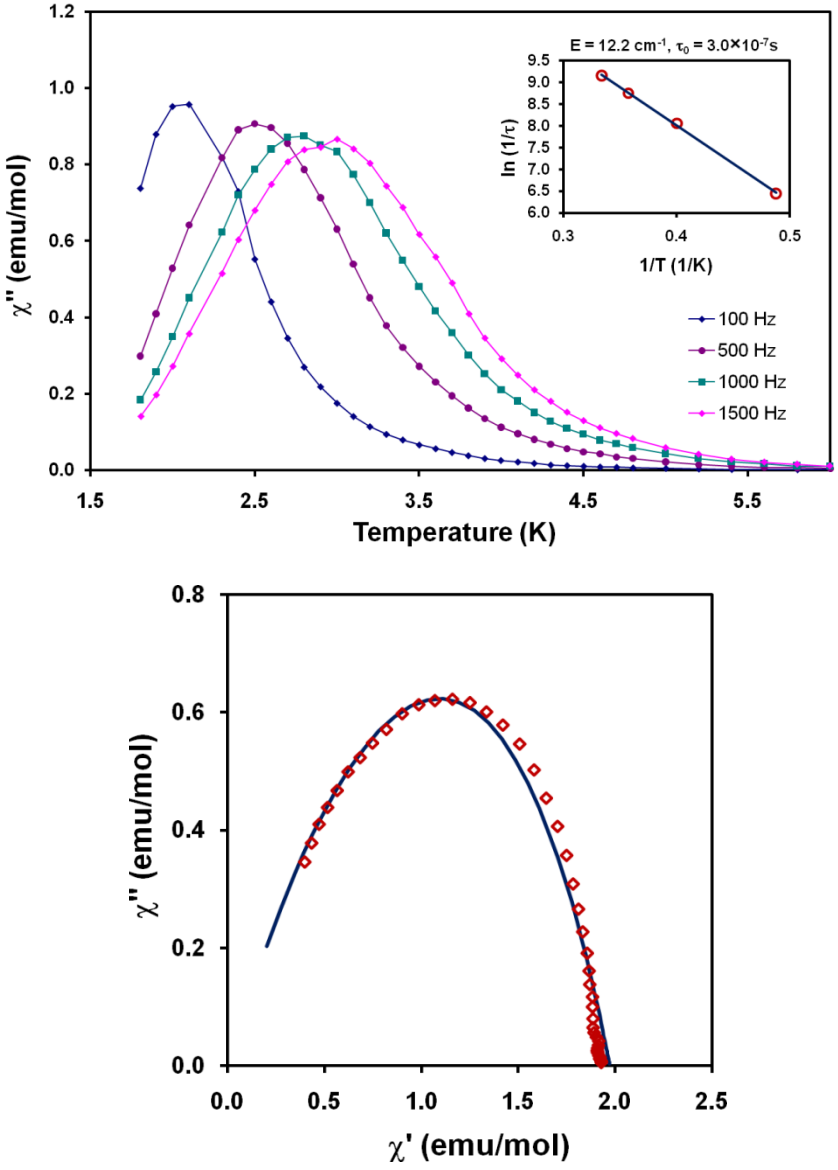

Figure 4.8. (a) Temperature dependence of the imaginary (χ'') part of the ac susceptibility for **19** measured under various oscillating frequencies (1-1500 Hz). The solid lines are a guide for the eyes. Inset: dependence of the logarithm of the relaxation rate ($1/\tau$) on the inverse temperature ($1/T$). The solid line represents the best linear fit to the Arrhenius law (U_{eff} = 12.2 cm^{-1} and τ_0 = 3.0 x 10^{-7} s). (b) Cole-Cole plot for **19** at 2.3 K. The solid line represents the least squares fit by a generalized Debey model.

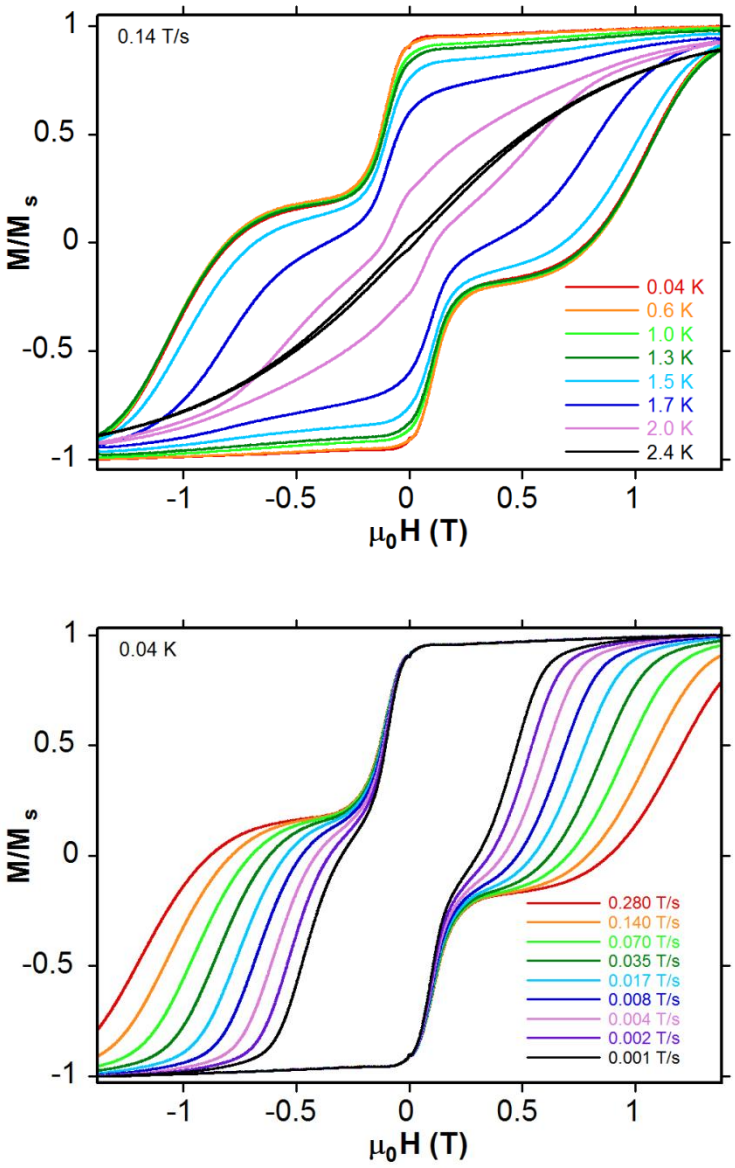

Figure 4.9. Field dependence of the magnetization on an oriented crystal of **19** along the *b* axis (a) below 2.4 K with a sweep field rate of 0.14 T/s and (b) below a sweep rate of 0.280 T/s at 0.04 K.

The magnetization reversal dynamics for compound **19** were probed by AC susceptometry methods. Variable frequency experiments at low temperatures showed a peak in the out-of-phase component of the signal (Figure 4.8a) indicating a blocking temperature of 3.0 K at 1.5 kHz. In addition, the shape of the Cole-Cole plot is nearly symmetrical (Figure 4.8b) indicating that a single relaxation time, τ, is taking place. The peak temperatures were fit to an Arrhenius relationship: $\tau = \tau_o \exp(U_{eff}/k_BT)$ (Figure 4.8a, inset), leading to an effective barrier height for magnetization reversal of $U_{eff} = 12.0$ cm^{-1} and a pre-exponential value $\tau_o = 3.00 \times 10^{-7}$ s. The combined AC and DC measurementsgathered at low temperatures on **19** are consistent with the conclusion that the compound exhibits SMM behavior.

To further explore the SMM behavior, hysteresis loops were collected on easy-axis oriented single crystal samples using a micro-SQUID apparatus by Dr. Wolfgang Wernsdorfer at Grenoble. Temperature dependent scans reveal hysteretic behavior for **19** at low temperatures, with strongly temperature- and sweep rate dependent coercivity. Below 2.3 K (Figure 4.9a), hysteresis loops are observed in the easy direction, and they become temperature independent below 1.0 K, staying however, sweep-rate dependent even at 0.04 K (Figure 4.9b). This result highlights the slow relaxation of the magnetization and indicates unambiguously that **19** behaves as a SMM. Analyzing these hysteresis loops in more detail, we observe two steps due to resonant quantum tunneling of the magnetization, a phenomenon unique to SMMs. Previous literature suggests that the step at zero field corresponds to the fast relaxation between the two lower-energy levels, $m_S = \pm 9/2$.[205] Around $\mu_o H_1 = 0.7$ T, a second fast relaxation process is observed

which corresponds to the first crossing between two energy levels (i.e., m_S = 9/2 and -7/2). From this H_1 field, the uniaxial anisotropy, $|D|$, of the trinuclear compound can be estimated to be 0.32 cm^{-1} ($|D_T| = g\mu_B H_{ex}$, g = 2, $H_1 = 2H_{ex}$). A fitting of the reduced magnetization data is necessary to further confirm the value of the D parameter calculated from the micro-SQUID measurements, nevertheless, the value agrees very well with the best-fit parameter (D = -0.3 cm^{-1}) obtained from the DC measurement.

The above work has clearly shown that the inclusion of a 5*d* hexacyanometallate results in a cluster that exhibits SMM behavior. Moreover, as compared to its 3*d* analog an increase of the blocking temperature by 23% is achieved. In addition to the SMM behavior another rare magnetic phenomenon was observed were the SMMs interact through space via weak intermolecular interactions resulting in a change of the magnetic properties. This phenomenon is more commonly known as "exchanged-bias SMMs".

For a single crystal of an SMM that has negligible intermolecular exchange interactions, the first step in the hysteresis loop due to quantum tunneling occurs at zero field when the external field is oriented parallel to the easy axis of the crystal. In contrast, when the interactions between the SMMs are not negligible a shift of the first step occurs with respect to the isolated SMM. The first SMM that was reported to exhibit such an exchange bias is the $[Mn_4]_2$ dimer, $[Mn_4O_3Cl_4(O_2CEt)_3(py)_3]_2$.[206] This complex is held together by six C-H---Cl hydrogen bonds and one Cl---Cl interaction. The supramolecular linkage leads to a weak antiferromagnetic exchange interaction (J = -0.035 cm^{-1}) between the two S = 9/2 SMMs. The hysteresis loop for non-interacting S = 9/2 Mn_4 SMMs show their first step at zero field. The weak antiferromagnetic

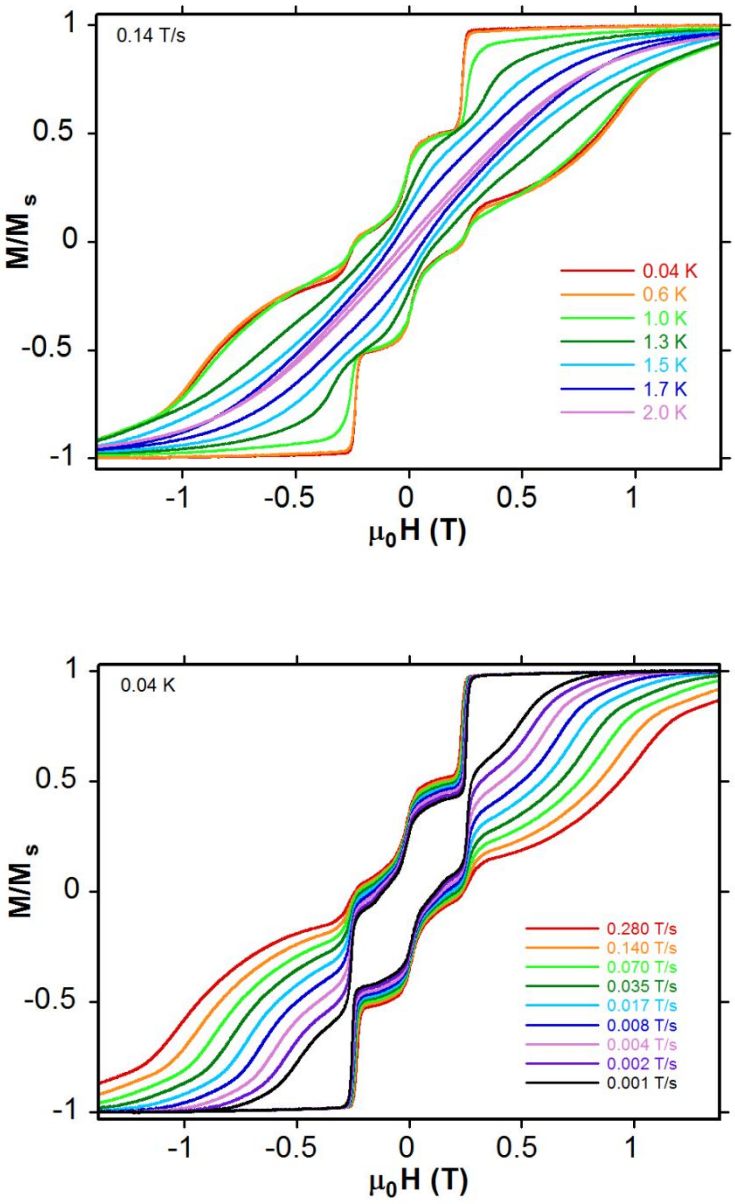

Figure 4.10. Field dependence of the magnetization on an oriented "dry" crystal of **19** along the *b* axis (a) below 2.4 K with a sweep field rate of 0.14 T/s and (b) below a sweep rate of 0.280 T/s at 0.04 K.

interaction between the two S = 9/2 SMMs in this dimer shifts the first step to -0.33 T.

In the case of compound **19**, similar behavior was observed in the hysteresis loops collected on single crystals at mK temperatures (Figure 4.10), where the first step observed at 40 mK occurs at -0.25 T. This shift of the first step indicates the presence of antiferromagnetic intermolecular interactions between the Mn_2Os clusters. Below 1.0 K (Figure 4.10a) the hysteresis loops become temperature independent, staying however, sweep-rate dependent even at 40 mK (Figure 4.10b) indicating that quantum tunneling of the magnetization is still present in the compound. This behavior is similar to other exchanged bias SMMs reported in the literature.[206-211]

As described in the structural section, the antiferromagnetic exchange interactions are most likely a result of the H-bonding and π-π stacking present between the Mn_2Os trimers along the *b*-axis. In addition, the structural determination, as well as the observation of two different hysteretic behaviors for compound **19** suggest that the interstitial solvent plays a crucial role in the observation of the "exchanged biased SMM" behavior.

In order to probe the role of the interstitial solvent on the magnetic properties of compound **19,** measurements were performed on bulk samples that were dried and also under solvent (25% Hexanes:75% MeOH). The samples ran under solvent exhibit typical SMM behavior, as previously presented, where the intermolecular interactions are negligible. On the other hand, the desolvated samples of compound **19** exhibit different magnetic behavior, especially in the magnetization reversal dynamics. The χT vs T curve behaves very similarly as the temperature is lowered from room temperature

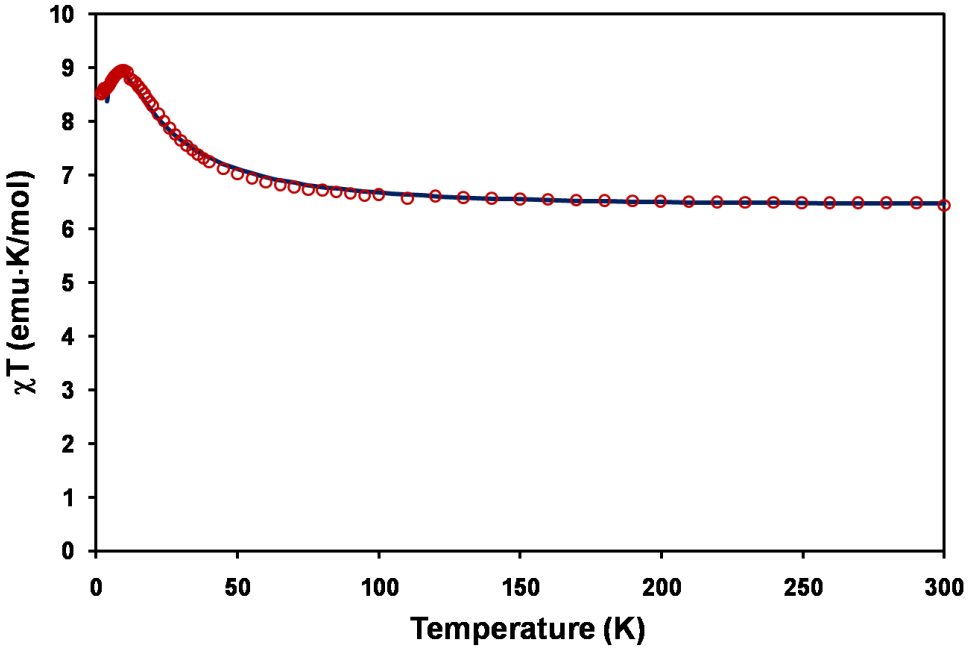

Figure 4.11. Temperature dependence of χT for a dried sample of **19** (**O**). The solid line corresponds to the MAGPACK[196] simulation (g_{Fe} = 2.0, g_{Mn} = 2.0 , J = 5.5 cm^{-1}, D = -0.3 cm^{-1}, zJ' = -0.12 cm^{-1}).

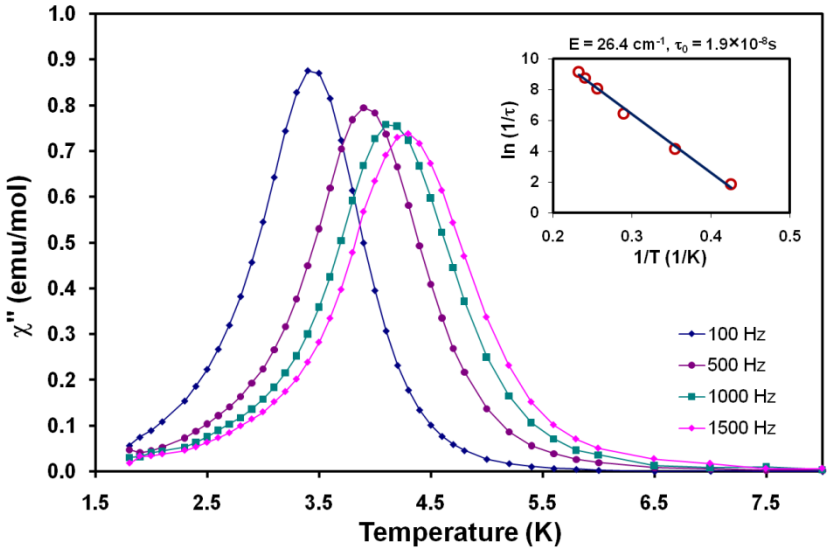

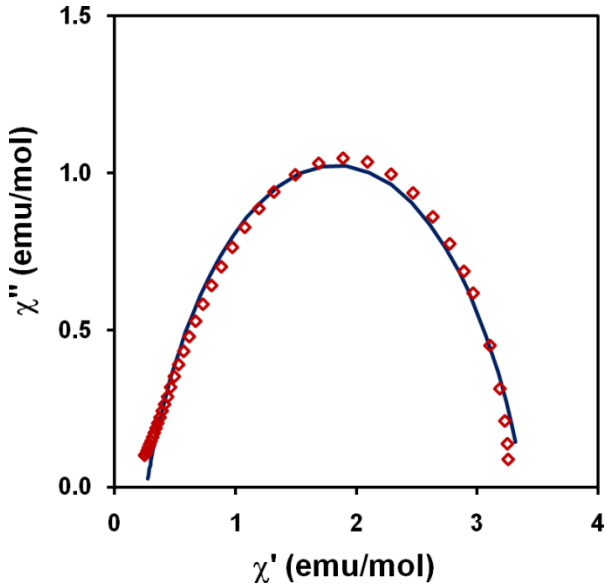

Figure 4.12. (a) Temperature dependence of the imaginary (χ″) part of the ac susceptibility for a dry sample of **19** measured under various oscillating frequencies (1-1500 Hz). The solid lines are a guide for the eyes. Inset: dependence of the logarithm of the relaxation rate ($1/\tau$) on the inverse temperature ($1/T$). The solid line represents the best linear fit to the Arrhenius law (U_{eff} = 26.4 cm^{-1} and τ_0 = 1.9 x 10^{-8} s). (b) Cole-Cole plot for **19** at 2.7 K. The solid line represents the least squares fit by a generalized Debey model.

(Figure 4.11), however, the best fit parameter for the intermolecular interaction, $zJ' = -0.12$ cm^{-1}, is significantly higher than the one observed for the isolated SMM ($zJ' = -0.05$ cm^{-1}). More importantly, the peaks in the out-of-phase AC susceptibility are frequency dependent indicative of a relaxation of the magnetization associated with an energy barrier to magnetization reversal and show that the dessolvated sample of **19** exhibits a blocking temperature of 4.3 K at 1.5 kHz (Figure 4.12a). In addition, the shape of the Cole-Cole plot was nearly symmetrical (Figure 4.12b) indicating that a single relaxation time, τ, can be considered. The peak temperatures can be fitted to an Arrhenius relationship: $\tau = \tau_o \exp(U_{eff}/k_BT)$ (Figure 4.12a, inset), leading to an effective barrier height for magnetization reversal of $U_{eff} = 26.4$ cm^{-1} and a preexponential value $\tau_o = 1.90 \times 10^{-8}$ s. These data are consistent with the hysteresis loops obtained from the micro-SQUID measurements (Figure 4.10) from which it could be ascertained that the 1-D network of exchanged coupled SMMs does not suppress the QTM. The intermolecular interactions are sufficiently strong to cause an obvious field bias, but too weak to transform the spin network into a classical antiferromagnetic material.

As previously observed in chains of ferro- or antiferromagentically coupled SMMs the observed dynamics are influenced by the intrachain magnetic interactions. Applying the approach described for these systems[212-214] to the supramolecular 1D network of canted antiferromagnetically coupled SMMs, the energy gap of the relaxation time should be $\Delta_\tau = 2\Delta_\xi + \Delta_A$ (Eq 4.3) within the Ising limit:

$$\Delta_A = \left| D \right| S_T^2/k_B \text{ and } \Delta_\xi = 4 \left| J' \right| S_T^2 \cos(\alpha)/k_B \qquad \text{(Eq. 4.4)}$$

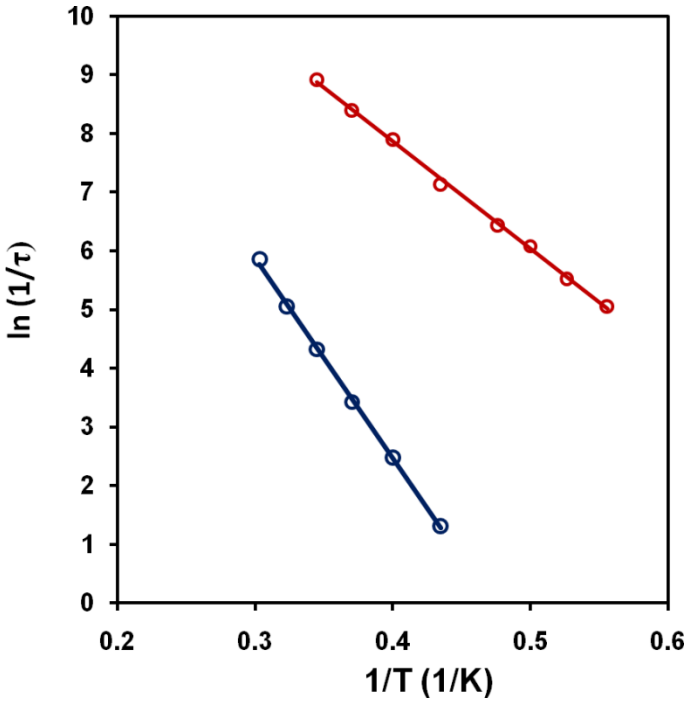

Figure 4.13. Logarithm of the relaxation rate ($1/\tau$) versus the inverse temperature ($1/T$) plot for a solvated (blue dots) and a dried (red dots) sample of **19**. The solid line represents the best linear fit to the Arrhenius law (blue: U_{eff} = 12.2 cm^{-1} and $\tau_0 = 3.0 \times 10^{-7}$ s; red: U_{eff} = 26.4 cm^{-1} and $\tau_0 = 1.9 \times 10^{-8}$ s).

In addition when Eq 4.4 is rearranged to solve for Δ_ξ, the experimental values for the energy barriers determined for the isolated SMM (SMM $U_{eff} = \Delta_A = 12.2$ cm^{-1}) and the coupled SMMs (coupled SMM $U_{eff} = \Delta_\tau = 26.4$ cm^{-1}) can be used to calculate the value of Δ_ξ to be 7.10 cm^{-1}, which corresponds to a $J' = -0.11$ cm^{-1} ($\alpha = 37°$) which is in good agreement with the value determined from the magnetic susceptibility measurements ($J' = -0.12$ cm^{-1}).

The obtained τ values for the solvated and desolvated samples of compound **19** were plotted in Figure 4.13. As expected, the thermal variations of the relaxation time observed for a desolvated and a solvated sample of **19** are completely different and attest to the fact that the exchange coupling between the SMM trimers dramatically influences the relaxation of the magnetization.

CONCLUSIONS

The trinuclear complexes in this chapter constitute the first clusters to incorporate both Mn^{III} ions and $[Os^{III}(CN)_6]^{3-}$ anions in the form of trinuclear complexes in the A{[Mn(salen-type ligand)(solv)]$_2$[M(CN)$_6$]} family in which PPN^+ is used as a cation. The magnetic data indicate that the trinuclear clusters, PPN{[Mn(salphen)(MeOH)]$_2$[M(CN)$_6$]}, exhibit SMM behavior similar to that reported previously by Miyasaka *et al.* and Long *et al.*[90, 205] Moreover, the data collected demonstrates that the blocking temperature can be enhanced when a more anisotropic ion such as Os^{III} is incorporated into the compound. Further magnetic analysis of the Fe analog under both the dried and the solvated conditions are underway to elucidate

whether the Os^{III} ion has any additional effects on the magnetic properties of the molecules.

Furthermore, the packing of the trimers induced by the choice of the salen-type ligand (salphen) and the cation (PPN) resulted in clusters that experience weak intermolecular interactions leading to the first observation of significant exchanged biased SMMs in cyanide-bridged assemblies. This 1D network of exchange coupled SMMs demonstrates that QTM can be controlled using exchange interactions, opening up new perspectives for the use of supramolecular interactions to modulate the quantum physics of molecular nanomagnets. More importantly, these results lend further credibility to the notion that aspects of SMM behavior can be controlled by fine-tuning the molecular properties and the resulting intermolecular interactions, an important issue for the possible application of SMMs in devices.

CHAPTER V

NEW BUILDING BLOCKS FOR THE SYNTHESIS OF DISCRETE CLUSTERS BASED ON THE {[(6-(PIVALAMIDO)-2-PYRIDYL]METHYL}BIS-(2-PYRIDYLMETHYL)AMINE LIGAND

INTRODUCTION

The rapid development of the field of molecular magnetism over the last decades is due, in large measure, to the discovery of high-temperature molecule-based magnets that order above room temperature and exhibit large coercivities.[52, 170, 171] As mentioned in previous chapters, some of the most widely studied molecular magnets are Prussian blue, $Fe_4[Fe(CN)_6]_3$, and its analogues. The high interest in these compounds is a result of the exciting findings that cyanide materials behave as high-temperature molecular magnets,[54, 55, 171] photo-switchable magnetic solids,[215] molecular sieves,[124] and hydrogen storage materials.[125, 126] The interesting properties notwithstanding, it is a challenge to model the properties of these ill defined materials whose composition is dictated by rapid precipitation which results in the presence of statistically distributed vacancies in the positions of metal ions. This issue led many researchers to explore the chemistry of discrete cyanide clusters[88] such as the ones presented in Chapters III and IV as model systems for studying the effect of the identities of the metal centers and their coordination environments on the magnetic properties of cyanide compounds. Such clusters allow for a thorough investigation of structure-property relationships due to their well-defined compositions and geometries.

With this aim in mind, our research group has developed approaches in which the formation of an extended solid is limited by the introduction of multidentate organic ligands capable of blocking a specific number of coordination sites on the transition metal ions.[216] This strategy has led to the syntheses of discrete cyanide clusters with a variety of geometries and rich magnetic properties (Figure 5.1), work that has contributed to the development of fields such as single molecule magnets (SMMs) and multifunctional materials.[88]

In recent years, as the field of cyanide-based SMMs and functional materials has matured, several major thrusts have become obvious. Firstly, since a number of the reported cyanide-bridged clusters were found to be stable in solution,[217] they are being used as building blocks for the preparation of higher nuclearity clusters[184, 218] and extended solids (building block approach). Secondly, an interest is currently emerging to study the chemical behavior of the cyanide-bridged clusters and functionalizing them for possible electronic and spintronic applications.[219, 220] Finally, increased emphasis is being placed on the development of theoretical models that go beyond explaining the properties of existing clusters to predict possible new molecules with elusive magnetic properties such as SMM behavior.[221, 222] This latter point is the driving force for the work presented in this chapter.

Linear trinuclear clusters constitute one of the simplest model systems that can be used for the study of magnetic properties and the development of theoretical models as a function of the nature of metal ions and their coordination geometries. The search for building blocks that could be useful for the preparation of trinuclear clusters led us to

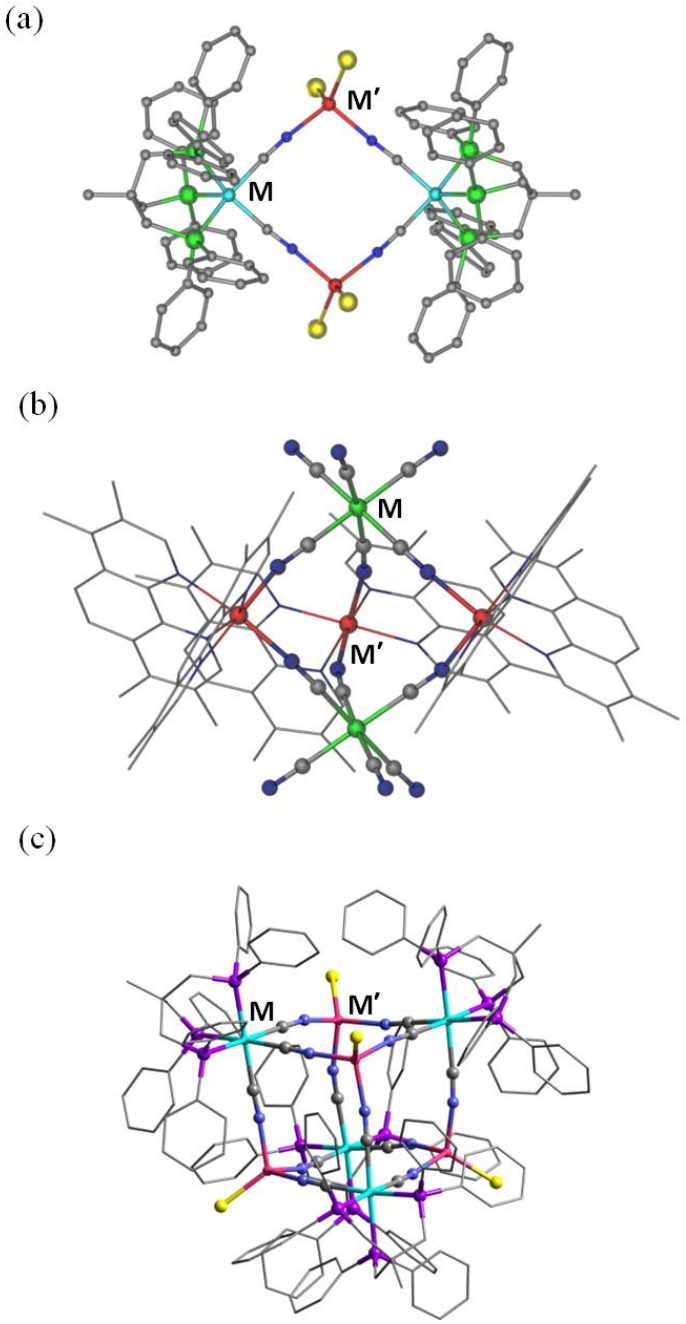

Figure 5.1. Structures of cyanide bridged molecular (a) squares (M = Co^{II}; M′ = Mn^{II}, Fe^{II}, Co^{II}, Ni^{II}, Zn^{II}), (b) trigonal bipyramids (M = Cr^{III}, Mn^{III}, Fe^{III}, Co^{III}, Os^{III}; M′ = Cr^{II}, Mn^{II}, Fe^{II}, Co^{II}, Ni^{II}, Zn^{II}), and (c) cubes (M = Re^{II}, M′ = Mn^{II}, Co^{II}, Ni^{II}, Zn^{II}; M = Re^{I}, M′ = Fe^{III}).

the use of the phosphine complexes of Co^{II} presented in Chapter III. In these compounds, Co^{II} ions are typically in pentacoordinate environments[176,179] where four coordination sites around the Co^{II} center are blocked by two bis-chelating dppe ligands, and only one site is available for further chemistry. Nevertheless, this approach, while convenient for Co^{II}, does not translate well to other first row transition metals, as they are not prone to forming pentacoordinate precursors with dppe or other phosphine ligands.[179] Likewise, in Chapter IV we highlighted the results obtained using the $[Mn^{III}(salphen)(H_2O)_2][BF_4]$ precursor, which is an appropriate building block for the synthesis of new SMMs,[90, 204] but, as in the case of the phosphine ligands, salphen and other salen-type ligands do not easily accommodate a variety of 3*d* metal ions. Moreover, the salen type ligands stabilize the trivalent oxidation state in most cases which hinders the preparation of a series of 3*d* precursors with varying oxidation states.

As a result, the search for a new ligand that could accommodate the various 3*d* metal ions in their different oxidation states became an important goal. As has been shown in the first part of this dissertation, in order to deliberately synthesize trimers, it is necessary to prepare transition metal precursors with only one open or labile coordination site for further chemistry. In the general case of an octahedrally coordinated transition metal ion, this requires the use of a pentadentate blocking ligand. We have chosen as a blocking ligand {[(6-(pivalamido)pyrid-2-yl]methyl}bis-(pyrid-2-ylmethyl)amine (MPPA, Scheme 5.1), which we hoped would facilitate the crystallization of both the precursors and the trinuclear products.

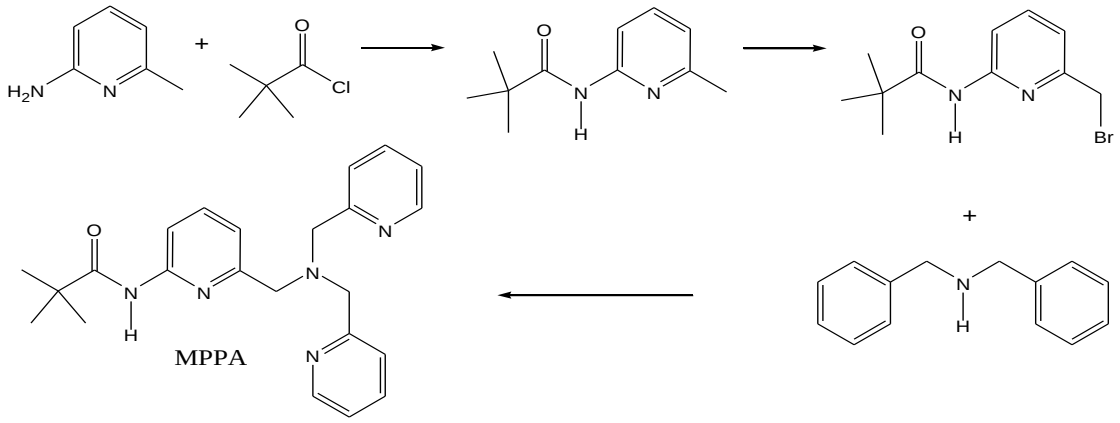

Scheme 5.1. Synthesis of the pentacoordinate ligand MPPA.

This chapter describes the syntheses of new building blocks based on reactions of the MPPA ligand with transition metal salts of V, Cr, Mn, Fe, Co, and Ni. The results of the structural investigations and magnetic properties measurements are discussed in detail. In addition, the successful implementation of the $[Fe(MPPA)]^{3+}$ precursor for the synthesis of a discrete cluster is also presented.

EXPERIMENTAL

Syntheses

Starting materials. Di-2-(picolyl)amine (Aldrich), $Mn(ClO_4)_2 \cdot 6H_2O$ (Aldrich), $Co(BF_4)_2 \cdot 6H_2O$ (Aldrich), $Ni(BF_4)_2 \cdot 6H_2O$ (Aldrich), VCl_3THF_3 (THF: tetrahydrofuran, Aldrich), $CrCl_3THF_3$ (Aldrich), $FeCl_3$ (Alfa Aesar) were used as received. The compound 2-(pivaloylamido)-6-(bromomethyl)pyridine was prepared as previously reported[223, 224] but isolated by a modification of the chromatographic procedure reported (CH_2Cl_2/Hexanes). The starting material $Fe_4Cl_8THF_6$ was prepared as reported from the anhydrous metal chloride.[225] Acetonitrile and diethyl ether were dried over 3 Å molecular sieves and distilled prior to use. Unless stated otherwise, all compounds were prepared under anaerobic conditions. The reactions for the V^{III} and Cr^{III} ions were performed by Codi Sanders under my guidance as part of an undergraduate research program.

CAUTION! Perchlorate complexes of organic ligands are potentially explosive. They should be handled in small quantities with great care under conditions that do not exclude water.

{[(6-(pivalamido)-2-pyridyl]methyl}bis-(2-pyridylmethyl)amine (20: MPPA/L_5). To a 250 mL round bottom flask containing 2-(pivaloylamido)-6-(bromomethyl)pyridine (2.0 g, 7.3 mmol) in dry acetonitrile (70 mL) was added di-2-(picolyl)amine (1.47 g, 7.3 mmol), Na_2CO_3 (1.54 g, 14.6 mmol), and a catalytic amount of tetrabutylammonium bromide (~5 mg). The reaction mixture was purged with N_2 and refluxed for 12 h. After cooling the solution to room temperature, 1 M sodium hydroxide was added (90 mL). The resulting biphasic solution was extracted with CH_2Cl_2 (3 × 150 mL) and the organic fractions were combined and dried over anhydrous sodium sulfate. After filtration, the organic solution was taken to dryness on a rotary evaporator to yield a yellow oil. Dissolution of the resultant crude oil in diethyl ether at room temperature yielded light yellow needle-like crystals of MPPA (2.3 g, 82 % yield). ^{1}H NMR ($CDCl_3$): δ = 1.33 (s, 9 H), 3.78 (s, 2 H), 3.89 (s, 2 H), 7.15 (m, 2 H), 7.28 (d, 2 H), 7.64 (d, 2 H), 7.66 (t, 3 H), 7.95 (b, 1 H), 8.10 (d, 1 H), 8.53 (d, 2 H) ppm. ESI^+-MS (CH_2Cl_2): m/z 390.22 ($[M+H]^+$).

$[Mn^{II}(MPPA)(MeCN)_2][ClO_4]_2$ (21). To an acetonitrile (5 mL) solution of MPPA (0.250 g, 0.64 mmol) was added an acetonitrile solution of $Mn(ClO_4)_2{\cdot}6H_2O$ (0.217 g, 0.60 mmol). The resulting yellow solution was stirred overnight in an inert atomosphere dry-box at ambient temperature. The solvent was then removed under reduced pressure. The remaining solid was dissolved in ~4 mL of acetonitrile and diethyl ether (~10 mL) was added until a tan-yellow solid was observed to precipitate. The solid was collected by filtration and washed with diethyl ether (3 × 5 mL). Yield = 0.278 g (64%). Elemental analysis indicated the presence of interstitial water molecules: Calcd. for

$MnC_{27}H_{37}N_7O_{11}Cl_2$ (**21**·$2H_2O$): C, 42.62; H, 4.91; N, 12.90; O, 23.15; Found: C, 42.52; H, 4.73; N, 11.32; O, 23.53%. ESI^+-MS (CH_3CN): m/z 223 ($[(Mn(L_5)]^{2+}$), 480 ($[Mn(L_5)Cl]^+$). Single crystals of the compound were grown by dissolving the solid in ~4 mL of acetonitrile and slowly adding diethyl ether (~10 mL) until the solution became cloudy. The solution was then placed at -40°C in the dry-box for ~3 weeks after which time yellow-block crystals were isolated that were suitable for single crystal X-ray diffraction measurements.

$[Co^{II}(MPPA)][BF_4]_2$ (22). To a 20 mL acetonitrile solution of MPPA (0.250 g, 0.64 mmol) was added a solution of $Co(BF_4)_2·6H_2O$ (0.218 g, 0.64 mmol) in 20 mL of dry acetonitrile. The orange-colored solution was stirred overnight and the solvent was removed under reduced pressure. The remaining solid was dissolved in ~5 mL of acetonitrile and diethyl ether (~10 mL) was added until a red-pink solid precipitated. The solid was collected by Schlenk filtration methods and washed with diethyl ether (3 × 5 mL). Yield = 0.303 g (75%). Elemental analysis indicated the presence of interstitial acetonitrile molecules: Calcd. for $CoC_{23}H_{27}N_7OB_2F_8$ (**22**·CH_3CN): C, 45.28; H, 4.56; N, 12.67; F, 22.92; Found: C, 44.63; H, 4.55; N, 12.46; F, 21.89%. ESI^+-MS (CH_3CN): m/z 224 ($[Co(L_5)]^{2+}$), 447 ($[Co(L_5)\text{-}H]^+$), 467 ($[Co(L_5)F]^+$). UV-vis(CH_3CN): λ_{max}, nm (ε, $M^{-1}cm^{-1}$) = 570.5 (32.537), 464.5 (108.668). Single crystals of the compound were grown after 2 weeks in a 3 mm diameter sealed thin tube by slow diffusion of diethyl ether into a concentrated solution of the compound.

$[Ni^{II}(MPPA)(MeCN)][BF_4]_2$ (23). A quantity of MPPA (0.250 g, 0.64 mmol) was added to a solution of $Ni(BF_4)_2·6H_2O$ (0.218, 0.64 mmol) in 40 mL of acetonitrile. The

purple solution was stirred overnight in air. The solution was then taken to dryness on a rotary evaporator. The remaining solid was dissolved in ~5 mL of acetonitrile and diethyl ether (~10 mL) was added until a light purple solid precipitated. The solid was collected by filtration in air and washed with diethyl ether (3 × 5 mL). Yield = 0.260 g (61%). Elemental analysis indicated the presence of interstitial water molecules: Calcd. for $NiC_{25}H_{30}N_8OB_2F_8$ (**23**·$3H_2O$): C, 41.88; H, 5.06; N, 11.73; F, 21.22; Found: C, 42.43; H, 4.71; N, 11.26; F, 21.36 %. ESI^+-MS (CH_3CN): m/z 466 ($[Ni(L_5)F]^+$), 482 ($[Ni(L_5)(H_2O)_2]^+$), 534 ($[Ni(L_5)(BF_4)]^+$). UV-vis(CH_3CN): λ_{max}, nm (ε, $M^{-1}cm^{-1}$) = 869.5 (37.792), 537.5 (20.063). Single crystals of the compound were grown after dissolving the solid in ~4 mL of acetonitrile followed by slow addition of diethyl ether (~10 mL) until the solution became cloudy. The solution was then placed in the freezer for ~3 weeks after which time purple-block crystals were isolated that were suitable for single crystal X-ray diffraction measurements.

Cr^{III}(MPPA)Cl_3 (24). A quantity of MPPA (0.250 g, 0.64 mmol) was added to a solution of $CrCl_3(THF)_3$ (0.300 g, 0.64 mmol) in 40 mL of acetonitrile. The dark green solution was stirred overnight. The solvent was then removed under reduced pressure. The remaining solid was dissolved in ~5 mL of acetonitrile and diethyl ether (~15 mL) was added until a light green solid precipitated. The solid was collected by filtration and washed with diethyl ether (3 × 5 mL). Yield = 0.157 g (45%). Elemental analysis calcd. for $CrC_{23}H_{27}N_5OCl_3$: C, 47.80; H, 4.71; N, 12.12; O, 2.77; Found: C, 47.08; H, 4.75; N, 11.65; O, 2.98 %. ESI^+-MS (CH_3CN): m/z 509 ($[Cr(L_5)Cl_2]^+$), 545 ($[Cr(L_5)Cl_3\text{-}H]^+$). Single crystals of the compound were grown after dissolving the solid in ~3 mL of

acetonitrile followed by slow diffusion of diethyl ether (~4 mL) in an H-tube. After ~3 weeks dark green crystals were isolated that were suitable for single crystal X-ray diffraction measurements.

[V^{III}(MPPA)Cl_2]Cl (25). To an acetonitrile solution of MPPA (0.250 g, 0.64 mmol) was added an acetonitrile solution of $VCl_3(THF)_3$ (0.230 g, 0.62 mmol) (40 mL). The resulting dark purple solution was stirred overnight. The next day, the solution was taken to dryness on the Schlenk line. The remaining solid was dissolved in ~5 mL of acetonitrile and diethyl ether (~25 mL) was added until a purple solid precipitated. The solid was collected by filtration, washed with diethyl ether (3 × 5 mL), and vacuum dried. Yield = 0.224 g (67%). Elemental analysis indicated the presence of interstitial water and acetonitrile molecules: Calcd. for $VC_{23}H_{27}N_5OCl_3$(**25**·2CH_3CN·H_2O): C, 48.22; H, 5.50; N, 13.05; Cl, 16.86; Found: C, 49.67; H, 5.44; N, 12.37; Cl, 16.92 %. ESI^+-MS (CH_3CN): m/z 454 ($[V(L_5)(H_2O)\text{-}2H]^+$), 470 ($[V(L_5)Cl\text{-}H]^+$), 487 ($[V(L_5)(CH3CN)\text{-}2H]^+$). Single crystals of the compound were grown after dissolving the solid in ~3 mL of acetonitrile followed by slow diffusion of diethyl ether (~4 mL) in an H-tube. After ~3 weeks dark green crystals were isolated that were suitable for single crystal X-ray diffraction measurements.

[Fe^{III}(MPPA)Cl_2]Cl (26). In the dry-box, MPPA (0.250 g, 0.64 mmol) and $FeCl_3$ (0.100 g, 0.64 mmol) were placed into a 100 mL Schlenk flask. The solids were dissolved in ~40 mL of dry acetonitrile and allowed to stir overnight. The yellow-brown solution was vacuum dried to afford a yellow solid. The remaining solid was dissolved in ~11 mL of acetonitrile and diethyl ether (~20 mL) was added until a yellow solid precipitated. The

solid was collected by Schlenk filtration and washed with diethyl ether (3 × 5 mL). Yield = 0.246 g (70%). Elemental analysis calcd. for $FeC_{23}H_{27}N_7OCl_3$ (**26**): C, 50.18; H, 4.95; N, 12.73; O, 2.91; Cl, 19.07; Found: C, 50.45; H, 4.94; N, 12.93; O, 2.94; Cl, 19.20 %. ESI^+-MS (CH_3CN): m/z 476 ($[Fe(L_5)Cl\text{-}H]^+$), 515 ($[Fe(L_5)Cl_2]^+$). Single crystals of the compound were grown after 2 weeks in an H-tube by slow diffusion of diethyl ether into a concentrated solution of the compound.

Fe^{II}(MPPA)Cl_2 (27). In the dry-box, MPPA (0.250 g, 0.64 mmol) and $Fe_4Cl_8THF_6$ (0.140 g, 0.150 mmol) were placed in a 50 mL Schlenk flask. The solids were dissolved in ~10 mL of dry acetonitrile and the mixture was stirred. Immediately after adding the solvent, a bright yellow solid was observed to precipitate from solution. After being stirred overnight, the solid was collected by filtration and washed with diethyl ether (3 × 5 mL). Yield = 0.245 g (74%). Elemental analysis calcd. for $FeC_{23}H_{27}N_7OCl_2$ (**27**): C, 53.51; H, 5.27; N, 13.57; O, 3.10; Found: C, 53.48; H, 5.24; N, 13.53; O, 3.16 %. ESI^+-MS (CH_3CN): m/z 223 ($[Fe(L_5)]^{2+}$), 445 ($[Fe(L_5)]^+$), 479 ($[Fe(L_5)Cl]^+$), 522 ($[Fe(L_5)(CH_3CN)Cl]^+$). Single crystals of the compound were grown after 2 weeks in an H-tube by slow diffusion of diethyl ether into the isolated filtrate.

{[Fe^{III}(MPPA)]$_2$-μ-O}[BF_4]$_4$ (28). Amounts of $Fe(BF_4)_2 \cdot 6H_2O$ (0.200 g, 0.587 mmol) and MPPA (0.250 g, 0.64 mmol) were weighed into a 50 mL Schlenk flask. The solids were dissolved in ~30 mL of acetonitrile and stirred in air overnight. The dark orange solution was dried under reduced pressure resulting in the isolation of a dark red-brown solid. Single crystals suitable for X-ray diffraction experiments of the compound were grown after re-dissolving the solid in ~5 mL of acetonitrile and allowing slow diffusion

of diethyl ether into the solution. The crystals were collected by filtration and washed with diethyl ether (3 × 5 mL). Yield = 0.231 g (63%). Elemental analysis indicated the presence of interstitial methanol molecules: Calcd. for $Fe_2C_{46}H_{54}N_{10}O_3B_4F_{16}$ (**28·CH$_3$OH**): C, 43.85; H, 4.54; N, 10.88; F, 23.63; Found: C, 43.07; H, 4.57; N, 10.78; F, 23.57 %.

Single Crystal X-ray Diffraction

In a typical experiment, a crystal selected for study was suspended in polybutene oil (Aldrich) and mounted on a cryoloop which was placed in a N_2 cold stream. Single-crystal X-ray data were collected on a Bruker APEX or Bruker SMART 1000 diffractometer equipped with a CCD detector at 110 K. The data sets were recorded as three ω scans of 606 frames each, at a 0.3° step width, and integrated with the Bruker SAINT[187] software package. The absorption correction (SADABS[188]) was based on fitting a function to the empirical transmission surface as sampled by multiple equivalent measurements. Solution and refinement of the crystal structures was carried out using the SHELX[189] suite of programs and the graphical interface X-SEED.[190] Structure solution by direct methods resolved positions of all metal atoms as well as most of the C and N atoms. The remaining non-hydrogen atoms were located by alternating cycles of least-squares refinements and difference Fourier maps. Hydrogen atoms were placed at calculated positions. In the case of compounds with $[BF_4]^-$ counterions, these were disordered and were restrained to meaningful geometries. Similarly, whenever disordered solvent molecules were present in a structure, their bond distances were restrained to chemically meaningful values. The final refinements were performed with

Table 5.1. Crystal structural data and refinement parameters for compounds **21–25**.

Formula	**$[Mn^{II}(MPPA)(MeCN)_2][ClO_4]_2$ (21)**	**$[Co^{II}(MPPA)][BF_4]_2$ (22)**	**$[Ni^{II}(MPPA)(MeCN)][BF_4]_2$ (23)**	**$Cr^{III}(MPPA)Cl_3$ (24)**	**$[V^{III}(MPPA)Cl_2]Cl$ (25)**
Space group	$P2_1/n$	P-1	$P2_1$	P1	$P2_1/c$
Unit cell	*a*= *10.901(3)*Å *b* = 12.462(4) Å *c* =23.722(7)Å β = 90.283(5) º	*a*= *9.841(2)*Å *b* = 11.865(2)Å *c* = 14.128(3)Å α= *89.86(3)* β = 76.07(3) γ= 68.21(3) º	*a*= *15.547(3)*Å *b* = 16.709(3)Å *c* = 12.432(2)Å β = 92.524(3) º	*a*= *7.0196(11)*Å *b* = 13.312(2)Å *c* = 14.531(2)Å α= *104.642(2)* β = 98.100(2) γ= 97.378(2) º	*a*= *13.023(10)*Å *b* = 17.292(13)Å *c* =14.479(11)Å β = 109.350(8) º
Unit cell volume, *V*	3222.7(16)Å^3	1479.8(5) Å^3	3226.4(10) Å^3	1281.4(3) Å^3	3076(4)Å^3
Z	4	1	4	2	4
Density, ρ_{calc}	1.332 g/cm^3	1.420 g/cm^3	1.449 g/cm^3	1.755 g/cm^3	1.088 g/cm^3
Abs. coeff., μ	0.627 mm^{-1}	0.659 mm^{-1}	0.681 mm^{-1}	0.806 mm^{-1}	0.599 mm^{-1}
Crystal color and habit	Yellow block	Orange block	Purple block	Dark green block	Dark green block
Crystal size, mm^3	0.24x0.22x0.14	0.18x0.22x.014	0.32x0.28x0.22	0.54x0.48x0.38	0.42x0.38x0.33
Temperature	110 K	110K	110K	110K	110 K
Radiation, λ	Mo-Kα, 0.71073 Å	Mo-Kα, 0.71073 Å	Mo-Kα, 0.71073 Å	Mo-Kα, 0.71073 Å	Mo-Kα, 0.71073 Å
Min. and max. θ	1.72 to 28.35 º	1.49 to 28.25 º	1.31 to 28.29 º	1.47 to 28.22 º	1.90 to 28.47 º
Reflections collected	15093 [R_{int} =.1238]	8078[R_{int} =.1411]	18411[R_{int} =.1078]	14894[R_{int} =.0423]	36520 [R_{int} =0.0349]
Independent reflections	7418	5812	7508	11367	7687
Data/parameters/restraints	7418 /416 /0	5812/393/0	7508/423/0	11367/601/3	7687 /133 /0
R [$F_o > 4\sigma(F_o)$]	R_1 = 0.1297 wR_2 = 0.3222	R_1 = 0.1149 wR_2 = 0.2900	R_1 = 0.0701 wR_2 = 0.1662	R_1 = 0.0328 wR_2 = 0.0927	R_1 = 0.0948 wR_2 = 0.3041
G.o.f. on F^2	1.014	1.029	1.047	1.062	1.415
Max./min. residual densities, e·Å^{-3}	2.67, -1.08	1.77, -2.23	0.7, -1.32	0.94, -0.54	3.52, -0.52

Table 5.2. Crystal structural data and refinement parameters for compounds **27 - 28**.

Formula	**Fe^{II}(MPPA)Cl_2 (27)**	**{[(Fe^{III}(MPPA)]$_2$-μ-O}$[BF_4]_4$ (28)**
Space group	$P2_1/c$	$P2_1$
Unit cell	a= 9.959(3)Å b = 13.271(4)Å c =18.182(6)Å β = 101.429(13) º	a = 13.6271(14)Å b = 11.8008(12)Å c = 19.988(2)Å β = 106.813(2)°
Unit cell volume, V	2355.6(12)Å^3	3077.0(5)Å^3
Z	4	1
Density, ρ_{calc}	1.323 g/cm^3	0.345 g/cm^3
Abs. coeff., μ	0.768 mm^{-1}	0.141 mm^{-1}
Crystal color and habit	Yellow block	Dark Yellow block
Crystal size, mm^3	0.24x0.19x0.22	0.37x0.29x0.22
Temperature	110 K	110 K
Radiation, λ	Mo-Kα, 0.71073 Å	Mo-Kα, 0.71073 Å
Min. and max. θ	1.92 to 28.22 º	1.56 to 28.37 º
Reflections collected	25948[R_{int} =0.0314]	26675 [R_{int} =0.054]
Independent reflections	5604	13892
Data/parameters/restraints	5604 /292 /0	13892 /739 /1
R [$F_o > 4\sigma(F_o)$]	R_1 = 0.0398 wR_2 = 0.1034	R_1 = 0.0991 wR_2 = 0.2964
G.o.f. on F^2	1.093	1.330
Max./min. residual densities, e·Å^{-3}	0.72, -0.81	5.05, -0.74

anisotropic thermal parameters for all non-hydrogen atoms, except for the non-hydrogen atoms of the disordered solvent molecules which were refined isotropically. A summary of pertinent information relating to unit cell parameters, data collection, and refinements is provided in Table 5.1 and 5.2.

RESULTS AND DISCUSSION

Syntheses

The revised synthetic method for the preparation of the MPPA ligand resulted in a higher yield (82%) and in a more efficient synthetic scheme than the one previously reported. The conditions used for the chromatographic purification of the starting material 2-(pivaloylamido)-6-(bromomethyl)pyridine are described in Appendix B.

Reactions of the MPPA ligand with solvated divalent metal salts of Mn^{II}, Co^{II}, and Ni^{II} in acetonitrile afforded compounds **21**, **22**, and **23** respectively. The reactions proceed instantaneously with color changes from the light yellow color of the ligand to intense yellow, orange and purple colors from the reactions with Mn^{II}, Co^{II}, and Ni^{II}, respectively. The resulting compounds are soluble in MeCN, MeOH, CH_2Cl_2, and EtOH. Compounds **21** and **22** are air sensitive and consequently were prepared and handled under anaerobic conditions. When a solution of compound **21** is exposed to air an immediate color change occurs from an intense yellow color to a dark brown solution indicative of the formation of Mn^{III} species in solution. Similarly, when compound **22** is exposed to air over a period of 2 days it transforms from the light pink solid to an intensely colored dark red solid which was determined by magnetic measurements to be

a material composed of only Co^{III} ions. Compound **23**, however, can be handled in air and further chemistry can be performed in air without complications.

Reactions of the MPPA ligand with transition metal chloride salts in acetonitrile afforded compounds **24-26** in high yields. The reactions proceed instantaneously with color changes from the light yellow color of the ligand to intense dark green, purple and orange-brown colors from the reactions with Cr^{III}, V^{III}, and Fe^{III}, respectively. The resulting compounds are soluble in MeCN, MeOH, and CH_2Cl_2. The chloride anion introduced to the reaction via the metal salt starting material competes with the ligand for binding sites on the transition metal ion, resulting in precursors with varying degrees of open coordination sites for further chemistry. The preferential binding of the chloride anion instead of the ketone of the MPPA ligand to the metal ion was previously observed for MPPA compounds of Cu and Zn.[223]

Interestingly, the reaction of $[Fe(MeCN)_6][BF_4]_2$ with the MPPA ligand under both anaerobic and aerobic conditions resulted in the isolation of a linear oxo-bridged dimer of Fe^{III} ions, $\{[Fe^{III}(MPPA)]_2$-μ-$O\}[BF_4]_4$ (**28**). Clearly this is a very sensitive reaction and oxygen is being scavenged from very minor sources, perhaps the surface of the glassware. Although low yields of single crystals of the compound were isolated from the air-free reaction, in order for the reaction to go to completion, the solution must be exposed to air. As a result, compound **28** was deliberately synthesized in air in order to obtain the product in high yields. Compound **28** is soluble in MeCN, MeOH, and CH_2Cl_2 and can be isolated in high yield for further characterization. In an attempt to isolate a *bona fide* Fe^{II} precursor, the reaction of the MPPA ligand with the $Fe_4Cl_8THF_6$

complex was performed. The reaction was performed in acetonitrile and as a result of the neutrality of the final product, $Fe^{II}(MPPA)Cl_2$ (**27**), the solid precipitates out of solution and pure yellow microcrystalline material is obtained for further characterization.

For all the compounds, single crystals were easily obtained by slow diffusion of diethyl ether into a concentrated acetonitrile solution of the desired compound. Further characterization of the compounds was performed on microcrystalline material isolated in bulk by the slow addition of diethyl ether into a concentrated acetonitrile solution of the compound. The purity of the microcrystalline solid was determined by elemental analysis.

Single Crystal X-ray Diffraction Studies

Seven crystal structures were determined from single crystal diffraction measurements, ranging from V^{III}, Cr^{III}, Mn^{II}, Fe^{II}, Co^{II}, Ni^{II} to a dinuclear complex of Fe^{III}. The mononuclear complex $\{Fe^{III}(MPPA)\}^{3+}$ yielded only microcrystalline solid, but the elemental analysis and magnetic data corroborated that the material is, in fact, the anticipated complex. The compounds exhibit different coordination environments with the MPPA ligand. In general, when chlorides are present in the reaction, they will prevent the ketone from coordinating to the metal ion. Compounds **21-23** were prepared from solvated metal salts with $[ClO_4]^-$ or $[BF_4]^-$ as the counterion. The Mn^{II} structure exhibits a a heptacoordinate geometry, where the MPPA coordinates with all its donor atoms with an additional two acetonitrile molecules being bound to the Mn center; there are also two outer sphere $[BF_4]^-$ anions (Figure 5.2a). In compound **22**, Co^{II} is pentacoordinate leading to a TBP geometry with all of the sites occupied by the binding

sites of the MPPA ligand. At first glance, this may appear as defeating the purpose of leaving one open site for further chemistry, however strong field ligands such as cyanide are expected to displace a ketone binding site. Of the series thus far, Ni^{II} is the first to exhibit octahedral geometry, albeit slightly distorted with the MPPA occupying five positions and the sixth position being filled by an acetonitrile molecule.

Compounds **24**, **25** and **27** were prepared with chloride metal salts and, in each case, chloride ligands are bound to the metal ion in the products. The Cr^{III} complex (Figure 5.3a) demonstrates the extent of the chloride competition with the MPPA ligand for binding sites to the metal ion. In this compound three chloride atoms are bound to the metal center and only three sites are coordinated by the MPPA ligand, leaving the remaining pendant group dangling off to the side. The V^{III} complex (Figure 5.3b) exhibits an unexpected binding mode wherein all 5 binding sites of the ligand are coordinated to the vanadium center in addition to two chloride atoms leading to a heptacoordinate geometry around the metal ion. The remaining chloride ion is outer sphere. When the MPPA ligand coordinates to Fe^{II}, a six coordinate Fe^{II} ion in an octahedral geometry (Figure 5.4a) is obtained where four sites are occupied by the MPPA ligand, with the ketone group pendant, and the other two sites coordinated by chloride ions.

In the case of the reaction of the solvated salt $[Fe^{II}(MeCN)_6][BF_4]_2$ with MPPA the result is a linear oxo bridged dimer with the oxidation of each of the Fe centers being Fe^{III} (Figure 5.4b) where the MPPA fully coordinates to the Fe center leaving one open site for the oxygen to bind to each $\{Fe^{III}(MPPA)\}^{3+}$ unit.

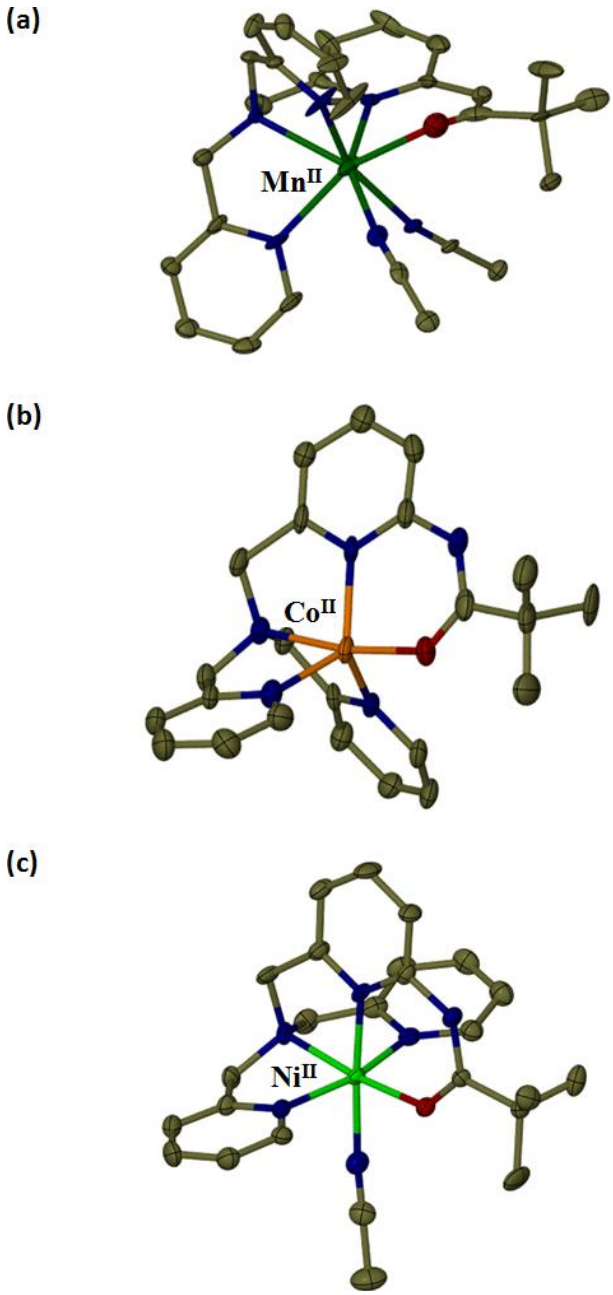

Figure 5.2. Thermal ellipsoid plots at the 50% probability level, where the hydrogen atoms have been omitted for the sake of clarity of (a) Compound **21** (b) Compound **22** and (c) Compound **23**. Blue atoms are nitrogen, red are oxygen, and grey are carbon.

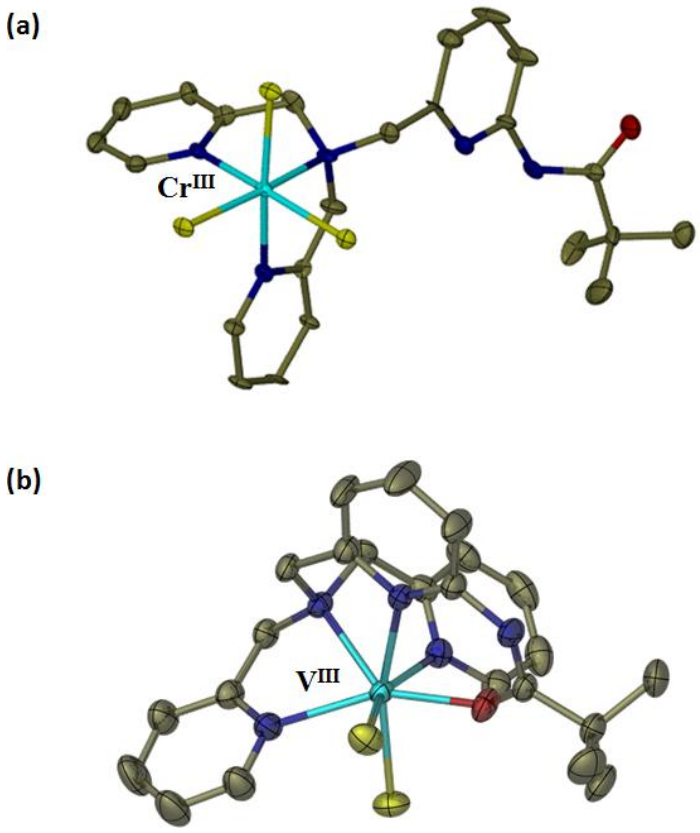

Figure 5.3. Thermal ellipsoid plots at the 50% probability level, where the hydrogen atoms have been omitted for the sake of clarity of (a) Compound **24** and (b) Compound **25**. Blue atoms are nitrogen, red are oxygen, and grey are carbon.

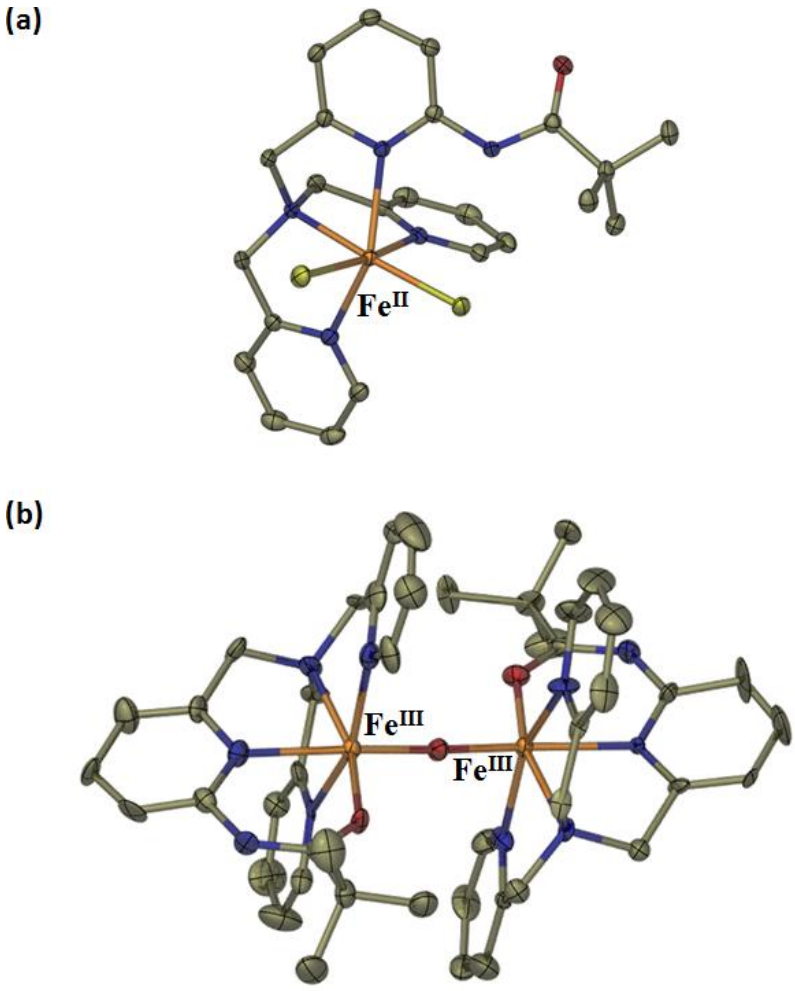

Figure 5.4. Thermal ellipsoid plots at the 50% probability level, where the hydrogen atoms have been omitted for the sake of clarity of (a) Compound **27** and (b) Compound **28**. Blue atoms are nitrogen, red are oxygen, and grey are carbon.

Overall, it can be seen that these precursors exhibit highly interesting geometries which renders them useful potential building blocks for magnetic clusters with a variety of different magnetic properties.

Electrospray Mass Spectrometry

Electrospray mass spectrometry (Appendix A) provided additional support for the assignment of the formulae obtained from the X-ray experiments. ESI-MS experiments performed on a sample of **21** dissolved in acetonitrile led to the observation of two features at *m/z* = 223 ($[(Mn(L_5)]^{2+}$) and 480 ($[Mn(L_5)Cl]^{+}$). The appearance of both features indicates that the precursor is stable in solution and, moreover, that the coordinated acetonitrile molecules in the solid form are easily labilized in solution rendering the complex a good precursor for further chemistry. Similarly, the ESI-MS experiments performed on samples of **22** and **23** dissolved in acetonitrile revealed major features at *m/z* = 467 ($[Co(L_5)F]^{+}$) and 466 ($[Ni(L_5)F]^{+}$), respectively. The coordination of fluoride is not surprising, as it is well known that the $[BF_4]^{-}$ anion can be a source of F^{-} during the ESI-MS experiment. In the mass spectra for both compounds **22** and **23**, additional features were observed that correspond to the coordination of other molecules present during the measurement (*e.g.* water, $[BF_4]^{-}$, etc.) to the $M(L_5)$ moeity indicating that the ligand remains tightly bound to the metal ion in solution.

The spectra collected for compounds **24**-**27** show major features that correspond to the loss of choride ions from the outer- and/or inner-coordination sphere of the corresponding compound. In the case of compound **24** the major feature at *m/z* = 545 ($[Cr(L_5)Cl_3\text{-}H]^{+}$) corresponds to only the loss of a hydrogen atom from the ligand

suggesting that the chloride atoms are tightly bound to the Cr^{III} ion in accord with the well known high stability of trivalent chromium complexes. For compound **26**, the major feature at *m/z* = 515 ($[Fe(L_5)Cl_2]^+$) corresponds to the loss of one choride anion, most likely the outer-sphere chloride anion, with the MPPA ligand and the coordinated chloride ion remaining bound in the gas phase. Interestingly, the major feature for compounds **25** and **27** at *m/z* = 487 and 522 respectively, correspond to species where an acetonitrile is coordinated to the metal complex, suggesting that the chloride atoms are being replaced for solvent molecules in the gas phase.

Overall, the ESI-MS experiments peformed on compounds **21-27** indicate that the complexes are stable in solution and as a result can be used as building blocks in further chemistry. It is important to point out that compouds **24-27** can be used in further chemistry with the coordinated choride atoms, or if desired, the precursors can be treated with $AgPF_6$ or $TlPF_6$ to remove the choride atoms and replace them with more labile ligands in order to render them useful precursors for further chemistry.

Magnetic Properties

The magnetic properties of the clusters were investigated by magnetic susceptibility measurements (Appendix A) in the temperature range of 2–300 K and field dependent magnetization measurements in applied fields up to 7 Tesla. Measurements were carried out on microcrystalline samples.

$[Mn^{II}(MPPA)(MeCN)_2][ClO_4]_2$ (21). For compound **21** the value of χT at 300 K is 4.46 emu·K·mol^{-1}, which corresponds well to the value of 4.37 emu·K·mol^{-1} expected for an

isolated Mn^{II} ion (S = 5/2, g = 2.08). The slight deviation from the isotropic value is consistent with the deviation of the geometry of the compound from an octahedral symmetry resulting from a hepta-coordinate Mn^{II} ion. The χT value is essentially constant over the entire temperature range from 300 to 2 K (Figure 5.5). The Brillouin function calculated for S = 5/2 and g = 2.08 fits well with the experimental data obtained by the measurement of the field-dependent magnetization at 1.8 K (Figure 5.5, inset).

$[Co^{II}(MPPA)][BF_4]_2$ (22). A χT value of 2.34 emu·K mol^{-1} was observed at 300 K which is much higher than the isotropic spin-only value (1.87 emu·K mol^{-1}) expected for three unpaired electrons; Figure 5.6). This is easily understood by the fact that there are significant orbital contributions from the HS Co^{II} (S = 3/2) center. Magnetism of Co(II) complexes is a challenging topic because the orbital angular momentum causes difficulties in the magnetic analysis.[16, 17] In general, the orbital angular momentum is totally or partially quenched in a ligand field of a certain symmetry.[226] As a result, the effect of the orbital angular momentum is highly dependent on the symmetry around the metal ion. The magnetism of HS Co^{II} complexes of a TBP symmetry can be classified into two categories: (1) in a normal TBP symmetry, the ground term does not have an orbital angular momentum, thus a spin-only treatment is valid for them; (2) in a highly distorted lower symmetrical case, the ground term possesses an orbital angular momentum due to the admixture with higher states, thus a spin–orbit coupling treatment is valid for them.[16] For compound **22** the treatment of the magnetic data based on a distorted TBP is consistent with the structure determined. The χT value of 2.34 emu·K mol^{-1} observed at 300 K corresponds well for a Co^{II} ion under the strong influence of

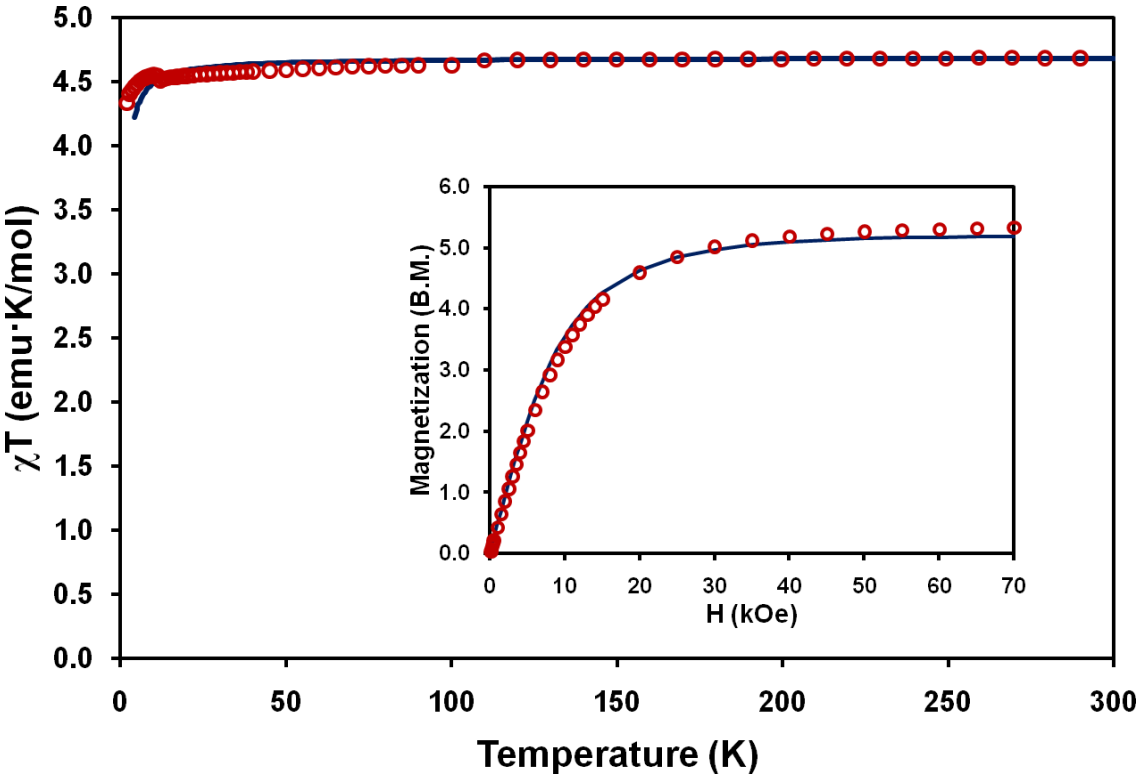

Figure 5.5. Temperature dependence of χT for **21** (**O**). The solid line correspond to the MAGPACK simulation (g_{Mn} = 2.08, zJ = -0.5 cm^{-1}). Inset: Field dependent magnetization: The solid line corresponds to the best fit to the Brillouin function (S = 5/2, g_{avg} = 2.08).

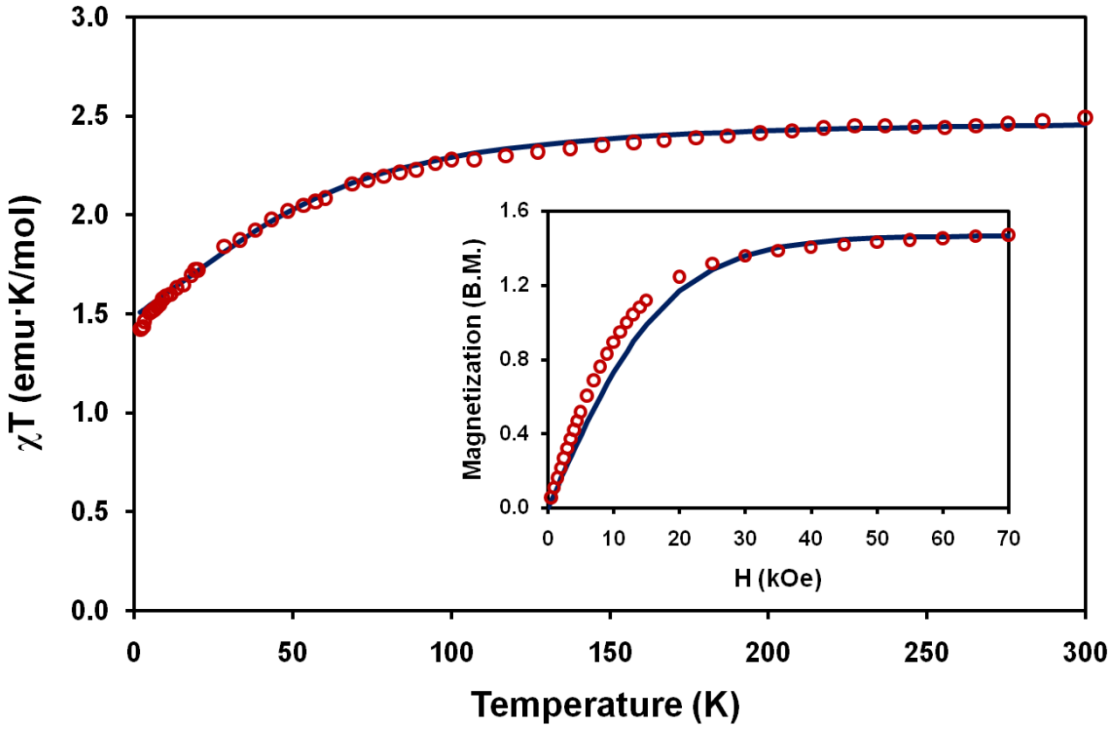

Figure 5.6. Temperature dependence of χT for **22** (**O**). The solid line correspond to the fitting with the best fit parameters of g_{Co} = 2.3, D = 58 cm^{-1}). Inset: Field dependent magnetization: The solid line corresponds to the best fit to the Brillouin function (S' = 1/2, g_{avg} = 2.3).

spin–orbital coupling (g =2.3).[17] Therefore, as the temperature is lowered, the χT value decreases as a result of the depopulation of the excited states and reaches a minimum of 1.42 emu·K mol^{-1} at 2 K. If one considers that the main contribution to the decrease of the magnetic moment is due to ZFS effects, the following expressions for the magnetic susceptibility for S = 3/2 are applicable:

$$\chi_{\parallel} = \frac{Ng^2\mu_B^2}{k_B T}\frac{1 + 9e^{-2x}}{4(1 + e^{-2x})} \qquad \text{(Eq. 5.1)}$$

$$\chi_{\perp} = \frac{Ng^2\mu_B^2}{k_B T}\frac{4 + \frac{3}{x}(1 - e^{-2x})}{4(1 + e^{-2x})} \qquad \text{(Eq. 5.2)}$$

where x is $D/(k_B T)$ and D is the magnitude of the ZFS. The average molar magnetic susceptibility for a powder sample is given by the well-known relationship:

$$\langle\chi\rangle = \frac{\chi_{\parallel} + 2\chi_{\perp}}{3} \qquad \text{(Eq. 5.3)}$$

The best agreement between model and experiment was obtained using Eq. 5.3 and the best fit parameters g = 2.3 and D = 58 cm^{-1}. At low temperatures, the Co^{II} ion behaves as an effective S' = 1/2 center. Field-dependent magnetization data collected at 1.8 K were fitted to the Brillouin function for a Co^{II} center with effective S' = 1/2 (Figure 5.6, inset).

[Ni^{II}(MPPA)(MeCN)][BF$_4$]$_2$ (23). The room-temperature χT value for **23** is 1.24 emu·K·mol^{-1}, which is slightly higher than the expected spin-only value of 1.00 emu·K·mol^{-1} for two unpaired electrons (S=1) as expected for an orbital contribution. The value of χT remains constant over the entire temperature interval (Figure 5.7). The temperature dependence of the magnetic susceptibility was modeled using Eq. 5.4 (g =

2.23 , D = 3.5 cm^{-1}) given that the main contribution to the decrease of the magnetic moment at low temperatures is due to ZFS effects.

$$\langle \chi \rangle = \frac{2Ng^2\mu_B^2}{3k_BT}\left[\frac{\frac{2}{x} - \frac{2e^{-x}}{x} + e^{-x}}{1 + 2e^{-x}}\right] \qquad \text{(Eq. 5.4)}$$

A fitting of the field-dependent magnetization data measured at 1.8 K using MAGPAK[196] resulted in the best fit parameters S = 1, g_{avg} = 2.23, and D_{Ni} = 3.35 cm^{-1} typically observed for Ni^{II} complexes (Figure 5.7, inset).

Cr^{III}(MPPA)Cl$_3$ (24). For compound **24** the value of χT at 300 K is 1.84 emu·K·mol^{-1}, which corresponds well to the value of 1.87 emu·K·mol^{-1} expected for an isolated Cr^{III} ion (S = 3/2, g = 2.0). The χT value is essentially constant over the entire temperature range from 300 to 2 K (Figure 5.8), with a slight decrease at low temperatures due to zero field splitting (D = 1.5 cm^{-1}). The χT vs. T data was modeled using Eq 5.3 where $\chi_\parallel$is defined by Eq. 5.1 and $\chi_\perp$ is defined by Eq. 5.5 where x is $D/(k_BT)$ and D is the magnitude of the ZFS.

$$\chi_\perp = Ng^2\mu_B^2\left[\frac{1}{k_BT(1 + e^{-2x})} + \frac{3\tanh x}{4k_BTx}\right] \qquad \text{(Eq. 5.5)}$$

An examination of the ground states for **24** was carried out by field-dependent magnetization measurements at 1.8 K. The data are in excellent agreement with the Brillouin function for an S = 3/2 ion (Figure 5.8).

[V^{III}(MPPA)Cl$_2$]Cl (25). A χT value of 0.91 emu·K·mol^{-1} was observed at 300 K which is lower than the isotropic spin-only value (1.00 emu·K mol^{-1}) expected for a V^{III} ion (S = 1); Figure 5.9), but matches well if one takes into account the anisotropic g value

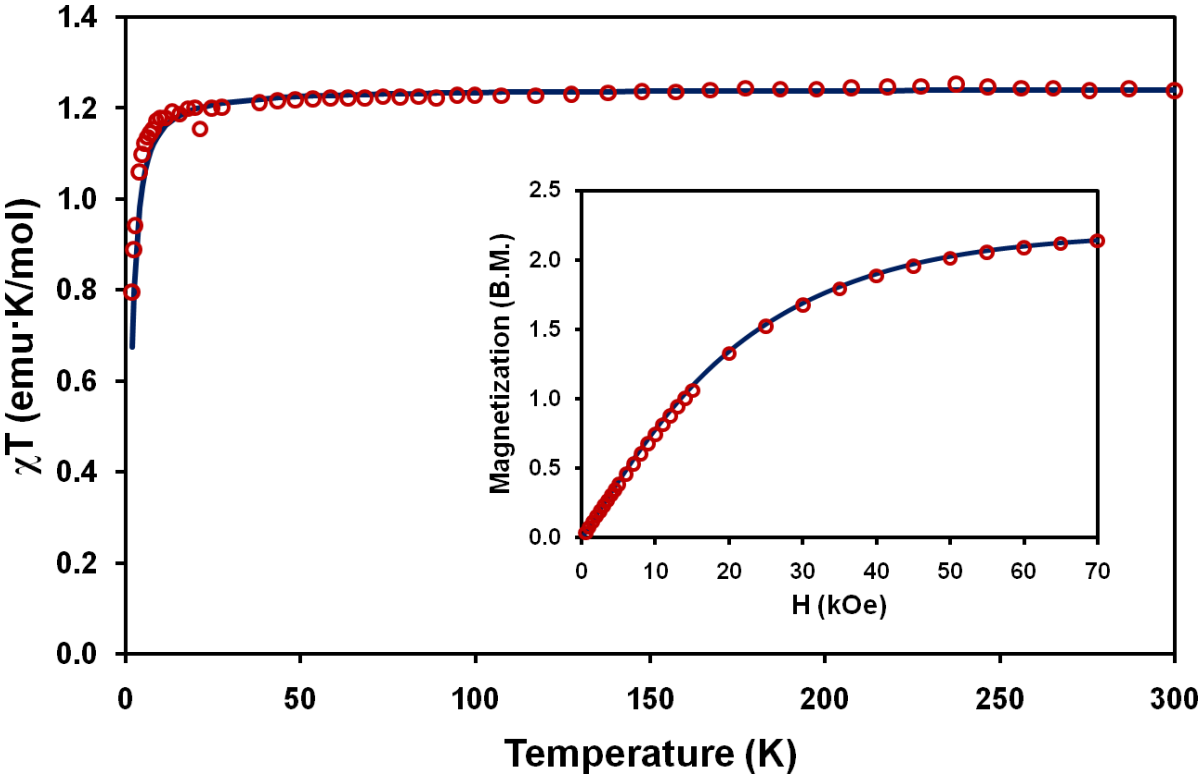

Figure 5.7. Temperature dependence of χT product for **23** (**O**). The solid line correspond to the fitting with the best fit parameters of g_{Ni} = 2.23, D = 3.5 cm^{-1}, zJ′ = -0.5 cm^{-1}). Inset: Field dependent magnetization: The solid line corresponds to the MAGPACK simulation (*S* = 1, g_{avg} = 2.23, D = 3.5 cm^{-1}, zJ′ = -0.5 cm^{-1}).

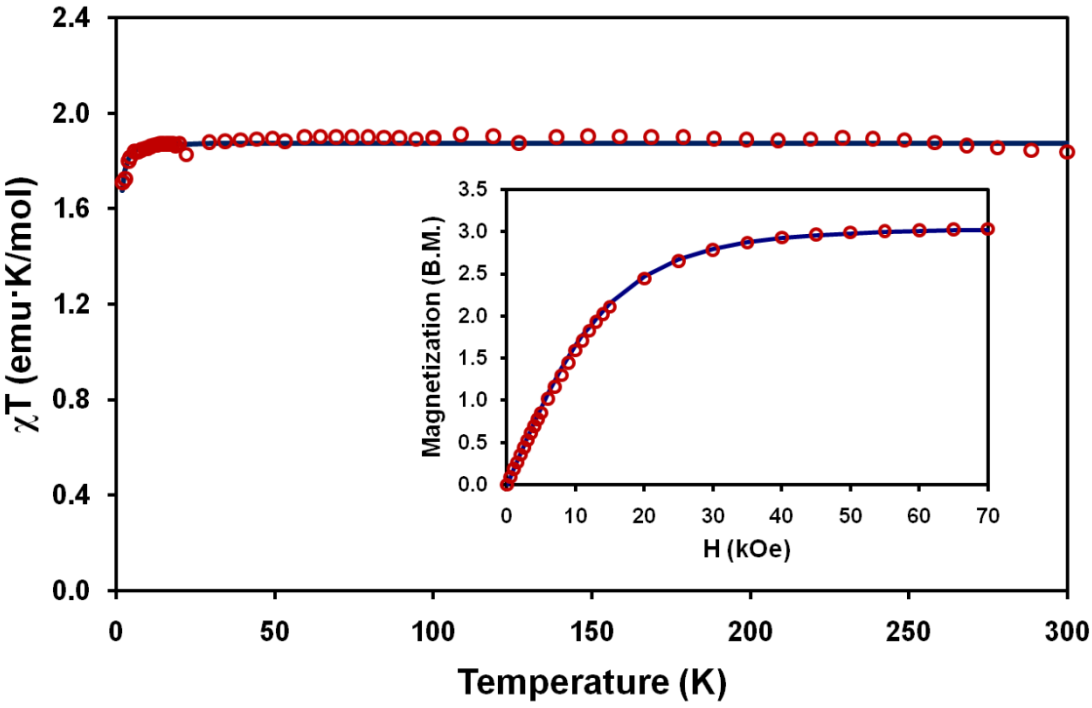

Figure 5.8. Temperature dependence of χT product for **24** (**O**). The solid line correspond to the fitting with the best fit parameters of g_{Ni} = 2.0, D = 1.5 cm^{-1}). Inset: Field dependent magnetization: The solid line corresponds to the best fit to the Brillouin function (S = 3/2, g_{avg} = 2.0).

expected for V^{III} (g = 1.92) into Eq 5.1-5.3.[17] The χT value is essentially constant over the entire temperature range from 300 to 2 K , with a slight decrease at low temperatures due to zero field splitting (D = 1.5 cm^{-1}). Field-dependent magnetization data collected at 1.8 K were fitted to the Brillouin function for a V^{III} center with effective S = 1 and g = 1.92 (Figure 5.9, inset).

$[Fe^{III}(MPPA)Cl_2]Cl$ (26). For compound **26** the value of χT at 300 K is 4.31 emu·K·mol^{-1}, which corresponds well to the value of 4.37 emu·K·mol^{-1} expected for an isolated high spin Fe^{III} ion (S = 5/2). The χT value is essentially constant over the entire temperature range from 300 to 2 K (Figure 5.10), with a decrease at low temperatures due to zero field splitting (D = 3.0 cm^{-1}) and weak intermolecular interactions (zJ = -0.15 cm^{-1}). A simulation of the temperature-dependent magnetic susceptibility and the field-dependent magnetization data measured at 1.8 K using MAGPAK[196] resulted in the best-fit parameters S = 5/2, g_{avg} = 2.05, and D_{Fe} = 3.00 cm^{-1} typically observed for Fe^{III} complexes (Figure 5.10, inset).

$Fe^{II}(MPPA)Cl_2$ (27). Compound **27** exhibits a value of χT = 3.52 emu·mol^{-1}·K at 300 K, higher than the isotropic spin-only value expected for a high-spin S = 2 Fe^{II} ion (3.00 emu·mol^{-1}·K). Such a deviation is mainly due to the significant anisotropy introduced by the HS Fe^{II} ion. The susceptibility value remains constant as the temperature is lowered to 50 K (Figure 5.11). The sharp decrease in the susceptibility at very low temperatures modeling of the magnetic properties using MAGPAK[196] resulted in the best fit parameters of S = 2, g_{avg} = 2.15, and D = 12 cm^{-1}. The field-dependent magnetization

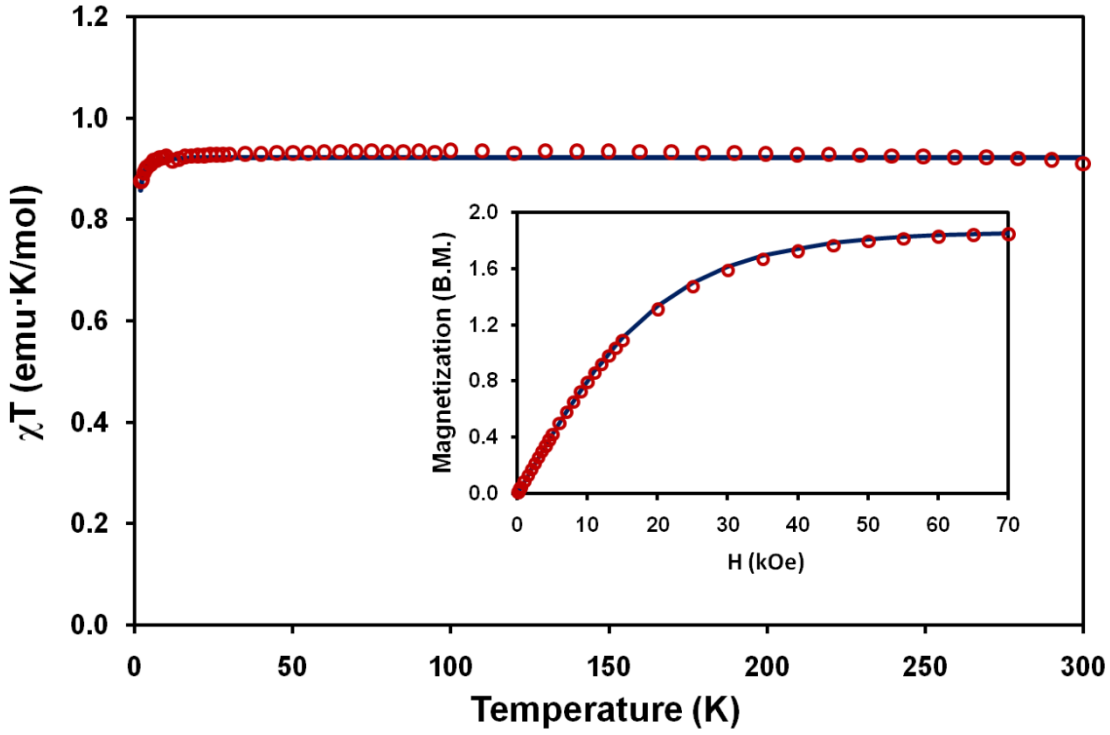

Figure 5.9. Temperature dependence of χT for **25 (O)**. The solid line correspond to the fitting with the best fit parameters of g_V = 1.92, D = 1.5 cm^{-1}). Inset: Field dependent magnetization: The solid line corresponds to the best fit to the Brillouin function (S = 1, g_{avg} = 1.92).

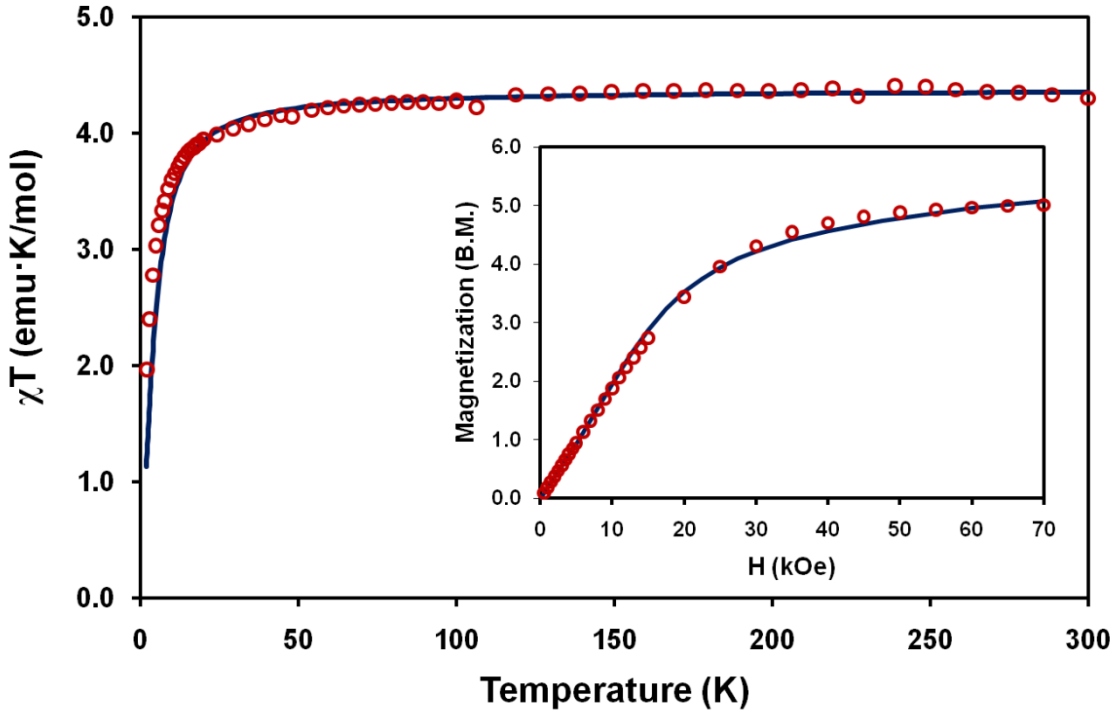

Figure 5.10. Temperature dependence of χT for **26 (O)**. The solid line correspond to the MAGPACK simulation (g_{Fe} = 2.05, D_{Fe} = 3.0 cm^{-1}, zJ = -0.15 cm^{-1}). Inset: Field dependent magnetization: The solid line corresponds to the MAGPACK simulation (S = 5/2, g_{avg} = 2.05).

{(Fe^{III}(MPPA)$_2$(μ-O)l[BF_4]$_4$ (28). The room-temperature χT value for **28** is 0.81 emu·K·mol^{-1} and it rapidly decreases as the temperature is lowered until it reaches a diamagnetic ground state at ~ 50 K indicative of strong antiferromagnetic coupling between the Fe^{III} centers (Figure 5.12). The magnetic properties were modeled taking into account the effect of intracluster superexchange using the HDVV Hamiltonian (H = -2J·S_1·S_2). The simulation obtained using MAGPACK[196] resulted in best fit parameters of S = 3/2, g_{avg} = 2, and $J_{Fe\text{-}Fe}$ = -107 cm^{-1} confirming the antiferromagnetic coupling between the Fe^{III} centers. Moreover, in order to confirm that the electronic configuration of the Fe^{III} ions was high spin (S = 3/2), attempts were made to simulate the experimental data using S = 1/2 (spin state for LS Fe^{III}) and a variety of g values (Figure 5.12) which failed to reproduce the experimental data confirming that the Fe^{III} centers are present in a high spin configuration.

CONCLUSIONS

The results presented in this chapter support the conclusion that we have in hand new versatile magnetic building blocks in our toolkit based on the fact that the MPPA ligand can form mononuclear complexes with a variety of transition metal ions in both the divalent and trivalent oxidation states. One of the most useful observations vis-à-vis the magnetic properties of these complexes is the fact that they are all in a high spin configuration indicating that the MPPA ligand does not promote a strong ligand field environment around the metal ion. This fact renders these building blocks highly useful as capping groups for the preparation of higher nuclearity clusters for which there is a

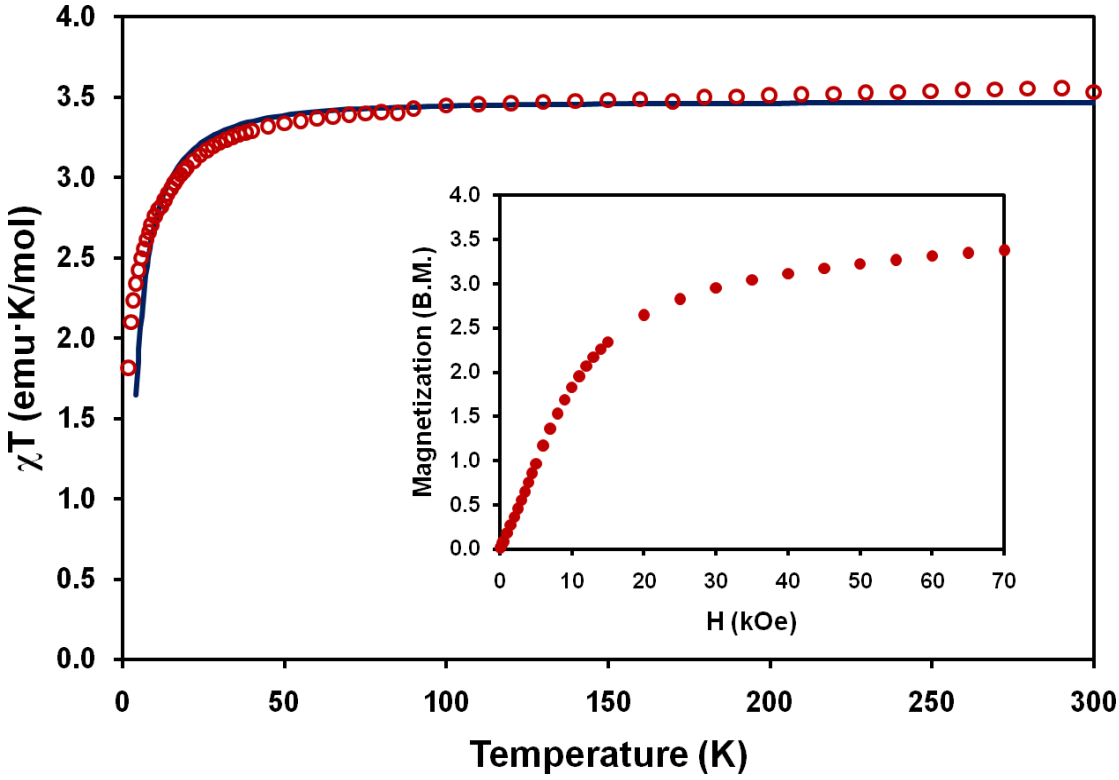

Figure 5.11. Temperature dependence of χT for **27** (**O**). The solid line corresponds to the MAGPACK simulation (S = 2, g_{Fe} = 2.15, D_{Fe} = 12.0 cm^{-1}). Inset: Field dependent magnetization data collected a 1.8 K.

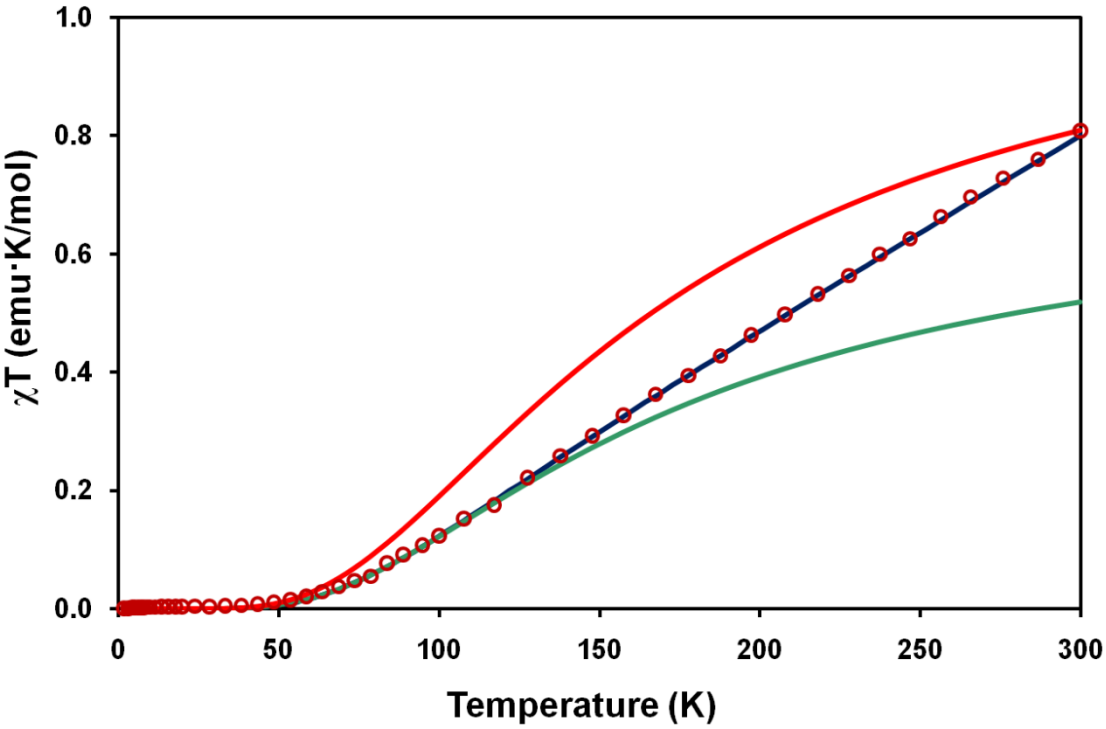

Figure 5.12. Temperature dependence of χT for **28** (**O**). The solid blue line correspond to the MAGPACK simulation (g_{Fe} = 2.0, J = -107 cm^{-1}). The red and green solid lines correspond to the MAGPACK simulation with S = ½, g = 2 and g=2.5 respectively.

desire to increase the overall ground state spin value of the clusters. While this ability is foreseen to be quite useful, they are, in fact, most ideally suited for the preparation of model compounds, such as dimers and trimers, that will be highly useful for the development of theoretical models. The ability of the "M(MPPA)" units to become connected is evidenced by the serendipitous isolation of the oxo bridged dimer, $\{(Fe^{III}(MPPA)_2(\mu\text{-}O)\}^{4+}$. The linear binding of the oxygen atom leads to an orbital overlap favoring very strong antiferromagnetic coupling ~107 cm^{-1}. Future directions of this work will involve the use of these building blocks in the synthesis of cyanide and organocyanide bridged discrete mixed-metal magnetic molecules.

CHAPTER VI

SUMMARY AND OUTLOOK

The study of molecule-based magnets is a burgeoning area of chemistry that focuses on the preparation of materials using molecular building blocks. The aim is to obtain architectures with specific physical properties owing to a judicious choice of the molecular precursor(s).[1-4] The resulting materials offer numerous potential advantages over conventional solid state materials, *e.g.*, lower density, higher solubility, lower temperature assembly, and mechanical flexibility.[5-7] These characteristics are complemented by the ability to obtain molecules whose properties are governed by the nanoscale size regime which renders them attractive for a variety of technological applications.[3, 8-10]

The underlying principle for the use of molecules or molecular assemblies in information processing or storage is *molecular bistability* which is the ability to exhibit two stable states under the influence of an external stimulus (*e.g.* temperature, light, pressure, field, etc.).[56, 57] The work in this dissertation has focused on the ability of cyanide bridged materials to exhibit magnetic bistability properties based on a photoinduced state or by the presence of a thermal barrier for reversing the magnetization which manifests itself in SMM or exchange biased SMM behavior.

In Chapter II, the first reported photomagnetic Prussian blue containing the hexacyanoosmate(III) ion was presented, which is only the third PB analog reported to date to exhibit this behavior. In addition to this exciting magnetic phenomenon, gas

uptake studies were also performed, revealing a hydrogen gas uptake of 0.6% at the limit of the instrument which is not the actual saturation value for the storage capacity. A detailed study incorporating alkali metal ions led to the discovery of both photomagnetic and temperature induced excited state spin trapping for these materials, properties that vary greatly according to the alkali metal in the framework. The largest response was observed for the K^+ analog for which the excited state exhibits a T_C of 27.5 K, the highest observed for a Prussian blue analog incorporating a 4*d* or 5*d* hexacyanometallate. The complex electronic states of this material would make it an excellent candidate for advanced spectroscopy techniques such EXAFS and XANES in order to ascertain the ratios of the oxidation states of the metal ions in the materials, which will greatly enhance the understanding of the redox properties between 5*d* and 3*d* metal ions. This chemistry can also be expanded to the preparation of the PB analogs that incorporate the $[Ru(CN)_6]^{3-}$ with the Co^{II} ion in order to complete the Group 8 series. The "RuCo PB" analogs if obtained will allow for a better understanding of the how a 4*d* versus a 5*d* metal ion affects the magnetic properties of the PB materials. In addition, studies involving the ratios of the alkali metal as well as the solvent dependence of the magnetic properties of the Co/Os PB could be performed.

As previously mentioned, certain Prussian blue analogs exhibit a property known as cyanide linkage isomerism where the CN ligand can change its binding mode between the metal centers. The research in Chapter III focuses on the use of the building block $[Co(dppe)(MeCN)]^+$ for the synthesis of trinuclear complexes based on the first row hexacyanometallates, $[Fe^{III}(CN)_6]^{3-}$, $[Co^{III}(CN)_6]^{3-}$ and $[Cr^{III}(CN)_6]^{3-}$. While the reaction

with the hexacyanometallates of Fe^{III} and Co^{III} formed the predicted linear cyanide bridged molecules, the reaction with Cr^{III} resulted in the formation of $[Co(dppe)CN]^{+}$ as the major product. The systematic study by a combination of X-ray crystallography and solution IR spectroscopy and the fortuitous isolation of a short lived intermediate trigonal bipyramidal cluster provided valuable insight into the mechanism of cyanide linkage isomerism and liability of the $[Cr(CN)_6]^{3-}$ ion in the presence of Lewis acids, a topic of considerable importance in the area of cyanide chemistry.

Moreover, in the field of molecular magnetism there is a lack of detailed understanding of how single ion anisotropy and anisotropic exchange interactions affect the magnetic properties of molecular magnets. This behavior is often complex and difficult to model with current methodologies but small molecules would provide a feasible target. From a synthetic standpoint, the synthesis of linear trinuclear complexes represents an excellent small molecule system to help develop theoretical magnetic models. Previous work on the study of the $\{[Mn^{III}(salen)(solv)]_2[Fe^{III}(CN)_6]\}^{-}$ trimers helped to elucidate some of this behavior, where the anisotropy due to unquenched orbital angular momentum of the $[Fe^{III}(CN)_6]^{3-}$ center was adequately modeled.[204] Chapter IV focuses on the preparation of a trimer of $[PPN]\{[Mn^{III}(salphen)(solv)]_2[Os^{III}(CN)_6]\}$, which is the first trinuclear molecule that contains the $[Os^{III}(CN)_6]^{3-}$ anion. This compound exhibits SMM behavior, with a T_B of 3.0 K at 1.5 kHz one of the highest for a cyanide based SMM, but even more interesting, however, is the observation of the magnetic phenomenon known as exchange biased SMM behavior which actually increases the observed blocking temperature to 4.3 K at

1.5 kHz. What makes this system unique is that the same crystals can exhibit one property or the other based on the solvent conditions; a lack of solvent increases intermolecular interactions sufficiently to engender exchange biased SMM behavior but incorporation of methanol decreases the intermolecular interactions which leads to isolated SMM behavior. An additional structural feature of this material is in the nature of the packing, due to the inclusion of the PPN cation, forming layers of trinuclear clusters sandwiched between layers of PPN cations. The PPN{[Mn^{III}(salphen)(solv)]$_2$[Fe^{III}(CN)$_6$]} trimer was also prepared, which was determined to only exhibit SMM behavior, however the PPN cation does engender a similiar blocking temperature of 2.3 K in agreement with that reported for a similar congener with a T_B of 2.4 K.[205] These intriguing properties warrant further study on the reversibility of this behavior in the Os trimers, as well as further detailed microSQUID experiments with the continued collaboration of Dr. Wolfgang Wernsdorfer who initially identified the SMM and exchange biased SMM behavior in this material.

Chapter IV clearly shows the ability of trinuclear systems to exhibit slow relaxation of the magnetization, which will be of great importance not only in studying the properties of the complexes, but for theoreticians seeking to model this complex magnetic behavior. The [Mn^{III}(salen-type)(solv)]$^+$ are useful building blocks, but it is limited in the formation of new trimers with other transition metals coordinated to the salen-type ligand. The work represented in Chapter V focuses on the synthesis of a pentadentate ligand, MPPA, and subsequent formation of transition metal building blocks for the synthesis of new small molecule model compounds. The MPPA ligand

has proven versatile, binding to a variety of transition metal ions in both the divalent and trivalent state. This work will be an excellent toolkit for the magneto-chemist seeking to use these as molecular building blocks for new magnetic materials.

One of the initial goals of the field of molecular magnetism was to deliberately engender a desired magnetic property in the final product by the judicious choice of the ligands and the metal ions used. The results presented in this dissertation, overall, indicate that the building block approach is an appropriate path to this endeavor. The deliberate mixture of Os^{III} and Co^{II} in a 3D network led to the desired photomagnetic material and the combination of anisotropic ions such as Os^{III} and Mn^{III} in an anisotropic geometry (e.g. linear) resulted in the sought after nanomagnet. Future work in the field will allow for further understanding of the "right conditions" that engender the desired magnetic properties with the ultimate goal of attaining technologically applicable magnetic materials.

Research in molecular magnetism revolves around the two main classes of materials presented in this dissertation, viz., multifunctional magnetic materials and molecular nanomagnets. An extensive class of multifunctional magnetic materials falls into the category of photomagnetic materials, such as the CoOs PB analogs presented in Chapter II. On the other hand, the topic of molecular nanomagnets/SMMs has been vital for the field. These molecular materials exhibit slow paramagnetic relaxation of the magnetization at low temperatures and display magnetic hysteresis analogous to that observed in bulk magnets. Even more fascinating is the fact that they show evidence of quantum effects such as the quantum tunneling observed for the

PPN{[Mn^{III}(salphen)(solv)]$_2$[Os^{III}(CN)$_6$]} trimer, rendering this type of molecules useful as potential *qubits* . There are two challenging goals in this area, namely, to raise the operating temperatures at which these phenomena occur and to prepare the materials as organized thin films and multilayers for possible applications.

Moreover, immense and virtually unexplored possibilities exist for molecular nanomagnets in spintronics. Until recently, *spintronics* has been almost exclusively the realm of conventional inorganic metals and semiconductors. Spintornics is a subfield of molecular electronics, and the latter emerged several decades ago as a new approach for replacing conventional inorganic electronics. In this context, a natural evolution of molecular electronics is that of using magnetic molecules as well as molecule-based magnetic materials as components for new spintronic devices. The area of single-molecule spintronics until recently has almost entirely focused on theoretical proposals and speculations. Very few examples of electron transport properties through SMMs and other magnetic molecules have been reported thus far.[13] These measurements are at the very early stage, and many problems, which are intrinsic to the molecules (such as their chemical stabilities when they are deposited on a metallic surface) and to the control of the positioning of the molecules need to be solved to obtain reliable results.

In this vein, our group is currently in collaboration with the Teizer group in the Physics department at Texas A&M. Studies have been undertaken to grow nanoscale layers of the Co-Os Prussian blue in order to study their magnetic and electron transport properties on gold surfaces (Figure 6.1).

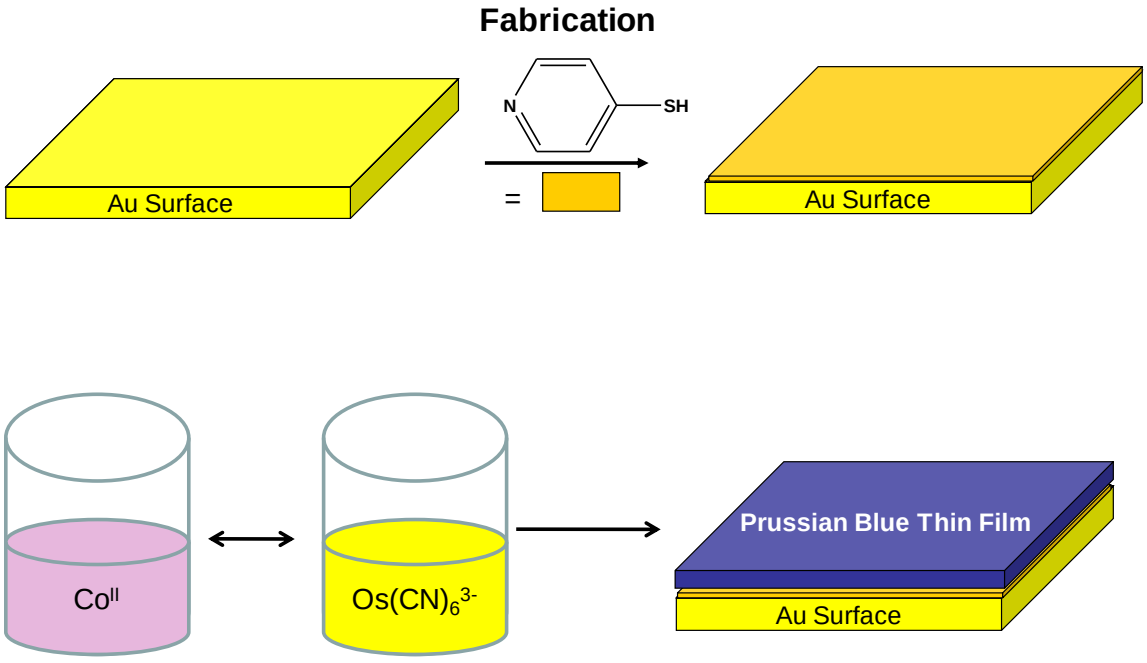

Figure 6.1. Sequential dipping methods were used to prepare thin films of the CoOs PB on a gold surface.

As described above, the synthesis of new polynuclear coordination compounds with unusual magnetic properties is one of the main goals in the field of molecular magnetism, and it is relatively safe to state that the pursuit of this goal typically revolves around the use of small bridging ligands such as oxide, cyanide, azide *etc*., which provide a short exchange pathway for coupling between metal spins. Nevertheless, some of the most promising coordination compounds in the field of molecular magnetism involve transition metal ions bridged by expanded ligands such as TCNE (tetracyanoethylene), TCNQ (7,7,8,8-tetracyanoquinodimethane) and, DCNQI (N,N'-dicyanoquinonediimine) into covalent networks.[52, 227-229] With the proper energy match of metal and organic orbitals it may be possible to achieve interplay between superexchange and charge-transport pathways, perhaps leading to a synergistic state wherein conductivity and magnetism co-exist.

At the very least it appears that the strategy of transition metal ions bridged by organocyanide ligands holds promise for the design of highly conducting metal-organic polymers, as evidenced by the work of Hünig and co-workers, who synthesized crystalline network charge-transfer solids of stoichiometry $Cu(DCNQI)_2$ that exhibit metallic properties that persist to very low temperatures (5K).[230, 231] With this in mind, the work in Chapter VII focuses on the use of the organocyanide ligand, TCNQ in combination with the main group Tl^I ion, in the formation of a new semiconducting binary phase, the first conducting main group binary TCNQ material.

In addition to studying binary phases which are the subject of high interest due to their promise as magnets and conductors, efforts should be expanded to include SMMs

co-crystallized with or connected by organocyanide ligands. The design of multifunctional materials is one of the most attractive and challenging goals in the field of molecular materials science and as a result the synthesis of molecular materials where conductivity and magnetism co-exist synergistically is a worthwhile endeavour.

CHAPTER VII

MAIN GROUP TCNQ CHEMISTRY: SYNTHESES AND PROPERTIES OF TWO POLYMORPHS OF THE Tl(TCNQ) BINARY MATERIAL*

INTRODUCTION

A great deal of current scientific research is being directed at the synthesis and fabrication of nanoscale materials for new types of electronic and magnetic devices. Pressure to reduce the size and improve response times of electronic components has always existed in information technology, but as we approach the miniaturization limits of traditional charge storage estimated to occur by 2016[11] the global quest for faster and more efficient data storage and processing is heightening.[232] One strategy that is being explored for the development of new device components is the pursuit of materials whose bistability is induced by a resistance change rather than current flow. Such "non-volatile" memory devices are capable of operating at increased speeds with less energy expenditure.

Materials that respond to the application of an electric field, light, pressure, or temperature could find use in electronic devices with ultra-fast operating speeds.[75, 146] For example, spincrossover complexes such as {Fe(picolylamine)$_3$Cl$_2$(C_2H_5OH)},[233, 234] neutral-ionic transition systems represented by {TTF-Chloranil}[235-237] (TTF =

---

* Portions of this chapter were taken from Avendano, C.; Zhang, Z.; Ota, A.; Bhuvanesh, N.; Zhao, H.; Dunbar, K. R. *Angew. Chem. Int. Ed.* **2010**, submitted with the permission of the Wiley-VCH publisher.

tetrathiafulvalene) the metallo-organic conductor $Cu(DMDCNQI)_2$,[229, 238-243] (DM-DCNQI = Dimethyl-*N*,*N*′-Dicyanoquinonediimine) and the salt $(EDO\text{-}TTF)_2PF_6$,[244, 245] (EDO-TTF = ethylendioxy-tetrathiafulvalene) constitute significant examples of simple organic containing materials that exhibit non-linear phenomena. These materials provide compelling evidence for the contention that molecular solids may eventually be useful in device applications. In terms of electric field induced behavior, one of the most extensively studied examples is Cu(TCNQ) (TCNQ = 7,7,8,8-tetracyanoquinodimethane) which exhibits reversible switching from a high resistance state to a conducting state promoted by the application of an electric field or upon irradiation.[228, 246, 247]

Molecule-based conductors, like molecule-based magnets, offer certain advantages over traditional solid state materials including the fact that they are light-weight, they can be prepared at ambient temperatures on the bench top, and their properties can be tuned by ligand modifications. The field of organocyanide chemistry has widely contributed to this effort with compounds that exhibit non linear phenomena such as the metallo-organic conductor $Cu(DM\text{-}DCNQI)_2$[229, 238-243] and the current-driven conductor KTCNQ salt.[248] The latter belongs to a prominent family of binary TCNQ compounds, namely the series of alkali metal salts of TCNQ.[249-251] These compounds behave as so-called “Mott insulators” at high temperatures due to the fact that the fully reduced monoanions are arranged in columns with evenly spaced TCNQ units. At lower temperatures, these soft materials undergo a phase transition in which the TCNQ units are brought in close proximity and π-dimerization occurs: T_c = 348 K (Na-TCNQ),[249]

395 K (K-TCNQ),[250] and 220 K (Rb-TCNQ phase II).[251] The electrons are then trapped in the dimers, the conductivity drops off and the materials fall into the category of Peierls insulators.

We would like to take advantage of the rich chemistry of alkali metals while altering the structural issues that influence their conducting properties. The Tl^{I} ion is an interesting choice in this regard since it can behave as a pseudo-alkali metal.[252] In contrast to other group 13 elements, Tl prefers the 1+ oxidation state (although Tl^{III} is known), and many similarities between the chemistry of alkali metals and Tl have been noted.[252, 253] The electronegativity of Tl (2.04) is much higher than that of any alkali metal, which should lead to less ionic compounds with smaller band gaps and thus higher carrier mobility. Unlike alkali metals, Tl^{I} has a lone pair of electrons that can be stereoactive and may be expected to lead to an even greater diversity of structures.[254] Precedence for this chemistry was previously observed in the $Tl(DM\text{-}DCNQI)_2$[231] 3D metal-organic framework prepared by Hünig *et.al*. This compound was shown to behave as a one-dimensional metal-like semiconductor (σ_{300K} = 50 **S**cm^{-1}).

Moreover, main group-TCNQ chemistry, indeed main group supramolecular chemistry in general, is underdeveloped in spite of the maturity of research on these topics for transition metal ions.[255] Studies of metal organic frameworks (MOF's) that incorporate main group elements and organocyanide ligands are very scarce, with only a few studies reported.[256-262] Most of these studies involve components other than just the metal ion and the organocyanide ligand, and as such cannot be considered binary phases. More important, these studies lack any structural determination or they are purely

structural studies were no properties are reported. As a result, the identification of structure-property relationships in main group-organocyanide chemistry has been hampered. For example, in the case of Tl, the only compounds reported that incorporate Tl and TCNQ are $\{Tl^{I}(18\text{-crown-6})\}TCNQ$[263], $Tl^{III}(TCNQ)Cl_2$[264], and $Tl^{III}(TCNQ)_3$[264], and only the study of $\{Tl^{I}(18\text{-crown-6})\}TCNQ$ reports structural parameters, but no property-structure relationships were determined. The lack of reports and of detailed structure-property relationships exemplifies how underexplored is the area of main group-organocyanide chemistry. Moreover, synthesizing new organocyanide binary phases with the main group elements is a promising endeavor given that it can lead to compounds that exhibit interesting optical or electronic properties, such as the metal-like semiconductor $Tl^{I}(DM\text{-}DCNQI)_2$.

This chapter details the chemistry of Tl^{I} with TCNQ which led to the determination of the single crystal structure of a Tl(TCNQ) binary phase and the characterization including conductivity properties of this material and a second polymorphic phase.

EXPERIMENTAL

Syntheses

Starting materials. The $TlPF_6$ starting material (Pfaltz and Bauer) was used as received and LiTCNQ and TBATCNQ (TBA = tetrabutylammonium) were prepared as previously reported.[265] Acetonitrile and methanol were dried over 3 Å molecular sieves

and distilled prior to use. Unless stated otherwise, all compounds were prepared under anaerobic conditions.

Tl(TCNQ) Phase I (29). A dark green solution of TBATCNQ (0.321 g, 0.7 mmol) in 10 mL of acetonitrile was slowly added to a colorless solution of $TlPF_6$ (0.175 g, 0.5 mmol) in 10 mL of acetonitrile. The mixture was stirred in an inert atmosphere dry box for 20 minutes. The resulting dark purple powder was removed by filtration and washed with copious amount of acetonitrile and diethyl ether. Yield = 0.219 g (0.50 mmol), 74 %. Elemental analysis calcd. for **29** $C_{14}N_4H_4Tl$: C, 35.21; H, 0.99; N, 13.69; Found: C, 35.89; H, 0.94; N, 13.89%. IR(Nujol): ν(C≡N) 2181, 2164, 2151 and δ(C-H) 823 cm^{-1}. Single crystals of compound were grown after 1 week in a 3mm diameter sealed thin tube by slow diffusion of a methanol solution of LiTCNQ into an aqueous solution of $TlPF_6$.

Tl(TCNQ) Phase II (30). A dark blue solution of LiTCNQ (0.150 g, 0.7 mmol) in 10 mL of methanol was slowly added to a colorless solution of $TlPF_6$ (0.175 g, 0.5 mmol) in 10 mL of water. The mixture was stirred in air for 20 minutes to yield a dark purple powder which was filtered and washed with copious amount of water and diethyl ether and allowed to dry in air. Yield = 0.180 g (0.41 mmol), 82 %. Elemental analysis calcd. for **30** $C_{14}N_4H_4Tl$: C, 35.21; H, 0.99; N, 13.69; Found: C, 35.83; H, 0.98; N, 13.90%. IR(Nujol): ν(C≡N) 2180, 2149 and δ(C-H) 822 cm^{-1}.

Table 7.1. Crystal data parameters for Tl(TCNQ) Phase I.

Formula	**TlTCNQ Phase I**
Space group	$P2_1/n$ (No. 14)
Unit cell	a = 7.063(2)Å
	b = 12.381(3)Å
	c = 12.973(4)Å
	β = 98.034 (1)°
Unit cell volume, V	1124(362)Å^3
Z	4
Density, ρ_{calc}	2.415 g/cm^3
Abs. coeff., μ	14.349 mm^{-1}
Crystal color and habit	Dark purple parallel piped
Crystal size	0.25 x 0.10 x 0.10 mm
Temperature	110 K
Radiation, λ	Mo-Kα, 0.71073 Å
Min. and max. θ	2.28 to 32.05 º
Reflections collected	12222 [R_{int} =0.0261]
Independent reflections	2694
Data/parameters/restraints	2694 /154 /0
R [$F_o > 4\sigma(F_o)$]	R_1 = 0.0353
	wR_2 = 0.1015
G.o.f. on F^2	1.237
Max./min. residual densities, e·Å^{-3}	2.82,-2.41

Table 7.2. Bond distances and angles for Tl(TCNQ) Phase I.

Bond Distances (Å)			**Bond Angle**			
Tl1	N3	2.7(2)	N3	Tl1	N4	76(8)
Tl1	N4	2.7(2)	N3	Tl1	N6	157.5(13)
Tl1	N6	2.7(3)	N4	Tl1	N6	124(6)
Tl1	N5	2.82(16)	N3	Tl1	N5	83(8)
Tl1	Tl1	3.5(10)	N4	Tl1	N5	157.4(17)
Tl1	Tl1	3.6(10)	N6	Tl1	N5	78(6)
C2	C22	1.30(10)	N3	Tl1	Tl1	115(6)
C2	C6	1.5(2)	N4	Tl1	Tl1	120(6)
C6	C10	1.36(11)	N6	Tl1	Tl1	66(6)
C6	C7	1.45(7)	N5	Tl1	Tl1	62(5)
C7	C13	1.31(11)	N3	Tl1	Tl1	60(5)
C11	N3	1.20(16)	N4	Tl1	Tl1	60(6)
C11	C15	1.5(2)	N6	Tl1	Tl1	118(5)
C12	N4	1.18(4)	N5	Tl1	Tl1	116(6)
C12	C15	1.44(6)	Tl1	Tl1	Tl1	175.0(14)
C13	C9	1.5(2)	C22	C2	C6	119(7)
C15	C9	1.36(11)	C10	C6	C7	118(6)
C22	C9	1.46(7)	C10	C6	C2	120(7)
N3	Tl1	2.7(2)	C7	C6	C2	122(3)
N4	Tl1	2.7(2)	C13	C7	C6	119(6)
N5	C1	1.17(6)	N3	C11	C15	179.5(6)
N5	Tl1	2.82(16)	N4	C12	C15	179.1(6)
N6	C8	1.18(16)	C7	C13	C9	119(7)
C1	C10	1.46(8)	C9	C15	C12	120(6)
C8	C10	1.4(2)	C9	C15	C11	120(7)
			C12	C15	C11	119(2)
			C2	C22	C9	118(6)
			C11	N3	Tl1	125(10)
			C12	N4	Tl1	122(10)
			C1	N5	Tl1	128(10)
			C8	N6	Tl1	141(10)
			N5	C1	C10	178.9(7)
			N6	C8	C10	179.1(6)
			C15	C9	C22	119(6)
			C15	C9	C13	119(7)
			C22	C9	C13	122(3)
			C6	C10	C8	120(7)
			C6	C10	C1	119(6)
			C8	C10	C1	121(2)

Single Crystal X-ray Diffraction

In a typical experiment, the crystal selected for study was suspended in polybutene oil (Aldrich) and mounted on a cryoloop which was placed in a N_2 cold stream. Single-crystal X-ray data were collected on a Bruker APEX diffractometer equipped with a CCD detector at 110 K. The data sets were recorded as three ω scans of 606 frames each, at a 0.3° step width, and integrated with the Bruker SAINT[187] software package. An absorption correction (SADABS[188]) was based on fitting a function to the empirical transmission surface as sampled by multiple equivalent measurements. Solution and refinement of the crystal structure was carried out using the SHELX[189] suite of programs and the graphical interface X-SEED.[190] Structure solution by direct methods resolved positions of all metal and most of the C and N atoms. The remaining non-hydrogen atoms were located by alternating cycles of least-squares refinements and difference Fourier maps. Hydrogen atoms were placed at calculated positions. The final refinement was performed with anisotropic thermal parameters for all non-hydrogen atoms. A summary of pertinent information relating to unit cell parameters, data collection, and refinements is provided in Table 7.1. Selected metal–ligand bond distances are provided in Table 7.2.

RESULTS AND DISCUSSION

Syntheses

The synthetic method used for the preparation of the MOFs Tl(TCNQ) I (**29**) and Tl(TCNQ) II (**30**) follows a convenient strategy of using a salt that contains the already

reduced $TCNQ^{\bullet-}$ moiety, such as LiTCNQ or TBATCNQ which, in reactions with metal ions, typically leads to the isolation of metal-organic frameworks. [247, 266-270] The initial bulk reaction of a methanolic solution of LiTCNQ and an aqueous solution of $TlPF_6$ led to the isolation of a purple powder which was characterized by powder X-ray diffraction, IR spectroscopy and elemental analysis and determined to be the material Tl(TCNQ). In order to grow single crystals of this compound the methanolic solution of LiTCNQ was layered over an aqueous solution of $TlPF_6$ in a 3mm diameter thin tube using a buffer layer of MeOH or EtOH. A comparison of the X-ray powder diffraction pattern of the initial powder prepared from the bulk reaction with the simulated powder pattern of the single crystal (Figure. 7.1) revealed that the metal organic framework Tl(TCNQ) exhibits polymorphism.

Powder X-ray Diffraction Studies

The most convincing evidence that two distinctly different forms of Tl(TCNQ) exist can be found in the diffraction studies of microcrystalline samples prepared by the bulk solution routes. The initial synthetic conditions led to the isolation of a pure sample of Tl(TCNQ) II (**30**) (Figure. 7.1), therefore variations in the reaction conditions (time, temperature, or solvent) were necessary in order to obtain a pure bulk sample of the Tl(TCNQ) I (**29**) polymorph. As can be seen in Figure 7.1 the most dramatic feature in the powder patterns of both polymorphs is the first peak found at low angles; the lack of or the presence of these features in the powder patterns collected for each sample prepared for this study was used to determine the purity of each sample.

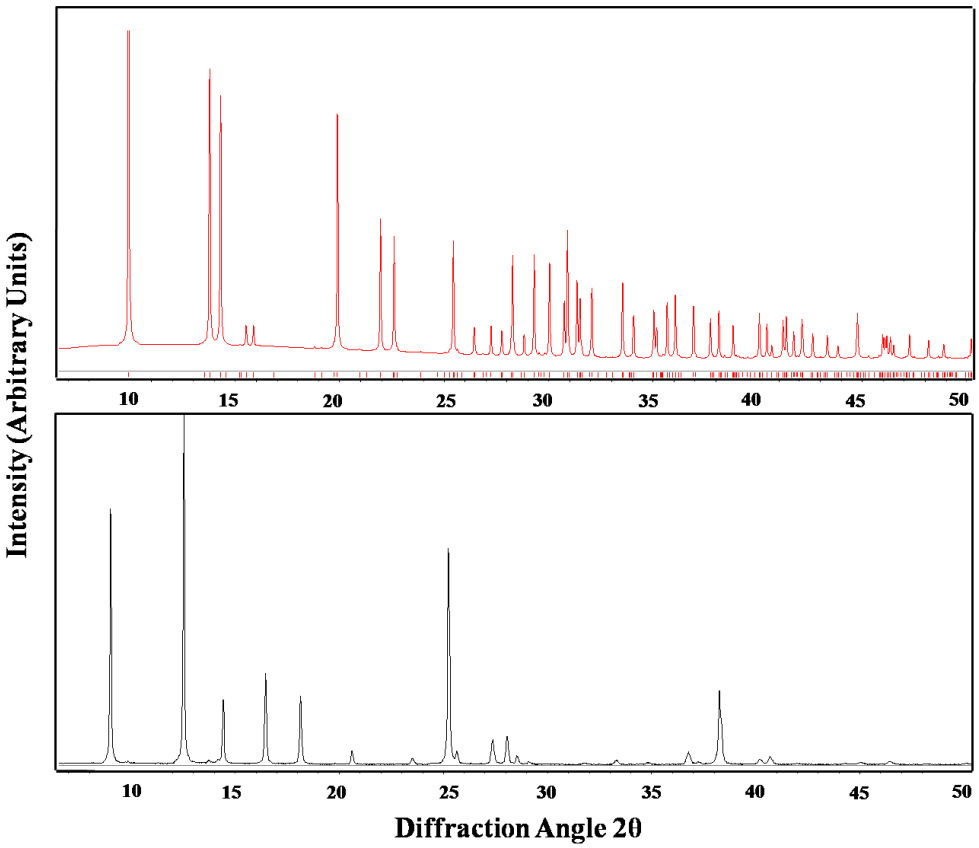

Figure 7.1. Simulated X-ray powder diffraction pattern of the single crystal of Tl(TCNQ) Phase I (top) and the experimental X-ray powder pattern of the microcrystalline purple powder of Tl(TCNQ) Phase II.

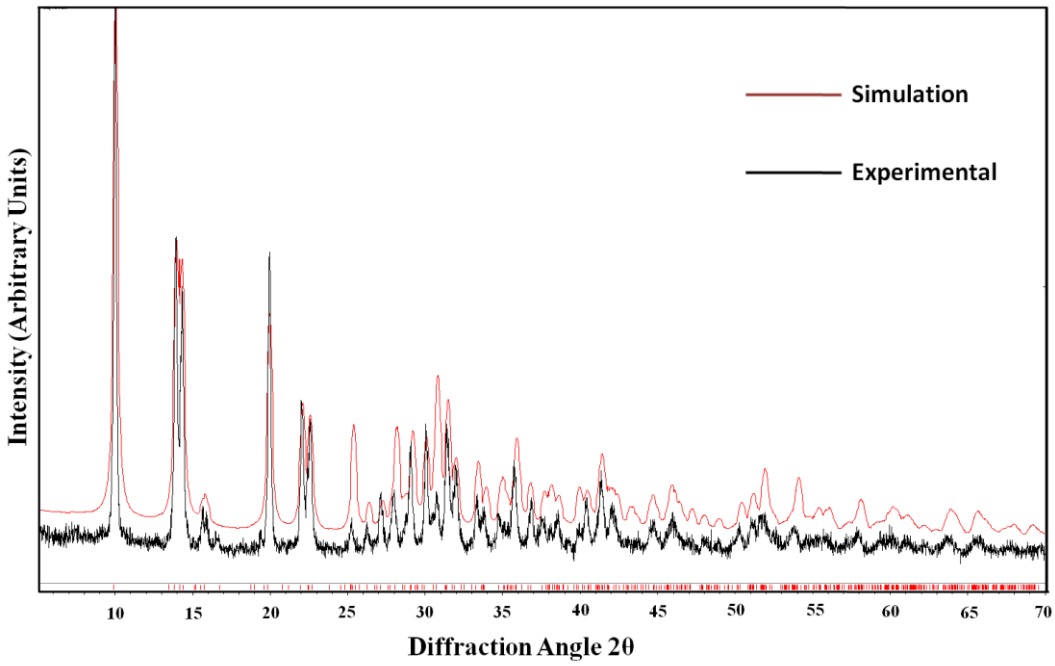

Figure 7.2. Experimental X-ray powder pattern of a microcrystalline sample (black) and a simulated pattern (red) of Tl(TCNQ) Phase I.

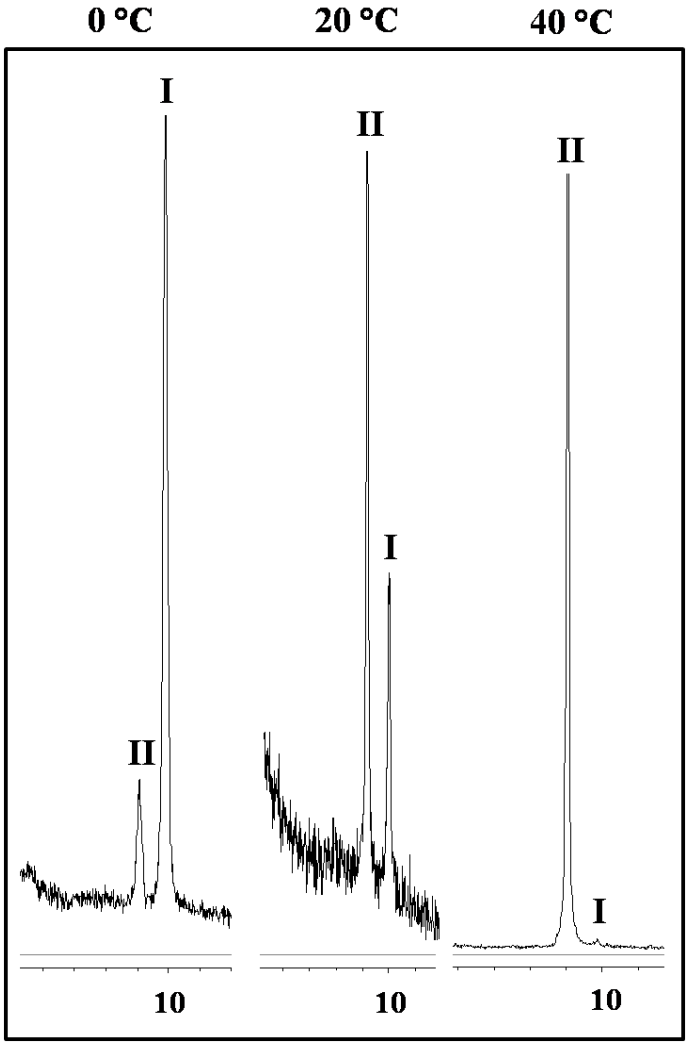

Figure 7.3. X-ray powder patterns of samples of Tl(TCNQ) synthesized at 0, 20 and 40 °C. The increase in temperature results in an increase of Phase II.

Initially, the reaction was stirred from 2 min to 2 days which led to the isolation of a pure sample of **29** (10 min) as evidenced by powder X-ray diffraction (Figure. 7.2). Nevertheless, this synthetic route was not reproducible and, as such, it was discounted as a viable route for the bulk synthesis of Tl(TCNQ) I (**29**). Another attempt to obtain a pure bulk sample of **29** involved varying the temperature of the reaction between 0 and 40 °C, but this method led to the isolation of mixtures of the two polymorphs or the isolation of pure samples of **30** (Figure 7.3). Finally, the solvent used in the reaction was varied by performing the reaction anaerobically in pure H_2O, MeOH, or acetonitrile. The latter solvent led to the precipitation of a purple solid which corresponds to a pure bulk sample of Tl(TCNQ) I (**29**) as evidenced by powder X-ray diffraction (Figure 7.4).

During this systematic study it was also observed that when a pure sample of Tl(TCNQ) I (**29**) is exposed to moist air a solid-to-solid transformation takes place; after 2 weeks the sample of Tl(TCNQ) I (**29**) has converted to Tl(TCNQ) II (**30**) (Figure 7.5). It is postulated that the solid of Tl(TCNQ) I (**29**) is being "dissolved" at the surface by the moisture in the air and slowly converted to the more thermodynamically stable polymorph, Tl(TCNQ) II (**30**). The effects of other external stimuli, such as pressure or vacuum were studied but in both cases no appreciable changes in the structure were observed (Figure 7.6). Such a phase transformation at ambient temperatures and pressures and in the solid state without the involvement or loss of guest molecules such as interstitial solvent is remarkable and rare in metal-organic framework solids (MOFs).

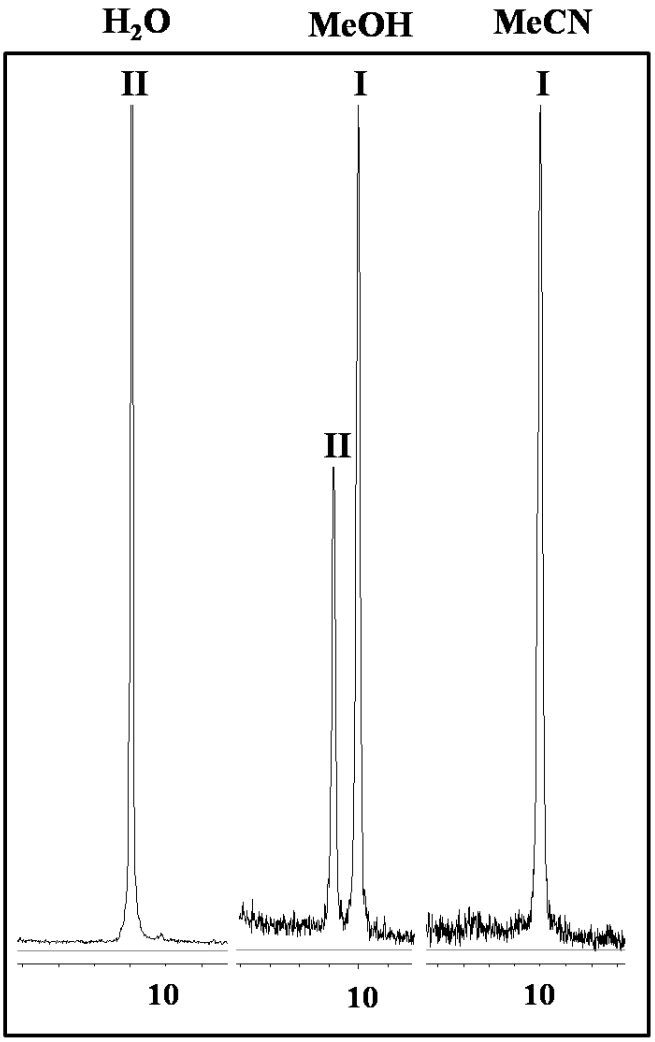

Figure 7.4. Powder X-ray diffraction patterns of samples of Tl(TCNQ) synthesized using H_2O, MeOH, and MeCN as the solvent media. Water leads to the synthesis of primarily Phase II, MeOH leads to a mixture of phases, and MeCN leads to the synthesis of pure Tl(TCNQ) Phase I.

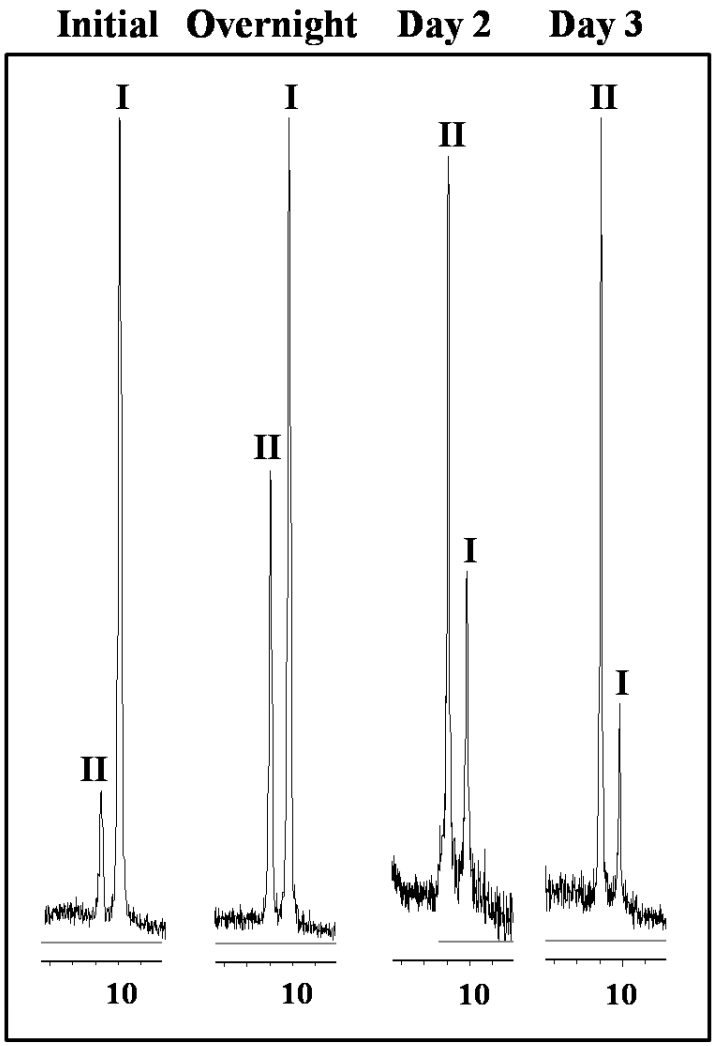

Figure 7.5. X-ray diffraction powder patterns of the same sample of Tl(TCNQ) after prolonged exposure to a moist ambient environment. The patterns show that a solid-to-solid transformation from Phase I to Phase II occurs as the sample is exposed to a moist environment over time.

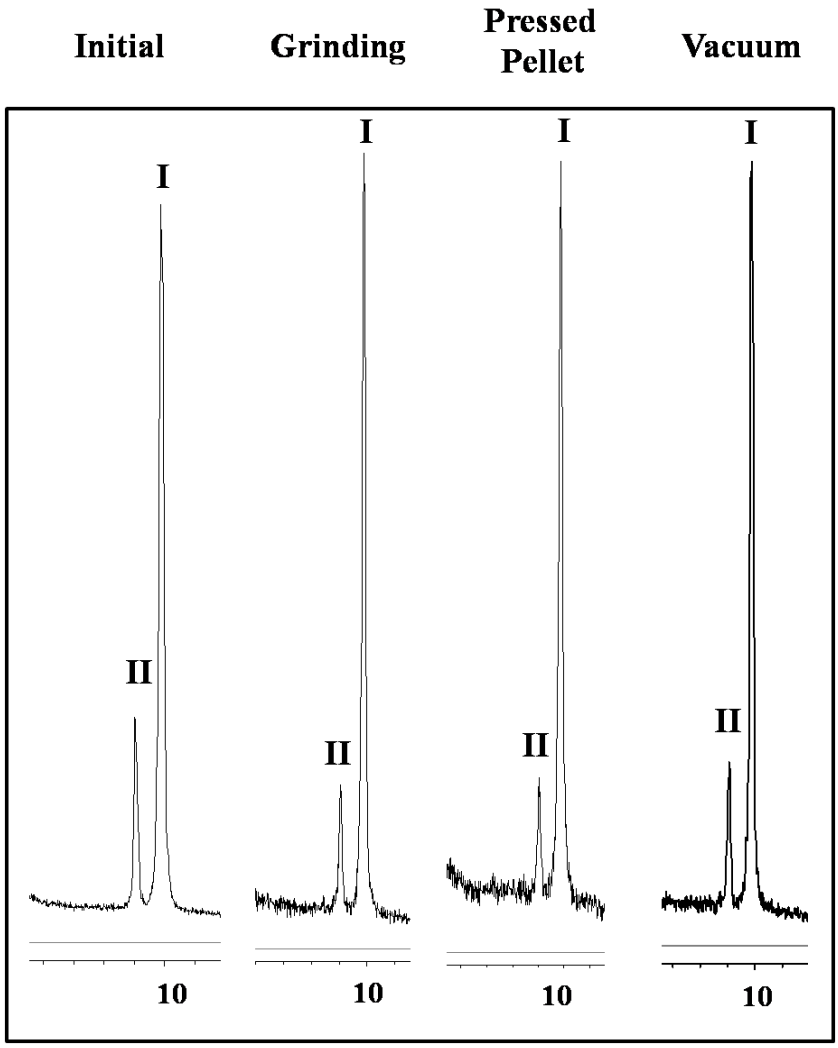

Figure 7.6. Powder patterns of samples of Tl(TCNQ) after grinding, pressing a pellet, and under a dynamic vacuum. No transformation from Phase I to Phase II, or the reverse was observed with the application of pressure or vacuum.

Single Crystal X-ray Diffraction Studies

Slow diffusion of a methanol solution of LiTCNQ and an aqueous solution of $TlPF_6$ in a 2:1 ratio leads to the isolation of single crystals of the product Tl(TCNQ) I (**29**). An X-ray structural determination revealed that **29** crystallizes in the $P2_1/n$ space group in a 3D network whose structure consists of metal ions arranged in linear strings, each surrounded by four stacks of TCNQ acceptor molecules (Figure 7.7a). The TCNQ units are arranged in columnar stacks that propagate along the short axis with alternating distances of 3.167 Å and 3.353 Å between the π systems along the stacks. The adjacent TCNQ stacks are rotated by 90° with respect to each other, and each Tl^I center is coordinated to eight TCNQ molecules and in a distorted cubic geometry with weak Tl ••• Tl interactions along the linear strings of metal ions. The distances between the Tl ions along the short axis alternate from 3.632 Å and 3.453 Å (Figure 7.7b). These distances are slightly less than the sum of the van der Waals radii of two Tl ions (3.92 Å). Interactions between the Tl atoms are rare and have only been documented in two other Tl supramolecular assemblies.[231, 271] For example, the crystal structures of $Tl(DCNQI)_2$ and Tl_2(phthalocyanine) have Tl – Tl distances of 3.81 Å and 3.69 Å respectively, both longer than the distances found in Tl(TCNQ) Phase I.

It is well known that Tl compounds are similar in structure and chemical properties to K and Ag salts (Table 7.3). **A** comparison of the ionic radii shows that the crystal structures of the different radical ion salts are not determined solely by the sizes of the metal ions. Whereas in the series M(TCNQ) (M = Na, K, Rb) the space group changes as the ionic radius increases (*C*-1, $P2_1/n$, and P-1 respectively), similar space

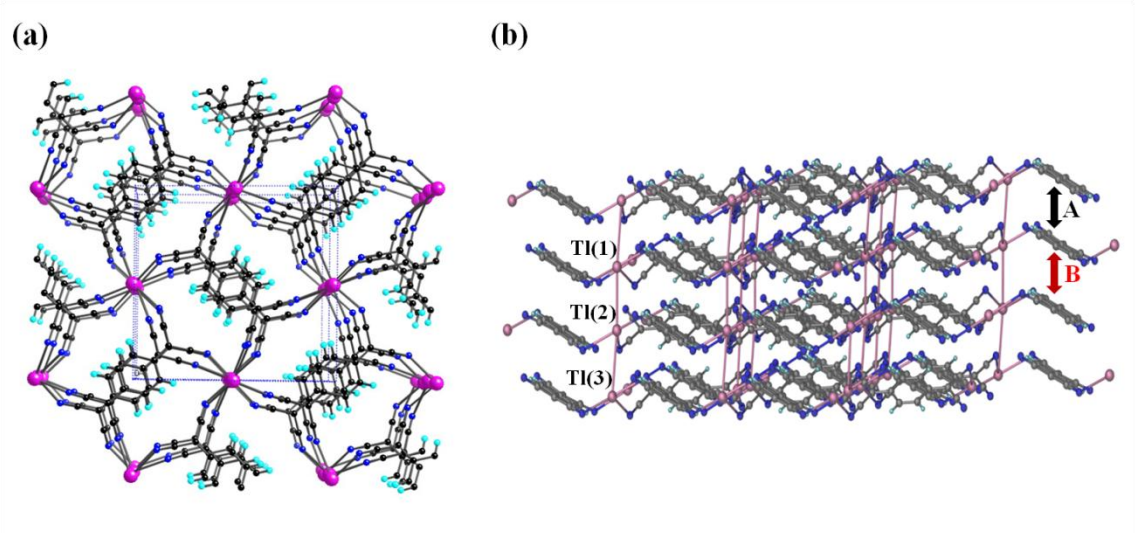

Figure 7.7. Crystal structure of Tl(TCNQ) Phase I (a: top view, b: side view along the c axis). There are two distinct π-π stacking distances along the TCNQ stack. Distance A = 3.167 and distance B = 3.353 Å. The distance between Tl1···T l2 is 3.453 Å and between Tl2···T l3 is 3.620 Å. Both interactions are less than the sum of the van der Waals radii of 2 Tl atoms (3.92 Å).

Table 7.3. Geometrical data and room temperature conductivities for TCNQ radical ion salts: S.G. = space group, r_i = ionic radius (Å), $\mathbf{r}_i + \mathbf{r}_N$ = sum of van der Waals radii, *d*(M-N) = distance between metal ion and nitrile N atom (Å), *d*(A-A) = average distance between acceptor molecules (Å), σ_{300K} = room temperature conductivity ($S^{-1}cm^{-1}$) (N radius $\mathbf{r}_N$ = 1.50 Å).

Compound	**S.G.**	$\mathbf{r}_i$	$\mathbf{r}_i + \mathbf{r}_N$	***d*(M – N)**	***d*(A – A)**	$\boldsymbol{\sigma}_{300K}$	**Ref.**
Cu(TCNQ) I	*Pn*	0.60	2.10	1.95	3.24	2.5×10^{-1}	247
Ag(TCNQ)	*Pnnm*	1.00	2.50	2.33	3.50	3.6×10^{-4}	272
Tl(TCNQ) I	$P2_1/n$	1.59	3.09	2.75/3.21	3.17/3.35	2.4×10^{-4}	-
Na(TCNQ)	*C*-1	1.02	2.52	2.50	3.22/3.50	1.0×10^{-5}	249
K(TCNQ)	$P2_1/n$	1.59	3.09	3.01	3.24/3.57	1.0×10^{-5}	248
Rb(TCNQ) II	*P*-1	1.65	3.15	3.08	3.25	1.0×10^{-5}	251

groups are found for both the Cu(TCNQ) and Ag(TCNQ) metal organic frameworks (Table 7.3). These structural differences are not caused either by the distances between the acceptor molecules or the metal ions, which remain unchanged as they are fixed by the thickness of the TCNQ moiety. Instead they could be due to the different metal-nitrile group distances, d(M – N), which are shortest for the Cu-, Ag- and Tl- TCNQ compounds. In the alkali-TCNQ materials the d(M – N) distance is equal to the sum of the van der Waals radii. In contrast, in the Tl(TCNQ) I polymorph the metal-nitrogen distance is considerably less than the sum of the van der Waals radii (Table 7.3), an indication of a degree of back bonding of the nitrile groups. Nevertheless, Tl(TCNQ) I exhibits structural similarities to the alkali-TCNQ materials. The Tl(TCNQ) I coordination environment resembles the characteristic six-fold coordination of Na, in contrast with the four-fold coordination of Cu- and Ag-TCNQ metal organic frameworks.

Attempts to grow single crystals of the Tl(TCNQ) II polymorph (**30**) were unsuccessful. All the attempts led to microcrystalline needles that were too small for single crystal diffraction experiments or were severely twinned. In order to obtain some insight into the structure of this polymorph, attempts were made to solve the structure using powder diffraction methods. These efforts are still underway and so far have only yielded a preliminary unit cell for the Tl(TCNQ) II (**30**) polymorph. Powder diffraction patterns from a Bruker-AXS D8 Advanced Bragg-Brentano X-ray powder diffractometer were used for indexing by the program Topaz. This led to the triclinic cell with a = 4.7279 Å, b = 7.4008 Å, c = 20.1239 Å, and V = 657.47 Å^3 for Tl(TCNQ) I (Figure 7.8).

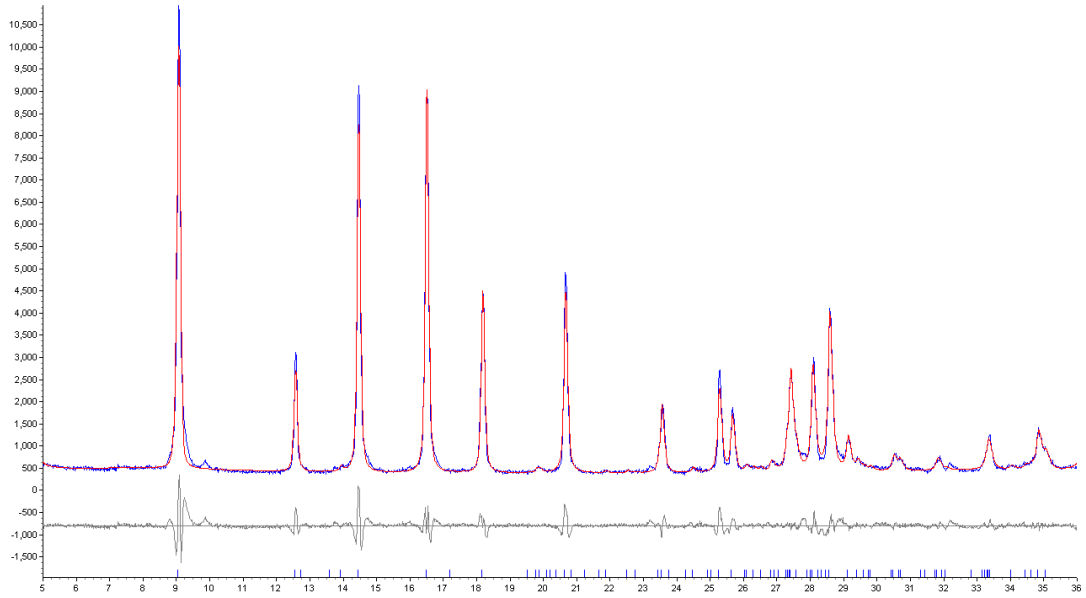

Figure 7.8. Indexing of Tl(TCNQ) Phase II powder pattern with unit cell parameters: $a = 4.7279$ Å, $b = 7.4008$ Å, $c = 20.1239$ Å, and $V = 657.47$ Å^3.

Infrared Spectroscopy

Infrared spectroscopy is a useful tool for characterizing TCNQ materials, in particular for discerning the oxidation state of the molecule in its charge transfer salts or metal organic frameworks. Infrared spectra of the two polymorphs of Tl(TCNQ) are quite similar as would be expected on the basis of their formulations as compounds of $TCNQ^-$. Compound **29** exhibits three strong, broad ν(C≡N) absorptions at 2181, 2164, and 2151 cm^{-1} whereas **30** exhibits one strong, sharp stretch at 2180 and one strong, broad stretch at 2149 cm^{-1}. Perhaps even more indicative of the similarity of the TCNQ unit in the two phases is the δ(C-H) mode at 823 cm^{-1}, which is very sensitive to changes in oxidation state. These data are consistent with the presence of $TCNQ^-$ and not TCNQ, $TCNQ^{2-}$, or mixed-valence stacks of $TCNQ^-$ and TCNQ.[273-275]

Magnetic and Conductivity Properties

Variable temperature magnetic susceptibility data for the samples were measured by the SQUID technique. Plots of χ versus T are given in Figure 7.9. Both polymorphs show behavior typical of a TCNQ radical anion salt with TCNQ stacking, *viz*., strong coupling of the unpaired spins. The very low susceptibility of both polymorphs (Figure 7.9) indicates considerable magnetic coupling of the unpaired electrons, which renders the sample essentially diamagnetic. Most simple TCNQ radical anion salts are paramagnetic, but the susceptibilities are only about 10% of that expected for a system with non-interacting spins.[247]

The two structural forms of Tl(TCNQ) were subjected to pressed pellet conductivity measurements, and it was found that they exhibit quite different charge-

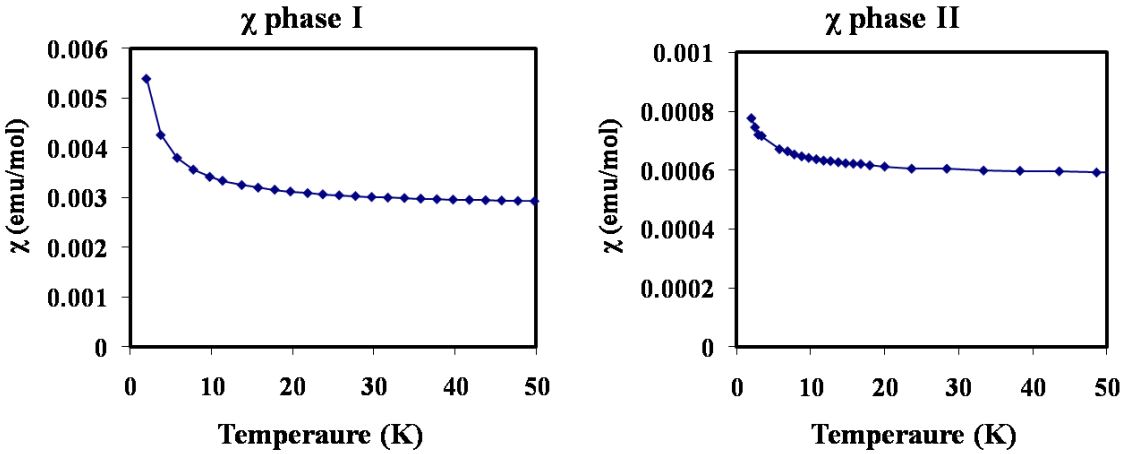

Figure 7.9. Temperature dependence of χ for Tl(TCNQ) Phase I (left) and Tl(TCNQ) Phase II (right) both of which exhibit only weak paramagnetic behavior due to appreciable antiferromagnetic coupling between TCNQ radicals.

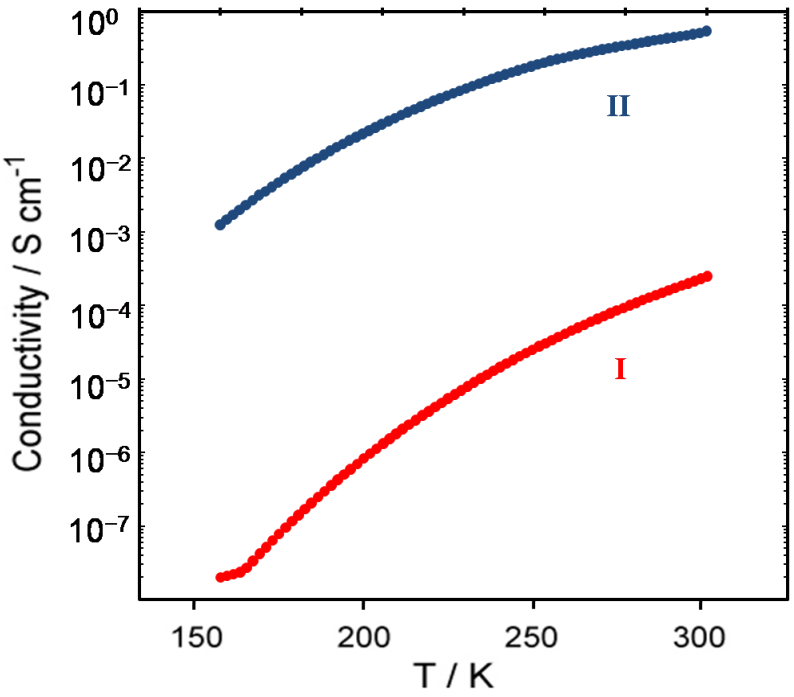

Figure 7.10 Conductivity measurements were carried out on pressed pellets of both Tl(TCNQ) Phase I (red) and Phase II (blue). Phase II has a room-temperature conductivity of 5.4×10^{-1} S·cm^{-1} whereas Phase I is nearly insulating with a room-temperature conductivity of only 2.4×10^{-4} S·cm^{-1}.

transport properties, as illustrated in the plots provided in Figure 7.10. Both behave as semiconductors, but Phase II (**30**) has a room-temperature conductivity of 5.4×10^{-1} $S\cdot cm^{-1}$ whereas Phase I (**29)** is nearly insulating with a room-temperature conductivity of only 2.4×10^{-4} $S\cdot cm^{-1}$. The low conductivity for **29** is expected as a result of the alternating distances observed in the crystal structure between the TCNQ units along the stack. The superior conducting properties of the Tl(TCNQ) II (**30**) polymorph suggest that the structure of this polymorph would contain evenly spaced $TCNQ^{-}$ units along the stack. In comparison to the Alkali-TCNQ MOFs, the TlTCNQ polymorphs show no phase transition as temperature decreases. Further structural evidence for the Tl(TCNQ) II (**30**) polymorph is required in order to understand the difference in the conductivity between the two polymorphs.

CONCLUSIONS

The results of this study establish the existence of two markedly different polymorphs of Tl(TCNQ) as evidenced by infrared spectroscopy, powder X-ray diffraction techniques, and single-crystal X-ray methods. The key to solving the problem of obtaining pure phases was the recognition that the kinetic product (phase I) slowly converts to a more thermodynamically stable material (phase II) when exposed to water from a moist ambient laboratory atmosphere. Both polymorphs exist as dark purple, crystalline materials, and without the use of powder X-ray methods, it is impossible to distinguish between the two different samples or mixtures of them.

The chemical composition and electronic characteristics of the two phases of Tl(TCNQ) are identical, but the structures and properties are quite different. Powder X-ray diffraction studies revealed that subtle differences in the reaction conditions (e.g. time, temperature, solvent) lead to variable quantities of the two phases. Conductivity data on pressed pellets of pure bulk samples of the two phases revealed that phase I is a weak semiconductor, which is not unexpected given the alternating distances between the $TCNQ^-$ units along the stack. The Tl(TCNQ) II (**30**) polymorph, however, exhibits much higher conductivity, although it still a semiconductor. Given this fact, it is reasonable to predict that the structure of this polymorph exhibits a regular spacing between the $TCNQ^-$ units along the stack. Efforts are still in progress to obtain the structure of phase II, whether by single crystal or high resolution powder XRD. This goal is vital for a full understanding of the structure-property correlations of the Tl(TCNQ) polymorphs and will lend insight into the possible role of the Tl---Tl contacts in dictating properties.

SYMBOLS AND ABBREVIATIONS

1D	one dimensional
3D	three dimensional
Å	angstrom
A	alkali metal cation
AC	alternating current
bpy	bipyridine
χ_D	diamagnetic molar susceptibilities
χ_P	paramagnetic molar susceptibilities
χ	magnetic susceptibility
cm^{-1}	wavenumbers
CTIST	charge transfer induced spin transition
D	zero field splitting parameter
DC	direct current
DM-DCNQI	dimethyl-*N*,*N*′-dicyanoquinonediimine
dppe	1,2-Bis(diphenylphosphino)ethane
EDO-TTF	ethylendioxy-tetrathiafulvalene
emu	electromagnetic unit
ESI-MS	electrospray ionization mass spectrometry
EXAFS	extended X-ray absorption fine structure
fcc	face-centered cubic
FC	field cooled

g	grams
H	applied magnetic field
HDVV	Heisenberg, Dirac, Van Vleck Hamiltonian
HS	high-spin
HT	high temperature
Hz	hertz
IR	infrared
J	magnetic exchange constant
K	Kelvin
k	kilo
k_B	Boltzmann's constant
λ	wavelength
LD-LISC	Ligand Driven Light-Induced Spin Changes
LIESST	Light Induced Exited Spin State Trapping
LS	low-spin
LT	low temperature
M	magnetization
Me	methyl
MeCN	acetonitrile
MeOH	methanol
Me_3tacn	*N*,*N*′,*N*″-trimethyl-1,4,7-tri- azacyclononane
mg	milligram

min	minute
mL	milliliter
mmol	milimole
Mn_{12}	$[Mn_{12}O_{12}(O_2CR)_{16}(H_2O)_4]$
MO	molecular orbital
MPPA	{[(6-(pivalamido)pyrid-2-yl]methyl}bis-(pyrid-2-ylmethyl)amine)
MXCD	magnetic X-ray circular dichroism
m/z	mass to charge ratio
PB	Prussian blue analog
phen	1,10-phenanthroline
PPN	Bis(triphenylphosphine)iminium
pzTp	tetra(pyrazolyl)borate
py_5Me	2,6-bis(1,1-bis(2-pyridyl)ethyl)pyridine
S	total spin ground state
S_X	spin center
salphenH_2	*N*,*N*'-bis(salicylidene)-1,2-diaminobenzene
SCO	spin-crossover
SMM	single molecule magnetism/single molecule magnet
SQUID	superconducting quantum interference device
τ	relaxation time
τ_o	pre-exponential factor
T	temperature

T	Tesla
T_B	blocking temperature
TBP	trigonal bipyramidal
T_C	Curie temperature
TCNE	tetracyanoethylene
TCNQ	7,7,8,8- tetracyanoquinodimethane
TEA	tetraethyl ammonium
TIESST	thermal induced excited spin state trapping
TIP	temperature independent paramagnetism
tmphen	3,4,7,8-tetramethyl-1,10-phenanthroline
T_N	Neel temperature
tren	tris(2-aminoethyl)amine
triphos	tris(diphenylphosphinomethyl)ethane
TTF	tetrathiafulvalene
μ_B	Bohr magneton
U	magnitude of the theoretical barrier for magnetization reversal
U_{eff}	magnitude of the effective barrier for magnetization reversal
UV	ultraviolet
V	volt
vis	visible
XANES	X-ray absorption near edge structure
ZFC	zero-field cooled

REFERENCES

1. Day, P., *Science* **1993,** *261* (5120), 431-2.
2. Miller, J. S.; Drillon, M.; Editors, *Magnetism: Molecules to Materials III*. Wiley-VCH: New York, 2002; p 381.
3. Coronado, E.; Galan-Mascaros, J. R.; Murcia-Martinez, A.; Romero, F. M.; Tarazon, A., *NATO Sci. Ser., II* **2004,** *139*, 127-142.
4. Kahn, O., *Acc. Chem. Res.* **2000,** *33* (10), 647-657.
5. Kurmoo, M., *Chem. Soc. Rev.* **2009,** *38* (5), 1353-1379.
6. Verdaguer, M.; Bleuzen, A.; Marvaud, V.; Vaissermann, J.; Seuleiman, M.; Desplanches, C.; Scuiller, A.; Train, C.; Garde, R.; Gelly, G.; Lomenech, C.; Rosenman, I.; Veillet, P.; Cartier, C.; Villain, F., *Coord. Chem. Rev.* **1999,** *190-192*, 1023-1047.
7. Coronado, E.; Day, P., *Chem.Rev.* **2004,** *104* (11), 5419-5448.
8. Gatteschi, D.; Caneschi, A.; Pardi, L.; Sessoli, R., *Science* **1994,** *265* (5175), 1054-1058.
9. Guetlich, P.; Goodwin, H. A., *Spin Crossover in Transition Metal Compounds III*. Springer-Verlag: Berlin, 2004; Vol. 235, p 268.
10. Coronado, E.; Delhaes, P.; Gatteschi, D.; Miller, J. S., *Molecular Magnetism: From Molecular Assemblies to the Devices.* Springer: New York, 1996; p 590.
11. Meijer, G. I., *Science* **2008,** *319* (5870), 1625-1626.
12. Wolf, S. A.; Awschalom, D. D.; Buhrman, R. A.; Daughton, J. M.; von Molnar, S.; Roukes, M. L.; Chtchelkanova, A. Y.; Treger, D. M., *Science* **2001,** *294* (5546), 1488-1495.
13. Bogani, L.; Wernsdorfer, W., *Nat. Mat.* **2008,** *7* (3), 179-186.
14. Awschalom David, D.; Flatte Michael, E.; Samarth, N., *Sci Am* **2002,** *286* (6), 66-73.
15. Sharma, P., *Science* **2005,** *307* (5709), 531-533.
16. Kahn, O., *Molecular Magnetism*. Wiley-VCH Inc.: New York, 1993; p 380.
17. Carlin, R. L., *Magnetochemistry*. Springer-Verlag: New York, 1986; p 328.
18. Bain, G. A.; Berry, J. F., *J. Chem. Educ.* **2008,** *85* (4), 532-536.
19. Cotton, F. A.; Goodenough, J. B., *Magnetism and the Chemical Bond*. John Wiley & Sons, Inc: New York-London, 1963; Vol. 1, p 393.
20. Van Vleck, J. H., *The Theory of Electric and Magnetic Susceptibilities*. Oxford University Press: London, 1965; p 384.
21. Neel, L., *Annales de Physique* **1948,** *3* (2), 137-198.
22. Bleaney, B.; Bowers, K. D., *Philos. Mag. (1798-1977)* **1952,** *43*, 372-4.
23. Bleaney, B.; Bowers, K. D., *Proc. R. Soc. London, Ser. A* **1952,** *214*, 451-65.
24. Van Niekerk, J. N.; Schoening, F. R. L., *Acta Crystallogr.* **1953,** *6*, 227-32.
25. Van Niekerk, J. N.; Schoening, F. R. L., *Nature* **1953,** *171*, 36-7.
26. Barclay, G. A.; Harris, C. M.; Hoskins, B. F.; Kokot, E., *Proc. Chem. Soc., London* **1961**, 264-5.
27. Kokot, E.; Martin, R. L., *Inorg. Chem.* **1964,** *3* (9), 1306-12.

28. Bieksza, D. S.; Hendrickson, D. N., *Inorg. Chem.* **1977,** *16* (4), 924-929.
29. Moreland, J. A.; Doedens, R. J., *Inorg. Chem.* **1978,** *17* (3), 674-9.
30. Dickman, M. H.; Doedens, R. J., *Inorg. Chem.* **1981,** *20* (8), 2677-81.
31. Porter, L. C.; Doedens, R. J., *Inorg. Chem.* **1984,** *23* (8), 997-9.
32. Crawford, V. H.; Richardson, H. W.; Wasson, J. R.; Hodgson, D. J.; Hatfield, W. E., *Inorg. Chem.* **1976,** *15* (9), 2107-10.
33. Scaringe, R. P.; Hodgson, D. J.; Hatfield, W. E., *Transition Met. Chem. (Weinheim, Ger.)* **1981,** *6* (6), 340-4.
34. Cotton, F. A.; Wilkinson, G., *Basic Inorganic Chemistry*. John Wiley & Sons, Inc.: New York, 1978; p 656.
35. Cotton, F. A.; Wilkinson, G.; Bochmann, M.; Murillo, C., *Advanced Inorganic Chemistry*. 6th ed.; John Wiley & Sons, Inc.: New York, 1998; p 1248.
36. Landee, C. P.; Willett, R. D., *Inorg. Chem.* **1981,** *20* (8), 2521-5.
37. Livermore, J. C.; Willett, R. D.; Gaura, R. M.; Landee, C. P., *Inorg. Chem.* **1982,** *21* (4), 1403-5.
38. Fletcher, R.; Hansen, J. J.; Livermore, J.; Willett, R. D., *Inorg. Chem.* **1983,** *22* (2), 330-4.
39. Figgis, B. N., *Trans. Far. Soc.* **1961,** *57*, 204-9.
40. Figgis, B. N., *Trans. Far. Soc.* **1961,** *57*, 198-203.
41. Mayoh, B.; Day, P., *J. Chem. Soc., Dalton Trans.* **1976,** (15), 1483-1486.
42. Anderson, P. W., *Phys. Rev. B: Condens. Matter Mater. Phys.* **1959,** *115*, 2-13.
43. Good-enough, J. B., *Phys. Chem. Solids* **1958,** *6*, 287-97.
44. Kanamori, J., *Phys. Chem. Solids* **1959,** *10*, 87-98.
45. Hay, P. J.; Thibeault, J. C.; Hoffmann, R., *J. Am. Chem. Soc* **1975,** *97* (17), 4884-99.
46. Bencini, A.; Ciofini, I.; Uytterhoeven, M. G., *Inorg. Chim. Acta* **1998,** *274* (1), 90-101.
47. Bencini, A.; Benelli, C.; Gatteschi, D., *Coord. Chem. Rev.* **1984,** *60*, 131-69.
48. Gatteschi, D.; Sorace, L., *J. Solid State Chem.* **2001,** *159* (2), 253-261.
49. Willett, R. D.; Gatteschi, D.; Kahn, O., *Magneto-Structural Correlations in Exchange Coupled Systems*. Springer: New York, 1985; Vol. 140, p 616.
50. Kahn, O., *Angew. Chem.* **1985,** *97* (10), 837-53.
51. Pei, Y.; Verdaguer, M.; Kahn, O.; Renard, J. P.; Sletten, J., *NATO ASI Ser., Ser. B* **1987,** *168* (Org. Inorg. Low-Dimens. Cryst. Mater.), 393-6.
52. Manriquez, J. M.; Yee, G. T.; McLean, R. S.; Epstein, A. J.; Miller, J. S., *Science* **1991,** *252* (5011), 1415-17.
53. Entley, W. R.; Girolami, G. S., *Science* **1995,** *268* (5209), 397-400.
54. Ferlay, S.; Mallah, T.; Ouahes, R.; Veillet, P.; Verdaguer, M., *Nature* **1995,** *378* (6558), 701-3.
55. Holmes, S. M.; Girolami, G. S., *J. Am. Chem. Soc* **1999,** *121* (23), 5593-5594.
56. Miller, J. S., *Angew. Chem. Int. Ed.* **2003,** *42* (1), 27-29.
57. Li, D.; Clerac, R.; Roubeau, O.; Harte, E.; Mathoniere, C.; Le Bris, R.; Holmes, S. M., *J. Am. Chem. Soc* **2008,** *130* (1), 252-258.
58. Guetlich, P.; Goodwin, H. A., *Top. Curr. Chem.* **2004,** *233*, 1-47.

59. Aromi, G.; Brechin, E. K., Synthesis of 3d metallic single-molecule magnets. In *Single-Molecule Magnets and Related Phenomena*, 2006; Vol. 122, p 67.
60. Kahn, O.; Martinez, C. J., *Science* **1998,** *279* (5347), 44-48.
61. Guetlich, P.; Goodwin, H. A., *Spin Crossover in Transition Metal Compounds I*. Springer-Verlag: Berlin, 2004; Vol. 233, p 341.
62. Gutlich, P.; Hauser, A.; Spiering, H., *Angew. Chem. Int. Ed.* **1994,** *33* (20), 2024-2054.
63. Roux, C.; Zarembowitch, J.; Gallois, B.; Granier, T.; Claude, R., *Inorg. Chem.* **1994,** *33* (10), 2273-2279.
64. Gutlich, P., *Structure and Bonding* **1981,** *44*, 83-195.
65. Adams, D. M.; Dei, A.; Rheingold, A. L.; Hendrickson, D. N., *J. Am. Chem. Soc* **1993,** *115* (18), 8221-8229.
66. Sato, O.; Einaga, Y.; Iyoda, T.; Fujishima, A.; Hashimoto, K., *J. Electrochem. Soc.* **1997,** *144* (1), L11-L13.
67. Bleuzen, A.; Lomenech, C.; Escax, V.; Villain, F.; Varret, F.; Moulin, C. C. D.; Verdaguer, M., *J. Am. Chem. Soc* **2000,** *122* (28), 6648-6652.
68. Escax, V.; Bleuzen, A.; Moulin, C. C. D.; Villain, F.; Goujon, A.; Varret, F.; Verdaguer, M., *J. Am. Chem. Soc* **2001,** *123* (50), 12536-12543.
69. Shimamoto, N.; Ohkoshi, S.; Sato, O.; Hashimoto, K., *Inorg. Chem.* **2002,** *41* (4), 678-684.
70. Gutlich, P.; Garcia, Y.; Woike, T., *Coord. Chem. Rev.* **2001,** *219*, 839-879.
71. Decurtins, S.; Gutlich, P.; Kohler, C. P.; Spiering, H.; Hauser, A., *Chem. Phys. Lett.* **1984,** *105* (1), 1-4.
72. Decurtins, S.; Gutlich, P.; Kohler, C. P.; Spiering, H., *J. Chem. Soc., Chem. Commun.* **1985,** (7), 430-432.
73. Sato, O.; Iyoda, T.; Fujishima, A.; Hashimoto, K., *Science* **1996,** *272* (5262), 704-705.
74. Real, J. A.; Andres, E.; Munoz, M. C.; Julve, M.; Granier, T.; Bousseksou, A.; Varret, F., *Science* **1995,** *268* (5208), 265-7.
75. Sato, O.; Tao, J.; Zhang, Y.-Z., *Angew. Chem. Int. Ed.* **2007,** *46* (13), 2152-2187.
76. Caneschi, A.; Gatteschi, D.; Sessoli, R.; Barra, A. L.; Brunel, L. C.; Guillot, M., *J. Am. Chem. Soc* **1991,** *113* (15), 5873-5874.
77. Aubin, S. M. J.; Wemple, M. W.; Adams, D. M.; Tsai, H. L.; Christou, G.; Hendrickson, D. N., *J. Am. Chem. Soc* **1996,** *118* (33), 7746-7754.
78. Christou, G.; Gatteschi, D.; Hendrickson, D. N.; Sessoli, R., *MRS Bull.* **2000,** *25* (11), 66-71.
79. Gatteschi, D.; Sessoli, R., *Angew.Chem., Int.Ed.* **2003,** *42* (3), 268-297.
80. Thomas, L.; Lionti, F.; Ballou, R.; Gatteschi, D.; Sessoli, R.; Barbara, B., *Nature* **1996,** *383* (6596), 145-147.
81. Wernsdorfer, W., Classical and quantum magnetization reversal studied in nanometer-sized particles and clusters. In *Adv. Chem. Phys.*, 2001; Vol. 118, pp 99-190.
82. Wernsdorfer, W.; Sessoli, R., *Science* **1999,** *284* (5411), 133-135.
83. Christou, G., *Polyhedron* **2005,** *24* (16-17), 2065-2075.

84. Sessoli, R.; Tsai, H. L.; Schake, A. R.; Wang, S.; Vincent, J. B.; Folting, K.; Gatteschi, D.; Christou, G.; Hendrickson, D. N., *J. Am. Chem. Soc* **1993,** *115* (5), 1804-1816.
85. Lis, T., *Acta Crystallogr., Sect. B: Struc. Scien.* **1980,** *36* (SEP), 2042-2046.
86. Sessoli, R.; Gatteschi, D.; Caneschi, A.; Novak, M. A., *Nature* **1993,** *365* (6442), 141-143.
87. Milios, C. J.; Vinslava, A.; Wernsdorfer, W.; Moggach, S.; Parsons, S.; Perlepes, S. P.; Christou, G.; Brechin, E. K., *J. Am. Chem. Soc* **2007,** *129* (10), 2754-+.
88. Shatruk, M.; Avendano, C.; Dunbar, K. R., *Prog. Inorg. Chem.* **2009,** *56*, 155-334.
89. Li, D.; Clerac, R.; Parkin, S.; Wang, G.; Yee, G. T.; Holmes, S. M., *Inorg. Chem.* **2006,** *45* (14), 5251-5253.
90. Choi, H. J.; Sokol, J. J.; Long, J. R., *Inorg. Chem.* **2004,** *43* (5), 1606-1608.
91. Wang, C. F.; Zuo, J. L.; Bartlett, B. M.; Song, Y.; Long, J. R.; You, X. Z., *J. Am. Chem. Soc* **2006,** *128* (22), 7162-7163.
92. Li, D.; Parkin, S.; Wang, G.; Yee, G. T.; Prosvirin, A. V.; Holmes, S. M., *Inorg. Chem.* **2005,** *44* (14), 4903-4905.
93. Li, D.; Clerac, R.; Wang, G.; Yee, G. T.; Holmes, S. M., *Eur. J. Inorg. Chem* **2007,** (10), 1341-1346.
94. Bartlett, B. M.; Harris, T. D.; Degroot, M. W.; Long, E. R., *Z. Anorg. Allg. Chem.* **2007,** *633* (13-14), 2380-2385.
95. Yoon, J. H.; Lim, J. H.; Kim, H. C.; Hong, C. S., *Inorg. Chem.* **2006,** *45* (24), 9613-9615.
96. Kim, J.; Han, S.; Lim, J. M.; Choi, K. Y.; Nojiri, H.; Suh, B. J., *Inorg. Chim. Acta* **2007,** *360* (8), 2647-2652.
97. Sokol, J. J.; Hee, A. G.; Long, J. R., *J. Am. Chem. Soc* **2002,** *124* (26), 7656-7657.
98. Wang, S.; Zuo, J. L.; Zhou, H. C.; Choi, H. J.; Ke, Y.; Long, J. R.; You, X. Z., *Angew. Chem. Int. Ed.* **2004,** *43* (44), 5940-5943.
99. Berlinguette, C. P.; Vaughn, D.; Canada-Vilalta, C.; Galan-Mascaros, J. R.; Dunbar, K. R., *Angew. Chem. Int. Ed.* **2003,** *42* (13), 1523-1526.
100. Song, Y.; Zhang, P.; Ren, X. M.; Shen, X. F.; Li, Y. Z.; You, X. Z., *J. Am. Chem. Soc* **2005,** *127* (11), 3708-3709.
101. Freedman, D. E.; Bennett, M. V.; Long, J. R., *Dalton Trans.* **2006,** (23), 2829-2834.
102. Schelter, E. J.; Prosvirin, A. V.; Dunbar, K. R., *J. Am. Chem. Soc* **2004,** *126* (46), 15004-15005.
103. Freedman, D. E.; Jenkins, D. M.; Iavarone, A. T.; Long, J. R., *J. Am. Chem. Soc* **2008,** *130* (10), 2884-2885.
104. Lim, J. H.; Yoon, J. H.; Kim, H. C.; Hong, C. S., *Angew. Chem. Int. Ed.* **2006,** *45* (44), 7424-7426.
105. Ni, Z. H.; Zhang, L. F.; Tangoulis, V.; Wernsdorfer, W.; Cui, A. L.; Sato, O.; Kou, H. Z., *Inorg. Chem.* **2007,** *46* (15), 6029-6037.

106. Schelter, E. J.; Karadas, F.; Avendano, C.; Prosvirin, A. V.; Wernsdorfer, W.; Dunbar, K. R., *J. Am. Chem. Soc* **2007,** *129* (26), 8139-8149.
107. Coronado, E.; Dunbar, K. R., *Inorg. Chem.* **2009,** *48* (8), 3293-3295.
108. Ruiz, E.; Rodriguez-Fortea, A.; Alvarez, S.; Verdaguer, M., *Chem.--Eur.J.* **2005,** *11* (7), 2135-2144.
109. Gadet, V.; Mallah, T.; Castro, I.; Verdaguer, M.; Veillet, P., *J. Am. Chem. Soc* **1992,** *114* (23), 9213-9214.
110. Rodriguez-Fortea, A.; Alemany, P.; Alvarez, S.; Ruiz, E.; Scuiller, A.; Decroix, C.; Marvaud, V.; Vaissermann, J.; Verdaguer, M.; Rosenman, I.; Julve, M., *Inorg. Chem.* **2001,** *40* (23), 5868-5877.
111. Nakamoto, K., *Infrared and Raman Spectra of Inorganic and Coordination Compounds, Part A: Theory and Applications in Inorganic Chemistry*. 5th ed.; John Wiley & Sons, Inc.: New York, 1997; p 387.
112. Dunbar, K. R.; Heintz, R. A., *Prog. Inorg. Chem.* **1997,** *45*, 283-391.
113. Kettle, S. F. A.; Aschero, G. L.; Diana, E.; Rossetti, R.; Stanghellini, P. L., *Inorg. Chem.* **2006,** *45* (13), 4928-4937.
114. Coronado, E.; Gimenez-Lopez, M. C.; Levchenko, G.; Romero, F. M.; Garcia-Baonza, V.; Milner, A.; Paz-Pasternak, M., *J. Am. Chem. Soc* **2005,** *127* (13), 4580-4581.
115. Avendano, C.; Karadas, F.; Hilfiger, M.; Shatruk, M.; Dunbar, K. R., *Inorg. Chem.* **2010,** *49* (2), 583-594.
116. Woodward, J., *Philos. Trans.* **1724,** *33*, 15.
117. Robin, M. B., *Inorg. Chem.* **1962,** *1*, 337-342.
118. Sano, H.; Hashimoto, F., *Bull. Chem. Soc. Jpn.* **1965,** *38* (4), 684-685.
119. Walker, R. G.; Watkins, K. O., *Inorg. Chem.* **1968,** *7* (5), 885-888.
120. Ito, A.; Suenaga, M.; Ono, K., *J. Chem. Phys.* **1968,** *48* (8), 3597-3599.
121. Buser, H. J.; Schwarzenbach, D.; Petter, W.; Ludi, A., *Inorg. Chem.* **1977,** *16* (11), 2704-2710.
122. Verdaguer, M., *Science* **1996,** *272* (5262), 698-9.
123. http://www.fda.gov/cder/drug/infopage/prussian_blue, 2006.
124. Boxhoorn, G.; Moolhuysen, J.; Coolegem, J. G. F.; Van Santen, R. A., *J. Chem. Soc., Chem. Commun.* **1985,** (19), 1305-7.
125. Chapman, K. W.; Southon, P. D.; Weeks, C. L.; Kepert, C. J., *Chem. Comm.* **2005,** (26), 3322-3324.
126. Kaye, S. S.; Long, J. R., *J. Am. Chem. Soc* **2005,** *127* (18), 6506-6507.
127. Sharpe, A. G., *The chemistry of cyano complexes of the transition metals*. Academic Press: New York, 1976.
128. Babel, D., *Comments on Inorganic Chemistry* **1986,** *5* (6), 285-320.
129. Rebilly, J. N.; Mallah, T., *Structure and Bonding* **2006,** *122* (Single-Molecule Magnets and Related Phenomena), 103-131.
130. Sieklucka, B.; Podgajny, R.; Przychodzen, P.; Korzeniak, T., *Coord. Chem. Rev.* **2005,** *249* (21-22), 2203-2221.

131. Przychodzen, P.; Korzeniak, T.; Podgajny, R.; Sieklucka, B. In *Supramolecular coordination networks based on octacyanometalates: From structure to function*, 2006; pp 2234-2260.
132. Verdaguer, M.; Girolami, G. S., *Magn.: Mol. Mater.* **2005,** *V*, 283-346.
133. Ohkoshi, S.-i.; Tokoro, H.; Hashimoto, K., *Coord. Chem. Rev.* **2005,** *249* (17-18), 1830-1840.
134. Cartier dit Moulin, C.; Villain, F.; Bleuzen, A.; Arrio, M.-A.; Sainctavit, P.; Lomenech, C.; Escax, V.; Baudelet, F.; Dartyge, E.; Gallet, J.-J.; Verdaguer, M., *J. Am. Chem. Soc* **2000,** *122* (28), 6653-6658.
135. Goujon, A.; Roubeau, O.; Varret, F.; Dolbecq, A.; Bleuzen, A.; Verdaguer, M., *Eur. Phys. J. B* **2000,** *14* (1), 115-124.
136. Pejakovic, D. A.; Manson, J. L.; Miller, J. S.; Epstein, A. J., *J. Appl. Phys.* **2000,** *88* (7), 4457.
137. Pejakovic, D. A.; Manson, J. L.; Miller, J. S.; Epstein, A. J., *Phys. Rev. Lett.* **2000,** *85* (9), 1994-1997.
138. Bleuzen, A.; Lomenech, C.; Escax, V.; Villain, F.; Varret, F.; Cartier dit Moulin, C.; Verdaguer, M., *J. Am. Chem. Soc* **2000,** *122* (28), 6648-6652.
139. Pejakovic, D. A.; Manson, J. L.; Miller, J. S.; Epstein, A. J., *J. Appl. Phys.* **2000,** *87* (9, Pt. 3), 6028-6030.
140. Varret, F.; Goujon, A.; Bleuzen, A., *Hyperfine Interact.* **2001,** *134* (1-4), 69-80.
141. Champion, G.; Escax, V.; Moulin, C. C. D.; Bleuzen, A.; Villain, F. O.; Baudelet, F.; Dartyge, E.; Verdaguer, N., *J. Am. Chem. Soc* **2001,** *123* (50), 12544-12546.
142. Goujon, A.; Varret, F.; Escax, V.; Bleuzen, A.; Verdaguer, M., *Polyhedron* **2001,** *20* (11-14), 1347-1354.
143. Goujon, A.; Varret, F.; Escax, V.; Bleuzen, A.; Verdaguer, M., *Polyhedron* **2001,** *20* (11-14), 1339-1345.
144. Shimamoto, N.; Ohkoshi, S.-I.; Sato, O.; Hashimoto, K., *Chem. Lett.* **2002,** (4), 486-487.
145. Liu, H. W.; Matsuda, K.; Gu, Z. Z.; Takahashi, K.; Cui, A. L.; Nakajima, R.; Fujishima, A.; Sato, O., *Phys. Rev. Lett.* **2003,** *90* (16), 167403.
146. Sato, O.; Kawakami, T.; Kimura, M.; Hishiya, S.; Kubo, S.; Einaga, Y., *J. Am. Chem. Soc* **2004,** *126* (41), 13176-13177.
147. Bleuzen, A.; Escax, V.; Ferrier, A.; Villain, F.; Verdaguer, M.; Muensch, P.; Itie, J.-P., *Angew. Chem. Int. Ed.* **2004,** *43* (28), 3728-3731.
148. Bleuzen, A.; Cafun, J.-D.; Bachschmidt, A.; Verdaguer, M.; Munsch, P.; Baudelet, F.; Itie, J.-P., *J. Phys. Chem. C* **2008,** *112* (45), 17709-17715.
149. Schelter, E. J.; Prosvirin, A. V.; Reiff, W. M.; Dunbar, K. R., *Angew. Chem. Int. Ed.* **2004,** *43* (37), 4912-4915, S4912/1-S4912/2.
150. Hilfiger, M. G.; Zhao, H.; Prosvirin, A.; Wernsdorfer, W.; Dunbar, K. R., *Dalton Trans.* **2009,** (26), 5155-5163.
151. Hilfiger, M. G.; Shatruk, M.; Prosvirin, A.; Dunbar, K. R., *Chem. Comm.* **2008,** (44), 5752-5754.

152. Palii, A. V.; Reu, O. S.; Ostrovsky, S. M.; Klokishner, S. I.; Tsukerblat, B. S.; Hilfiger, M.; Shatruk, M.; Prosvirin, A.; Dunbar, K. R., *J. Phys. Chem A* **2009,** *113* (25), 6886-6890.
153. Hilfiger, M. G. Incorporation of 4d and 5d transition metal cyanometallates into magnetic clusters and materials. 2010.
154. Deshpande, R. S.; Sharp-Goldman, S. L.; Willson, J. L.; Bocarsly, A. B.; Gross, J.; Finnefrock, A. C.; Gruner, S. M., *Chem. Mater.* **2003,** *15* (22), 4239-4246.
155. Kaye, S. S.; Long, J. R., *Chem. Comm.* **2007,** (43), 4486-4488.
156. Kaye, S. S.; Long, J. R., *Catal. Today* **2007,** *120* (3-4), 311-316.
157. Reguera, L.; Reguera, E.; Balmaseda, J.; Rodriguez-Hernandez, J.; Yee-Madeira, H., *J. Porous Mater.* **2008,** *15* (6), 719-729.
158. Reguera, L.; Balmaseda, J.; Krap, C. P.; Avila, M.; Reguera, E., *J. Phys. Chem. C* **2008,** *112* (44), 17443-17449.
159. Reguera, L.; Krap, C. P.; Balmaseda, J.; Reguera, E., *J. Phys. Chem. C* **2008,** *112* (40), 15893-15899.
160. Culp, J. T.; Smith, M. R.; Bittner, E.; Bockrath, B., *J. Am. Chem. Soc* **2008,** *130* (37), 12427-12434.
161. Culp, J. T.; Natesakhawat, S.; Smith, M. R.; Bittner, E.; Matranga, C.; Bockrath, B., *J. Phys. Chem. C* **2008,** *112* (17), 7079-7083.
162. Culp, J. T.; Matranga, C.; Smith, M.; Bittner, E. W.; Bockrath, B., *J. Phys. Chem. B* **2006,** *110* (16), 8325-8328.
163. Behera, J. N.; D'Alessandro, D. M.; Soheilnia, N.; Long, J. R., *Chem. Mater.* **2009,** *21* (9), 1922-1926.
164. Rouquerol, F.; Rouquerol, J.; Sing, K. S. W., *Chem. Thermodyn.* **1999**, 77-84.
165. Wong-Foy, A. G.; Matzger, A. J.; Yaghi, O. M., *J. Am. Chem. Soc* **2006,** *128* (11), 3494-3495.
166. Chen, B.; Ockwig, N. W.; Millward, A. R.; Contreras, D. S.; Yaghi, O. M., *Angew. Chem. Int. Ed.* **2005,** *44* (30), 4745-4749.
167. Yan, Y.; Lin, X.; Yang, S.; Blake, A. J.; Dailly, A.; Champness, N. R.; Hubberstey, P.; Schroeder, M., *Chem. Comm.* **2009,** (9), 1025-1027.
168. Rowsell, J. L. C.; Millward, A. R.; Park, K. S.; Yaghi, O. M., *J. Am. Chem. Soc* **2004,** *126* (18), 5666-5667.
169. Rosi, N. L.; Eckert, J.; Eddaoudi, M.; Vodak, D. T.; Kim, J.; O'Keeffe, M.; Yaghi, O. M., *Science* **2003,** *300* (5622), 1127-1130.
170. Mallah, T.; Thiebaut, S.; Verdaguer, M.; Veillet, P., *Science* **1993,** *262* (5139), 1554-7.
171. Entley, W. R.; Girolami, G. S., *Science (Washington, D. C.)* **1995,** *268* (5209), 397-400.
172. Przychodzen, P.; Korzeniak, T.; Podgajny, R.; Sieklucka, B., *Coord. Chem. Rev.* **2006,** *250* (17+18), 2234-2260.
173. Karadas, F.; Schelter, E. J.; Prosvirin, A. V.; Bacsa, J.; Dunbar, K. R., *Chem. Comm.* **2005,** (11), 1414-1416.

174. Karadas, F.; Schelter, E. J.; Shatruk, M.; Prosvirin, A. V.; Bacsa, J.; Smirnov, D.; Ozarowski, A.; Krzystek, J.; Telser, J.; Dunbar, K. R., *Inorg. Chem.* **2008,** *47* (6), 2074-2082.
175. Schelter, E. J.; Bera, J. K.; Bacsa, J.; Galan-Mascaros, J. R.; Dunbar, K. R., *Inorg. Chem.* **2003,** *42* (14), 4256-4258.
176. Rupp, R.; Huttner, G.; Kircher, P.; Soltek, R.; Buchner, M., *Eur. J. Inorg. Chem* **2000,** (8), 1745-1757.
177. Jacob, V.; Huttner, G.; Kaifer, E.; Kircher, P.; Rutsch, P., *Eur. J. Inorg. Chem* **2001,** (11), 2783-2795.
178. Jacob, V.; Mann, S.; Huttner, G.; Walter, O.; Zsolnai, L.; Kaifer, E.; Rutsch, P.; Kircher, P.; Bill, E., *Eur. J. Inorg. Chem* **2001,** (10), 2625-2640.
179. DuBois, D. L.; Miedaner, A., *Inorg. Chem.* **1986,** *25* (26), 4642-50.
180. Harris, T. D.; Long, J. R., *Chem. Comm.* **2007,** (13), 1360-1362.
181. Coronado, E.; Gimenez-Lopez Mari, C.; Levchenko, G.; Romero Francisco, M.; Garcia-Baonza, V.; Milner, A.; Paz-Pasternak, M., *J. Am. Chem. Soc* **2005,** *127* (13), 4580-1.
182. Brown, D. B.; Shriver, D. F., *Inorg. Chem.* **1969,** *8* (1), 37-42.
183. Shatruk, M.; Chambers, K. E.; Prosvirin, A. V.; Dunbar, K. R., *Inorg. Chem.* **2007,** *46* (13), 5155-5165.
184. Shatruk, M.; Dragulescu-Andrasi, A.; Chambers, K. E.; Stoian, S. A.; Bominaar, E. L.; Achim, C.; Dunbar, K. R., *J. Am. Chem. Soc* **2007,** *129* (19), 6104-6116.
185. Schelter, E. J.; Shatruk, M.; Heintz, R. A.; Galan-Mascaros, J. R.; Dunbar, K. R., *Chem. Comm.* **2005,** (11), 1417-1419.
186. Rigo, P.; Bressan, M., *Inorg. Nucl. Chem. Lett.* **1973,** *9* (5), 527-32.
187. *SMART and SAINT* **1996,** *Siemens Analytical X-ray Instruments Inc.*, Madison, WI.
188. Sheldrick, G. M., *SADABS,* **1996**, University of Gottinggen: Gottingen, Germany.
189. Sheldrick George, M., *Acta Crystallogr A* **2008,** *64* (Pt 1), 112-22.
190. Barbour, L. J., *J. Supramol. Chem.* **2003,** *1* (4-6), 189-191.
191. Mangani, S.; Orioli, P.; Ciampolini, M.; Nardi, N.; Zanobini, F., *Inorg. Chim. Acta* **1984,** *85* (1), 65-72.
192. Stalick, J. K.; Corfields, P. W. R.; Meek, D. W., *Inorg. Chem.* **1973,** *12* (7), 1668-75.
193. Ciancanelli, R.; Noll, B. C.; DuBois, D. L.; DuBois, M. R., *J. Am. Chem. Soc* **2002,** *124* (12), 2984-2992.
194. Rigo, P.; Longato, B.; Favero, G., *Inorg. Chem.* **1972,** *11* (2), 300-3.
195. Hathaway, B. J.; Holah, D. G.; Underhill, A. E., *J. Chem. Soc* **1962,** (JUN), 2444-2448.
196. Borras-Almenar, J. J.; Clemente-Juan, J. M.; Coronado, E.; Tsukerblat, B. S., *J. Comput. Chem.* **2001,** *22* (9), 985-991.
197. Jian, F. F.; Xiao, H. L.; Li, L.; Sun, P. P., *J. Coord. Chem.* **2004,** *57* (13), 1131-1137.

198. Miyasaka, H.; Saitoh, A.; Abe, S., *Coord. Chem. Rev.* **2007,** *251* (21-24), 2622-2664.
199. McAuliffe, C. A.; Nabhan, A.; Pritchard, R. G.; Watkinson, M.; Bermejo, M.; Sousa, A., *Acta Crystallographica, Section C Crystal Structure Communications* **1994,** *C50* (11), 1676-8.
200. Useful Reagents and Ligands. In *Inorg. Synth.*, Dimitri, C., Ed. 2002; pp 75-121.
201. Cauzzi, D. A.; Mori, G.; Predieri, G.; Tiripicchio, A.; Cavatorta, F., *Inorg. Chim. Acta* **1993,** *204* (2), 181-7.
202. Miyasaka, H.; Takahashi, H.; Madanbashi, T.; Sugiura, K. i.; Clerac, R.; Nojiri, H., *Inorg. Chem.* **2005,** *44* (17), 5969-5971.
203. Lehn, J. M., *Supramolecular Chemistry: Concepts and Perspectives*. VCH: Weinheim, 1995; p 262.
204. Tregenna-Piggott, P. L. W.; Sheptyakov, D.; Keller, L.; Klokishner, S. I.; Ostrovsky, S. M.; Palii, A. V.; Reu, O. S.; Bendix, J.; Nannestad, T. B.; Pedersen, K.; Weihe, H.; Mutka, H., *Inorg. Chem.* **2009,** *48* (1), 128-137.
205. Ferbinteanu, M.; Miyasaka, H.; Wernsdorfer, W.; Nakata, K.; Sugiura, K.; Yamashita, M.; Coulon, C.; Clerac, R., *J. Am. Chem. Soc* **2005,** *127* (9), 3090-3099.
206. Wernsdorfer, W.; Aliaga-Alcalde, N.; Hendrickson, D. N.; Christou, G., *Nature* **2002,** *416* (6879), 406-409.
207. Boskovic, C.; Bircher, R.; Tregenna-Piggott, P. L. W.; Guedel, H. U.; Paulsen, C.; Wernsdorfer, W.; Barra, A.-L.; Khatsko, E.; Neels, A.; Stoeckli-Evans, H., *J. Am. Chem. Soc* **2003,** *125* (46), 14046-14058.
208. Tiron, R.; Wernsdorfer, W.; Aliaga-Alcalde, N.; Christou, G., *Phys. Rev. B: Condens. Matter Mater. Phys.* **2003,** *68* (14), 140407/1-140407/4.
209. Yang, E.-C.; Wernsdorfer, W.; Hill, S.; Edwards, R. S.; Nakano, M.; Maccagnano, S.; Zakharov, L. N.; Rheingold, A. L.; Christou, G.; Hendrickson, D. N., *Polyhedron* **2003,** *22* (14-17), 1727-1733.
210. Bagai, R.; Wernsdorfer, W.; Abboud, K. A.; Christou, G., *J. Am. Chem. Soc* **2007,** *129* (43), 12918-12919.
211. Inglis, R.; Jones, L. F.; Mason, K.; Collins, A.; Moggach, S. A.; Parsons, S.; Perlepes, S. P.; Wernsdorfer, W.; Brechin, E. K., *C-AEJ* **2008,** *14* (30), 9117-9121.
212. Lecren, L.; Roubeau, O.; Coulon, C.; Li, Y.-G.; Le Goff, X. F.; Wernsdorfer, W.; Miyasaka, H.; Clerac, R., *J. Am. Chem. Soc* **2005,** *127* (49), 17353-17363.
213. Coulon, C.; Miyasaka, H.; Clerac, R., *Structure and Bonding* **2006,** *122* (Single-Molecule Magnets and Related Phenomena), 163-206.
214. Lecren, L.; Wernsdorfer, W.; Li, Y.-G.; Vindigni, A.; Miyasaka, H.; Clerac, R., *J. Am. Chem. Soc* **2007,** *129* (16), 5045-5051.
215. Sato, O.; Iyoda, T.; Fujishima, A.; Hashimoto, K., *Science (Washington, D. C.)* **1996,** *272* (5262), 704-5.
216. Dunbar, K. R., *Polyhedron* **2001,** *20* (11-14), xxvii-xxviii.

217. Berlinguette, C. P.; Dragulescu-Andrasi, A.; Sieber, A.; Galan-Mascaros, J. R.; Guedel, H.-U.; Achim, C.; Dunbar, K. R., *J. Am. Chem. Soc* **2004,** *126* (20), 6222-6223.
218. Berlinguette, C. P.; Dunbar, K. R., *Chem. Comm.* **2005,** (19), 2451-2453.
219. Tyagi, P.; Li, D.; Holmes, S. M.; Hinds, B. J., *J. Am. Chem. Soc*, ACS ASAP.
220. He, J.; Chen, F.; Liddell, P. A.; Andreasson, J.; Straight, S. D.; Gust, D.; Moore, T. A.; Moore, A. L.; Li, J.; Sankey, O. F.; Lindsay, S. M., *Nanotechnology* **2005,** *16* (6), 695-702.
221. Palii, A.; Ostrovsky, S. M.; Klokishner, S. I.; Tsukerblat, B. S.; Dunbar, K. R., *ChemPhysChem* **2006,** *7* (4), 871-879.
222. Ruiz, E.; Rodriguez-Fortea, A.; Alvarez, S., *Inorg. Chem.* **2003,** *42* (16), 4881-4884.
223. Harata, M.; Jitsukawa, K.; Masuda, H.; Einaga, H., *Chem. Lett.* **1995,** (1), 61-2.
224. Yamaguchi, S.; Wada, A.; Funahashi, Y.; Nagatomo, S.; Kitagawa, T.; Jitsukawa, K.; Masuda, H., *Eur. J. Inorg. Chem* **2003,** (24), 4378-4386.
225. Zhao, H.; Clerac, R.; Sun, J. S.; Ouyang, X.; Clemente-Juan, J. M.; Gomez-Garcia, C. J.; Coronado, E.; Dunbar, K. R., *J. Solid State Chem.* **2001,** *159* (2), 281-292.
226. Figgis, B. N.; Hitchman, M. A., *Ligand Field Theory and Its Applications*.Wiley-VCH: New York, 2000; p 354.
227. Kaim, W.; Moscherosch, M., *Coord. Chem. Rev.* **1994,** *129* (1-2), 157-193.
228. Potember, R. S.; Poehler, T. O.; Cowan, D. O., *Appl. Phys. Lett.* **1979,** *34* (6), 405-7.
229. von Schuetz, J. U.; Gomez, D.; Wachtel, H.; Wolf, H. C., *J. Chem. Phys.* **1996,** *105* (15), 6538-6545.
230. Hunig, S.; Erk, P., *Advanced Materials* **1991,** *3* (5), 225-236.
231. Huenig, S.; Meixner, H.; Metzenthin, T.; Langohr, U.; Von Schuetz, J. U.; Wolf, H. C.; Tillmanns, E., *Advanced Materials* **1990,** *2* (8), 361-3.
232. Metzger, R. M., *Chem. Rev.* **2003,** *103* (9), 3803-3834.
233. Okamura, H.; Matsubara, M.; Nanba, T.; Tayagaki, T.; Mouri, S.; Tanaka, K.; Ikemoto, Y.; Moriwaki, T.; Kimura, H.; Juhasz, G., *Phys. Rev. B: Condens. Matter Mater. Phys.* **2005,** *72* (7), 073108/1-073108/4.
234. Okamura, H.; Matsubara, M.; Tayagaki, T.; Tanaka, K.; Ikemoto, Y.; Kimura, H.; Moriwaki, T.; Nanba, T., *J. Phys. Soc. Jpn.* **2004,** *73* (5), 1355-1361.
235. Batail, P.; LaPlaca, S. J.; Mayerle, J. J.; Torrance, J. B., *J. Am. Chem. Soc* **1981,** *103* (4), 951-3.
236. Torrance, J. B.; Girlando, A.; Mayerle, J. J.; Crowley, J. L.; Lee, V. Y.; Batail, P.; LaPlaca, S. J., *Phys. Rev. Lett.* **1981,** *47* (24), 1747-50.
237. Metzger, R. M.; Torrance, J. B., *J. Am. Chem. Soc* **1985,** *107* (1), 117-21.
238. Kato, R.; Kobayashi, H.; Kobayashi, A., *J. Am. Chem. Soc* **1989,** *111* (14), 5224-32.
239. Nakano, M.; Kato, M.; Yamada, K., *Phys. Rev. B: Condens. Matter Mater. Phys.* **1993,** *186-188*, 1077-9.

240. Karutz, F. O.; von Schutz, J. U.; Wachtel, H.; Wolf, H. C., *Phys. Rev. Lett.* **1998,** *81* (1), 140-143.
241. Schmitt, H.; von Schutz, J. U.; Wachtel, H.; Wolf, H. C., *Synth. Met.* **1997,** *86* (1-3), 2257-2258.
242. von Schuetz, J. U.; Bauer, D.; Wachtel, H.; Wolf, H. C., *Synth. Met.* **1995,** *71* (1-3), 2089-90.
243. von schutz, J. U.; Gomez, D.; Schmitt, H.; Wachtel, H., *Synth. Met.* **1997,** *86* (1-3), 2095-2096.
244. Ota, A.; Yamochi, H.; Saito, G., *J. Mater. Chem.* **2002,** *12* (9), 2600-2602.
245. Chollet, M.; Guerin, L.; Uchida, N.; Fukaya, S.; Shimoda, H.; Ishikawa, T.; Matsuda, K.; Hasegawa, T.; Ota, A.; Yamochi, H.; Saito, G.; Tazaki, R.; Adachi, S.-i.; Koshihara, S.-y., *Science* **2005,** *307* (5706), 86-89.
246. Potember, R. S.; Poehler, T. O.; Benson, R. C., *Appl. Phys. Lett.* **1982,** *41* (6), 548-50.
247. Heintz, R. A.; Zhao, H.; Ouyang, X.; Grandinetti, G.; Cowen, J.; Dunbar, K. R., *Inorg. Chem.* **1999,** *38* (1), 144-156.
248. Kumai, R.; Okimoto, Y.; Tokura, Y., *Science* **1999,** *284* (5420), 1645-1647.
249. Konno, M.; Saito, Y., *Acta Crystallogr., Sect. B* **1974,** *30* (5), 1294-9.
250. Konno, M.; Ishii, T.; Saito, Y., *Acta Crystallogr., Sect. B* **1977,** *B33* (3), 763-70.
251. Kobayashi, H., *Bull. Chem. Soc. Jpn.* **1981,** *54* (12), 3669-72.
252. Greenwood, N. N.; Earnshaw, A., *Chemistry of the Elements*. 2nd ed.; Elsevier Science Ltd.: Oxford, 1997.
253. McGuire, M. A.; Reynolds, T. K.; DiSalvo, F. J., *Chem. Mater.* **2005,** *17* (11), 2875-2884.
254. Bouhadir, G.; Bourissou, D., *Chem. Soc. Rev.* **2004,** *33* (4), 210-217.
255. Pitt, M. A.; Johnson, D. W., *Chem. Soc. Rev.* **2007,** *36* (9), 1441-1453.
256. Ravindran, T.; Subramanyam, S. V., *Synth. Met.* **1992,** *46* (3), 317-324.
257. Abrahams, B. F.; Hudson, T. A.; Robson, R., *Crystal Growth & Design* **2008,** *8* (4), 1123-1125.
258. Haneline, M. R.; Gabbai, F. P., *Comp. Rend.* **2004,** *7* (8-9), 871-876.
259. Ashizawa, M.; Nakao, A.; Yamamoto, H. M.; Kato, R., *J. Low Temp. Phys.* **2006,** *142* (3-4), 449-452.
260. Johnson, M. T.; Campana, C. F.; Foxman, B. M.; Desmarais, W.; Vela, M. J.; Miller, J. S., *C-AEJ* **2000,** *6* (10), 1805-1810.
261. Fadly, M.; Elgandoor, M. A.; Sawaby, A., *J. Mater. Sci.* **1992,** *27* (5), 1235-1239.
262. Dick, A. W. S.; Holliday, A. K.; Puddephatt, R. J., *J. Organomet. Chem.* **1975,** *96* (2), C41-C42.
263. Grossel, M. C.; Weston, S. C., *J. Chem. Soc., Chem. Commun.* **1992,** (20), 1510-12.
264. Kim, M.-K.; Kim, Y.-I.; Moon, S. B.; Choi, S.-N., *Bull. Korean Chem. Soc.* **1996,** *17* (5), 424-428.
265. Melby, L. R.; Harder, R. J.; Hertler, W. R.; Mahler, W.; Benson, R. E.; Mochel, W. E., *J. Am. Chem. Soc* **1962,** *84*, 3374-87.

266. Zhao, H. H.; Heintz, R. A.; Dunbar, K. R.; Rogers, R. D., *J. Am. Chem. Soc* **1996,** *118* (50), 12844-12845.
267. Zhao, H.; Heintz, R. A.; Ouyang, X.; Dunbar, K. R.; Campana, C. F.; Rogers, R. D., *Chem. Mater.* **1999,** *11* (3), 736-746.
268. O'Kane, S. A.; Clerac, R.; Zhao, H. H.; Xiang, O. Y.; Galan-Mascaros, J. R.; Heintz, R.; Dunbar, K. R., *J. Solid State Chem.* **2000,** *152* (1), 159-173.
269. Zhao, H.; Bazile, M. J., Jr.; Galan-Mascaros, J. R.; Dunbar, K. R., *Angew. Chem. Int. Ed.* **2003,** *42* (9), 1015-1018.
270. Clerac, R.; O'Kane, S.; Cowen, J.; Ouyang, X.; Heintz, R.; Zhao, H. H.; Bazile, M. J.; Dunbar, K. R., *Chem. Mater.* **2003,** *15* (9), 1840-1850.
271. Janczak, J.; Kubiak, R., *J. Alloys Compd.* **1993,** *202* (1-2), 69-72.
272. Shields, L., *J. Chem. Soc., Faraday Trans. 2* **1985,** *81* (1), 1-9.
273. Inoue, M.; Inoue, M. B., *J. Chem. Soc., Faraday Trans. 2* **1985,** *81* (4), 539-47.
274. Inoue, M.; Inoue, M. B., *Inorg. Chem.* **1986,** *25* (1), 37-41.
275. Inoue, M. B.; Inoue, M.; Fernando, Q.; Nebesny, K. W., *J. Phys. Chem.* **1987,** *91* (3), 527-30.
276. Schelter, E. J.; Prosvirin, A. V.; Reiff, W. M.; Dunbar, K. R., *Angew. Chem., Int. Ed. Engl.* **2004,** *43* (37), 4912-4915, S4912/1-S4912/2.
277. Nunzi, F.; Ruiz, E.; Cano, J.; Alvarez, S., *J. Phys. Chem. C* **2007,** *111* (2), 618-621.
278. Lavrenova, L. G.; Bogatikov, A. N.; Sheludyakova, L. A.; Ikorskii, V. N.; Larionov, S. V.; Gaponik, P. N., *Zh. Neorg. Khim.* **1991,** *36* (5), 1220-5.
279. Gaponik, P. N.; Karavai, V. P.; Davshko, I. E.; Degtyarik, M. M.; Bogatikov, A. N., *Khim. Geterotsikl. Soedin.* **1990,** (11), 1528-32.

APPENDIX A

PHYSICAL METHODS

Infrared Spectroscopy (IR)

Infrared (IR) spectra were measured as Nujol mulls or solutions between KBr plates on a Nicolet 740 Fourier transform IR spectrometer.

Electrospray Ionization Mass Spectra (ESI-MS)

Electrospray-ionization mass spectra were acquired using a PE Sciex (Concord, Ontario, Canada) API Qstar Pulsar using an Ionwerks time-to-digital converter, TDCx4, for data recording at 625 ps time resolution. Solutions of the samples were electrosprayed and the data were acquired in the positive-ion mode. The ionspray (needle) voltage was held constant at –4.5 kV. The nozzle skimmer potential was set to –10 V to minimize fragmentation in that region. Time-of-flight (TOF) voltages were tuned to optimize the resolving power over the mass range observed, but usually the following parameters were used: grid +338 V, plate –360 V, mirror –960 V, and liner –4000 V. Acquisition were performed with the Analyst QS software.

Optical Reflectivity Measurements

Surface reflectivity measurements were performed on a home built system in the lab of Prof. Corine Mathoniere (ICMB) at temperatures ranges between 10 and 300 K. A tungsten-halogen light source was used (Leica CLS 150 XD, adjustable from 0.5 to 1 W cm^{-2}) at wavelengths between 400 and 1000 nm. All measurements were calibrated against a NIST traceable reflectance standard (sphereOptics, ref SG3054). Optical measurements have been investigated with the CRPP reflectivity set-up. This set-up

collects the light reflected by the sample (that is the sum of direct and diffuse reflected light).

Low-Pressure Gas Adsorption Measurements

Low-pressuregas adsorption measurements were performed by Dan Zhao in Prof H –C Zhou's lab. The measurements were performed with a Beckman Coulter SA 3100 surface area and pore size analyzer. A sample of the CoOs PB was soaked in choroform for 24 h, and the extract was discarded. Fresh choroform was subsequently added, and the microcrystalline sample was allowed to soak for another 24 h to remove H_2O solvates. After the removal of chloroform by decanting, the sample was dried under vacuum at room temperature overnight. Before gas adsorption measurement, the sample was dried again by using the "outgas" function of the surface area analyzer for 1 h at 60 °C. A sample of 100.0 mg was used for N_2 adsorption measurement and was maintained at 77 K with liquid nitrogen. In the hydrogen storage measurement, high-purity hydrogen (99.9995%) and an 80.0 mg sample were used. The regulator and pipe were flushed with hydrogen before being connected to the analyzer. The internal lines of the instrument were flushed three times by utilizing the "flushing lines" function of the program to ensure the purity of H_2. The measurement was maintained at 77 K with liquid nitrogen. The temperature at 87 K was maintained with a liquid argon bath.

Single Crystal X-Ray Crystallography

In a typical experiment, the crystal selected for study was suspended in paraffin oil and mounted on a cryoloop which was placed in an N_2 cold stream. Single crystal X-ray data were collected on a Bruker APEX diffractometer equipped with a CCD detector at 110

K. The data sets were recorded as ω-scans at a 0.3° step width and integrated with the Bruker SAINT software package. The absorption correction (SADABS) was based on fitting a function to the empirical transmission surface as sampled by multiple equivalent measurements. Solution and refinement of the crystal structures were carried out using the SHELX suite of programs and the graphical interface X-SEED. All the structures were solved by direct methods which resolved the positions of all the metal atoms and most of the C and N atoms. The remaining non-hydrogen atoms were located by alternating cycles of least squares refinements and difference Fourier maps. Hydrogen atoms were placed at calculated positions, with the exception of some water molecules, for which the hydrogen atoms were located from the difference Fourier maps. Whenever disordered solvent molecules were present in a structure, their bond distances were restrained to chemically meaningful values. The final refinement was carried out with anisotropic thermal parameters for all non-hydrogen atoms, except for the non-hydrogen atoms of the disordered solvent molecules which were refined isotropically.

Powder X-ray Diffraction (PXRD)

All samples were collected on a holder composed of a single silicon crystal to minimize background interference on a Bruker D8 Advance X-ray diffractometer with LynxEye detector using Cu K-α radiation. Samples were ground and gently pressed onto the surface and the data were collected from 5 – 55° in 2θ at room temperature.

Magnetic Susceptibility Measurements

Magnetic and photomagnetic susceptibility and magnetization measurements were carried out with a Quantum Design SQUID magnetometer MPMS-XL. DC magnetic

measurements were performed with an applied field of 1000 G in the 2 - 300 K temperature range. AC magnetic susceptibility measurements were performed in a 3 Oe AC field at a operating frequencies in the 1-1500 Hz range. Magnetization data were collected in the 0-7 T range starting at zero field at 2 K and were corrected for the diamagnetic contributions calculated from the Pascal constants. Samples were placed into plastic bags and rolled into a cylindrical shape and placed into a plastic tube for measurements. The diamagnetic background of the sample holder is subtracted from previously measurements on the empty bags.

The photomagnetic irradiation of samples utilized a 150 W halogen/tungsten lamp (LEICA CLS 150XD) that was directed into the magnetometer cavity via an optical fiber. Finely ground samples were packed into the photomagnetic sample holder. The incident light intensity power was determined ex-situ to be 575(40) mW cm^{-2}.

Micro-SQUID Measurements

Field-dependent micro-SQUID magnetization scans were performed at 0.04 K with sweep rates varying from 40 G s^{-1} to 2800 G s^{-1} on an individual single crystal at a time, which was oriented on its easy axis of magnetization found by the transverse field method. All measurements were performed with a micro-SQUID array.

APPENDIX B

ADDITIONAL EXPERIMENTS*

A. Electrochemistry of the [{MCl}$_4${Re(triphos)(CN)$_3$}] Cubes

Synthesis of the [{MCl}$_4${Re(triphos)(CN)$_3$}] (M = Mn (**B2**), Fe (**B3**), Co (**B4**), Ni (**B5**), Zn (**B6**)) cubes was performed by the reaction of [Et$_4$N][Re(triphos)(CN)$_3$] (**B1**) and MCl_2 M = Mn, Ni, Zn or $M_4Cl_8(THF)_6$ M = Fe, Co as previosuly described in Dr. Eric Schelter's Ph. D. dissertation. The samples were stored and handled in air.

Solution electrochemical studies performed on **B2,** and **B4-B6** indicate significant metal-metal coupling occurs in these clusters. Redox potentials for the compounds are listed in Table B1. The starting material for the study, compound B**1**, exhibits redox processes assigned to the oxidation of Re^{II} to Re^{III} (+0.19 V), reduction to Re^{I} (-0.74 V), and oxidation of the Re^{III} product to Re^{IV} (+1.12 V).[175] Figure B1 depicts the cyclic voltammagrams (CV) and differential pulse voltammagrams (DPV) for **B6**, which is representative of the behavior observed for complexes **B2,** and **B4-B6**. The cyclic voltammagram for **B4** shows two sets of waves that each contain multiple split waves centered around +0.80 and –0.53 V, which were determined by electrolysis to be quasi-reversible oxidation and quasi-reversible reduction processes respectively. The splitting of these waves in both sets (up to 130 mV for the reduction and 90 mV for the oxidation waves) indicates multiple metal-based redox processes experiencing metal-metal electronic coupling. The DPV waves for **B4** indicate a total of seven waves corresponding to three oxidation- and four reduction processes. The four reduction processes ($E_{1/2}$ = -0.35, -0.48, -0.55, -0.71 V) are reasonably assigned to formally

*Part of Appendix B, Section A is reprinted with permission from Schelter, E. J.; Karadas, F.; Avendano, C.; Prosvirin, A. V.; Wernsdorfer, W.; Dunbar, K. R., **2007**, *J. Am. Chem. Soc* **2007,** 129, 8139-8149, Copyright [2007] by the American Chemical Society.

$Re^{II} \rightarrow Re^{I}$ due to their similarity to the potentials for the reduction potentials of **1** (-0.74 V).

Table B1 – Electrochemical processes (DPV) recorded for $[\{MCl\}_4\{Re(triphos)(CN)_3\}]$ Potentials reported versus Ag/AgCl reference electrode.

	B1	**B2**	**B3**	**B4**	**B5**	**B6**
E_{ox} (V)	+1.12	+1.28	+1.42[c]	+0.89	+1.20	+1.20
	+0.19	+1.01	+1.26	+0.80	+0.98	+1.12[c]
		+0.71	+1.00	+0.71	+0.81	+1.00
		+0.18[c]	+0.75[c]			+0.78
			+0.58			+0.70
			+0.23			
E_{red} (V)	-0.74	-0.03	-0.03[b]	-0.35	+0.33[c]	+0.34[c]
		-0.32[c]	-0.40	-0.48	+0.09	+0.12[c]
		-0.48[c]	-0.75	-0.55	-0.09	+0.04[c]
		-1.00[c]		-0.71	-0.18	-0.08[c]
		-1.24[c]			-0.31[c]	-0.19
					-0.39	-0.36
					-0.58[c]	-0.53
						-0.68
						-1.15[c]

All processes are one electron unless otherwise stated. [b]Two closely-spaced one-electron processes. [c]Weak current signal presumably due to chemical product formation following a redox event.

The rhenium-iron cluster, (**B3**), exhibits a markedly different electrochemistry from the other members of the series (Figure B2). Figure B2 shows the CV and DPV waves for this complex which reveals the large number of quasi-reversible and reversible redox events that occur in this cluster. As discussed previously, upon formation, compound **B3** exists in the formal oxidation states of Re^{I} and Fe^{III}.[276] The four couples at +1.26, +1.00, +0.58, and +0.23 V are assigned as $Re^{I} \rightarrow Re^{II}$ oxidation processes as judged by electrolysis experiments, while the three couples at –0.03, -0.40

and –0.75 V are assigned as $Fe^{III} \rightarrow Fe^{II}$ reductions. DPV also revealed that the process at –0.03 V involves two electrons, presumably the result of two closely spaced one-electron process waves. The electrochemistry for this cluster is remarkable in that there is very little decomposition of the cluster throughout the potential range of the eight electron changes observed on the window of the experiment, as judged by the relative current of the processes at +1.42 and +0.75 V, and the fact that the CV can be cycled without the appearance of new waves or disappearance of any waves.

Reactions were attempted to chemically reduce or oxidize compound **B3** and isolate single crystals of the products, but so far no crystals were obtained. This goal is worth pursuing due to the possibility of engendering SMM behavior in the Re_4Fe_4 cluster given that the complete oxidation of the Re^I ions would result in an electronically

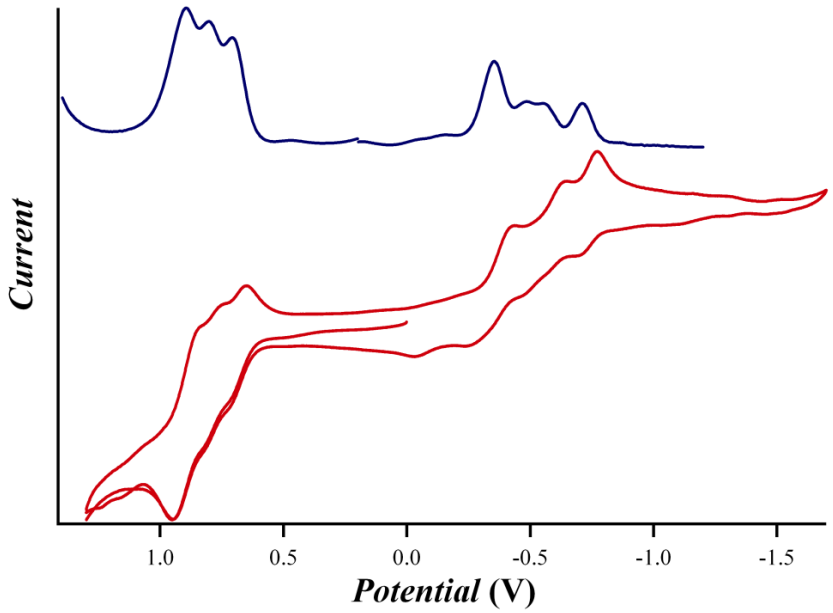

Figure B1. Electrochemical response (top: DPV, bottom: CV) of $[\{CoCl\}_4\{Re(triphos)(CN)_3\}]$ (B**6**) recorded in 0.1 M $[^nBu_4N][PF_6]$ / CH_3CN. Potentials reported versus Ag/AgCl reference electrode.

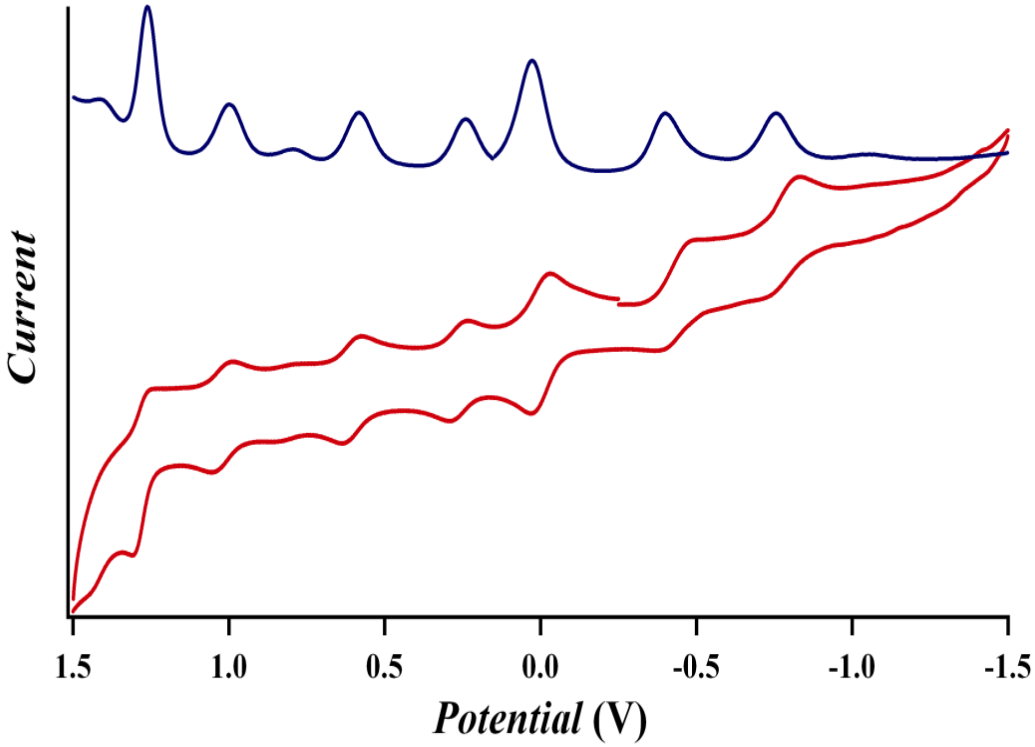

Figiure B2. Electrochemical response (top: DPV, bottom: CV) of [{FeCl}$_4${Re(triphos)(CN)$_3$}] (**B3**) recorded in 0.1 M [^{n}Bu$_4$N][PF$_6$] / CH$_3$CN. Potentials reported versus Ag/AgCl reference electrode.

analogous compound to the Re_4Mn_4 cluster which exhibits SMM behavior. In addition, the electrochemistry of **B3** suggests that the electrons are significantly delocalized, therefore any change in the electronic nature of the compound via reduction or oxidation can potentially lead to interesting magnetic behavior.

B. Reactions with $[Ph_4As]_2$[1,4-dicyanamidobenzene] and $[Ph_4As]_2$[1,3-dicyanamidobenzene].

According to the theoretical studies,[222, 277] dimers of M^{III} ions with deprotonated 1,4-dicyanamidebenzene dianion $[1,4\text{-dicyd}]^{2-}$ (Scheme B1) should exhibit strong antiferromagnetic coupling between metal ions. On the other hand, dimers with the 1,3-dicyanamidebenzene dianion $[1,3\text{-dicyd}]^{2-}$ (Scheme B1) will show strong ferromagnetic coupling. Here in, a report on the preliminary results obtained in this endeavor are presented.

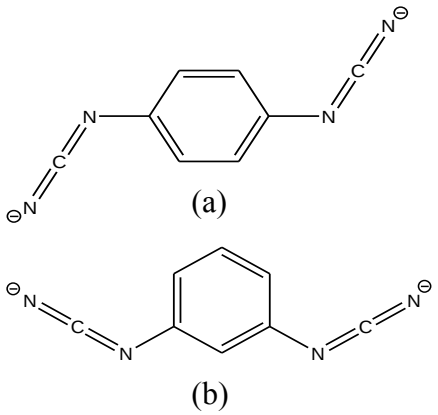

Scheme B1. a) 1,4-dicyd; b) 1,3-dicyd

EXPERIMENTAL

Starting materials. The 1,3-phenylenediamine, 1,4-phenyldiamine, and sodium azide, starting materials (Aldrich) were used as received. Reagent grade glacial acetic acid and triethyl orthoformate, $HC(OEt)_3$ (Acros) were used as recieved. Unless stated otherwise, all compounds were prepared under anaerobic conditions. The ligands H_2[1,4-dicyanamidebenzene] (1,3-dicyd) and H_2[1,3-dicyanamidebenzene] (1,4-dicyd) and the $[Mn(salen)(MeOH)_2][ClO_4]$ complex were prepared following a previously reported method.[278, 279] Only the experimental details for the $[Ph_4As]_2$[1,3-dicyd] are highlighted, but exactly the same steps were followed for the synthesis of $[Ph_4As]_2$[1,4-dicyd].

***meta*-phenyl-bistetrazole (B7).** An amount of 1,3-phenylenediamine (10.8 g, 0.1 mol) and sodium azide (15.6 g, 0.240 mol) was stirred in 50 mL of $HC(OEt)_3$ in a 500 mL round bottom flask in air. Slow addition of 100 mL of glacial acetic acid followed (5 drops/sec). The brown mixture quickly turned yellow, and after 15-20 s, as more acetic

acid was added, yellow precipitate separated from the brown solution. After the addition of acetic acid was complete, the mixture was heated ~ 100 °C until a clear brown solution was obtained. After 10-20 min of heating the brown color of the solution disappeared and a large amount of off-white precipitate formed. The literature procedure call for stirring the reaction for 3 h, but no discernible change of the reaction occurred after the precipitation of the off-white solid. After 3 h, the reaction was poured into 1 L of stirring water. The off-white precipitate was filtered through a course frit, washed with 200 mL of water, and dried in vaccuo overnight. (Yield = 20.0 g, 93.5 %)

[1,3-dicyanamidebenzene]H_2 (B8). In a 100 mL flask 2.18 g of KOH were dissolved in 10 mL of *i*-PrOH. The mixture was stirred at room temp for 30 min. the flask was the placed in a70-80 °C oil bath, and a suspension of **B7** (2.14 g, 0.01 mol) in 10 mL of DMSO was poured into the flask. Rapid evolution of N_2 was observed. The solution was refluxed at 80 °C for 24 h. The red solution was cooled down to room temperature, and 40 mL of water added to the solution resulting in a clear red solution. To the clear solution ~18 mL of 19% HCl (0.09 mol) were added, and the mixture stirred for ~ 5 min leading to the precipitation of a tan solid. The solid was filtered, washed with copious amounts of water, and dried in vaccuo over P_2O_5 for 24 h. (Yield = 1.04 g, 66 %)

[Ph_4As]$_2$[1,3-dicyanamidebenzene] (B9). A sample of **B8** (0.5 g, 3.16 mmol) and NaOH (3.07 g, 76.8 mmol) were dissolved in 30 mL of deoxygenated water. An amount of (Ph_4As)Cl (2.6 g, 5.95 mmol) was dissolved in 30 mL of 2.5 M NaOH. The solution of **B8** was added via cannula to the solution of (Ph_4As)Cl resulting in immediate precipitation of a yellow solid. The solvent was decanted and the remaining solid

washed with 20 mL (x3) of ice-cold deoxygenated water, and dried in vacuo. The sample was heated in a water bath until all the solid turned red. The solid was then recrystallized from acetonitrile. The crude product was dissolved in 80 mL of acetonitrile and heated slightly to dissolve all the material. The hot green mixture was filtered through celite via cannula and concentrated to ~ 40 mL of acetonitrile. The flask was then placed in the freezer in the dry-box, and a crop of crystals were isolated after ~ 1 week. The crystals were isolated by filtration in the box and washed with ether. The remaining filtrate was placed back in the freezer to isolate more product. This was repeated 2 more times to obtain a total of 2.09 g of crystalline product. (Yield = 72 %)

[Mn(salen-type)(MeOH)]$_2$[1,4-dicyd] (B10: salen; B11: salphen). To a solution of [Mn(salen-type)(MeOH)][ClO_4] (0.253 g, 0.434 mmol) in 70 mL of dry MeOH was added an acetonitrile solution (20 mL) of [Ph_4As]$_2$[1,4-dicyd] (0.20 g, 0.217 mmol) via cannula. Immediately after the solutions were mixed a crystalline precipitate was obtained. The solid was filtered in air, washed with 3 x 5 mL of MeOH and 3 x 5 mL of

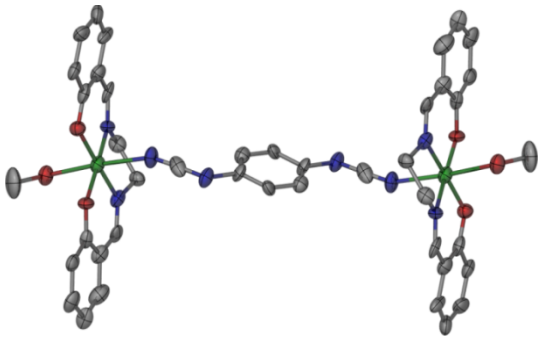

Figure B3. Crystal structure of [Mn(salen)(MeOH)]$_2$[1,4-dicyd]. Thermal ellipsoids represented at 50 % probability.

diethyl ether, and vaccum dried. Single crystals suitable for single crystal X-ray crystallography were obtained by the slow addition of the $[Ph_4As]_2$[1,4-dicyd] solution. Yield = 130 mg (63 %) for **B10** and 110 mg (59 %) for **B11**.

Table B2. Crystal structural data and refinement parameters for compound **B10**.

Formula	[Mn(salen)(MeOH)]$_2$[1,4-dicyd]
Space group	$P2_1/c$
Unit cell	a = 9.633(2) Å b = 18.623(2)Å c = 12.664(3)Å β = 107.71(1)°
Unit cell volume, V	2164.2(8)Å^3
Z	4
Density, ρ_{calc}	1.262 g/cm^3
Abs. coeff., μ	0.519 mm^{-1}
Crystal color and habit	Orange-red plate
Crystal size, mm^3	0.22x0.16x0.07
Temperature	110 K
Radiation, λ	Mo-Kα, 0.71073 Å
Min. and max. θ	1.14 to 27.22 °
Reflections collected	9744 [R_{int} =0.094]
Independent reflections	4955
Data/parameters/restraints	4955/262 /0
R [$F_o > 4\sigma(F_o)$]	R_1 = 0.083 wR_2 = 0.1614
G.o.f. on F^2	1.254

The EPR signal shown in Figure B4 is indicative of the presence of a radical species. The magnetic suceptibility curve has a room temperature χT value of 6.9 emu*K/mol, which is significantly higher than two isolated Mn^{III} ions (S=2; 6 emu*K/mol). These preliminary results suggest that the dicyanamidebenzene bridging ligand is present in its radical form ([1,4-dicyd]$^-$) in the final product, {[Mn(salen)(MeOH)]$_2$[1,4-dicyd]}. Further characterization is necessary to determine the oxidation state of the Mn ions in both compounds.

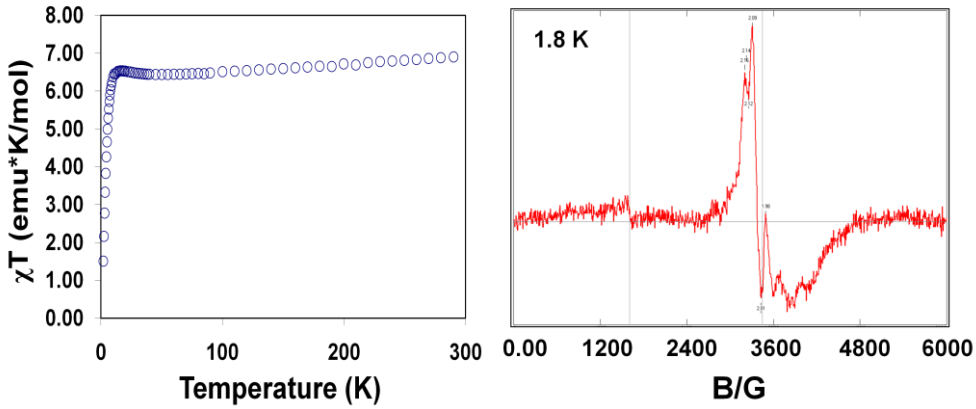

Figure B4. (a) Temperature dependence of the χT of **B10** and (b) EPR spectrum collected at 1.8 K for **B10**.

The results obtained so far indicate that it is possible to synthesized compounds that resemble the theoretical models used by Alvarez et. al. in their calculations. Further synthetic work should involve the synthesis of dinuclear clusters with other transition metals, e.g. Fe^{III}, in order to elucidate the electronic nature of the bridging [1,4-dicyd] ligand. Of great interest to this project is the electrochemical behavior of these systems given that information of the electronic nature of the metal ions and the ligand can potentially be understood through this technique.

VITA

CAROLINA AVENDAÑO
Department of Chemistry
Texas A&M University
P.O. Box 30012
College Station, TX 77842-3012

EDUCATION

Texas A&M University, College Station, TX, USA

Ph.D. Chemistry

Dissertation: Cyanide Bridged Molecular Magnetic Materials with Anisotropic Transition Metal Ions: Investigation of Bistable Magnetic Phenomena.

Advisor: Prof. Kim R. Dunbar

Viterbo University, La Crosse, WI, USA

B.S.Chemistry (*Summa Cum Laude*, 2004)

Minors in Biology and Mathematics

RESEARCH EXPERIENCE

Texas A&M University, College Station, TX, USA

Research Assistant, Department of Chemistry (2004-2010)

Teaching Assistant, Department of Chemistry (2004-2006, 2007-2009)

NSF-GK 12 Fellow, Department of Chemistry (2006-2007)

NSF-REU, Department of Chemistry (Summer 2003)

Advisor: Dr. Kim R. Dunbar

University of Minnesota, Minneapolis, MN, USA

LANDO-NSF REU, Department of Chemistry (Summer 2002)

Advisor: Dr. Andrew Taton

AFFILIATIONS

American Chemical Society (2003 – Present)

Phi Lambda Upsilon Chemistry Honors Society (2006 – Present)